UNIVERSIDADE FEDERAL DE MINAS GERAIS

PROGRAMA DE PÓS-GRADUAÇÃO EM FÍSICA

LUDMILA MARIA DINIZ LEROY

Valence tautomerism in Cobalt o-dioxolene complexes

BELO HORIZONTE

2021

LUDMILA MARIA DINIZ LEROY

Valence tautomerism in Cobalt o-dioxolene complexes

Tese apresentada ao Programa de Pós-Graduação em Física do Instituto de Ciências Exatas da Universidade Federal de Minas Gerais como requisito parcial para obtenção do título de Doutor em Ciências

Orientador: Dr Carlos Basílio Pinheiro
Coorientador: Dr Majed Chergui

Belo Horizonte

2021

UNIVERSIDADE FEDERAL DE MINAS GERAIS
INSTITUTO DE CIÊNCIAS EXATAS
PROGRAMA DE PÓS-GRADUAÇÃO EM FÍSICA

ATA DE DEFESA DE TESE

ATA DA SESSÃO DE ARGUIÇÃO DA 384ª TESE DO PROGRAMA DE PÓS-GRADUAÇÃO EM FÍSICA, DEFENDIDA POR LUDMILA MARIA DINIZ LEROY orientada pelo professor Carlos Basílio Pinheiro e coorientada pelo professor Majed Chergui, para obtenção do grau de **DOUTORA EM CIÊNCIAS, área de concentração física**. Às 13:00 horas de quinze de julho de dois mil e vinte e um reuniu-se, por videoconferência, a Comissão Examinadora, composta pelos professores **Carlos Basílio Pinheiro** (Orientador - Departamento de Física/UFMG), **Majed Chergui** (Coorientador - Laboratory of Ultrafast Spectroscopy/EPFL), **Ângelo Malachias de Souza** (Departamento de Física/UFMG), **Klaus Krambrock** (Departamento de Física/UFMG), **Javier Alcides Ellena** (Instituto de Física de São Carlos/USP) e **Eduardo Granado Monteiro da Silva** (Instituto de Física Gleb Wataghin/UNICAMP) para dar cumprimento ao Artigo 37 do Regimento Geral da UFMG, submetendo a Mestre **LUDMILA MARIA DINIZ LEROY** à arguição de seu trabalho de Tese de Doutorado, que recebeu o título de **"Valence tautomerism in Cobalt o-dioxolene complexes"**. A candidata fez uma exposição oral de seu trabalho durante aproximadamente 50 minutos. Após esta, os membros da comissão prosseguiram com a sua arguição, e apresentaram seus pareceres individuais sobre o trabalho, concluindo pela aprovação da candidata.

Belo Horizonte, 15 de julho de 2021.

Prof. Carlos Basílio Pinheiro   Prof. Majed Chergui

Orientador da estudante   Coorientador da estudante

Departamento de Física/UFMG   Laboratory of Ultrafast Spectroscopy/EPFL

Prof. Ângelo Malachias de Souza   Prof. Javier Alcides Ellena

Departamento de Física/UFMG   Instituto de Física de São Carlos/USP

Prof. Klaus Krambrock   Prof. Eduardo Granado Monteiro da Silva

Departamento de Física/UFMG   Instituto de Física Gleb Wataghin /UNICAMP

Candidata: Ludmila Maria Diniz Leroy

Referência: Processo nº 23072.236272/2021-31   SEI nº 0839322

"If I have seen further, it is by standing on the shoulders of Giants."

Newton, Isaac

Preface and Acknowledgements

A decade ago, I did not know what a doctorate degree consisted of and I did not wish for one either. Just the dream of a university degree already seemed far from reach, but it got closer once I got accepted to pursuit a bachelor's degree in Physics, at UFMG. For some, education is the only door. When I look back, I see how privileged I was to be one winner in the most capitalist lottery: the one that does not provide for all with the same opportunities. I am still not sure on how to be allured by a new title, but I am (and I always have been) delighted with the trajectory.

I was born and raised in a little town in Minas Gerais, Brazil. There was not much going on there (there still isn't) and the life perspectives were not exactly interesting either. But my mother made my brother and I study hard and always said that a university degree was the only requirement we had from her. Both of us went all the way to the PhD degree. Obrigada, mãe. E obrigada rô, meu melhor amigo. Obrigada, pai. Obrigada, Rafa, anjinho da dindinha. Eu estive longe, mas estivemos sempre juntos.

This doctorate thesis wouldn't have even been envisioned if not for my research initiation at LabCri UFMG, in September 2011. And for that I thank my advisor, Dr. Carlos Pinheiro, who believed in my potential and with whom I learned much beyond scientific contents and lab stuff. Thank you, Carlos, for the physics and life lessons, all the discussions and arguments, criticisms and praises, and thousands of red comments on Microsoft Word documents. LabCri was my second home, where I found my second family. I would like to acknowledge all the lab members whose path crossed with mine, for all I learned from you and all the coffee we had.

I have always been a tough advisee; I am sure about that. Determined to go for whatever was needed, therefore stubborn, insistent, and demanding (specially with myself). And going from Belo Horizonte to Switzerland came from one of these simple requests: "Chefe, I would like to work in a Free Electron Laser for my PhD.". *haha* funny. And I did. And for that I dearly thank Carlos and Majed. Dr. Majed Chergui hosted me in the LSU group and sent me to PSI, where I also joined the ALVRA group, SwissFEL. This was an unprecedent opportunity, and I am immensely thankful for it. For all the beamtimes, night shifts and python scripts.

Of course, I could not possibly write here the names of all people that, in a way or another, contributed and participated in this story. However, the research reported in this thesis counted on a group of clever scientists which I had the privilege to work with. Dr Marcos Ribeiro, Dr David Shultz, Dr David Scammon, in the chemistry lab. Dr Leonardo Calazans, in python work and Skype sessions. Dr Camila Bacellar, in LSU, PSI, beamtimes and beamtimes. MS Hui-Yuan Chen, Dr Joanna Hughes, Ellen Kiens, in LSU. Dr Simone Alexandre and MS Lucas

Pimenta, in DFT collaboration. Dr Andreij Sienkiewicz, in ESR experiments. MS Thiago Francisco, Dr Florian Dworkowski and Dr Ekaterina Pomjakushina, in XRD experiments.

Honestly, maintaining some mental sanity in a PhD in Physics is a degree by itself. Thankfully, good friends and colleagues made it incommensurably easier. Coffees, bars, beers, concerts, therapy, dance choreographies, hikes, photographs, and JamClub are the hidden chapters of this thesis.

Abstract

Bistability in the form of valence tautomerism (VT), that is, the combination of mixed valence and spin crossover processes, is present in numerous metal complexes that candidate to be used as electronic and magnetic switchers. For cobalt metallic complexes in which a redox-active ligand participates in the electron transfer, the cobalt atom alternates between the low-spin (d^6 Co^{III}) and high-spin (d^7 Co^{II}) states as a function of external stimuli in a reversible fashion. There has been an effort to understand, stimulate and control the VT in solid state and even to design complexes that candidate to be engineered as devices. In this work, two cobalt complexes and their VT properties are investigated. The controlled light-induced VT in single crystals of Co(dioxolene)$_2$(Cyan-pyridine)$_2$ is demonstrated, for the first time with an 80% interconversion yield of metastable states induced by visible light irradiation at low temperature. Additionally, Co(dioxolene)$_2$(pyridine)$_2$ was investigated for three different crystal forms and in solution, benchmarking key environmental conditions that modulate the VT for such complex. The results presented in this thesis for solid state and solutions illustrate the robustness and versatility of cobalt metal complexes as electronic labile materials.

Keywords: bistability, valence tautomerism, cobalt complexes.

Resumo

Biestabilidade na forma de tautomeria de valência (VT), que consiste da combinação dos processos de valência mista e *spin-crossover*, está presente em numerosos complexos que podem ser usados em chaveamento eletrônico e magnético. Em complexos metálicos de cobalto nos quais um ligante ativo-redox participa na transferência eletrônica, o íon de cobalto alterna entre os estados de *low-spin* (d^6 Co^{III}) e *high-spin* (d^7 Co^{II}) de forma reversível em função de estímulos externos. Nas últimas décadas, tem havido um esforço para entender, estimular e controlar o VT em estado sólido e até mesmo para desenhar moléculas candidatas a serem usadas como dispositivos. Neste trabalho, dois complexos de cobalto e o VT destes foram investigados. O VT controlado e induzido por luz em monocristais de Co(dioxolene)$_2$(Cyan-piridina)$_2$ foi aqui demonstrado, pela primeira vez com 80% de rendimento na indução de estados metastáveis por luz visível em baixa temperatura. Adicionalmente, Co(dioxoleno)$_2$(Piridina)$_2$ foi investigado em três formas cristalinas distintas e em solução, possibilitando a avaliação das condições chave que modulam o VT nesse complexo. Os resultados apresentados nesta tese para estado sólido e soluções ilustram a robustez e a versatilidade dos complexos metálicos de cobalto como materiais eletronicamente lábeis.

Palavras-chave: biestabilidade, tautomeria de valência, complexos de cobalto

Contents

1 Introduction

Smart materials are those which respond to stimuli from the surroundings having one or more of their properties significantly changed in a controlled manner. Among these, materials that present electronic bistability in solid state are promising to be used as sensors, signal processors and storage devices. Moreover, bistability in the form of valence tautomerism (VT) couples charge transfer and spin-crossover processes as a response to external stimuli, and controlling such response is key for engineering switcher devices. Cobalt dioxolene complexes are very well known for their VT and have been thoroughly studied over the last 30 years. The investigation of VT in such materials is the fundament of the research reported herein.

My doctoral work focused on the investigation of the valence tautomerism on the cobalt dioxolene complexes Co($diox$)$_2$(4-CN-Py)$_2$ and Co($diox$)$_2$Py$_2$ (where $diox$ = 3,5-di-tert-butyl-semiquinone/3,5-di-tert-butyl-cathecolate, Py = pyridine and 4-CN-Py = Cyan-pyridine) in solid state and in solution. This thesis constitutes the final report of this research, developed during my doctoral studies at the Physics Graduate school of Universidade Federal de Minas Gerais (UFMG), Brazil, from August 2017 to June 2021. My doctoral studies were advised by Dr. Carlos Pinheiro at the Laboratory of Crystallography, LabCri, UFMG. Part of the work here reported was performed during my interchange studies in Switzerland, where I was hosted by Dr. Majed Chergui in the Laboratoy of Ultrafast Spectroscopy (LSU) at the École Polytechnique Fédérale de Lausanne (EPFL) – Switzerland. While in Switzerland, I was based at PSI, where the ALVRA group hosts some of the members of the LSU X-ray team.

In this work, multiple experimental techniques were used, such as single crystal X-ray diffraction, electronic spin resonance, UV-visible spectroscopy, and transient absorption spectroscopy in pursuit of characterizing the stimulated VT and understanding key factors that play a role in allowing or forbidding such transition. Chemistry laboratory skills were also required in the synthesis and crystallization of the complexes. Therefore, the investigation of VT in Co($diox$)$_2$(4-CN-Py)$_2$ and Co($diox$)$_2$Py$_2$ constituted a very robust research project that involved several collaborations and experiments designed to be performed in large scale facilities (synchrotrons). The development of this doctoral project counted on LabCri, UFMG – Brazil, LSU, EPFL – Switzerland, the Shultz Lab, at North Carolina State University (NCSU) – USA, the Swiss Light Source (SLS) and the ALVRA group at Paul Scherrer Institute (PSI) – Switzerland, the Diamond Light Source – UK, and the Laboratory of Electronic Structure, UFMG.

This thesis is organized in 7 chapters. Chapter 1 brings a theoretical perspective of the valence tautomerism property, which is based on experimental results reported in the literature over the last three decades, and Chapter 2 gives a brief description of the fundaments of the experimental methods used in the complexes characterization along with examples of their

application in characterizing the VT. Chapters 3 and 4 report the motivation, experiments and results on the investigation of the VT in Co(*diox*)$_2$(4-CN-Py)$_2$ and Co(*diox*)$_2$Py$_2$, respectively. The final conclusion constitutes Chapter 5, and references listed in Chapter 6. Appendices, supplementary files and information can be found in Chapter 7. The results reported in Chapter 3 have been published in the Inorganic Chemistry journal, in a manuscript entitled "Controlled Light and Temperature Induced Valence Tautomerism in a Cobalt-o-Dioxolene Complex" https://doi.org/10.1021/acs.inorgchem.1c00638.

1. Valence tautomerism in Cobalt o-dioxolene complexes

1.1 Valence tautomerism

Electronic labile materials constitute a class of materials whose electronic structures can change dramatically and reversibly due to external factors such as temperature, pressure, illumination, irradiation, electric and magnetic fields. Such materials are inherently bistable and switch between two electronic forms under the processes named mixed-valence (MV), spin-crossover (SC) and valence tautomerism (VT). The MV consists of an interaction between two metal ions with different oxidation states but mediated by a ligand. The SC defines the entropy-driven change in spin multiplicity from high-spin (*hs*) to low-spin (*ls*) and vice-versa on transition metal ions, such as Cr^{II}, Mn^{III}, Fe^{II}, Fe^{III}, Co^{II} and Co^{III}. Finally, the VT can be seen as an intramolecular combination of the MV and SC processes within the same metallic center[1]. Materials that present electronic lability in the form of valence tautomerism in solid state can possibly be used as sensors, signal processors and storage devices[2,3]. Therefore, there has been an effort to understand, stimulate and control the VT in crystals[4–7], and even to design molecules[8] that candidate to be engineered as devices.

For the specific case of materials that have a cobalt metallic center, the VT can be seen as a SC that involves redox-active ligands that allow for the electron transfer. Such materials form a large family of mono and dinuclear complexes, coordinated by dioxolene redox-active ligands and mono, bi and tridentate nitrogen-based ancillary ligands[4]. In these complexes, within the metallic center, the Co d-orbitals change between the low-spin (d^6 Co^{III}) and high-spin (d^7 Co^{II}) configurations as a function of external stimuli, such as temperature [9,10], pressure [11], visible light [12–14], soft X-rays [15], hard X-rays [16] and electric and magnetic fields[6]. The redox-active ligand participates in such transition exchanging an electron with the metallic center. Most commonly, the redox-active ligand in cobalt complexes consists of dioxolene (*diox*) molecules in its semiquinone (SQ) and catecholate (Cat) forms (Figure 1.1), and the electron transfer involves either the oxidation of Co^{II} by a SQ or the reduction of Co^{III} by a Cat. The generic VT equilibrium is illustrated in Figure 1.2.

The two molecular species accessed during the VT interconversion display quite different macroscopic properties, with fundamental differences in their optical and magnetic responses, as will be discussed in the following sections and in Chapter 2.
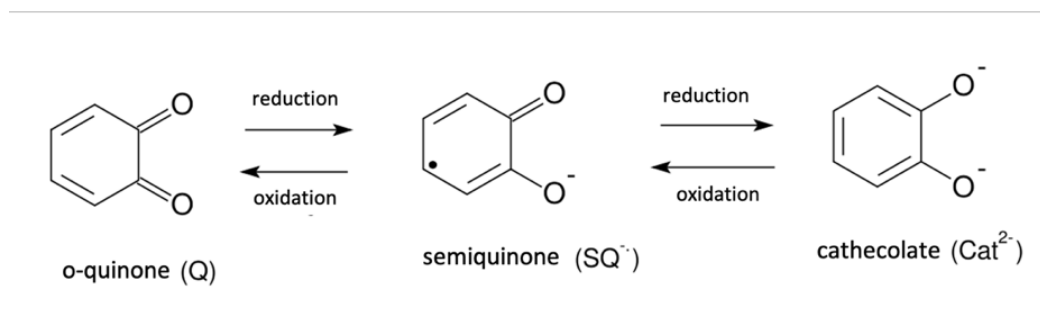
Figure 1.1 – The three different oxidation forms possible for the o-quinone molecule. (Adapted from [17])
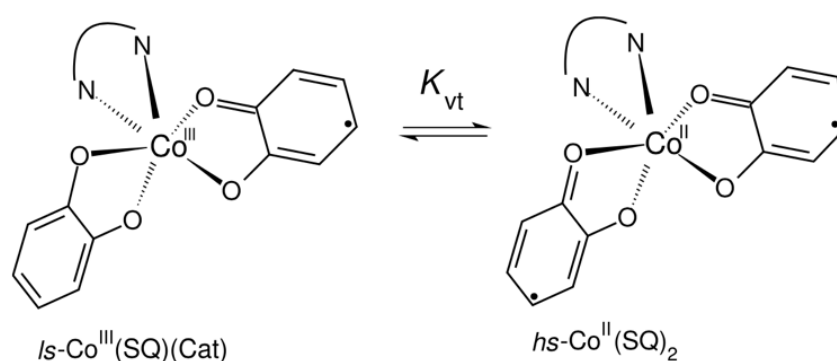
Figure 1.2 – The valence tautomerism equilibrium in Co(dioxolene)$_2$(N-ligand)$_X$ complexes, where X=1 or 2. (Adapted from [17])

1.2 Molecular orbitals and energy perspective

The description of the VT from a molecular orbital (MO) perspective can be simplified if we ignore the nitrogen orbitals and consider the MO's formed by the cobalt and dioxolene orbitals only. The cobalt t_{2g} d-orbitals (d_{xy}, d_{xz}, d_{yz}) mix with the dioxolene π^* orbitals in a π-fashion, and the remaining e_g metal d-orbitals (d_{x2-y2}, d_{z2}) mix with the dioxolene oxygen lone pair orbitals in a σ-fashion (Figure 1.3). Such mixing of orbitals allows for the interaction between metal and ligand, though it is moderate in such a way that results in the prevalence of the metal-based and ligand-based character. These features of the MO's formations are key for the VT to take place, because the electrons are still localized.

The cobalt atom in its *ls*-Co^{III} form assumes the $(\pi_{yz})^2(\pi_{xz})^2(\pi_{xy})^2$ electronic configuration and the *hs*-Co^{II} tautomer form assumes the $(\pi_{yz})^2(\pi_{xz})^2(\pi_{xy})^1(\sigma^*_{x2-y2})^1(\sigma^*_{z2})^1$ configuration. The latter occupation of σ orbitals result in 0.16 – 0.22Å longer bond lengths between the Co atom and its first neighboring atoms[4]. The expansion/contraction of the cobalt coordination sphere leads to considerable changes in the crystallographic parameters of crystals of the complexes.
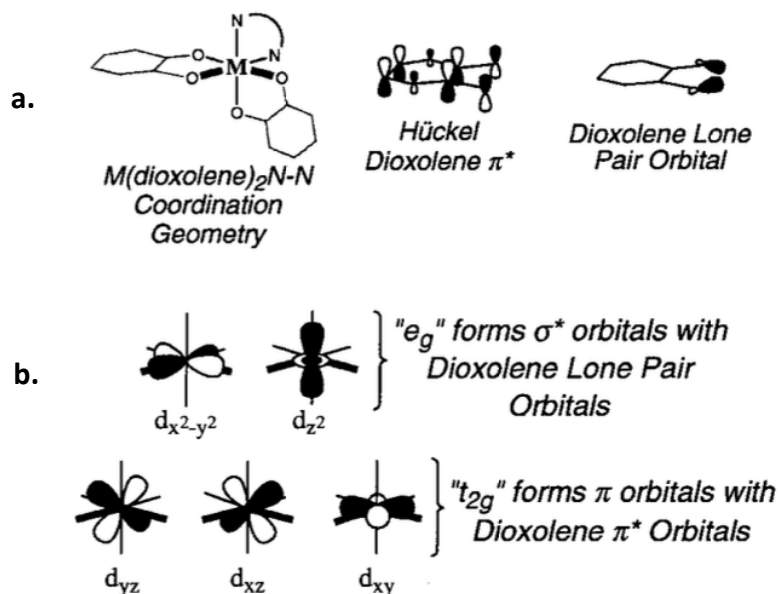
Figure 1.3 –a. Molecular orbitals for the dioxolene. b. Molecular orbitals for the d electrons of the Cobalt atom. (from [1])

It is known, however, that the nitrogen based auxiliary ligands also modulate the VT interconversion, being the key to the different critical temperatures ($T_{1/2}$) of a series of compounds [10,18,19]. This modulation was associated to the impact that the auxiliary ligand has on the reduction potential of the complexes, once more positive reduction potentials mean low-lying N-N π^* LUMOs. The N-N π^* LUMO interacts weakly with the occupied t_{2g} orbital (also π-type) of the metal, but such interaction is enough to lower the overall binding energy and to maintain the necessary field splitting that sustains electron rich *hs*-Co^{II}. The stabilization of the *hs*-Co^{II} species consequently lowers the $T_{1/2}$[20].
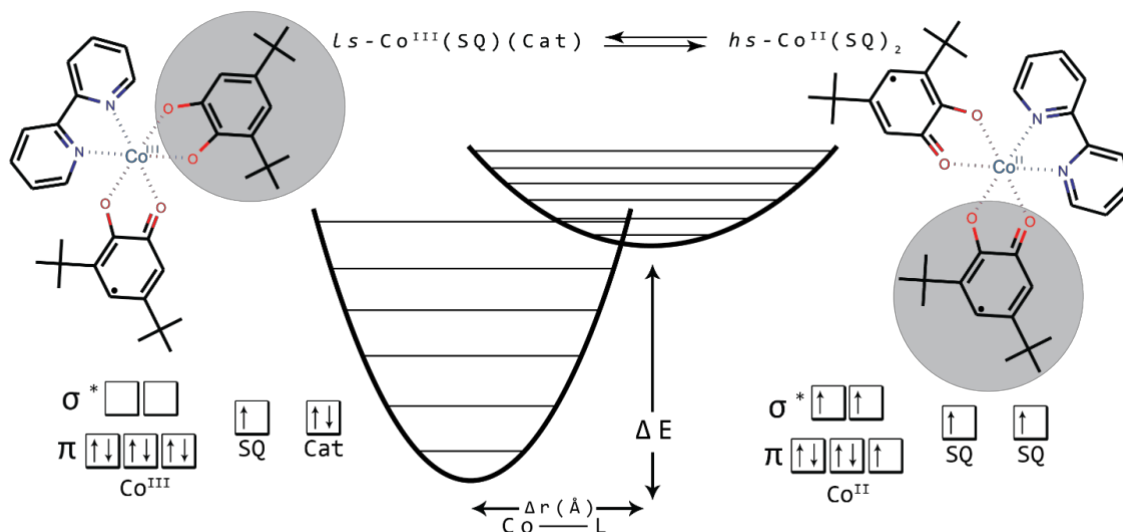
Figure 1.4 – Energy diagram for the ls-Co^{III} and hs-Co^{II} forms of Co(diox)$_2$(Phen) and electronic distribution in the metal-diox MO's. The highlighted dioxolene ligands illustrate the change from Cat to SQ once the electron transfer takes place. (Figure from [17])

The VT process can be represented in an energy diagram in which the states are represented by a harmonic potential well and the reaction coordinate is equivalent to the totally symmetric stretching of the Co-L (L stands for any ligand atoms) vibrational modes (Figure 1.4). The energy difference between the two lowest energy levels is given by $\Delta E \cong \Delta H = \Delta H_{hsCo^{II}} - \Delta H_{lsCo^{III}}$, which has experimentally been shown to be $\Delta E \cong k_B T$ [1,21,22]. Figure 1.4 illustrates the VT within a Co(*diox*)$_2$(Phen), where Phen = 1,10-phenantroline, from the energy and bond contraction/stretching perspectives, and it also shows the spin reorganization within the $e_g (\sigma^*)$ and $t_{2g} (\pi)$ MO's.

1.3 Nitrogen-based auxiliary ligands and VT

The valence tautomerism in cobalt dioxolene complexes involves a charge transfer between the metal center and the redox active ligand which is described in terms of the molecular orbitals formed between them, as described in the section above. In this sense, the nitrogen based ancillary ligand is described to modulate the VT, playing a role in the stabilization of *hs*-Co^{II} species, but not directly involved in the charge transfer[1,4,13]. Nevertheless, the ancillary ligand is determinant on the VT dynamics and has been an important target of VT investigation research over the years.

For instance, in the work of Jung *et al.*, 1997[23], the bidentate (bis)pyridine ancillary ligand with O, S, Se or Te as bridging atom (Figure 1.5) formed Co(*diox*)$_2$ complexes where *diox* = 3,6-di-tert-butyl-1,2-benzoquinone. Magnetic measurements of crystals of the 4 complexes as a function of temperature show a drastic impact of the bridging atom on the the T$_{1/2}$. Such modulation was associated to a low-energy shift in vibrational modes with increasing heteroatomic mass and a consequent increase in entropy.

X = O, S, Se, Te
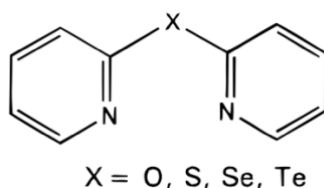
Figure 1.5 – (bis)pyridine ligand with X as bridging atom. X = O, S, Se or Te in py$_2$O, py$_2$S, py$_2$Se and py$_2$Te respectively. (Figure from [23])

The stabilization of *hs*-Co^{II} species in lower temperatures for the heavier bridging atoms was shown to hold true for S, Se and Te (Figure 1.6), but O-(bis)pyridine particularly deviates from this rule. This special case brough out planarity of the ancillary ligand as another factor that modulates the VT, because the stabilization of *ls*-Co^{III}(*diox*)$_2$(Py$_2$O) is dependent on the py$_2$O

folded form (Figure 1.7), in such a way that the VT conversion drives a severe geometrical change of the complex units and disrupts the solid-state structure of crystals.
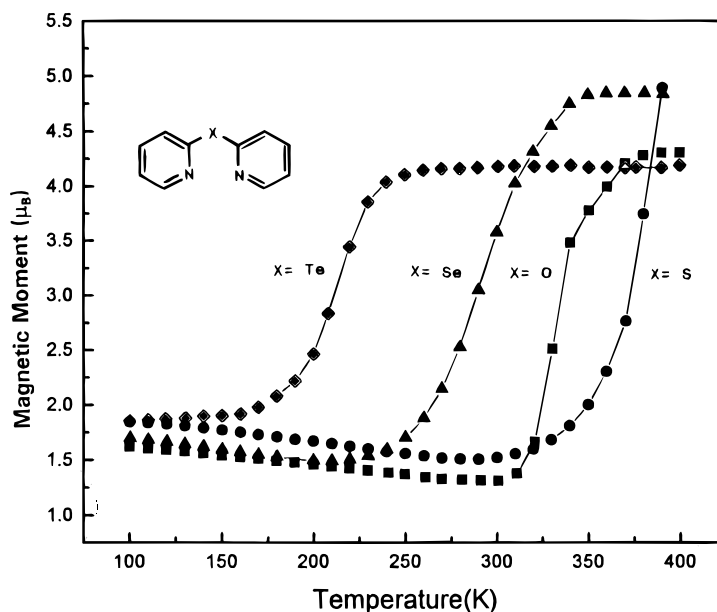
Figure 1.6 – Temperature dependent magnetic measurements on crystals of Co(diox)$_2$[X(bis)pyridine], with X = O, S, Se or Te. The X-(bis)pyridine ligand is also illustrated. (Figure from [23])
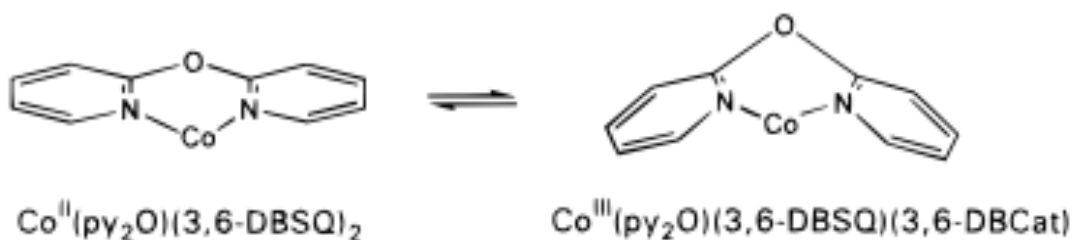
Figure 1.7 – planar and folded py$_2$O conformation equilibrium in the VT interconversion of Co(diox)$_2$(Py$_2$O). (Figure from [23])

For monodentate nitrogen based ancillary ligands, on the other hand, and extensive investigation of *trans*-Co(*diox*)$_2$ complexes with multiple pyridine derived ancillary ligands (PyL) has been reported by Schmidt *et al.*, 2010[14]. Py, (4-O-Me-Py), (4-Me-Py), (4-CN-Py), (4-Br-Py) and (4-NO$_2$-Py) were utilized as ancillary ligands yielding the complexes whose generic structure is shown in Figure 1.8. Temperature dependent magnetic susceptibility of crystals of each of these complexes showed that the ancillary ligand was determinant for allowing/forbidding the VT interconversion (Py, (4-O-Me-py), (4-Me-py) complexes show no VT), and also for modulating T$_{1/2}$ and modulating the order of the VT transition (first order transition for (4-CN-py), (4-Br-py), and second order for (4-NO$_2$-py)), as can be seen in Figure 1.9.
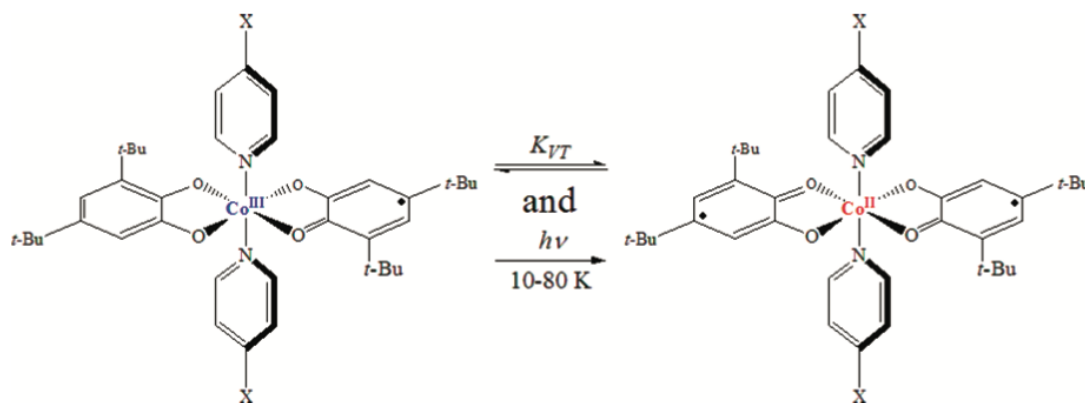
Figure 1.8 – VT equilibrium and generic conformation of trans-Co(diox)₂(Py)₂ (Figure from [14])
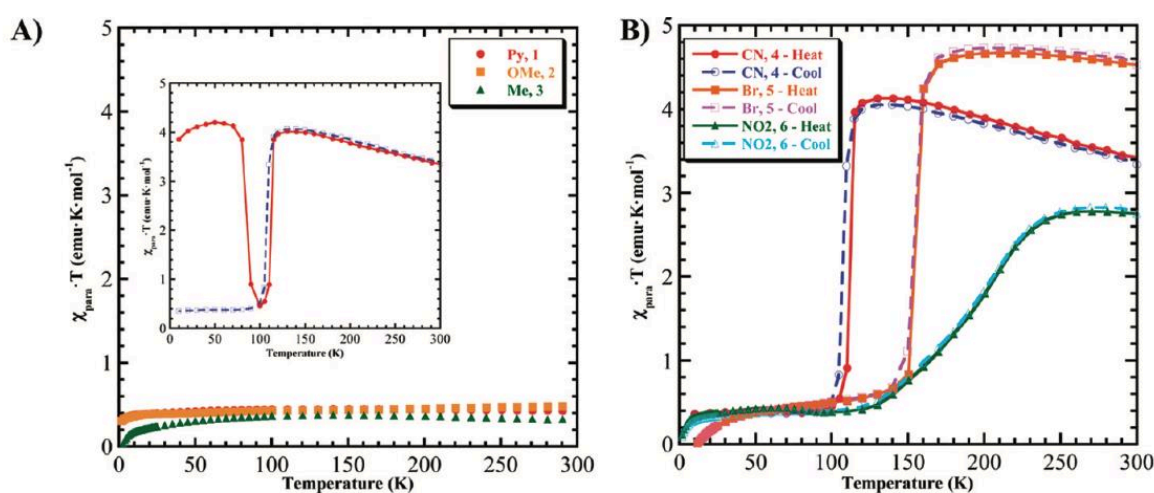
Figure 1.9 – Magnetic susceptibility measurements of the Co(diox)$_2$(PyL)$_2$ complexes for X = Py, (4-O-Me-py), (4-Me-py), (4-CN-py), (4-Br-py) and (4-NO$_2$-py) – 1,2,3,4,5 and 6, respectively.

1.4 Solvent modulation of the VT

In crystals of Cobalt dioxolene tautomers, the intermolecular interactions between neighboring complex units, and between solvent molecules and complex units fundamentally influence the valence tautomerism. Crystal packing and solvation can modulate the order of the VT transition and even allow or forbid the VT interconversion. These VT modulations have been thoroughly studied over the last three decades [24–28].

One of the pioneering studies on solvent modulation of the VT by Adams *et al.*, 1993[10], investigated crystals of Co(*diox*)$_2$(Phen)$_2$, diox = 3,5-di-tert-butyl-semiquinone/3,5-di-tert-butyl-cathecolate. Solvated crystals with toluene (C$_6$H$_5$CH$_3$) and chlorobenzene (C$_6$H$_5$Cl), and non-solvated crystals from recrystallization in methylcyclohexane and from heating Co(*diox*)$_2$(phen)$_2$·C$_6$H$_5$CH$_3$ under vacuum until 70 °C were investigated in temperature

dependent magnetic susceptibility measurements. The results shown in Figure 1.10 evidence that the chlorobenzene solvated crystals undergo a VT interconversion from *hs*-Co^{II} to *ls*-Co^{III} with $T_{1/2}$ ~ 215 K, while the toluene solvated crystal undergo the same transition in a sharper fashion with $T_{1/2}$ ~ 240 K. The non-solvated crystals recrystallized from methylcyclohexane persist as a *hs*-Co^{II} throughout the 2 – 320 K temperature interval, while the nonsolvated form obtained by heating toluene solvated crystals in vacuum is predominantly *ls*-Co^{III} at temperatures below ~ 150 K, but has converted to *hs*-Co^{II} states at 330 K.
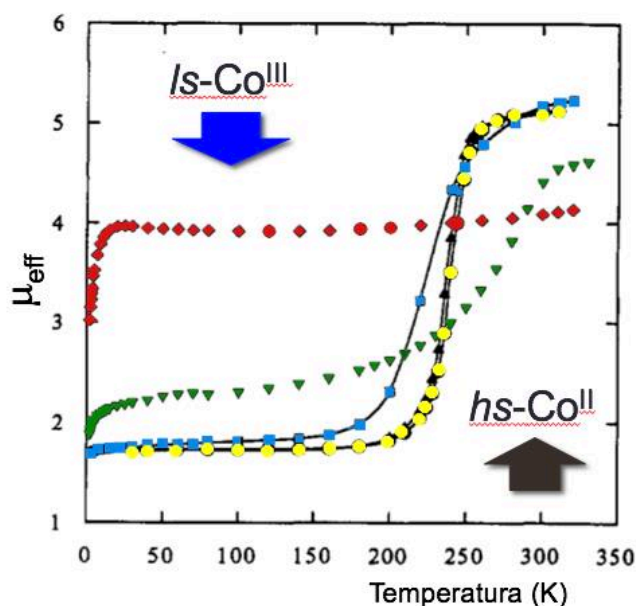
Figure 1.10 – Temperature dependent effective magnetic moment of (◆) Co(diox)$_2$(Phen)$_2$ recrystallized from methylcyclohexane (■) Co(diox)$_2$(Phen)$_2$· C$_6$H$_5$Cl (●) Co(diox)$_2$(Phen)$_2$· C$_6$H$_5$CH$_3$ increasing temperature (▲) Co(diox)$_2$(Phen)$_2$· C$_6$H$_5$CH$_3$ decreasing temperature (▼) Co(diox)$_2$(Phen)$_2$· C$_6$H$_5$CH$_3$ heated under vacuum. (Figure adapted from [10])

In later work by Ribeiro *et al.* 2016, on the Co(*diox*)$_2$(X-Py)$_2$ complexes (X = CN, NO$_2$; *diox* = 3,5-ditertbutylsemiquinone/3,5-ditertbutylcathecolate, Py = pyridine), a detailed solvation study carried out the comparison of crystals solvated with benzene and toluene[26]. For both crystals, the VT interconversion has its dynamics drastically changed depending on the solvent present.

The Co(*diox*)$_2$(4-CN-Py)$_2$ complex changes its VT interconversion from a highly cooperative first order transition, reported for its non-solvated form by Schmidt *et al.* 2010 with $T_{1/2}$ ~ 110 K (see Figure 1.9b), to low cooperative second order transition with $T_{1/2}$ ~ 220 K (see Figure 1.11) after the inclusion of toluene or benzene in the crystal lattice. The toluene/benzene solvated crystal packings closely resembles the solvent-free packing that separates the crystal into sheets. The solvent molecules insert between molecular layers within the crystal, which leads to the weakening of the *para-tert*-butyl interlayer interactions, therefore smoothing the VT interconversion as a function of temperature.
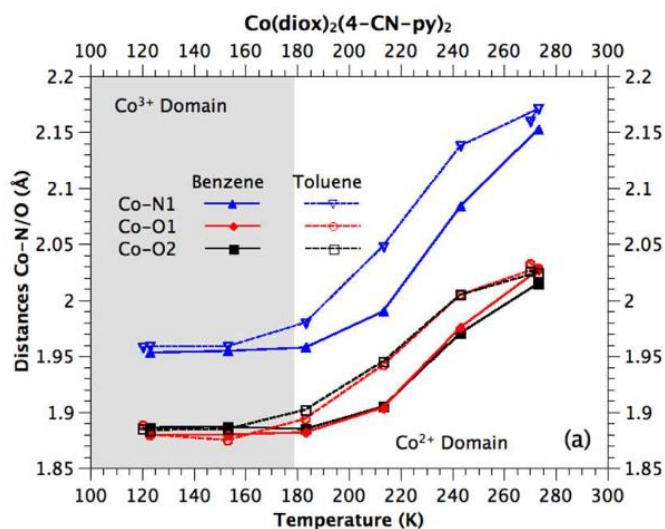
Figure 1.11 – temperature dependent evolution of Co-L distances (L = N, O1 and O2) obtained from single crystal XRD experiments of the benzene and toluene solvated Co(diox)$_2$(4-CN-Py)$_2$ crystals illustrating their VT interconversion.
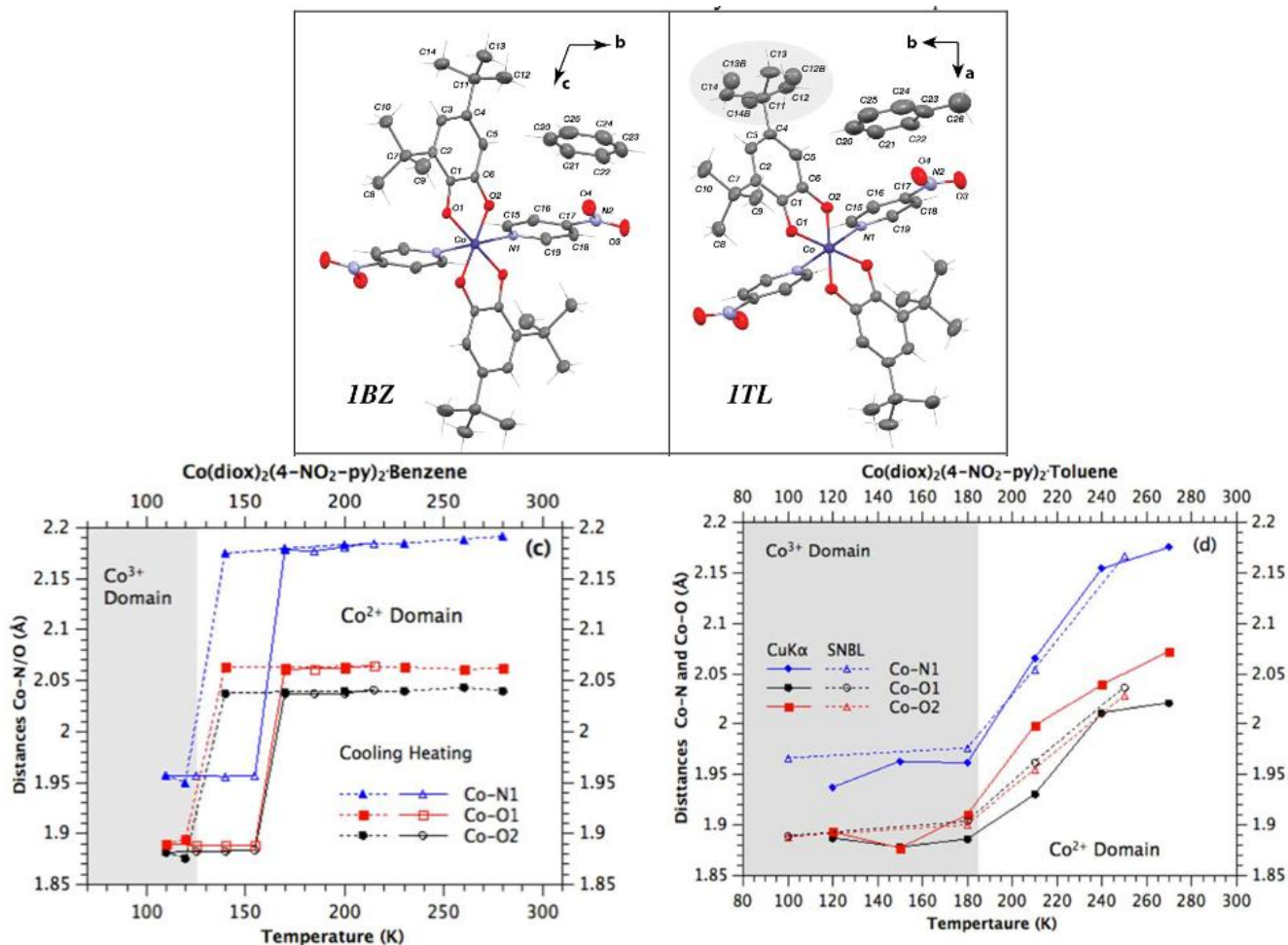
Figure 1.12 – Co(diox)$_2$(NO$_2$-Py)$_2$ solvated with a. benzene (1BZ) and b. toluene (1TL). The graphs show the evolution of the Co-O and Co-N distances for both crystals as a function of temperature when cooling (dashed) and heating (solid) the samples. From [26].

Also, non-solvated and toluene solvated Co(*diox*)$_2$(NO$_2$-Py)$_2$ crystals show low cooperative second order transition with T$_{1/2}$ ~ 200 K, as also reported by Schmidt *et al.* 2010 (see Figure 1.9b) and Ribeiro *et al.* 2016 (see Figure 1.12). On the other hand, benzene solvated Co(*diox*)$_2$(NO$_2$-Py)$_2$ crystals show highly cooperative first order transition with T$_{1/2}$ ~ 140 K.

These examples, along with the vast number of reports in the literature of the investigation of solvent effects on the valence tautomerism process evidences how the stabilization of both *ls*-Co^{III} and *hs*-Co^{II} species is very sensitive to the environment, openning a wide horizon of possibilities in the control, modulation and optimization of the VT process in cobalt complexes.

1.5 Photo-induced VT

As already mentioned, the VT is a process that can be driven by external stimuli such as temperature, irradiation, illumination, pressure, and magnetic field. Nonetheless, light-induced VT is of particular interest because controlling the switching between *hs*-Co^{II} and *ls*-Co^{III} with light irradiation would constitute the basis of photosensors and photorecording memory storage devices. Many Co complexes have been reported to display photo-induced VT[29,30,13,24,31,32,4], mostly observed in low temperatures ($< 150\ K$) in which the complexes are usually stable in their *ls*-Co^{III} form and can be excited to *hs*-Co^{II}. Some of these are reported in Table 1-1 along with their critical temperature T$_{1/2}$ = T$_C$, lifetimes and excitation wavelengths[13].

Table 1-1 – Co valence tautomers that exhibit photo-induced VT.

compound	T_c (K)	lifetime	excitation wavelength (nm)
[Co^{III-LS}(3,5-dbcat)(3,5-dbsq)(phen)]·(C$_6$H$_5$CH$_3$) $\leftrightharpoons$ [Co^{II-HS}(3,5-dbsq)$_2$(phen)]·(C$_6$H$_5$CH$_3$)	240	>3.6 × 10^3 s at 5 K	532
[Co^{III-LS}(3,5-dbcat)(3,5-dbsq)(phen)]·(C$_6$H$_5$Cl) $\leftrightharpoons$ [Co^{II-HS}(3,5-dbsq)$_2$(phen)]·(C$_6$H$_5$Cl)	225	6.8 × 10^3 s at 10 K	532 830^a
[Co^{III-LS}(3,5-dbcat)(3,5-dbsq)(tmeda)] $\leftrightharpoons$ [Co^{II-HS}(3,5-dbsq)$_2$(tmeda)]	195	1.05 × 10^4 s at 5 K 4.2 × 10^3 s at 15 K	532 830^a
[Co^{III-LS}(3,6-dbcat)(3,6-dbsq)(tmpda)] $\leftrightharpoons$ [Co^{II-HS}(3,6-dbsq)$_2$(tmpda)]	165	9.0 × 10^2 s at 5 K	532
[Co^{III-LS}(3,5-dbcat)(3,5-dbsq)(dpa)] $\leftrightharpoons$ [Co^{II-HS}(3,5-dbsq)$_2$(dpa)]	380	not reported	532 830^a
[{Co^{III-LS}(cth)}(dhbq){Co^{III-LS}(cth)}]·(PF$_6$)$_3$ $\leftrightharpoons$ [{Co^{II-HS}(cth)}(dhbq){Co^{III-LS}(cth)}]·(PF$_6$)$_3$	175	not reported	647.1–676.4
[{Co^{III-LS}(tpa)}(dhbq){Co^{III-LS}(tpa)}]·(PF$_6$)$_3$ $\leftrightharpoons$ [{Co^{II-HS}(tpa)}(dhbq){Co^{III-LS}(tpa)}]·(PF$_6$)$_3$	$T_c\uparrow = 310$ $T_c\downarrow = 297$	not reported	532
[(phen)Co^{III-LS}-μ-(Cat-Ph-SQ)]$_n$ $\leftrightharpoons$ [(phen)Co^{II-HS}-μ-(SQ-Ph-SQ)]$_n$	305	3.1 × 10^5 s at 9 K 1.5 × 10^5 s at 20 K	658

One remarkable example of light induced VT has been reported by Poneti *et al.* 2009[31], on the study of the Co(Me$_2$tpa)(BD*diox*)PF6·C$_6$H$_5$CH$_3$ complex, where Me$_2$tpa stands for the tetradentate tripodlike ligand bis(6-methyl-(2-pyridyl- methyl))(2-pyridylmethyl)amine and DBdiox is 3,5-di-tert-butyl-o-dioxolene (Figure 1.13). The complex undergoes temperature

induced VT with $T_{1/2}$ = 155 K, and the *ls*-Co^{III} states are excited to *hs*-Co^{II} with 904 nm irradiation at 6 K in a reversible fashion, as it is shown in Figure 1.13. The authors also report the back valence tautomerism interconversion from *hs*-Co^{II} to *ls*-Co^{III} when the photo-excited states are illuminated with 658 nm light, at 6 K as well.
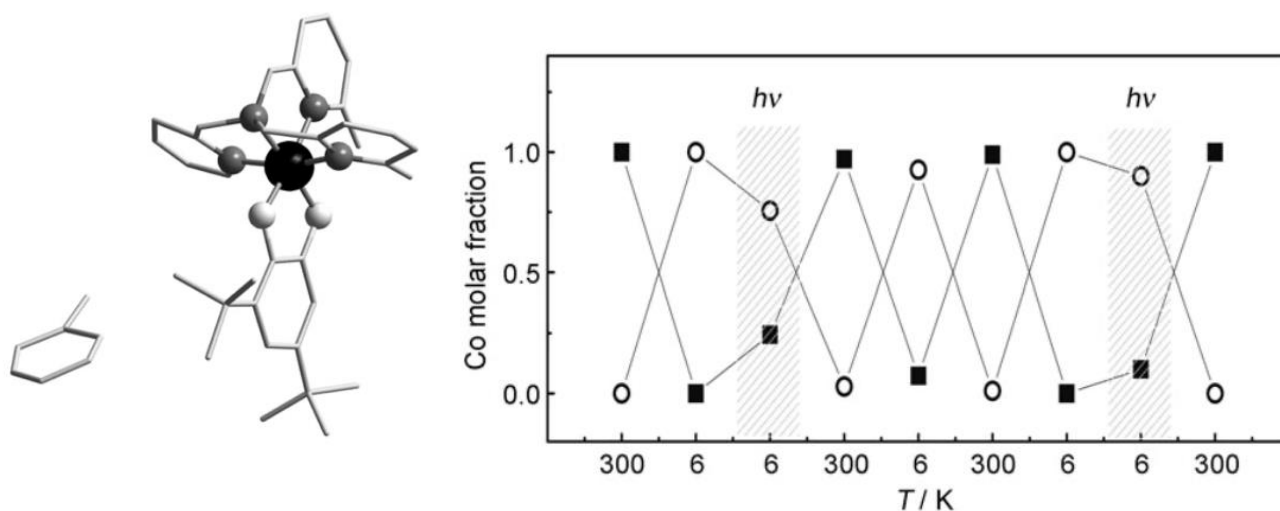
Figure 1.13 – (right) Co(Me$_2$tpa)(BDdiox)PF6·C$_6$H$_5$CH$_3$ structure resolved from X-ray diffraction experiments. (left) CoII and CoIII molar fractions obtained by varying the temperature and after irradiation of the sample with 904 nm laser light. The shaded points correspond to the measurements carried out after irradiation with the laser for 20 h (left) and 2 h (right).

Another Co(*diox*)$_2$ complex that undergoes photo-induced VT at low temperatures is the Co(*diox*)$_2$(4-CN-Py)$_2$. Its non-solvated crystals have been shown to respond to white light irradiation (450 to 800 nm – no spectrum reported) at 10 K in which, after 12 hours of irradiation, an yield of 30% *ls*-Co^{III} to *hs*-Co^{II} interconversion was observed. Figure 1.14a shows the value of the magnetic susceptibility of the complex during cycles of cooling, irradiating and heating, demonstrating the reversibility of the light-induced VT as well as the robustness of the crystal. The photo-excited states were observed to be long-lived in low temperatures, and their respective decay kinetics was also studied by Schmidt *et al.* 2010. Figure 1.14b shows the temperature dependence of the photo-excited state lifetimes, and for temperatures $T \leq 50\ K$, these states remain as *hs*-Co^{II} for more than 4 hours, resembling the light-induced excited state spin trapping (LIESST) in iron spin-crossover complexes, in which spin-forbidden relaxation processes guarantee the excited states metastability.
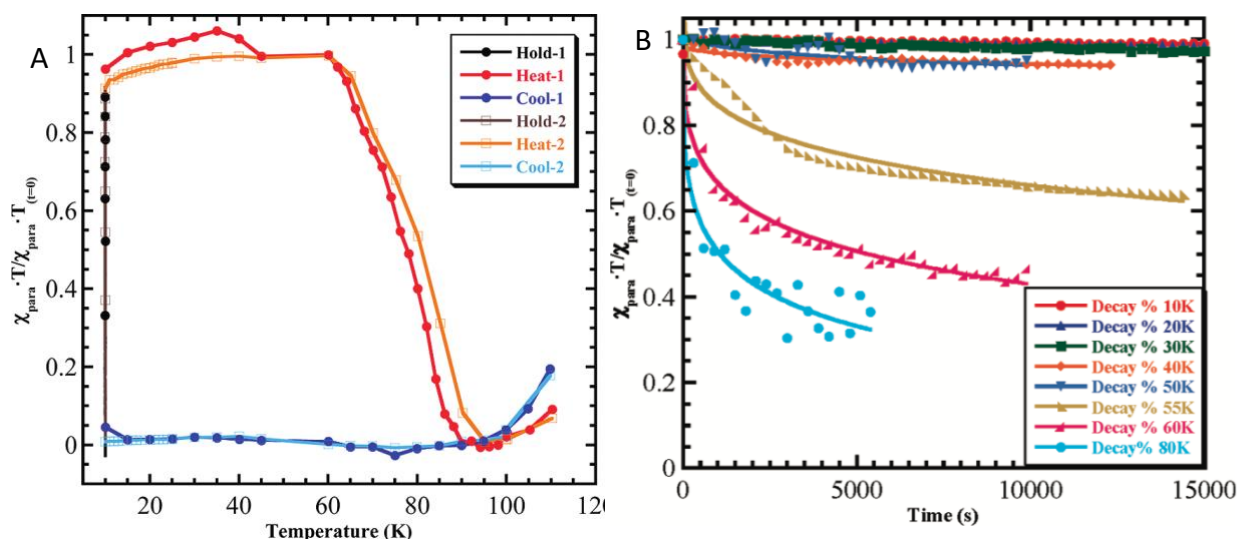
Figure 1.14 – A : Magnetic susceptibility of a Co(diox)$_2$(4-CN-Py)$_2$ crystal during thermal and irradiation cycles. B : temperature dependent decay kinetics of the photo-excited states.

1.6 Time dynamics of the VT

The valence tautomerism process is naturally intriguing for comprising both charge transfer and spin change processes. Understanding the mechanisms through which these two processes happen and the investigation of how they are coupled from electronic and time dynamics perspectives have led to the development of sophisticated experimental studies using ultrafast spectroscopy techniques[22,33–35]. Results reported in these studies point towards the valence tautomerism process dynamics, which has been understood to be composed of a complex chain of events, spanning from charge transfer, spin crossover, intersystem crossing and vibrational relaxation.

Early studies of the dynamics of cobalt complex tautomers in solution proposed the electronic steps within the photoinduced VT process when the excitation wavelength lies in the ligand to metal charge transfer (LMCT) region of the electronic absorption spectra (Figure 1.15b)[22]. The proposed mechanism by Adams *et al.*, 1996[22] starts with the charge transfer from the cathecolate to the metal center, triggered by the light excitation, leading the complex from *ls*-Co^{III} to an excited state form, after which rapid intersystem crossing would produce the *hs*-Co^{II} form (proposed reaction rate $k > 1.1 \times 10^{10} s^{-1}$), followed by a slower process of back valence tautomerization ($k \cong 10^8, 10^9 s^{-1}$). In their work, the VT dynamics was probed using nano and picosecond transient absorption spectroscopy techniques (see 2.4) with which the rate of the back valence tautomerization was shown to range from 6.1 × 10^7 to 6.7 × 10^8 s^{-1} for two Co(*diox*)$_2$(N-N) complexes (*diox* = 3,5-ditertbutylsemiquinone/3,5-ditertbutylcathecolate, N-N = 4,4'-dimethyl-2,2'-bipyridine or 4,4'-diphenyl-2,2'-bipyridine) dissolved in toluene, at room temperature. The slow time scales of the back valence tautomerization processes were attributed to the poor overlap between the molecular orbitals of the charge donor and

acceptor for the complex in the *hs*-Co^{II} state. Other faster steps of the VT process were not assessed with the experimental time scales used and were speculated to involve quantum mechanical tunneling.
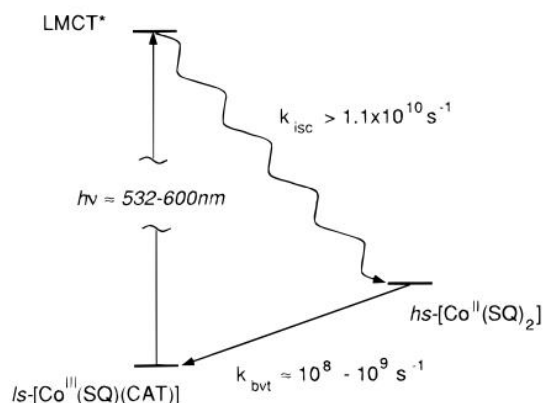
Figure 1.15 – Jablonski diagram with the VT mechanisms in Co(diox)$_2$(N-N) complexes, where N-N is bidentate nitrogen based ligand, as proposed by Adams et al., 1996[22] (figures from Adams et al., 1996). The laser irradiation leads to a charge transfer process, a subsequent intersystem crossing and the following back valence tautomerization.

Most recently, Azzaroli *et al.*, 2013, again used transient absorption spectroscopy to probe the VT dynamics in Co(tpy)(diox-N-diox) (tpy = terpyridine, diox-N-diox = Cat-N-BQ or Cat-N-SQ = 2-(2-hydroxy-3,5-ditert-butylphenyl-imino)-4,6-ditert-butylcyclohexa-3,5-dienone   or   its dianionic analogue) induced by light irradiation with wavelengths lying within the LMCT band (521 nm), just above the LMCT band in energy (490 nm) and within the lower energy tail of the ligand's internal transitions band (1170 nm). The new proposed mechanism splits the intersystem crossing from Figure 1.15 in two steps: ultrafast intersystem crossing, followed by vibrational cooling (Figure 1.16, processes 2 and 3, respectively). The sequence of transitions involved in the VT process was therefore explained to start with a light induced charge transfer taking the *ls*-Co^{III} complex into *ls*-Co^{II} (1), followed by intersystem crossing (2), which maintains the complex in the *ls* state, then vibrational cooling to the *hs*-Co^{II} state (3), and finally back valence tautomerization to the *ls*-Co^{III} (4). Time and kinetic constants involved in such process for each excitation wavelength used are shown on Table 1-2.

Table 1-2 Time (τ) and kinetic (k) constants for the light induced VT in Co(tpy)(diox-N-diox)

wavelength (nm)	τ_1 (ps)	std. dev. (ps)	k_1 (ps^{-1})	τ_2 (ps)	std. dev. (ps)	k_2 (ps^{-1})
$\lambda_0 = 490$	12.9	0.44	7.73×10^{-2}	349.7	6.28	2.86×10^{-3}
$\lambda_0 = 521$	14.2	0.67	7.01×10^{-2}	359.6	7.44	2.78×10^{-3}
$\lambda_0 = 1170$	7.43	0.87	1.34×10^{-1}	348.7	10.30	2.87×10^{-3}
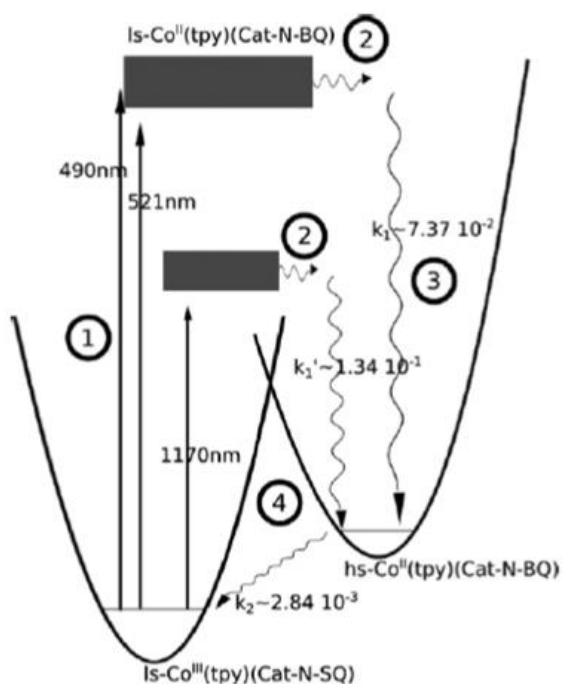
Figure 1.16 – Potential energy surfaces and schematic representation of the light induced VT in Co(tpy)(diox-N-diox). Light excitation from laser pulses is represented as solid straight arrows (1), wiggly arrows represent ultrafast intersystem crossing (2), vibrational cooling (3) and back valence tautomerization (4).

2 Experimental methods for VT characterization

2.1 Single crystal X-ray diffraction

X-rays are electromagnetic waves with wavelengths in the order of Ångström (10^{-10}m), generated in X-ray tubes, synchrotron light sources and free electron lasers[36]. Due to the compatibility of size between X-ray wavelengths and interatomic bonds, such radiation is the one used to investigate the structures of molecules and compounds in scattering experiments. For crystalline compounds, X-ray diffraction (XRD) is a powerful technique used in the determination of their three-dimensional structures. Particularly, single crystal XRD (SCXRD) stands out, once the diffracted X-rays form a discreet interference pattern that is related to the structure of the material.

According to the International Union of Crystallography (IUCR) a material can be considered a crystal if when illuminated by radiation having a wavelength on the order of Å, it generates a three-dimensional diffraction pattern primarily characterized by discrete peaks[37].The positions of such peaks can be expressed by the vector:

$$\boldsymbol{h} = \sum_{i=1}^{n} h_i \boldsymbol{a}_i^* \ (n \geq 3) \tag{1}$$

in which $\boldsymbol{a}_i^*$ are the base vectors of the reciprocal space and h_i are integers. If we describe the crystal lattice in terms of its basis vectors, $\boldsymbol{a}_i$ for $i = 1, 2, 3$, the Laue condition for diffraction can be written as:

$$\boldsymbol{a}_i \cdot \boldsymbol{h} = \ h_i \tag{2}$$

The electron cloud in a crystal is the main contributor in the scattering phenomena, therefore the total amplitude A_T scattered by a real crystal is proportional to its electron density ρ_{crys}. Considering the repetition of the unit cell in 3 dimensions and approximating the charge distribution around atoms to be spherically symmetric, we can write:

$$A_T \propto \sum_{j=1}^{N} \left[\varepsilon \int_0^R \rho_{ej}(\boldsymbol{r}')e^{2\pi i \boldsymbol{h} \cdot \boldsymbol{r}'} d\boldsymbol{r}' \right] e^{2\pi i \boldsymbol{h} \cdot \boldsymbol{r}_j} \tag{3}$$

where ε is the scattering power of the electron and ρ_{ej} is the electron density of the atom j in the unit cell, localized by the vector $\boldsymbol{r'}$. The sum in (3) is known as the crystal structure factor $F(\boldsymbol{h})$, commonly written in terms of the atomic form factor of the atom j, f_{ej}:

$$F(\boldsymbol{h}) = \sum_{j=1}^{N} f_{ej}e^{2\pi i \boldsymbol{h} \cdot \boldsymbol{r}_j} \tag{4}$$

$$f_{ej} = \varepsilon \int_0^R \rho_{ej}(\boldsymbol{r'})e^{2\pi i \boldsymbol{h} \cdot \boldsymbol{r'}} d\boldsymbol{r'} \tag{5}$$

The structure factor is a complex quantity and can be written in terms of its module F_{hkl} and phase φ_{hkl}:

$$F(\boldsymbol{h}) = |F_{hkl}|e^{i\varphi_{hkl}} \tag{6}$$

of which Fourier transform is the electron density of the unit cell of volume V:

$$\rho(\boldsymbol{r}) = \frac{1}{V}\sum_{hkl} F(\boldsymbol{h})e^{-2\pi \boldsymbol{h} \cdot \boldsymbol{r}} \tag{7}$$

In an XRD experiment we can measure the diffracted intensity $I(\boldsymbol{h})$, which is proportional to the total diffracted amplitude squared, and consequently to the square of the module of the structure factor[38].

$$I(\boldsymbol{h}) \propto |F(\boldsymbol{h})|^2 \tag{8}$$

Equations (7) and (8) together summarize how the diffraction pattern from a crystal brings information of the position of the electrons (scatterers) within the crystal lattice. However, from equation (8), the complex part of the structure factor does not contribute to the intensity in such a way that the phase φ_{hkl} is lost. A series of mathematical phasing methods have been developed and are routinely used to deduce, indirectly measure or speculate the relation between the phases and the measured structure factor modules[39,40].

Such combination of XRD and its developed computational methods are robust and well stablished so as to fundament data banks such as the Cambridge Crystallographic Data Centre (CCDC)[41], with more than 1 million structures of small molecules, the Protein Data Bank (PDB)[42], with around 140 thousand protein structures resolved by XRD techniques and the Inorganic Crystal Structure Database (ICSD)[43], with more than 240 thousand crystal structures of inorganic compounds.

Given the structural changes caused by the VT in cobalt complexes, SCXRD has proven to be a powerful technique to probe the VT interconversion when the conditions are such that the *ls*-Co^III or *hs*-Co^II states are long lived. The bond lengths between cobalt and its first neighbors can be assessed with such precision that allows the differentiation of the two states of the tautomers. Moreover, the site specificity of X-ray crystallography data also allows the differentiation of symmetry inequivalent crystal sites which may present different VT properties. For instance, in the work by Mulyana *et al.* 2009[25], (see also section 1.4) the Co(*diox*)$_2$(Py)$_2$ + 0.5 Py crystal has two complex molecules in its assymetric unit, although only one of them undergoes the temperature induced or light induced VT due to solvent present in the lattice. This result could only be confirmed through the monitoring of the bond lengths of Co-L (L = O or N) of the two complex units as a function of temperature (Figure 2.1) using the structures solved by SCXRD. In the figure, Co-N and Co-O distances for the two complex units in the unit cell are shown, and only one of them presents the characteristic bond length stretching due to VT interconversion.
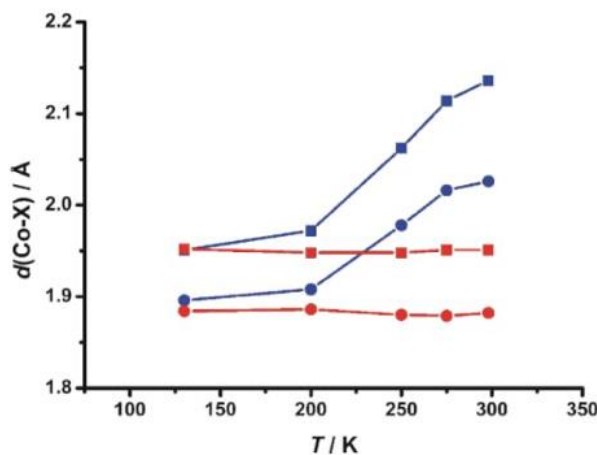
Figure 2.1 Co-O (●) and Co-N (■) bond lengths versus temperature for the two symmetry-inequivalent Co(diox)$_2$(Py)$_2$ units (red and blue). Adapted from [25]

Ribeiro *et al.* 2016[26] proposed a mathematical method to compute the molar fraction of *hs*-Co^II species in a crystal undergoing VT transition from the crystallographic determined distances between the cobalt center and its first neighbors, O and N, and the typical distances between the same atoms when all cobalt centers are in either *hs*-Co^II or *ls*-Co^III states (typical distances are surveyed from the CCDC[41] databank). For a given crystal that underwent XRD and had its structure determined, the molar fraction of *hs*-Co^II is given by:

$$\gamma(hs - Co^{II})_L = (D_{exp}^{Co-L} - D_{Co^{III}}^{Co-L})/(D_{Co^{II}}^{Co-L} - D_{Co^{III}}^{Co-L}) \qquad (9)$$

$$\gamma(hs - Co^{II}) = \frac{1}{3}\sum_L \gamma(hs - Co^{II})_L \qquad (10)$$

where L denominates the first neighbor atoms of the cobalt center, D^{Co-L} stands for the atomic distance between Co and L and the subscripts denominate the experimental value (*exp*) and the standard distances for both oxidation states of Co (Co^{II} and Co^{III}).

The *hs*-Co^{II} mole fraction during the temperature induced VT transition of complexes $Co(diox)_2(NO_2-Py)_2$ and $Co(diox)_2(4-CN-Py)_2$ in crystals solvated with toluene and with benzene were evaluated using the Co – L and equations (9) and (10) for the first time in the work of Ribeiro *et al.* 2016 (Figure 2.2). Such approach has successfully probed the VT, providing the accurate determination of the molar fraction of cobalt centers within a crystal as a function of temperature. From this, the critical $T_{1/2}$ can be assessed, and the distinction between first order (cooperative) and second order (non-coperative) VT transitions can be done.
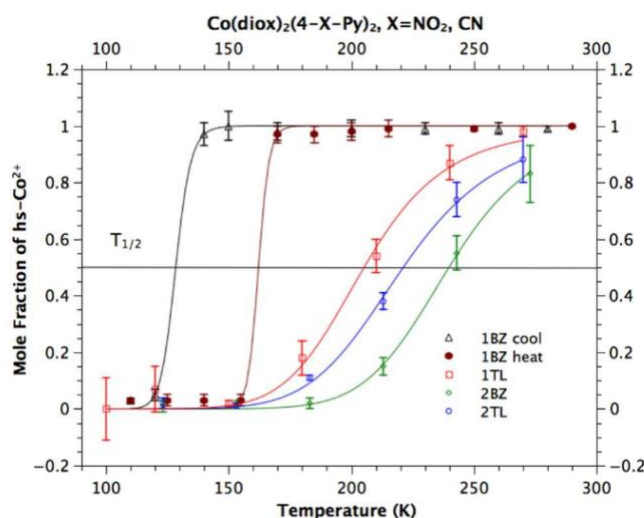
Figure 2.2 Mole fraction of hs-Co^{II} species in crystals of $Co(diox)_2(NO_2-Py)_2(1)$ and $Co(diox)_2(4-CN-Py)_2$ solvated with benzene (BZ) and toluene (TL). Adapted from [26].

2.2 UV-vis spectroscopy

Spectroscopy is the study of the interaction of electromagnetic radiation with matter as a function of the radiation energy. As molecules consist of electrically charged electrons and nuclei, they may interact with the electric and magnetic fields of incident radiation. When the energy of such fields corresponds to the energy difference between the molecule's energy levels, the molecules absorb the incident radiation energy and are promoted to an excited state. When this happens, we say that the molecule underwent a transition between the ground state to an excited state. Within the spectrum of commonly used energies in spectroscopy measurements, infrared (IR) frequencies have energies that are compatible with transitions between vibrational levels of molecules and more energetic ultraviolet and visible (UV-vis) light have energies that can promote the redistribution of electrons within the molecular orbitals[44].

UV-vis and IR light absorption experiments on gases and solutions have their mathematical and physical basis in the Bourguer-Lambert-Beer law[44,45], equation (11). The absorbance A (also called optical density, OD) of the sample is related to the transmittance T:

$$A = log_{10} \left(\frac{I_0}{I} \right)_v = log_{10} \left(\frac{1}{T} \right) \tag{11}$$

where T is the ratio between the the transmitted light intensity (I) and the incident light intensity (I_0); v is the light frequency. The absorbance is directly proportional to the length of the light path l through the sample cell, the concentration C of the sample, equalized by the proportionality quantity, ϵ, named extinction coefficient:

$$A = \epsilon C l \tag{12}$$

and Bourguer-Lambert-Beer's law can be written as:

$$log_{10} \left(\frac{I_0}{I} \right)_v = \epsilon C l \tag{13}$$

Cobalt dioxolene tautomers have also been characterized using UV-vis and IR spectroscopies[22,24,33,46]. In the work of Adams *et al.*, 1996, temperature dependent UV-vis spectroscopy of a polystyrene film of [Co(*diox*)$_2$(Phen)] (*diox* = 3,5-ditertbutylsemiquinone/3,5-ditertbutylcathecolate, Phen = 1-10-phenanthroline) shows the evolution of the absorption spectra as the complexes go from *hs*-Co^{II} to *ls*-Co^{III}. Main characteristic absorption features of each tautomer appear between the isosbestic points (Figure 2.3). The absorption of the *ls*-Co^{III} form is characterized by a band at ~600 nm and a band at ~2500 nm, being the latter associated to a ligand-based intervalence transition. The *hs*-Co^{II} has its characteristic MLCT absorption band at ~770 nm and no absorption features in the IR region [1,22,24].
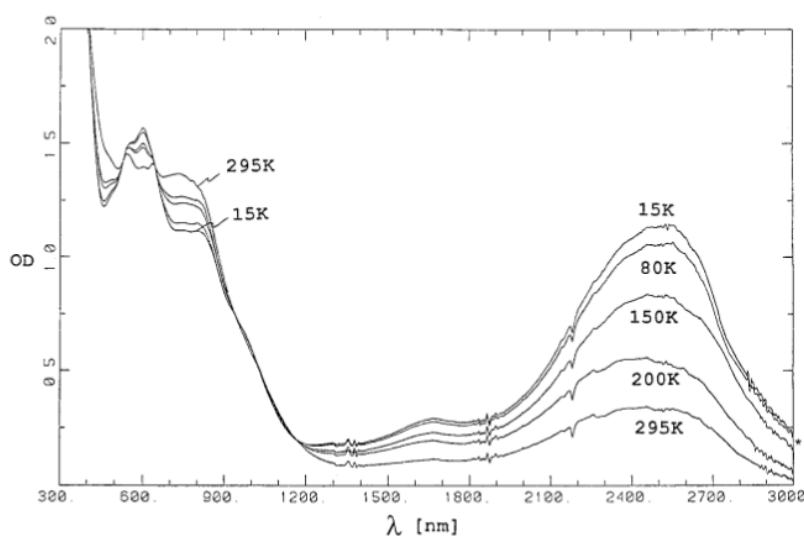
Figure 2.3 Temperature dependent UV-vis spectroscopy of a polystyrene film of Co(diox)$_2$(phen). The optical density (OD) is plotted as a function of wavelength (λ). Adapted from [22].

The values of the peak absorption wavelengths can shift slightly from complex to complex in different solvents but are extremely useful in the evaluation of the oxidation states of the complexes. Also, the interpretation of each spectral feature involves a series of theoretical calculations[22] and can be ambiguous. More recent work by Beni *et al.* 2008[24] (Figure 2.4) assigned broad bands in the red region to symmetry-forbidden LMCT transitions in Co^{III}-cathecolate chromophores, and transitions near 430 nm and 465 nm to d-d transitions. For the Co^{II}-semiquinone chromophores, on the other hand, broad transitions centered around 800 nm were assigned to internal ligand transitions, and the bands at 525 − 665 nm were attributed to charge-transfer transitions involving the d-orbitals of the metal ion and the singly occupied π^* orbital of the ligand.
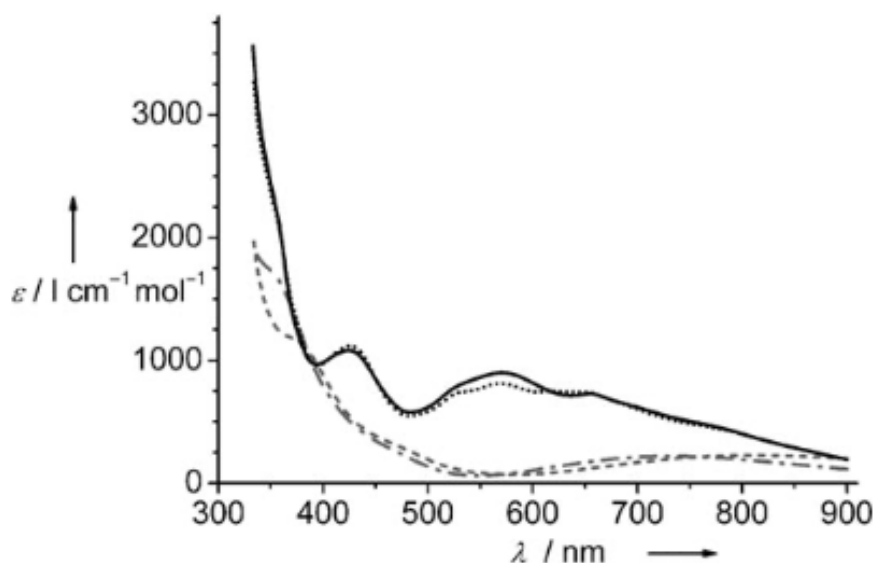
*Figure 2.4 Electronic spectra of Co[(X)(DBdiox)]PF₆, X = tpa (**1**) (gray, dash-dotted line), Me₁tpa (**2**) (gray, dashed line), Me₂tpa (**3**) (black, continuous line), Me₃tpa (**4**) (black, dotted line). **1** and **2** were assigned to Co(III)-cathecolate chromophores, 3 and 4, to Co(II)-semiquinonate chromophores. Adapted from [24].*

2.3 Electronic spin resonance

Electronic spin resonance (ESR) is an experimental technique based on the interaction between the electromagnetic radiation and the magnetic moments of the electrons. It focuses particularly in the interaction of the magnetic component of the radiation with the magnetic moment of the electrons $\boldsymbol{\mu_e}$ conferred by the spin[47]:

$$\boldsymbol{\mu_e} = -g_e \mu_B \boldsymbol{S} \qquad (14)$$

where $\boldsymbol{S}$ is the electronic spin angular momentum, g_e is a non-dimensional constant named free electron factor, and μ_B is the Bohr magneton, $\mu_B = e\hbar/2mc$, in which e and m are the

electron charge and mass, respectively. The interaction between the electronic magnetic moment of the free electron and the magnetic component of the radiation, H, when the latter is on the z direction, is described by the Hamiltonian:

$$\mathcal{H} = \boldsymbol{\mu_e} \cdot \boldsymbol{H} = g_e\mu_B HS_z \tag{15}$$

The dipole magnetic moment associated to the spin of a free electron has two possible orientations, the eigenstates $|\alpha_e\rangle$ and $|\beta_e\rangle$, from which degeneracies is brought about by the magnetic field $\boldsymbol{H}$. These eigenstates are respectively associated to the quantum numbers $m_s = \frac{1}{2}$ and $m_s = -\frac{1}{2}$, that correspond to the parallel and anti-parallel alignment of the spins with the field, and respectively the higher and lower energy eigenstates. Due to an effect named electronic Zeeman effect, the energy separation ΔU between the two eigenstates varies linearly with the applied static magnetic field and have typical values of $\Delta U = h\nu$ for ν in the microwave region (from 300 GHz to 300 MHz).

Other contributions to the Hamiltonian in equation (15) must also be considered in the presence of a non-zero nuclear spin. The nuclear spin states will have their degeneracies split, given the nuclear Zeeman interaction with the incident magnetic field. Also, the nuclear magnetic moment will interact with the dipole moment of the free electron, in what is called the hyperfine interaction. The interaction with the incident magnetic field can then be written:

$$\mathcal{H} = g_e\mu_B HS_z + aS_zI_z - g_N\mu_N HI_z \tag{16}$$

Where the second term on the right side describes the interaction between the electronic and nuclear magnetic moments, which is three orders of magnitude smaller than the first term, and the third term describes the nuclear Zeeman interaction, which is even smaller.

In order to the spin state transitions to happen however, an electromagnetic field with energy $E = h\nu$ equivalent to the energy difference ΔU between two eigenstates of (17) must be applied to the system, so it meets the resonance condition. Additionally, an oscillating magnetic field (microwaves) must be perpendicular to the static magnetic field $\boldsymbol{H}$.

The relationship between the intensity of the applied magnetic field and the energy absorbed by the system in resonance condition in an ESR experiment is empirically described by a function $g(\nu) = 2\pi \cdot g(\omega)$, named the line-shape of ESR. The magnetic resonance lines in liquids usually have the shape of a damped harmonic oscillator described by the Lorentzian:

$$g(\omega) = \frac{T_r}{\pi}\frac{1}{[1 + T_r^2(\omega - \omega_0)]} \tag{17}$$

in which T_r is the spin-spin relaxation time which characterizes the relative energy shift between the energy levels of the eigenstates, and ω_0 is the resonance frequency. Most commonly observed in ESR of crystalline solids, however, is a Gaussian:

$$g(\omega) = \frac{T_r}{\sqrt{2\pi}} e^{-\frac{1}{2}T_r^2(\omega-\omega_0)^2} \tag{18}$$

In a standard ESR measurement, in which field modulation together with phase-sensitive detection is used, it is the first derivative of the response line that is recorded (see appendix 7.1).

Transition-metal molecules and complexes have played an important role in the development of the ESR technique due to their variable valence. Such complexes have been largely studied and stablished ESR as a powerful technique to characterize compounds that contain atoms with free d-electron shells[48]. For instance, complexes of the form $LCoO_2$ (L = other ligands bonded to Co) have free electrons localized on the superoxide (O_2^-). The ESR signal of such free electrons is modulated by the Co^{III} ion nuclear magnetic moment, leading to a hyperfine structure of eight adjacent equally spaced lines[48]. On the other hand, Co^{II} ion is paramagnetic and its electronic spin magnetic moment in an octahedral field has a characteristic transition line with $g \approx 4.2$ [49]. These ESR signatures are fundamentally important in the evaluation of the VT in cobalt complexes using ESR techniques.
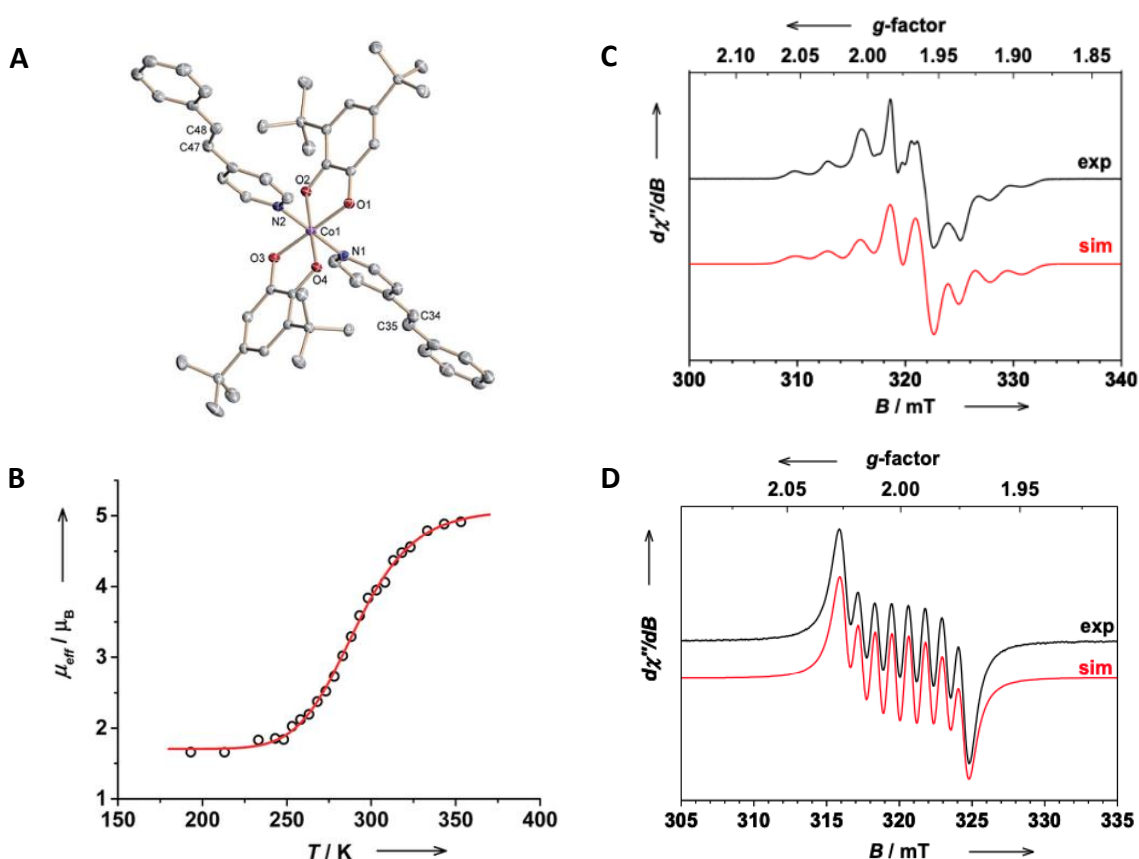
Figure 2.5 – A. structure of the [Co(tbdiox)$_2$(trans-4-stypy)$_2$] complex (trans-6); B. temperature dependent effective magnetic moment of trans-6 in toluene. Measured (black) and calculated (red) ESR spectra of trans-6 in toluene at C. 14 K and D. room temperature. From [50]

For example, in the [Co(*diox*)$_2$(*trans*-4-stypy)$_2$] complex, trans-6 here on, (*diox* = 3,5-di-tert-butyl-o-dioxolene, *trans*-4-stypy = trans-4-Styrylpyridine), the VT can be temperature-induced and photo-induced (Figure 2.5). Its synthesis and thorough study were carried out by Witt *et al.*, 2015[50]. In their work, temperature dependent magnetic moment measurements show the VT interconversion of the complex dissolved in toluene with an estimated transition temperature of $T_{1/2} = 299\ K$, with all Co centers in the *hs*-Co^{II} configuration at 350 K. ESR was also used to characterize the *ls*-Co^{III} states of the complex in toluene solution at 4 K and at room temperature (RT) (Figure 2.5c,d). The simulated and measured ESR spectra around $B\ =\ 320\ T$ shows the magnetic response of the free electron of the semiquinone in the cryogenic temperature regime and at RT, g = 2. Note that at RT, which is very close to $T_{1/2}$, the ESR signal still corresponds to the *ls*-Co^{III} species. The hyperfine splitting is structured at 14 K, but equally spaced at RT.

ESR has also been used to characterize the *hs*-Co^{II} cobalt dipyridyl verdazyl complex [Co(dipyvd)$_2$](PF$_6$) (Figure 2.6) in its crystalline form and in acetonitrile solution. The ESR spectra of the crystals at 5 K (Figure 2.7b) exhibit two resonances with effective g value of 4.5 and 2, which originate from the $|S, m\rangle\ =\ |3/2, \pm 1/2\rangle$. For the complex in acetonitrile solution at 77 K, however, the signal centered at g = 2 shows a rich hyperfine structure (Figure 2.7a). Analysis of the hyperfine splitting pattern originating from the interaction of the electronic spin with the I = 7/2 of ^{59}Co nuclei reveals a practically quenched hyperfine coupling tensor. Together with the nearly isotropic g-tensor for which g$_{iso}$ = 1.998 this observation indicates that the unpaired electron is localized on the ligand and that the cobalt ion is diamagnetic, consistent with the presence of a low-spin Co^{III} metal center. The results in solution reinforced the valence tautomeric equilibrium in solution between an S = 3/2 Co^{II}/diradical species and an S = 1/2 Co^{III}/radical/anion species observed in UV-vis experiments, being the Co^{II} ESR silent at such temperatures.
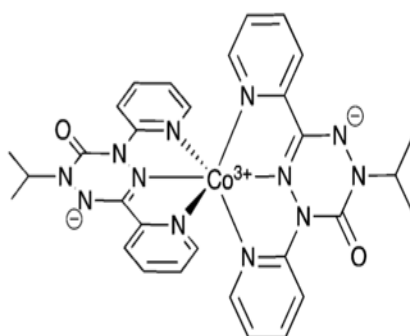
[Co(dipyvd)$_2$]$^+$(PF$_6$)$^-$

Figure 2.6 - Structure of [Co(diox)$_2$(trans-4-stypy)$_2$] (trans-6.)
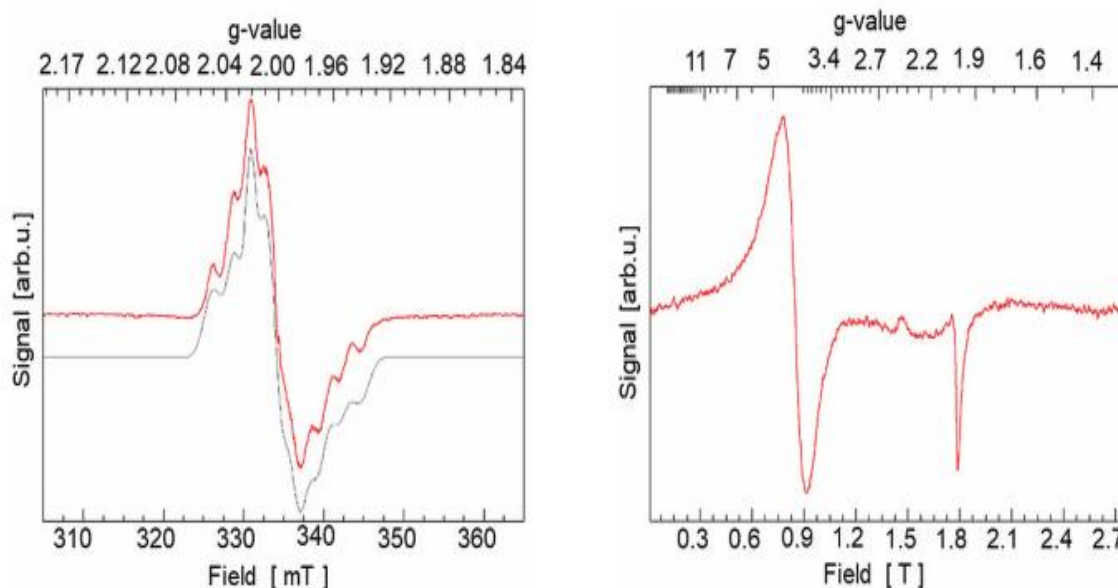
Figure 2.7 - Left: X-band EPR spectrum recorded at 77 K for a MeCN solution of [Co(dipyvd)$_2$]$_2$+(PF$_6$)$_2$] (red) and simulated spectra for S = 1/2 and I = 7/2 (gray). Right: CW EPR spectra recorded for [Co(dipyvd)$_2$]^{II} (PF$_6$)$_2$. Spectrum recorded at 5 K and 50.3 GHz for a neat powder sample of [Co(dipyvd)$_2$]$_2$+(PF$_6$)$_2$. Figure from[51].

2.4 Transient absorption spectroscopy

The advent of pulsed LASERS with fs and sub-fs pulse durations has expanded the horizons of ultrafast science and allowed for the advances in spectroscopy techniques that probe physical properties of systems in ultrafast time scales. Transient absorption (TA) is a spectroscopy technique that follows the pump probe scheme in which a fraction of the molecules in the sample are electronically excited due to an incident laser pulse (pump), ideally monochromatic, and are probed by a second pulse (probe) with a wider spectral range and delayed by τ with respect to the pump[52–55]. As the molecules in excited states will absorb light differently with respect to the ground state ones, the overall absorption spectra of the sample changes due to the pump. Both spectra, from the pumped and unpumped sample are recorded and a difference absorption spectrum is then calculated for each fixed pump-probe delay τ:

$$\Delta A = A_p - A_{unp} \tag{19}$$

in which A_p and A_{ump} are the absorption spectra of the pumped and unpumped sample respectively. The pump-probe delay is then varied to scan over time and the multiple difference spectra recorded over time provide with a profile of ΔA as a function of pump probe delay (τ)

and probe wavelength (λ). $\Delta A(\tau, \lambda)$ comprises contributions of multiple processes triggered by the pump pulse:

1. Ground state bleach: it is a negative feature in the region of the ground state absorption due to the reduction of the number of molecules in the ground state and a consequent reduction on the features of A_{unp}.

2. Stimulated emission: it is a feature that roughly follows the fluorescence spectra of the excited chromophore, as given the population of the excited state, the probe pulse will induce stimulated emission to the ground state for the allowed optical transitions as it passes through the pumped volume. This feature on the ΔA spectra is Stokes shifted with respect to the ground state bleach. The photons emitted increase the intensity recorded by the detector when A_p is measured, therefore it is a negative absorption feature.

3. Excited state absorption: it is the contribution of the excited states in the pumped sample to the absorption of the probe pulse due to optically allowed electronic transitions from the excited states to higher excited states that may have energy lying within the probe spectrum. This brings and increase of the A_p term, and consequently a positive contribution to ΔA.

4. Product absorption: upon excitation of the sample, there might occur reaction which leads to the production of long-lived molecular states (product or transient), which will absorb light at certain regions of the probe spectra and contribute positively to ΔA. The promotion of such new molecular states will also cause a ground state bleach at the spectral region of the probe pulse in which the ground state of the product absorbs.

Time constants of each process probed in a TA experiment is assessed via exponential decay fitting of each spectral feature. The deconvolution of overlapping contributions is not a straightforward procedure and global analysis software[56,57] are currently available and often used for the analysis and interpretation of TA data.

Given that the differences in the electronic absorption spectra of the *ls*-Co[III] and *hs*-Co[II] are clear within the infrared, visible and UV spectral regions, and the availability of short-pulsed lasers of compatible wavelengths, transient absorption spectroscopy has been widely used in the investigation of VT dynamics in the electronic level[22,58,59,34,55,35].

Pioneering work on the investigation of the ultrafast dynamics of VT was performed by Adams *et al.*, 1996[22], who traced the photo-induced dynamics of the VT in Co(*diox*)$_2$(N-N) complexes (where *diox* = 3,5-ditertbutylcathecolate/3,5-ditertbutylsemiquinone, N-N = 1,10-phenantroline, 2,2'-bipyridine, 4,4'-dimethyl-2,2'-bipyridine or 4,4'-diphenyl-2,2'-bipyridine) using nanosecond transient absorption. In their TA experiments, the probe pulse was generated by a Xe flash lamp, and its emitted light passed through a monochromator, which only allows for the monitoring of transient signals in specific probe wavelengths. The transient signals obtained for the Co(*diox*)$_2$(4,4'-diphenyl-2,2'-bipyridine) complex in toluene at 298 K are

shown in Figure 2.8. Pump/probe wavelengths had been chosen to lie near isosbestic points of temperature dependent electronic absorption spectra for each of the complexes investigated (see Figure 2.3 for Co(*diox*)$_2$(1,10-phenantroline)).
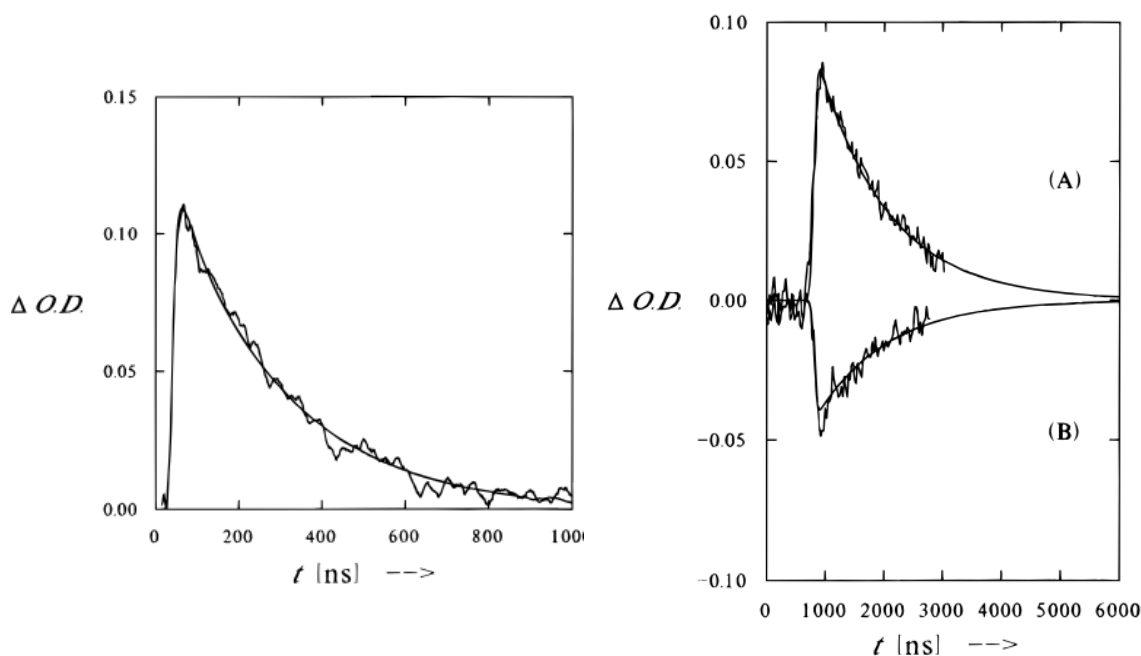
Figure 2.8- Right: Transient absorption decay for in toluene at 209.9 K, pump = 560 nm, probe = 740 nm. Data was fitted with a single exponential decay function, and the calculated time constant was τobs = 262 ns. Left: (A) Transient absorption signal (ΔOD = change in absorption) of Co(diox)$_2$(4,4'-diphenyl-2,2'-bipyridine) in toluene at 298 K, pump = 532 nm, probe = 720 nm. (B) Transient bleach monitored at 600 nm after excitation at 532 nm. Data were again fitted with a single exponential decay function, and the calculated time constants were τobs = 1.2 ns for both data sets. Figure from Adams et al., 1996[22].

More recent work by Wu *et al.*, 2020[60] also used transient absorption spectroscopy to investigate the VT in [Co(phendiox)(rac-cth)](ClO4)·0.5EtOH (H$_2$phendiox = 9,10-dihydroxyphenanthrene, rac-cth = racemic 5,5,7,12,12,14-hexamethyl-1,4,8,11-tetraazacyclotetradecane) and the electronic pyroelectricity led by the VT. Figure 2.9 shows the difference between the IR absorption spectra for the compound at 295 K and at 7 K, and the evolution of the same spectra over time in a picosecond timescale when the system is pumped with 380 nm light at 190 K, evidencing the similar nature of the temperature induced and light induced processes for longer time scales ($> 100\ ps$).
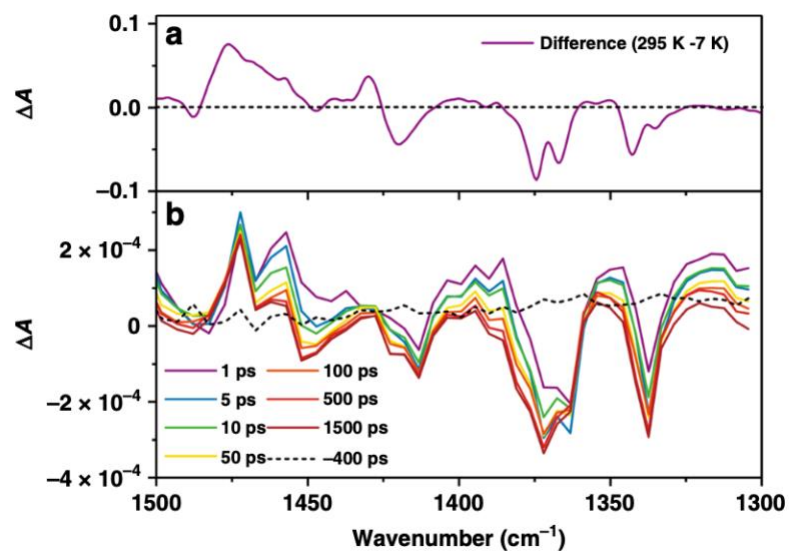
Figure 2.9 – IR difference spectrum for the [Co(phendiox)(rac-cth)](ClO₄)·0.5EtOH complex (a) temperature-induced difference spectra between 295 K and 7 K; (b) temporal evolution of transient IR difference spectra, pump wavelength of 380 nm, at 190 K. Figure from Wu et al., 2020[44].

3   Controlled valence tautomerism in a Cobalt-o-Dioxolene complex

The study of the light induced valence tautomerism in benzene solvated crystals of Co(*diox*)$_2$(4-CN-Py)$_2$ is reported in this chapter. The compound was crystallized in the P2$_1$/c, with two (Co*(diox)*$_2$(4-CN-py)$_2$) molecules in the unit cell (Z=2). SCXRD has been used to characterize the valence tautomerism in the crystal irradiated with 450 nm blue light and 660 nm red light at 30K. Our results show a very high (80%) VT interconversion yield from *ls*-Co^{III} to *hs*-Co^{II} when the crystal was irradiated with blue light and a 18% yield back VT interconversion, from *hs*-Co^{II} to *ls*-Co^{III}, when the light induced metastable excited states are irradiated with red light. Such high yield light-induced VT had never been experimentally observed in molecular crystals of cobalt tautomers, proving that the 450 nm light illumination is triggering all chain of events that leads to the *ls*-Co^{III} to *hs*-Co^{II} interconversion. The work has been communicated in the format of an article which has been submitted to and accepted by the Inorganic Chemistry Journal (https://doi.org/10.1021/acs.inorgchem.1c00638).

3.1 Motivation

Smart materials are those designed to respond to mechanical, chemical, electric or magnetic stimuli from the surrounding environment having one or more of their properties significantly changed in a controlled manner. Among these materials, those that present electronic bistability in the form of spin-crossover[61] (SC) or valence tautomerism[62] (VT) can be used potentially as sensors, signal processors and information storage devices for they can readily switch between two spin and/or electronic states[2,63,13]. Of particular interest are the solid-state materials composed by molecules that present valence tautomerism at a single metal center or within a molecular complex without substantial disruption of the solid-state structure[13,1,4].

Generally, the investigation of materials presenting VT is focused on the metal ions and the associated ligands that act as charge donors. In such materials, the VT process is accompanied by changes in structural, electronic and thermodynamic properties and can therefore be characterized with a number of experimental approaches and theoretical calculations. Of particular significance is the understanding of the effects of the variation of external factors on the VT properties and dynamics. It has been established that the symmetry of the environment, the nature of the ligands associated with the metal center, the presence and nature of solvate molecules and counter ions[4,25,64–66], as well as temperature[14], pressure[11], illumination[13],

magnetic and electric fields[6] and irradiation[13,15,16] will affect the VT process. The yield and rate of intramolecular electron transfer, the lifetime of induced metastable states and the stability of high-spin (*hs*) and low spin (*ls*) states are some of the important properties that can be modulated and controlled by external stimuli.

Complexes that display VT are composed by a transition metal ion center, organic redox-active ligands that act as charge donors/acceptors and organic ancillary ligands. Such complexes form solids in which intermolecular interactions extend over the lattice in one, two or three dimensions. Of the materials that present VT in the solid-state, the family of complexes with a cobalt metal center, dioxolene molecules that act as redox-active ligands and nitrogen based ancillary ligands have been thoroughly studied in the last decade[4]. These compounds undergo the reversible valence and spin interconversion from *ls*-Co^{III}(SQ)(Cat)R to *hs*-Co^{II}(SQ)$_2$R (*ls*: low spin, *hs*: high-spin; SQ: semiquinone; Cat: catecholate; R: 2 monodentate or 1 bidentate nitrogen based ligand). The interconversion is accompanied by a couple of reversible structural changes[16,26] that reflect the change of the electronic population of the metal and ligand orbitals. In particular, the isotropic contraction/expansion of the Co–L (L = O, N atoms) coordination sphere has been shown to be systematic in such a way that the interatomic distances between the Cobalt atom and its first neighboring atoms (the O atoms from the dioxolene and the N atoms from the ancillary ligand) can be used to compute the molar fraction of *hs*-Co^{II} and *ls*-Co^{III} within a crystal. Alternatively, the distances between the atoms of the redox-active ligand can also be used to compute the empirical "metrical oxidation state" (MOS), which gives a continuous measure of the apparent oxidation state of the ligand[67]. The values of all atomic distances within the complexes can be easily accessed through single crystal X-ray diffraction experiments.

Within the family of cobalt complexes that present VT, the octahedral cobalt with two 4-Cyan-pyridine (4-CN-Py) molecules as ancillary ligands and two 3,5-di-tert-butyl-semiquinonate/catecholate (3,5-DBSQ / 3,5-DBCat) as redox active ligands in trans configuration is a very versatile compound (named Co(*diox*)$_2$(4-CN-Py)$_2$ from here on, where *diox* is 3,5-DBSQ/3,5-DBCat). Its valence tautomerism has been shown to be controllable, being induced by temperature[14], visible light irradiation[12] and hard X-rays[16], and modulated by the absence or presence of solvent in the crystal lattice[26,64]. This complex was demonstrated to behave similarly to light-induced excited state spin trapping (LIESST) complexes for its highly stable photogenerated *hs*-Co^{II} form at temperatures lower than 50 K[12]. The stability of such excited states is believed to be due to lattice stabilization through hydrogen bonds[26]. However, the photo-conversion induced by white light was shown to be inefficient (30% yield), even though the wide spectrum of the white light seemed to have allowed for a higher interconversion rate in comparison to monochromatic laser illumination[12]. The electronic absorption spectrum of the Co^{II}(*diox*)$_2$(4-CN-Py)$_2$ cast as dilute polystyrene films has also been reported[14], and its metal to ligand charge transfer (MLCT) band is centered approximately at 740 nm (13500 cm^{-1}) and ranges from 500 nm to 1000 nm (20000 cm^{-1} to 10000 cm^{-1}). Co(*diox*)$_2$ complexes with different ancillary ligands have been shown to display MLCT bands near 800

nm (12500 cm^{-1}) and ligand to metal charge transfer (LMCT) transitions between 525-665 nm (15000 cm^{-1} to 19000 cm^{-1})[22,20,46,24,35]. Subsequent research showed that the photo-interconversion yield can be as high as 100% when the sample is irradiated with hard X-rays (25.5keV)[16]. The underlying process, named hard-X-ray-induced excited-spin-state trapping (HAXIESST), and the electronic dynamics involved is not yet understood.

In the present work, we continue to investigate the VT interconversion in benzene solvated Co(*diox*)$_2$(4-CN-Py)$_2$ crystals, and we demonstrate the photogeneration of metastable *hs*-Co^{II} centers from *ls*-Co^{III} centers at 30 K with 80% yield using 450 nm blue light (22222 cm^{-1}). We also present evidence for the reverse de-excitation using 660 nm red light (15151.5 cm^{-1}).

3.2 Experimental section

3.2.1 Complex Synthesis and Crystallization

The synthesis of Co(*diox*)$_2$(4-CN-Py)$_2$ (diox: 3,5-di-tert-butyl-o-semiquinonate/3,5-di-tert-butyl-o-cathecolate, 4-CN-Py: Cyano-pyridine) followed the procedures reported previously[12]. All chemicals for syntheses and analysis were of analytical grade and used without further purification. In an oven dried Schlenk flask, a 0.11mM solution of [Co^{II}(*diox*)$_2$]$_4$ in toluene affords a green solution, to which another solution of 0.91 mmol 4-Cyanopyridine in toluene is added, in a 7:2 volume ratio. The reaction mixture is stirred, shielded from light, and kept at 35 °C for 5 h. Concentration of the dark blue mixture by slow evaporation of benzene under a N$_2$ atmosphere affords the benzene solvated complex as blue needled crystals, suitable for X-ray diffraction experiments.

3.2.2 Single crystal X-ray diffraction data collection

The benzene solvated crystals were submitted to single crystal X-ray diffraction (SCXRD) experiments at the I19-2 beamline of the Diamond Light Source (Oxfordshire, UK), using 25.5keV X-rays and multiple attenuation values for the 200 μm x 200 μm beam. Samples were manually mounted on MiTeGen UV mounts in copper magnetic bases. Light-induced VT was probed in samples kept at 30 K; temperature-induced VT was probed from 30 K to 300 K. All low temperature SCXRD measurements had samples cooled using an open flow He cryostat (nHeliX, Oxford Cryosystems). Sample illumination was achieved using blue (450 nm) and red (660 nm) light from laser diodes (L450P1600MM and L660P120, ThorLabs, see Table S6 and Figure S8 of the supplementary information). Homogenous illumination of the samples was possible using an in-house built illumination ring that was placed around the low temperature device nozzle. The hutch lights were kept off for all the experiments, and during the SCXRD experiments, the diodes were turned off.

SCXRD data processing was performed using XDS[68], structure solution and structure refinement using SHELXT[69] and SHELXL[40] respectively, with the aid of python scripts (available upon request) that automatically run XDS and SHELXL sequentially for all datasets. The retrieval and analysis of quality indicators of data processing and refinement were also made using python scripts.

SCXRD data and structure refinement statistics for all the crystals used in this work at 30 K are reported in Table S2 of the supplementary information. *I/sigma*, *cc1/2* and *r1* parameters evolution for each experiment as a function of temperature and irradiation time are reported in Figures S1, S2 and S3 of the supplementary information.

3.2.3 X-ray diffraction experiments description

Different single crystals of [Co(*diox*)$_2$(4-CN-Py)$_2$]·benzene complex (diox = 3,5-di-t-butylsemiquinonate, (SQ$^{•-}$) and/or 3,5-di-t-butylcatecholate (Cat2-) radical; 4-CN-py = 4-Cyano-pyridine) were probed in X-ray diffraction experiments using hard X-rays. The experiments aimed for assessing X-ray irradiation effects on the valence tautomerism interconversion (VTI) at 30 K, temperature dependent VTI and light induced VTI using blue and red laser diodes. Single crystal X-ray diffraction (SCXRD) data were collected at I19 - the small-molecule single-crystal diffraction beamline at Diamond Light Source, which has a flux of about 1010 photons s^{-1}, distributed over a spot of 0.2 x 0.2 mm^2 - using 0.4859 Å radiation (25516.4 eV). A commercially available open-flow He cryostat apparatus (n-HeliX, Oxford Cryosystems), with stability better than ±0.3 K, was used to control the sample temperature. Sample illumination was achieved using blue (450nm) and red (660nm) light from laser diodes (L450P1600MM and L660P120, ThorLabs). Many different single crystal samples suitable for X-ray diffraction experiments were mounted in a caption loop and investigated. Experiments with three different samples turned out to produce consistent data for the structure analysis under hard X-ray irradiation and light illumination (see Table 3-1).

In the xrayinduce_1 experiment (see Table 3-1), the effect of the X-ray irradiation on the VTI rates was investigated, aiming for determining an attenuation regime in which VTI was negligible. Crystal 1 was fast cooled from 290 K down to 30 K, and seven (7) SCXRD runs at 30 K were performed for various attenuation values. The four (4) first experiments were undertaken with transmission factor of 25%. Then the sample was left under full beam transmission for 30 minutes and XRD was subsequently measured with 25% transmission. Finally, two (2) more SCXRD runs with transmission factor of 60% were performed. This experiment was used to look for the best experimental condition to avoid the tautomeric interconversion from ground state *ls*-Co^{III} into the metastable *hs*-Co^{II} due to hard X-rays irradiation.

For the experiment named lightinduce_3 and tempinduce_1, (see Table 3-1) another crystal was used. Crystal 2 was first fast cooled to 30K and SCXRD data before illumination was acquired at run 1. The sample was kept at 30K and illuminated with a laser diode of 450 nm

light for the times described in Table 3-1. The sample was rotated while being illuminated by the diode, hutch lights were maintained off throughout the whole experiment. Laser diodes were switched off during XRD data collection (0.4s per image, 635 images per omega). After a plateau in the VTI rate was achieved at run 5, the temperature dependent VTI interconversion was evaluated from runs 6 to 20, going from 30 K to 300 K, and back to 30 K at run 21.

Table 3-1: Run map and experiment details for the X-ray diffraction measurements for the 3 crystals reported.

Experiment	Run number	Datasets	Scan of data - rotation	Temperature	Sample	Sample size	Transmission factor	Pump wavelength (nm)	Pump power (mA)	irradiation time (s)	Total illumination (s)	Rint	RI
xrayinduce_1	1	02_CoCNPy_30K_Xray_1	4x omega	30K	1	100x50x50	25					3.9	0.042
	2	02_CoCNPy_30K_Xray_2	4x omega	30K	1	100x50x50	25					3.8	0.042
	3	02_CoCNPy_30K_Xray_3	4x omega	30K	1	100x50x50	25					3.9	0.043
	4	02_CoCNPy_30K_Xray_4	4x omega	30K	1	100x50x50	25					4.0	0.044
	5	03_CoCNPy_30K_Xray_1	4x omega	30K	1	100x50x50	25					4.2	0.044
	6	04_CoCNPy_30K_Xray_1	4x omega	30K	1	100x50x50	60					3.5	0.042
	7	04_CoCNPy_30K_Xray_2	4x omega	30K	1	100x50x50	60					3.6	0.041
lightinduce_3 and tempinduce_1	1	38_CoCNPy_30K_GS	4x omega	30K	2	300X100X100	5					3.4	0.052
	2	39_CoCNPy_30K_450nm_300s_rotate	4x omega	30K	2	300X100X100	5	450	28.84	300	300	5.0	0.076
	3	40_CoCNPy_30K_450nm_1800s_rotate	4x omega	30K	2	300X100X100	5	450	28.84	1800	2100	5.2	0.075
	4	41_CoCNPy_30K_450nm_1200s_rotate	4x omega	30K	2	300X100X100	5	450	28.84	1200	3300	5.1	0.072
	5	42_CoCNPy_30K_450nm_4500s_rotate	4x omega	30K	2	300X100X100	5	450	28.84	1200	4500	5.0	0.070
	6	43_CoCNPy_TS_30K	5x same run	30	2	300X100X100	5					6.6	0.093
	7	43_CoCNPy_TS_35K	5x same run	35	2	300X100X100	5					6.0	0.088
	8	43_CoCNPy_TS_40K	5x same run	40	2	300X100X100	5					6.0	0.092
	9	43_CoCNPy_TS_45K	5x same run	45	2	300X100X100	5					6.8	0.096
	10	43_CoCNPy_TS_50K	5x same run	50	2	300X100X100	5					5.6	0.084
	11	43_CoCNPy_TS_55K	5x same run	55	2	300X100X100	5					4.6	0.067
	12	43_CoCNPy_TS_60K	5x same run	60	2	300X100X100	5					4.5	0.067
	13	43_CoCNPy_TS_70K	5x same run	70	2	300X100X100	5					4.5	0.071
	14	43_CoCNPy_TS_80K	5x same run	80	2	300X100X100	5					4.6	0.073
	15	43_CoCNPy_TS_90K	5x same run	90	2	300X100X100	5					4.6	0.074
	16	43_CoCNPy_TS_100K	5x same run	100	2	300X100X100	5					4.8	0.074
	17	43_CoCNPy_TS_150K	5x same run	150	2	300X100X100	5					5.3	0.078
	18	43_CoCNPy_TS_200K	5x same run	200	2	300X100X100	5					5.9	0.092
	19	43_CoCNPy_TS_250K	5x same run	250	2	300X100X100	5					6.4	0.103
	20	43_CoCNPy_TS_300K	5x same run	300	2	300X100X100	5					7.8	0.116
	21	44_CoCNPy_30K_GS_after_Temp	4x omega	30	2	300X100X100	5					3.8	0.058
lightinduce_5	1	66a_CoCNPy_30K_GS	1x omega	30K	3	80x80x40	15					7.5	0.117
	2	66b_CoCNPy_30K_GS	1x omega	30K	3	80x80x40	15					7.6	0.099
	3	67_CoCNPy_30K_450nm_300s	1x omega	30K	3	80x80x40	15	450	25.47	300	300	7.4	0.143
	4	68_CoCNPy_30K_450nm_600s	1x omega	30K	3	80x80x40	15	450	25.47	300	600	11.0	0.131
	5	69_CoCNPy_30K_450nm_1800s	1x omega	30K	3	80x80x40	15	450	25.47	1200	1800	10.8	0.135
	6	70_CoCNPy_30K_450nm_1800s	4x omega	30K	3	80x80x40	15	450	25.47	1200	1800	8.43	0.087
	7	71_CoCNPy_30K_660nm_300s	1x omega	30K	3	80x80x40	15	660	120	300	300	7.4	0.128
	8	72_CoCNPy_30K_660nm_600s	1x omega	30K	3	80x80x40	15	660	120	300	600	9.4	0.129
	9	73_CoCNPy_30K_660nm_1800s	1x omega	30K	3	80x80x40	15	660	120	1200	1800	9.4	0.130

Lastly, experiment lightinduce_5 was performed with crystal 3 (see Table 3-1), a smaller crystal which required larger transmission values for the XRD experiment. At this experiment, the VTI induced by X-rays (runs 1 and 2) and 450 nm light (runs 3 to 6) was assessed until reaching the interconversion plateau, and the de-excitation of *hs*-Co^{II} metastable states was probed using 660 nm laser diode (runs 7 to 9).

3.2.4 Data reduction and structure refinement statistics

For all experiments and runs described in Table 3-1, single crystal X-ray diffraction data integration and scaling of the reflection intensities were performed with the using XDS1, in which we were not able to optimize processing parameters for small molecule crystal any further. However, data quality and consistency indicators were very satisfactory, as shown in Figure 3.1, Figure 3.2 and Figure 3.3. The software was recurrently recruited for systematic data processing of datasets with the aid of python scripts. Structure was solved by direct methods using SHELXT 2. Refinements were performed using SHELXL[40]. Hydrogen atoms were located in Fourier difference maps and included as fixed contributions according to the riding model4 (C–H and N–H = 0.97 Å and $U_{iso}(H) = 1.2\ U_{eq}$ (C or N) for methylene and aromatic groups and carbon atoms). All non-hydrogen atoms were refined with anisotropic atomic displacement parameters.

Particularly, the X-ray diffraction dataset of the lightinduce_5 experiments were obtained from a crystal which was undergoing valence tautomerism interconversion induced by X-rays. Therefore, each group of images from the rotation around different degrees of freedom of the goniometer had to be processed separately in order to account for the structural changes accordingly. This led to data sets with reduced completeness that did not compromise the refinements i.e. in did not impact the interatomic distances used to compute metastable molar fractions.

Information regarding crystal data, measurement and refinement data, for crystal samples 1, 2 and 3 are shown in Table 3-2. CCDC[41] CIF files 2058451-2058453 contain the complete supplementary crystallographic data for three representative experiments performed and for the different crystals in this work. They can be obtained free of charge from The Cambridge Crystallographic Data Centre via https://www.ccdc.cam.ac.uk/structures/.

Table 3-2 SCXRD data and structure refinement statistics for the 3 crystals investigated at 30K.

Crystal number	1	2	3
Empirical formula	C52 H60 Co N4 O4	C52 H60 Co N4 O4	C52 H60 Co N4 O4
Formula weight	863.97	863.97	863.97
Temperature	30.15 K	30.15 K	30.15 K
Wavelength	0.4859 Å	0.4859 Å	0.4859 Å
Crystal system	Monoclinic	Monoclinic	Monoclinic
Space group	P 1 2$_1$/c 1	P 1 2$_1$/c 1	P 1 2$_1$/c 1
Unit cell dimensions	a = 14.96(2) Å	a = 14.90(3) Å	a = 15.01(6) Å
	b = 22.08(2) Å	b = 22.07(3) Å	b = 22.16(7) Å

	c = 7.303(7) Å	c = 7.297(8) Å	c = 7.34(3) Å
	β = 97.33(8)°.	β = 97.24(6)°.	β = 97.19(4)°.
Volume	2393(5) $Å^3$	2381(6) $Å^3$	2422(15) $Å^3$
Z	2	2	2
Density (calculated)	1.199 Mg/m^3	1.205 Mg/m^3	1.185 Mg/m^3
Absorption coefficient	0.406 mm^{-1}	0.408 mm^{-1}	0.401 mm^{-1}
F(000)	918	918	918
Crystal size	0.1 x 0.05 x 0.05 mm^3	0.3 x 0.1 x 0.1 mm^3	0.08 x 0.04 x 0.04 mm^3
Theta range	0.938 to 17.679°.	1.133 to 17.679°.	1.566 to 17.678°.
Index ranges	-18<=h<=17, -27<=k<=27, -9<=l<=7	-18<=h<=18, -27<=k<=23, -9<=l<=9	-18<=h<=9, -23<=k<=23, -7<=l<=8
Reflections collected	30071	29633	6601
Independent reflections	4889 [R(int) = 0.0448]	4865 [R(int) = 0.0414]	3328 [R(int) = 0.0673]
Completeness	100.0 %	99.9 %	68.7 %
Refinement method	Full-matrix least-squares on F^2	Full-matrix least-squares on F^2	Full-matrix least-squares on F^2
Data/restraints/parameters	4889 / 36 / 271	4865 / 36 / 271	3328 / 36 / 271
Goodness-of-fit on F^2	1.023	1.062	0.912
Final R indices [I>2sigma(I)]	R1 = 0.0340, wR2 = 0.0853	R1 = 0.0418, wR2 = 0.1115	R1 = 0.0820, wR2 = 0.2139
R indices (all data)	R1 = 0.0409, wR2 = 0.0893	R1 = 0.0465, wR2 = 0.1152	R1 = 0.1186, wR2 = 0.2555
Largest diff. peak and hole	0.443 and -0.347 e.$Å^{-3}$	1.514 and -0.628 e.$Å^{-3}$	1.721 and -1.025 e.$Å^{-3}$
CCDC code	2058451	2058452	2058453
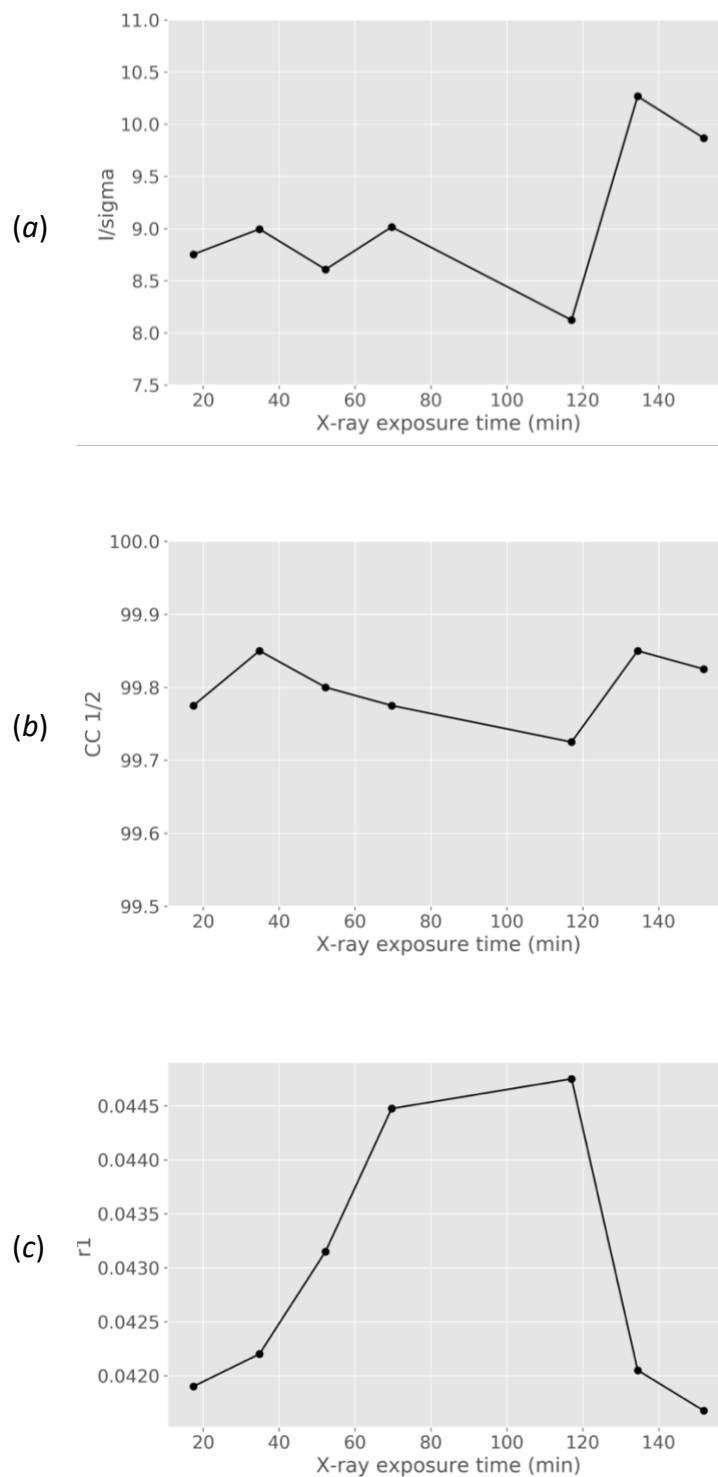
*Figure 3.1 - **Crystal 1**, experiment **xrayinduce_1**: VT induced by X-rays for different attenuations. The evolution of the statistics of the X-ray diffraction data and refinement for the crystals 1, 2 and 3. (a) I/sigma, (b) cc1/2, (c) r1.*
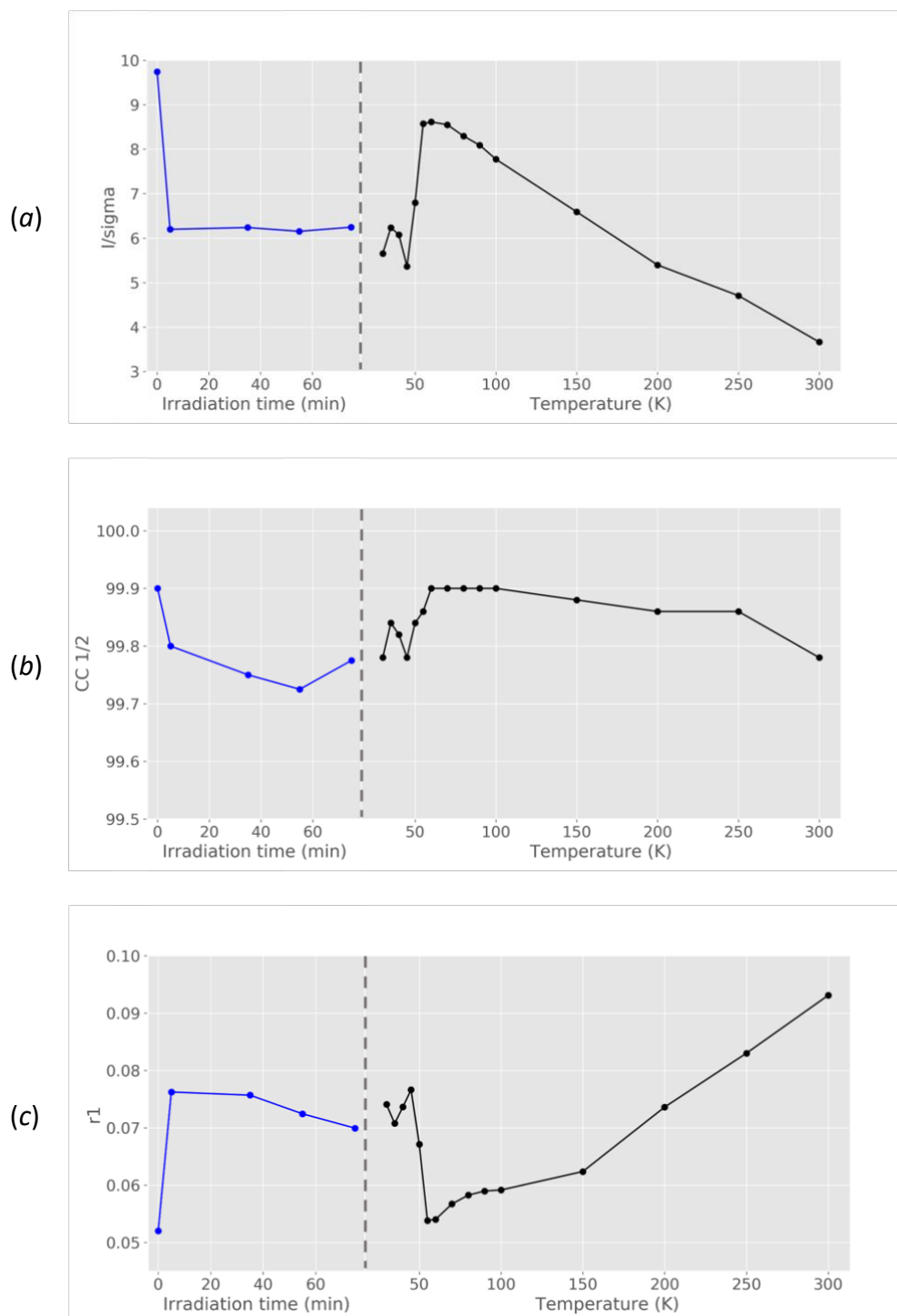
*Figure 3.2 – **Crystal 2**, experiment **lightinduce_3 and tempinduce_1**: VT induced by blue 450 nm light and sequentially by temperature increase. The evolution of the statistics of the X-ray diffraction data and refinement for the crystals 1, 2 and 3. (a) I/sigma, (b) cc1/2, (c) r1.*
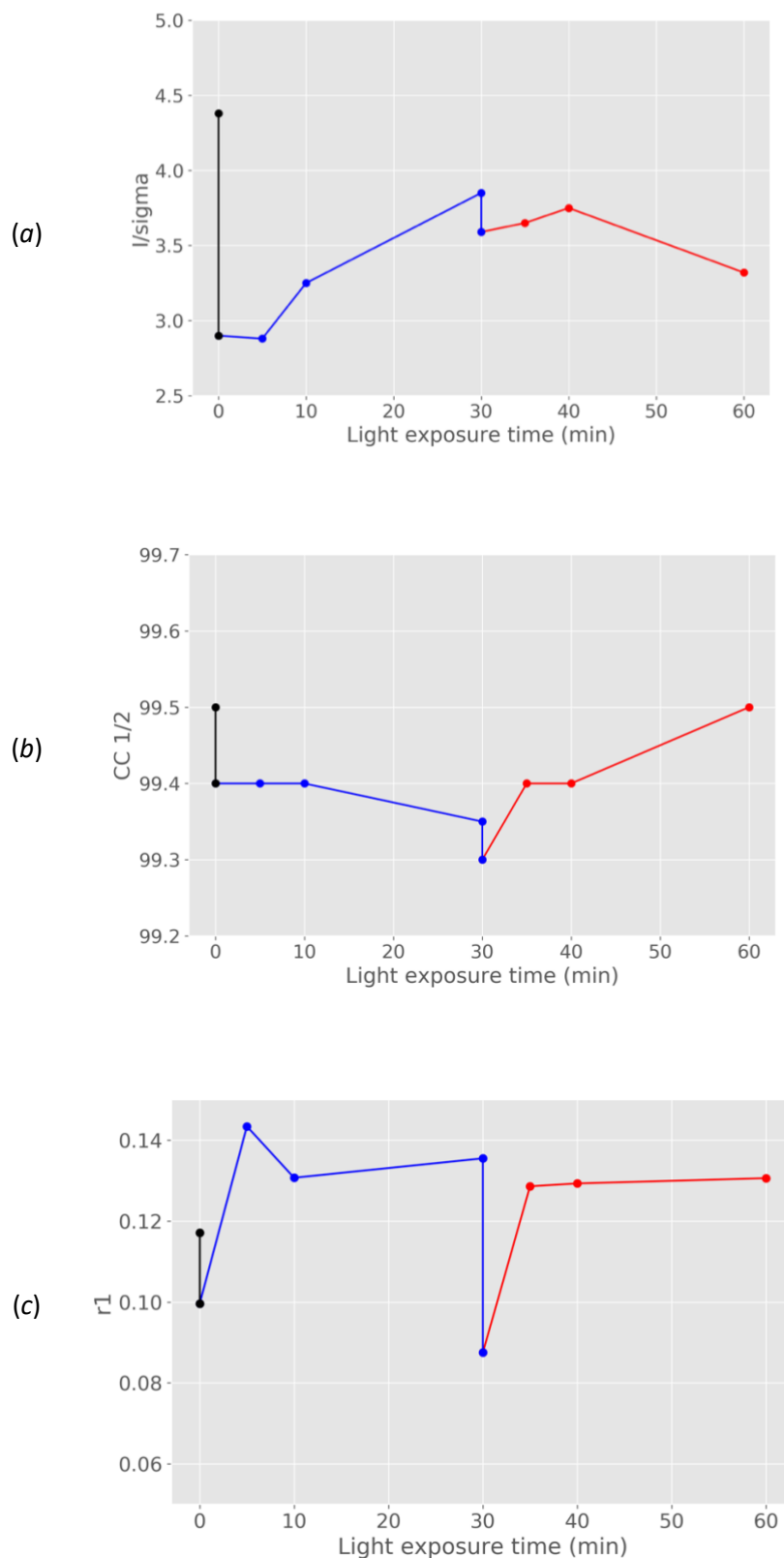
*Figure 3.3 - **Crystal 3**, experiment **lightinduce_5**: VT induced by X-rays, blue 450 nm light (0-30 min) and de-excitation of metastable states by red 660 nm light (30-60 min). The evolution of the statistics of the X-ray diffraction data and refinement for the crystals 1, 2 and 3. (a) I/sigma, (b) cc1/2, (c) r1.*

3.2.5 hs-Co^{II} molar fraction calculation

The molar fraction of the cobalt centers with different oxidation states were computed following equations (9) and (10), proposed by Ribeiro *et al.* 2016[26]. The standard distances for both oxidation states of Co (Co^{II} and Co^{III}) averaged from distances surveyed in the Cambridge Structural Database (CSD)[70] and indicated in Table 3-3. The error for the calculated values of *hs*-Co^{II} was evaluated by the partial derivatives method.

Table 3-3 Reference Co-N and Co-O distances surveyed from CIF files1559584–1559598 at the CCDC[41] databank.

$D^{Co-N}_{Co^{III}} = \mathbf{1.940(16)}\text{Å}$	$D^{Co-N}_{Co^{II}} = \mathbf{2.151(7)}\text{Å}$
$D^{Co-O1}_{Co^{III}} = \mathbf{1.889(6)}\text{Å}$	$D^{Co-O1}_{Co^{II}} = 2.060(5)\text{Å}$
$D^{Co-O2}_{Co^{III}} = \mathbf{1.872(12)}\text{Å}$	$D^{Co-O2}_{Co^{II}} = 2.045(2)\text{Å}$

3.2.6 MOS calculation

In order to corroborate with the *hs*-Co^{II} molar fraction calculation results, the assignment of the oxidation state of the metal and ligand involved in the valence tautomerism of complexes with cathecolate as redox-active ligand can also be performed using the metrical oxidation state (MOS) calculation method proposed by Brown, 2012[67]. In such method, the distances between carbon atoms in the dioxolene ring are considered given the linear relations between the C-C bond lengths and the oxidation state of the redox-active ligand.

The possible oxidation states of the dioxolene ligand are -2, -1 and 0, as shown in Figure 3.4. The calculation of the MOS for the dioxolene indirectly provides us with the oxidation state of the metal, once the total charge of the molecule does not change during the VT interconversion. The MOS method was used herein to support the results obtained in our work, in which we use solely the metal-L distances to compute *hs*-Co^{II} mole fraction as proposed by Ribeiro *et al.*, 2016[26].

For the Co(*diox*)$_2$(4-CN-Py)$_2$ complex, the VT transition reversibly assesses the [hs-Co^{II}(SQ)$_2$(4-CN-Py)$_2$] and [ls-Co^{III}(Cat)(SQ)(4-CN-Py)$_2$] states (SQ = semiquinone, Cat = cathecolate). In our work, the [Co(*diox*)$_2$(4-CN-Py)$_2$] crystalized in the monoclinic P2$_1$/c space group, with the Co atom sitting in a crystallographic center of inversion symmetry. Because of such, there is only one unique *diox* ligand for each complex molecule in the crystal structure and the SQ•- and Cat^{2-} forms are superimposed in the high-spin state of the complex. Given this, the MOS calculation for our crystal structure should give MOS $= -1$ for the *hs*-Co^{II} states, MOS $= [-1 + (-2)]/2 = -1.5$ for the *ls*-Co^{III} states, and values $-1.5 \leq MOS \leq -1$ during the VT interconversion.
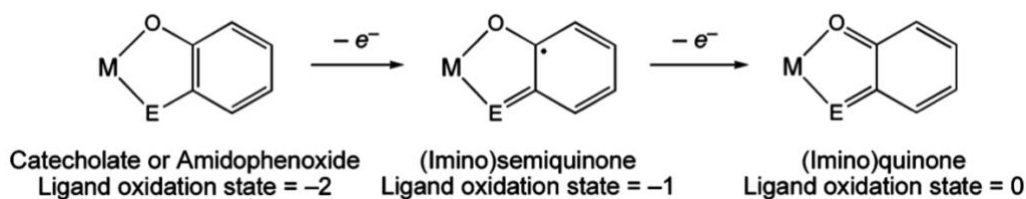
Figure 3.4 - Possible oxidation states of the cathecolate ligand (E = O). Figure from [67].

3.3 Results and discussion

3.3.1 Structure description

The (Co(diox)$_2$(4-CN-Py)$_2$·benzene crystallizes in the monoclinic space group P2$_1$/c, with two Co(diox)$_2$(4-CN-Py)$_2$ molecules in the unit cell (Z=2). The Co atom sits on a crystallographic center of symmetry, with one diox, one 4-CN-py ligand and one benzene solvent molecule in the asymmetric unit. Because of the symmetry requirement there is only one unique diox ligand so that in the high-spin state of the complex the resultant SQ and/or Cat^{2-} forms are superimposed. Therefore, X-ray diffraction technique affords only an average of the SQ$^{•-}$ and/or Cat^{2-} forms in the *ls*-[Co^{III}(SQ$^{•-}$)(Cat^{2-})] isomer. Figure 1 shows the molecular structure of the complex in a benzene solvated crystal at 30 K, solved by SCXRD. Selected intermolecular bond distances and angles as well as intermolecular hydrogen bonds for crystals 1, 2 and 3 at 30K are shown in tables 3.4, 3.5, 3.6 respectively. As expected, the bond length values for all crystals are similar indicating the quality of crystals at the beginig of the experiments and assuring that any observalble changes are due to the external stimulus (Table 3-4,

Table 3-5, Table 3-6).
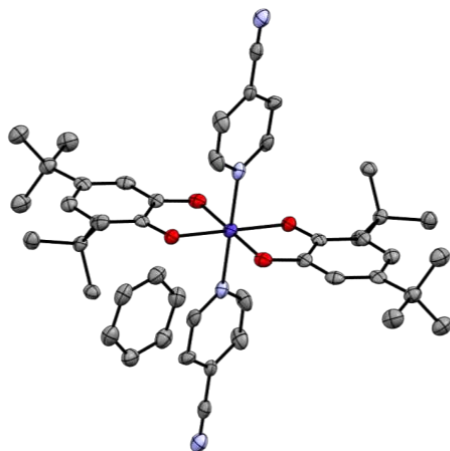
Figure 3.5 - Molecular structure of benzene solvated Co(diox)2(4-CN-Py)2 crystal at 30 K. Atom colors: Co (dark blue), C (gray), N (light blue), O (red). Hydrogens are hidden for clarity purposes.

Table 3-4 - Bond lengths between Co-N, Co-O and C-O for Crystal 1, experiment xrayinduce_1.

1. Metal-O/N bond lengths [Å] at 30K.

C(1)-O(1)	1.329(3)
C(2)-O(2)	1.329(2)
N(1)-Co	1.9569(19)
O(1)-Co	1.8842(17)
O(2)-Co	1.885(3)

2. Hydrogen bonds [Å and °].

D-H...A	d(D-H)	d(H...A)	d(D...A)	<(DHA)
C(15)-H(15)...O(1)	0.95	2.32	2.820(3)	111.9
C(16)-H(16)...O(2)#2	0.95	2.3	3.215(3)	160.8
C(18)-H(18)...N(2)#3	0.95	2.48	3.414(4)	168.1
C(19)-H(19)...O(1)#1	0.95	2.41	2.857(3)	108.5

Symmetry transformations used to generate equivalent atoms:

#1 -x,-y+1,-z+1; #2 x,y,z+1; #3 x,-y+1/2,z-1/2

Table 3-5 - Bond lengths between Co-N, Co-O and C-O for Crystal 2, experiment lightinduce_3 and tempinduce_1.

1. Metal-O/N bond lengths [Å] at 30K.

C(1)-O(1)	1.326(3)
C(2)-O(2)	1.328(2)
N(1)-Co	1.958(2)
O(1)-Co	1.886(2)
O(2)-Co	1.884(3)

2. Hydrogen bonds [Å and °].

D-H...A	d(D-H)	d(H...A)	d(D...A)	<(DHA)
C(15)-H(15)...O(1)	0.95	2.32	2.820(3)	111.9
C(16)-H(16)...O(2)#2	0.95	2.3	3.212(3)	160.7
C(18)-H(18)...N(2)#3	0.95	2.48	3.404(5)	167.8
C(19)-H(19)...O(1)#1	0.95	2.41	2.858(4)	108.6

Symmetry transformations used to generate equivalent atoms:

#1 -x,-y+1,-z+1; #2 x,y,z+1; #3 x,-y+1/2,z-1/2

Table 3-6 - Bond lengths between Co-N, Co-O and C-O for Crystal 3, experiment lightinduce_5

1. Metal-O/N bond lengths [Å] at 30K.

C(1)-O(1)	1.345(7)
C(2)-O(2)	1.336(7)
N(1)-Co	1.957(6)
O(1)-Co	1.888(6)
O(2)-Co	1.896(7)

2. Hydrogen bonds [Å and °].

D-H...A	d(D-H)	d(H...A)	d(D...A)	<(DHA)
C(15)-H(15)...O(1)	0.95	2.34	2.832(9)	112
C(16)-H(16)...O(2)#2	0.95	2.32	3.232(11)	161.1
C(18)-H(18)...N(2)#3	0.95	2.5	3.433(12)	168.2
C(19)-H(19)...O(1)#1	0.95	2.44	2.877(10)	108

Symmetry transformations used to generate equivalent atoms:

#1 -x,-y+1,-z+1; #2 x,y,z+1; #3 x,-y+1/2,z-1/2

3.3.2 X-ray induced VT

The valence tautomeric interconversion of Co($diox$)$_2$(4-CN-Py)$_2$ can be induced by X-ray irradiation of the benzene solvated crystals at low temperatures, though the yield of hs-Co^{II} photogeneration has been shown to be highly dependent on the incident X-ray flux[16]. This property has to be observed and controlled in order assure minimal interference of the X-ray irradiation when probing the VT induced by visible light illumination in SCXRD experiments. Initial SCXRD experiments were then used to probe the electronic state of the metallic center when the crystals were under hard X-ray (25.5keV) irradiation. The estimation of the molar fraction $\gamma(hs - Co^{II})$ of hs-Co^{II} states within the crystal was done based on the Co-L distances (L = O1, O2 and N) using equations 1 and 2.

The evaluation of the molar fraction of X-ray induced hs-Co^{II} in the crystal as a function of X-ray exposure time was achieved with multiple sequential SCXRD measurements performed on the same crystal at 30 K for 0.25 and 0.6 transmission (runs 1,2,3,4,5 and 6,7 respectively, see Table 3-1) of the X-ray beam. SCXRD datasets were acquired sequentially except for the fifth dataset obtained after 30 minutes of irradiation by the non-attenuated X-ray beam (Figure 2). No rotation of the crystal was performed when full transmission of the beam was used, leading to a lower X-ray induced VT interconversion when compared to the rotating sample exposed to 0.25 and 0.6 beam transmission. The crystal information and crystallographic quality indicators of these experiments are shown in Table S1 of the supplementary information.
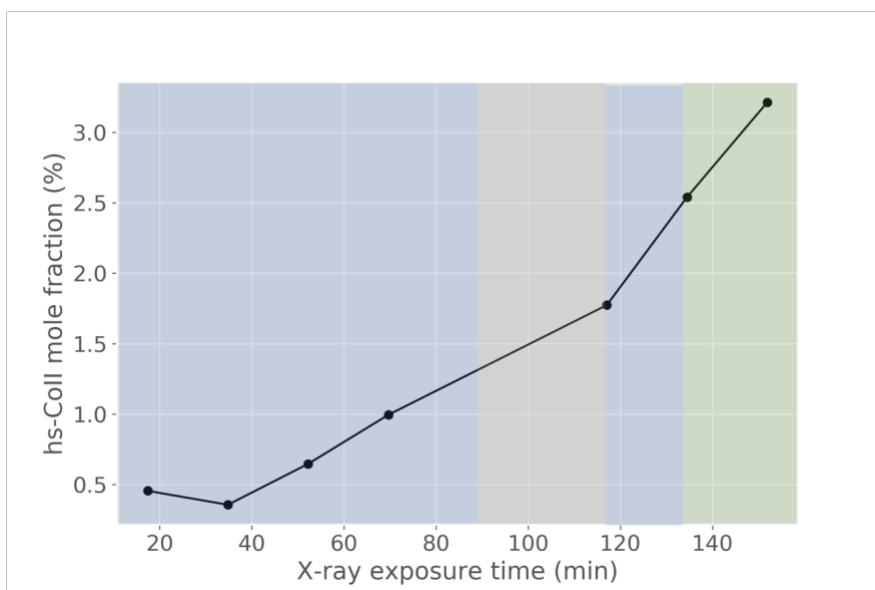
Figure 3.6 - Molar fraction of hs-Co^{II} species induced by X-ray irradiation during SCXRD experiments with the [Co(diox)$_2$(4-CN-Py)$_2$)]·benzene crystal at 30 K. The blue, grey and green shaded regions correspond respectively to time intervals in which the crystal was exposed to 0.25, 1 and 0.6 transmission of the X-ray beam.

Figure 3.6 shows the calculated Co^{II} molar fraction as a function of X-ray irradiation time. The results revealed that for that specific beamline and for a crystal with dimensions of 100 μm x 50 μm x 50 μm, the *hs*-Co^{II} molar fraction induced by X-ray irradiation was smaller than 3%, even for full beam transmission. In the experiments 6 and 7 the molar fraction of metastable *hs*-Co^{II} seems to grow faster than in the 5 previous experiments and this is likely to be due to the exposure to high X-ray intensity during the SCXRD data collection. Nevertheless, only 3% of metastable molar fraction was induced after all the 140 min of hard X-rays irradiation. The average error for the calculated molar fraction was calculated to be 4%, which is already larger than the values observed. Using a conservative approach for subsequent experiments, the attenuation of the X-ray beam was chosen to ensure negligible X-ray VT conversion, in which $\gamma(hs - Co^{II})$ is smaller than 1% after 60 min of X-ray exposure.

As expected, the calculated MOS of the dioxolene ligands corroborate with the change in the oxidation state of the Co calculated solely by Co-L (L = O1, O2 and N) interatomic distances (Figure 3.7). Moreover, the evolution of crystal quality indicators (*I/sigma*, *cc1/2* and *r1*) parameters this experiment as a function of X-ray exposure time is shown in the Appendix
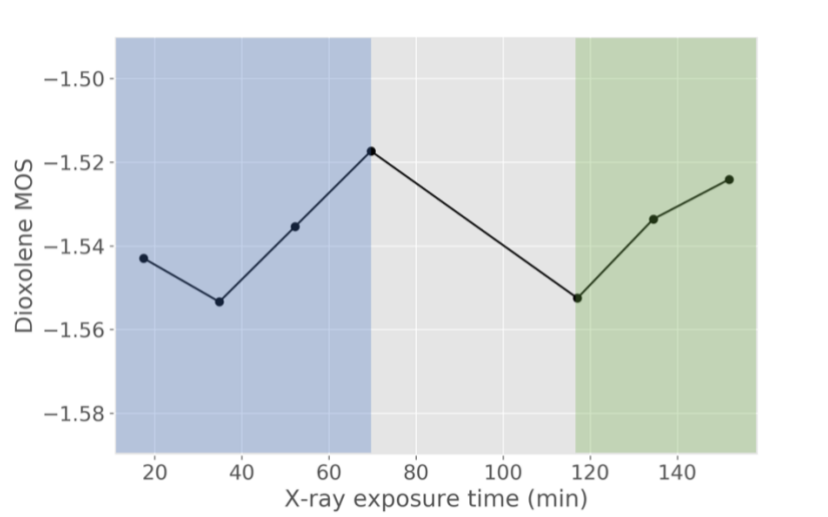
Figure 3.7 - MOS for the dioxolene ligand during the X-ray exposure when testing the X-ray induced VT at 30 K during SCXRD experiments with the [Co(diox)₂(4-CN-Py)₂)]·benzene crystal. The blue, grey and green shaded regions correspond respectively to time intervals in which the crystal was exposed to 0.25, 1 and 0.6 transmission of the X-ray beam.

3.4 Blue light induced VT

Crystals of the non-solvated Co(*diox*)$_2$(4-CN-Py)$_2$ have also been shown to display light induced valence-tautomerism VT by Schmidt *et al.* 2010[12]. In that work, samples were kept at 10 K and illuminated with white light (from 450 nm to 850 nm, no spectrum shape is reported) and the presence of *hs*-Co^{II} was monitored through magnetic susceptibility measurements. A photo-stationary limit for the metastable *hs*-Co^{II} redox isomer conversion was never achieved, as the value of the magnetic susceptibility continued to grow (albeit at a very slow rate) even after 12h of illumination, with maximum conversion percentages approaching 30%. Later, Francisco *et al.* 2017[16] showed that 100% conversion to the metastable *hs*-Co^{II} form at 30 K in solvated crystals is possible using non-attenuated hard X-rays, without any disruption of the crystal lattice or loss in crystal quality after recuperation of initial states. This last result proved that the crystal lattice does allow for the full VT interconversion. Moreover, it is known that the VT interconversion for certain Co complexes can be induced both ways, from *ls*-Co^{III} to *hs*-Co^{II} and vice versa, using different excitation and de-excitation wavelengths[31]. Therefore, it could be that for the Co(*diox*)$_2$(4-CN-Py)$_2$ crystal, in the work of Schmidt *et al.* 2010, both excitation and de-excitation wavelengths were contained within the wide spectrum used, and concomitant excitation de-excitation processes limited the VT interconversion rate[12].

In order to test such hypothesis, in this work, a benzene solvated crystal with dimensions of 300 μm x 100 μm x 100 μm was mounted, cooled down to 30 K, and illuminated with blue 450 nm laser diode light while being rotated with respect to the diode array using the goniometer. SCXRD datasets were acquired with 5% transmission of X-rays for 0, 5, 35, 55 and 75 min of LED illumination. The respective crystal structures were solved and the metastable *hs*-Co^{II} molar

fractions were calculated. Figure 3.8 shows that after 55min of light illumination, an 80% metastable *hs*-Co[II] conversion yield plateau is reached. This limit could be related to the penetration depth of the blue light through the crystal. The electronic absorption spectrum of the Co[III](*diox*)$_2$(4-CN-Py)$_2$ complex was supposed to have its LMCT centered approximately at 550 nm (~18181 cm^{-1})[20,24,35]. The 450 nm (22222 cm^{-1}) blue light used herein would lie in a low absorption cross section region of the electronic absorption spectrum of the Co(*diox*)$_2$(4-CN-Py)$_2$ molecule. Wavelengths lying in the edge of the LMCT band (<500 nm) have been reported to induce the VT in Cobalt complexes via charge transfer, intersystem crossing and vibrational relaxation[34,35,71], but have also been assigned to *d-d* transitions for *ls*-Co[III] [8,24,72–74]. In our experiments, 450 nm blue light irradiation at 30 K led to the highest (~80%) yield of photo-induced *hs*-Co[II] interconversion observed in a Co(*diox*)$_2$ complex in solid state.
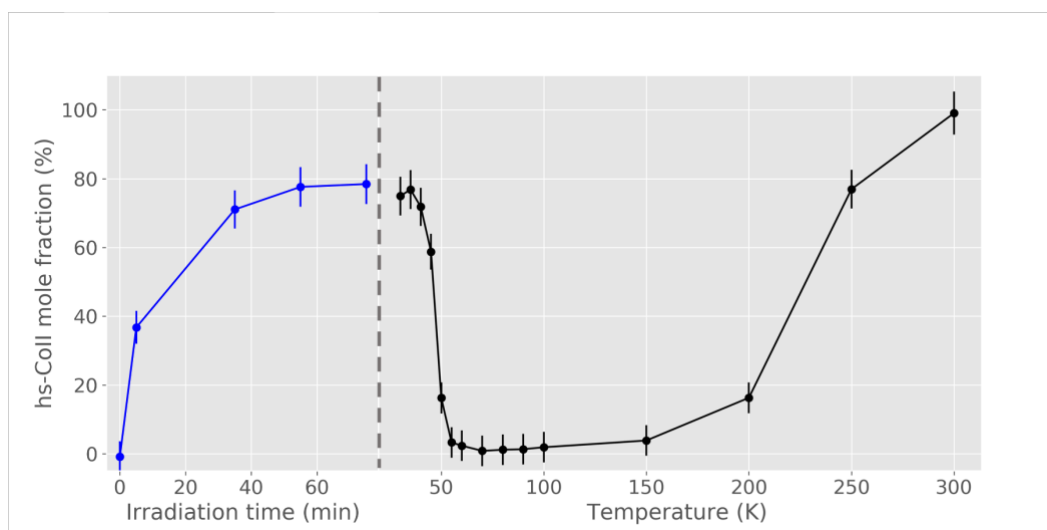
Figure 3.8 - Molar fraction of hs-CoII species in the [Co(diox)$_2$(4-CN-Py)$_2$)]·benzene crystal when exposed to blue 450 nm illumination (blue points) at 30 K and to an increase in temperature from 30 K to 300 K (black points).

After the plateau was reached, the illumination was turned off and a temperature dependent sequence of SCXRD experiments shows the full recovery of *ls*-Co[III] states (approximately 0% *hs*-Co[II] molar fraction between 55 K and 90 K) and the subsequent well-known second order (non-cooperative) VT interconversion in the characteristic temperature range of 150-230 K. At 300 K, 100% of the unit cells have units of the complex in the *hs*-Co[II] state. After reaching room temperature, the crystal was again cooled down to 30 K, and the SCXRD shows that the quality of the crystal is also recovered after all the interconversion cycles (Table 3-1, run 21).

As expected, the calculated MOS of the dioxolene ligands corroborate with the change in the oxidation state of the Co calculated solely by Co-L (L = O1, O2 and N) interatomic distances (Figure 3.9). And the evolution of the data statistics and structural refinements quality indictors as a function of light illumination time and temperature indicates that the illumination does no more damage to the crystal than the increase in temperature (see Figure 3.2), demonstrating the robustness of such material as a solid-state tautomer.
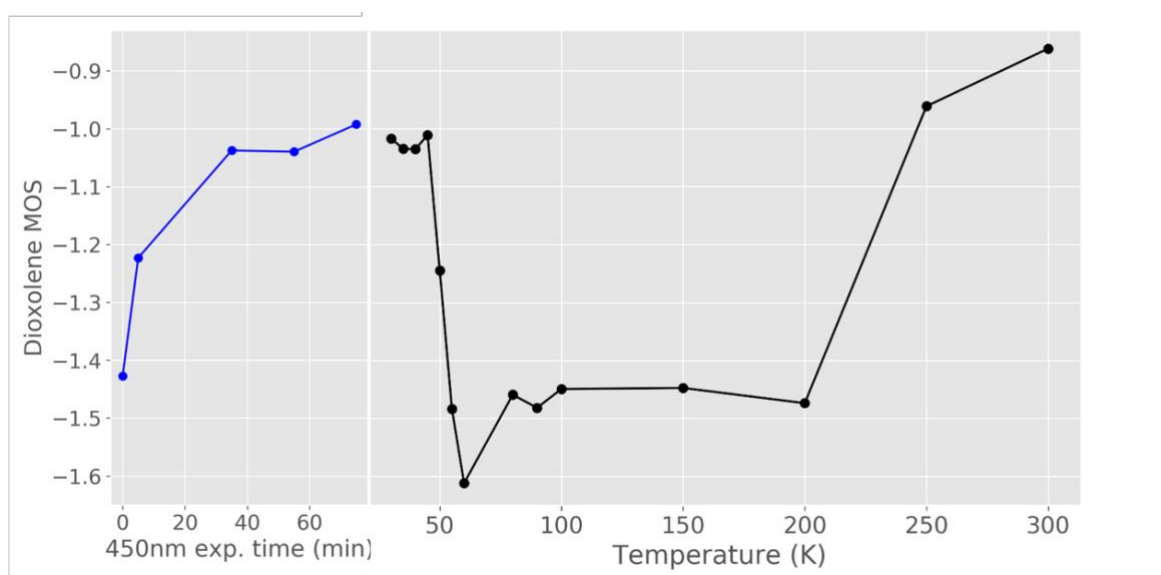
Figure 3.9 - MOS for the dioxolene ligand of the in the [Co(diox)₂(4-CN-Py)₂)]·benzene crystal when exposed to blue 450 nm illumination (blue points) and to an increase in temperature (black points).

3.4.1 Red light induced VT

The high photoconversion yield of 450 nm blue light illumination observed in our experiment reinforces the belief that the broad white light spectrum used by Schmidt *et al.* 2010[12] also contains the metastable state de-excitation wavelengths, limiting the observed interconversion yield. To test the hypothesis, a 660 nm laser diode was used to illuminate another benzene solvated crystal (80 μm x 40 μm x 40 μm) of Co($diox$)$_2$(4-CN-Py)$_2$ at 30 K, which was submitted first to blue 450 nm light irradiation to achieve the high-spin states and to SCXRD experiments with 40% X-ray transmission. The higher transmission was necessary for sharper and more intense SCXRD images, because the crystal was substantially smaller than the ones previously used. Initially, sequential dark measurements were taken to establish the baseline for the X-ray induced interconversion. After that, the blue 450 nm laser diode was turned on and used to illuminate the rotating sample. SCXRD experiments were performed after set intervals of light irradiation (5, 10 and 30 min). Two datasets were sequentially collected after 30min of blue light irradiation, and immediately after that, the red 660 nm laser diode was turned on to irradiate the rotating crystal. The SCXRD datasets were acquired after 5, 10 and 20 minutes of red-light irradiation.

The calculated *hs*-Co^{II} molar fraction for the solvated Co($diox$)$_2$(4-CN-Py)$_2$ crystal structure under illumination in the described experimental sequence is shown in Figure 3.10 The X-rays induced around 16.22%±0.05% of metastable *hs*-Co^{II} even before the blue 450 nm irradiation, though the blue light lifted the interconversion yield to 90.60%±0.05% after 30min of irradiation. The subsequent, partial de-excitation of the complexes is observed when the crystal

is irradiated with the red 660 nm laser diode light. A decrease in the *hs*-Co^{II} molar fraction is observed until it reaches a plateau of 72.12%±0.05%.
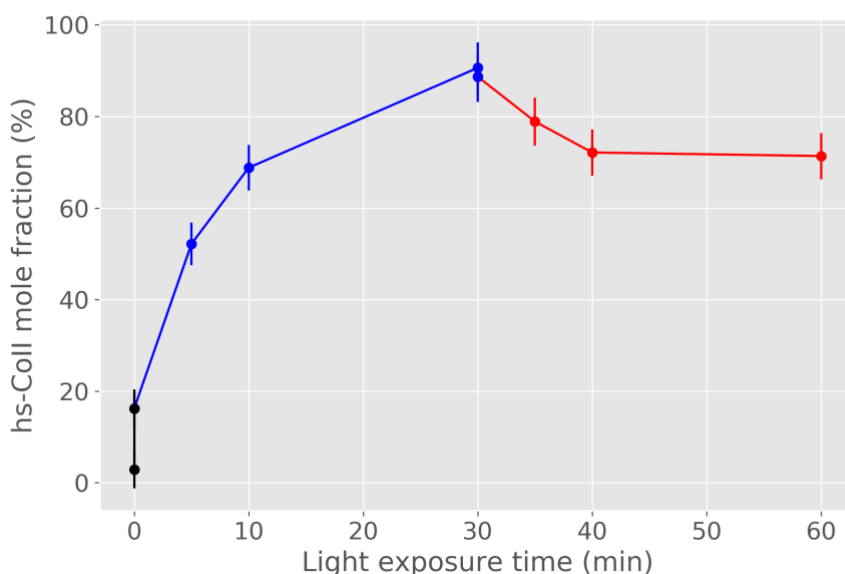
Figure 3.10- Molar fraction of hs-Co^{II} species induced by X-rays (black dots), blue 450 nm light (blue dots) and red 660 nm light (red dots) as a function of irradiation time for the [Co(diox)$_2$(4-CN-Py)$_2$)]·benzene crystal at 30 K.

As expected, the calculated MOS of the dioxolene ligands corroborate with the change in the oxidation state of the Co calculated solely by Co-L (L = O1, O2 and N) interatomic distances (Figure 3.11). The 660 nm (15151 cm^{-1}) light lies on the MLCT transfer band region of the electronic spectra of Co^{II}(*diox*)$_2$ complexes and would be expected to induce the charge transfer[14,22,24,35,46]. However, its lower efficiency in inducing the VT could indicate that the penetration depth of such wavelength may be a limiting factor. It is important to note that many effects are being considered: the VT induced by the X-rays irradiation, the stability of the photo-excited states from the blue light and the back valence-tautomerism observed after illumination with 660 nm red light. The crystals are only being exposed to X-rays during the SCXRD experiments, which last for 4.35 min (0.4s per image, 653 images per run – see Table 3-1) and the metastable *hs*-Co^{II} states are spin trapped at 30 K. The observed decay can only be due to the red 660 nm illumination, which is demonstrated to be more than sufficient to counterbalance the X-ray excitation.

The penetration depth issue for all the light radiation used in our experiments still remain unsolved, as we were not able to characterize it, or characterize the dependence of the VT interconversion yields to the crystal size. If it is the case that the penetration of red 660 nm light is too small, the back VT will be severely limited.
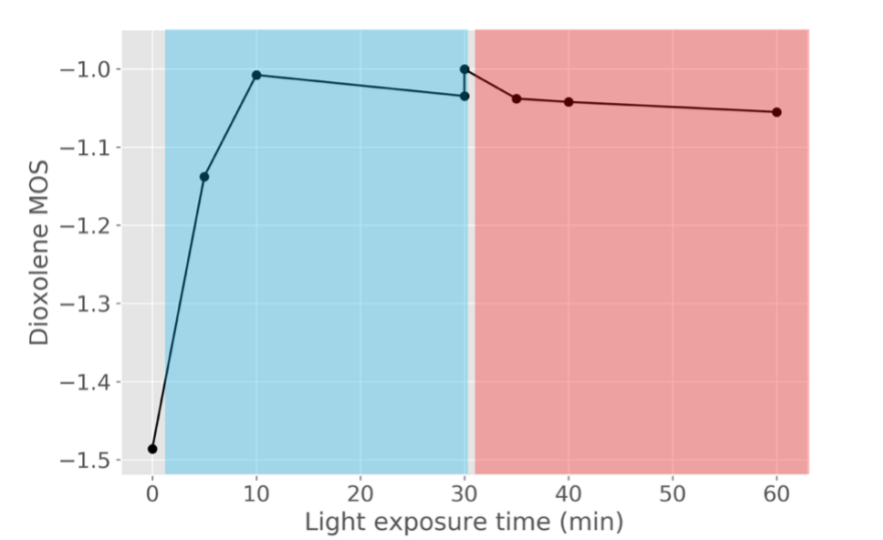
Figure 3.11 - MOS for the dioxolene ligand in an SCXRD experiment with no light (gray region), during blue 450 nm light irradiation (blue region), with subsequent 660 nm irradiation (red region) as a function of time for the [Co(diox)$_2$(4-CN-Py)$_2$]·benzene crystal.

3.5   Conclusions

In our work we presented the light-induced VT with high yield of metastable states of the benzene solvated Co(*diox*)$_2$(4-CN-Py)$_2$ crystal. The versatility of the tautomer studied here brings about a series of questions on the mechanisms of the tautomeric interconversion displayed by this material. Because of the very different nature of the visible white light and the hard X-rays used to induce the VT, along with their respective interconversion yields, it is plausible that they induce VT via different processes.

Despite the previously reported capability of hard X-rays to induce the VT interconversion, we demonstrated that the effect of the X-rays can be reduced and nearly eliminated by attenuating the X-ray beam to an appropriate flux. Therefore, the photo-induced VT interconversion was successfully probed using single crystal X-ray diffraction at a synchrotron source with an attenuated X-ray beam making sure that the X-rays were not inducing the formation of metastable states.

Our findings show that the *ls*-Co^{III} to *hs*-Co^{II} transition in the benzene solvated Co(*diox*)$_2$(4-CN-Py)$_2$ crystals, when induced either by X-rays, light or temperature, is reversible. Most importantly, we have shown that the *hs*-Co^{II} metastable state can be photo-induced in benzene solvated Co(*diox*)$_2$(4-CN-Py)$_2$ single crystals when illuminated with 450 nm blue light at 30 K with a very high interconversion yield (80%) and relaxed back to the *ls*-Co^{III} state when illuminated with a 660 nm red light. However, the latter has a much smaller yield, which could be due to a small penetration depth in the crystalline sample. The high yield light-induced

metastable state generation reported for the 450 nm blue light irradiation had never been experimentally observed in molecular crystals of cobalt dioxolane tautomers.

The results here presented assured that the blue light illumination is triggering all chain of events that lead to ls-Co^{III} to hs-Co^{II} interconversion and that red 660 nm light induces the hs-Co^{II} to ls-Co^{III} relaxation process in a $Co(diox)_2$ solid state crystal. They illustrate the overall picture of the VT phenomena in solid state, evidencing the complexity of electronic events comprised in the valence tautomerism interconversion and call for a deeper study of the electronic dynamics of the light induced VT in different solid-state transition metal complexes.

Finally, we showed that solvated $Co(diox)_2(4\text{-CN-Py})_2$ crystals can undergo the VT interconversion reversibly without disruption of or damage to its crystallinity, which ensures the robustness of such materials and their potential to be used as sensors. Controlling and understanding the electronic properties of related bistable solid-state materials is a fundamental step towards the development of new devices.

4 Solvent modulation of the VT in Co(*diox*)₂Py₂

This chapter reports the investigation of key environmental factors that modulate the valence tautomerism in Co(*diox*)$_2$(Py)$_2$ as a function of solvation in crystals and in solution for different solvents. SCXRD has been used to characterize the impact of the crystal packing and solvation in allowing or forbidding the VT interconversion in solid state, and UV-visible spectroscopy, ESR and TA were used on the evaluation of the impact of the solvent in the behavior of the complex in solutions at room temperature. Our results show that the mobility of the pyridine derivative ligand (PyL) in Co(*diox*)$_2$(PyL)$_2$ complexes is directly correlated to the Co-N and Co-O distances, therefore being key to the *hs*-Co^{II} to *ls*-Co^{III} interconversion to take place. For the complex in solution, on the other hand, the solvent polarity seems to determine the accessibility to the higher energy *hs*-Co^{II} states at room temperature. The manuscript that comprises these results is currently under preparation.

4.1 Motivation

Electronic bistability is an intriguing property which is the basis for molecular electronic devices. It is an inherent property of materials whose electronic structures are dramatically dependent on external properties and presents itself as mixed valence (MV), spin-crossover (SC) or valence tautomerism (VT). The latter can be seen as a special case of spin-crossover that involves electroactive ligands and a consequent ligand to metal charge transfer that takes place concomitantly to the SC [1,7].

VT is particularly interesting when displayed by molecules in the solid state as crystals which do not have their crystal structure disrupted because of the changes within its constituent molecules. It became a broad research field that has accumulated the results of great scientific effort to the development, characterization and understanding of such materials in the supramolecular and electronic level [75,22,20,7,35,4,2,8,60].

From all the materials reported to display VT, Cobalt o-dioxolene molecules have been extensively probed as valence tautomers in the presence of nitrogen based ancillary ligands [4,13,76]. Their VT can present itself in solution and in solid state as single crystals in a reversible fashion. It is also known to be modulated by the ancillary ligand, highly dependent on the solid state arrangement of the complexes and on crystal solvation [14,26,66,77]. Moreover, VT can be controlled and induced by a variety of external stimuli, including temperature, pressure and irradiation. Temperature induced interconversion takes place as first and second order transitions within a wide range of characteristic transition temperatures, and the photo

induced interconversion has been reported to be stimulated by multiple different wavelengths irradiation, from visible light[4,12,25,31] to soft [15] and hard X-rays[16].

In this work we have focused our studies on the cobalt dioxolene complex with pyridine as ancillary ligand, coordinated in *trans* configuration: Co(*diox*)$_2$Py$_2$ (*diox* = SQ or Cat, SQ: 3,5-di-tert-butyl-semiquinonate; Cat: 3,5-di-tert-butyl-cathecolate; Py: pyridine). This complex has its VT completely modulated by the crystal lattice and solvation and has been reported as a non-tautomer (in its non-solvated crystal form[14] and in its hexanes solvated form[25]), as a tautomer (after acetonitrile solvent molecules escaped the solvated crystal lattice[25]), but peculiarly displays temperature and light induced valence tautomerism in only half of the units that populate the solvated crystal with a 2:1 complex/pyridine solvent ratio[25]. The reason why the presence or absence of solvent molecules in the crystal lattices allows or prevents the VT interconversion in such fashion has not yet been investigated taking the bulk of reported results for this complex in consideration.

Here, we report the experimental work on the pursuit of the signatures of VT in Co(*diox*)$_2$Py$_2$, along with the experimental plans to conclude this investigation, both in solid state and solutions. A new crystal of Co(*diox*)Py$_2$ solvated with pyridine in a 1:2 complex/pyridine ratio is reported and shown to not display temperature induced VT within the temperature range between 100 and 300 K, from temperature dependent single crystal X-ray diffraction experimental results. Also, solutions of Co(*diox*)$_2$Py$_2$ have been investigated with electronic spin resonance (ESR) and UV-visible light absorption experiments to probe the influence of the solvent environment in the complex's electronic and magnetic properties. Initial experiments of transient absorption spectroscopy were performed and so far, no transient times were recorded, but the needed adjustments for the next experimental round have been addressed. The current results also permitted the elaboration of X-ray absorption (XAS) and X-ray emission (XES) experiments, which were submitted in the form a proposal to the Swiss Light Source, SLS (see 7.3.4). The proposal has been accepted and the experiments have been scheduled. Overall, the results of our study demonstrate the influence of solvation, crystal lattice, and solvent nature as key factors for allowing the valence tautomerism interconversion and the stability of high-spin Co^{II} and/or low-spin Co^{III} states.

4.2 Experimental methods

4.2.1 Complex Synthesis

All chemicals for syntheses and analysis were of analytical grade and used without further purification. The preparation of Co(*diox*)$_2$(Py)$_2$ (*diox*: 3,5-di-tert-butyl-o-semiquinonate / 3,5-di-tert-butyl-o-cathecolate, Py: pyridine) has been previously reported by Schimidt *et al.* 2010[12] and repeated as follows. In an oven dried Schlenk flask shielded from light, a solution of 0.05 mmol of [Co^{II}(*diox*)$_2$]$_4$ in toluene is prepared under N$_2$ atmosphere. To this mixture, pyridine

solvent is added with a syringe for a final concentration of 0.04 mmol. The mixture is kept at 40 °C and stirred for 12 hours. Concentration of the dark blue mixture affords Co($diox$)$_2$(Py)$_2$ as dark green needles. All solvents are dried and bubled with N_2 prior to the synthesis.

4.2.2 Complex crystallization

The crystals with a 1:2 complex/pyridine solvent ratio (crystal 1:2) were prepared with the dilution of 0.1g of the Co($diox$)$_2$Py$_2$ powder in 15ml of dried hexanes. The solution was stirred and heated up to 60°C, then left at room temperature for 15 minutes, after which 0.5ml pyridine was added. The final solution was left at room temperature partially covered to allow for slow evaporation overnight, which yielded dark green needled crystals suitable to SCXRD experiments.

4.2.3 Single crystal XRD and structure solution

Crystals 1:2 were submitted to SCXRD experiments at the PXII - X10SA beamline at the Swiss Light Source, using 15keV X-rays. Samples were manually mounted to MiTeGen cryo-loops in copper magnetic bases and cooled down to 100 K with a liquid nitrogen jet. XRD images were recorded using an EIGER2 16M detector and the highest resolution shell measured was 0.9Å. Sequentially, temperature dependent SCXRD experiments were performed for the same crystals for temperatures ranging from 100K to 300K in approximately 20K steps. SCXRD data processing was performed using XDS[68], structure solution using SHELXT[69] and structure refinement using SHELXL[40]. Hydrogen atoms were located in Fourier difference maps and included as fixed contributions according to the riding model (C–H and N–H = 0.97 Å and U_{iso}(H) = 1.2 U_{eq} (C or N) for methylene and aromatic groups and carbon atoms). Due to the geometrical limitations at the PXII - X10SA beamline, data was collected at low resolution (0.9 Å < d < 50 Å) and all atoms were refined with anisotropic atomic displacement parameters. The software Merury[78] was used for figures, crystal structure visualization, superposition and comparison. Crystal data quality indicators for the crystal at 100K and 300 K are shown in Table 4-1. Co($diox$)$_2$Py$_2$ crystallizes in the monoclinic space group P2$_1$/c with 1 complex molecule (Z=1) and two pyridine molecules in the asymmetric unit, which is shown in Figure 4.2 for the crystal at 100 K.

Table 4-1 – XRD data and structure refinement parameters for crystal 1:2 at 100 and 300 K.

	100 K	300 K
Empirical formula	C82 H100 Co N2 O4	C50 H62 Co N2 O4
Formula weight	1236.56	813.94
Temperature	100 (2) K	293(2) K
Wavelength	0.82655 Å	0.82655 Å

Crystal system	Monoclinic	Monoclinic
Space group	P 2_1/c	P2_1/c
Unit cell dimensions	a = 17.652(8) Å b = 18.799(3) Å c = 13.210(2) Å α= 90°. β = 96.905(12)°. γ = 90°.	a = 18.2170(10) Å b = 18.83600(10) Å c = 13.3400(10) Å α= 90°. β = 96.128(10)°. γ = 90°.
Volume	4352(2) Å^3	4551.3(4) Å^3
Z	2	2
Density (calculated)	0.944 Mg/m^3	1.188 Mg/m^3
Absorption coefficient	0.191 mm^{-1}	0.630 mm-1
F(000)	1330	1740
Theta range for data collection	1.067 to 19.647°	1.814 to 22.061°
Index ranges	-16<=h<=16, -17<=k<=18, -13<=l<=13	-15<=h<=15, - 17<=k<=17, -12<=l<=12
Reflections collected	27351	21924
Independent reflections	4309 [R(int) = 0.0383]	3338 [R(int) = 0.0595]
Completeness to theta = 19.647°	86.4 %	93.40%
Refinement method	Full-matrix least-squares on F^2	Full-matrix least-squares on F^2
Data / restraints / parameters	4309 / 0 / 527	3338 / 0 / 242
Goodness-of-fit on f^2	1.011	1.970
Final r indices [i>2sigma(i)]	R1 = 0.0537 wR2 = 0.2073	R1 = 0.1802 wR2 = 0.4731
R indices (all data)	R1 = 0.0619, wR2 = 0.2476	R1 = 0.2058 wR2 = 0.5335

4.2.4 UV-visible spectroscopy

UV-vis spectra of the Co(*diox*)$_2$Py$_2$ dissolved in hexanes and pyridine (0.76 μM each) were recorded at room temperature using a Shimadzu RF-5301PC (Shimadzu, Kyoto, Japan) covering the wavelength range from 200 nm to 800 nm. The solution was held in a quartz cuvette with 1 mm pathlength, covered with a Teflon lid.

4.2.5 Electronic spin resonance

The Co($diox$)$_2$(Py)$_2$ complex was dissolved at 40°C with constant stirring in hexanes (0.76 μM) and in pyridine (0.76 μM), separately. The ESR spectra for both solutions were acquired using a Bruker spectrometer. Samples were kept in a quartz capillary filled with helium gas. Measurements consisted of two scans over the magnetic field range from 0 to 5000 G, using a microwave frequency of 9.40 GHz, modulation amplitude of 5 G, modulation frequency of 100 kHz and microwave power of 0.6 mW at room temperature.

4.2.6 Transient absorption spectroscopy

The transient absorption setup used here is reported elsewhere[79] (Figure 4.1). The light source for such experiments consisted on a Ti:Sapphire oscillator pumped by a continuous-wave ND:YVO4 laser and pulses were amplified with a Ti:Saphire amplifier. Generated pulses repetition rate was 20 kHz, pulse width was 45 fs, and wavelength was 800 nm. Second harmonics (centered at 400 nm) generated by a BBO crystal were used as pump, and probe white light was generated from the 800 nm pulses with a CaF$_2$ crystal. Probe spectrum ranged from 450 nm to 750 nm.
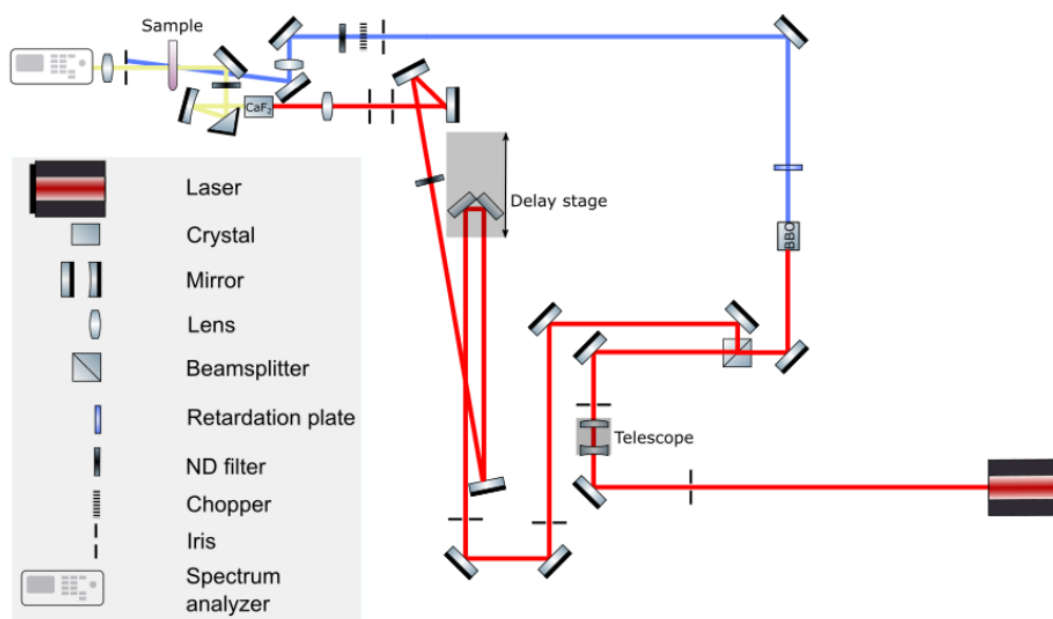
Figure 4.1 – Simplified scheme of the transient absorption setup used on test experiments with Co(diox)$_2$(Py)$_2$.

Co($diox$)$_2$Py$_2$ in hexanes solution was kept in a quartz cuvette of 1 mm optical pathlength and constantly stirred with a magnetic agitator. Sample stability to pump/probe light exposure was monitored with UV-visible absorption spectroscopy until significant damage was observed (~2h).

4.3 Results and discussion

4.3.1 Crystal lattice, solvation, and VT

Crystal 1:2 crystallizes in the P2$_1$/c space group with one Co($diox$)$_2$Py$_2$ complex molecule and 2 solvated pyridine molecules in the asymmetric unit (Figure 4.2).
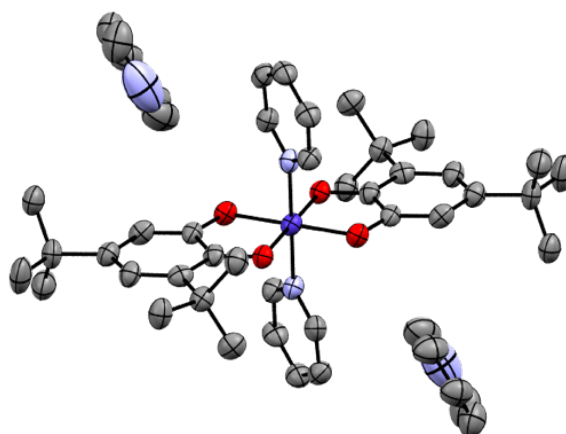
Figure 4.2 – Asymmetric unit of the pyridine solvated crystal of Co(diox)Py$_2$ at 100 K. Carbon atoms are displayed in gray, oxygen in red, nitrogen in light blue, cobalt in dark blue, and hydrogen atoms are hidden for clarity.

The interatomic distances between Co-L (L = N, O) obtained from temperature dependent SCXRD data are listed in Table 4-2. These values do not vary considerably over this temperature range considering the characteristic Co-L distances of the hs-Co^{II} and ls-Co^{III} forms of this complex surveyed from the CCDC[41]. Therefore, we conclude that the complex units within crystal 1:2 prevail in their ls-Co^{III} form from 100 K to 300 K. Therefore, in crystal 1:2, Co($diox$)$_2$(Py)$_2$ does not undergo VT. From the literature, it is known that this molecule can present VT in certain crystal forms, including a pyridine solvated crystal[25], but the VT is intriguingly hindered in certain environments. In order to understand the role of the crystal packing and solvation in this case, 2 other crystals were taken into consideration: a non-solvated crystal, reported by Schmidt *et al.* 2010[14] and the partially solvated crystal, reported by Mulyana *et al.,* 2009[25].

Table 4-2 – Co-L distances and hs-Co^{II} molar fraction for the 1:2 crystal at 100 and 300 K.

Temperature	100 K	300 K
Co – N	1.938 Å	1.954 Å
Co – O1	1.881 Å	1.892 Å
Co – O2	1.887 Å	1.896 Å

The non-solvated crystal form of Co($diox$)$_2$Py$_2$ (crystal 1:0) has been reported to crystallize in the monoclinic space group P2$_1$/n with 0.5 complex molecule in the asymmetric unit, so that the entire molecule is obtained from inversion symmetry (-x,1-y,-z) (Figure 4.3a). In such crystal form, the complex has been reported to not display VT over the temperature range between 0 and 300 K given the magnetometry results which show that the crystal maintains its Co^{III}(SQ)(Cat)(Py)$_2$ state (Figure 1.9a).

1:0	1:2	2:1
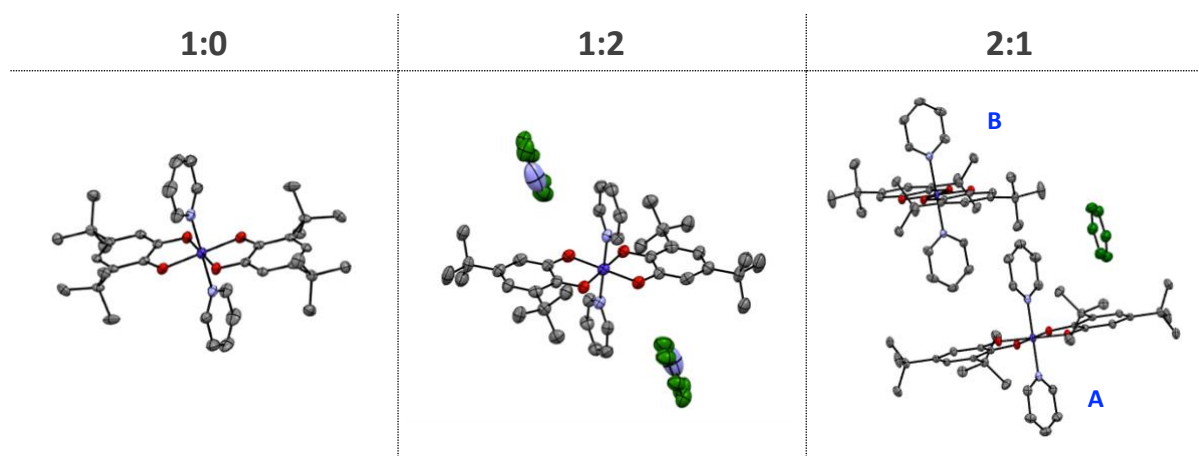
*Figure 4.3 – Units of Co(*diox*)$_2$(Py)$_2$ in crystals 1:0 (a), 1:2 (b) and 2:1 (c). Carbon atoms are depicted in gray, oxygen in red, nitrogen in blue, cobalt in dark blue. Pyridine solvent carbon atoms are depicted in green and hydrogen atoms are hidden for clarity*

The partially solvated Co($diox$)$_2$Py$_2$ crystal form (crystal 2:1) crystallizes in the P2$_1$/c space group with one half of each of two crystallographically independent complex molecules and half a pyridine solvent molecule in the asymmetric unit (Figure 4.3c), such that half of its Co($diox$)$_2$Py$_2$ sites (site A) interact with the pyridine solvent in a π-π stacking fashion[25]. The magnetic susceptibility measurements for such crystal show a sigmoidal profile of the $\chi_M T$ over the temperature range between 10 and 350 K, with a $T_{1/2} \sim 250K$, which plateaus at 350K for a value of $\chi_M T$ that indicates that only half of the Co($diox$)$_2$Py$_2$ sites undergo the VT transition (Figure 4.4). SCXRD studies over the same temperature range proved that only one of the two crystallographic independent sites undergo the VT: site B, which does not interact with the pyridine solvent in the lattice. The VT in crystal 2:1 is illustrated Figure 4.4 with a simplistic representation of the crystal lattice units at 100 K and 290 K. The π-π stacking interaction between one of complexes in site A and the solvated pyridine has been assigned to be responsible for the hindrance for the molecular expansion and consequently for precluding the VT. Figure 4.4 shows the unit cells of crystals 1:0, 1:2 and 2:1, with pyridine solvent molecules depicted in green.
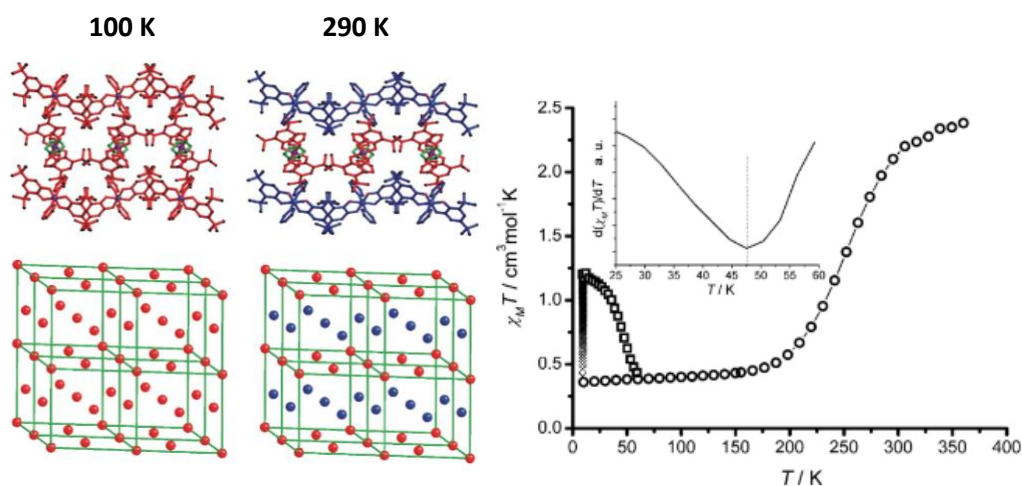
Figure 4.4 – Left: representation of the Co(diox)$_2$Py$_2$ + 0.5Py crystal at 100 K and 290 K. Red complex units are ls-CoIII, and blue units are hs-CoII. Pyridine solvent molecules are shown in green. Right: plot of the magnetic susceptibility times temperature $\chi_M T$ versus T for the thermally induced and photo-induced VT of the Co(diox)$_2$Py$_2$ + 0.5Py crystal. (Figure from [25])

The different behavior of the same molecule in different crystal arrangements and solvation calls for a deeper investigation on the structural factors that might limit, forbid, or allow the VT. At 100 K, the complex units within all the 3 crystals are believed to assume the same structure given the *ls*-Co^{III} configuration confirmed by magnetometry and SCXRD experiments. Hence, the structures of the complexes at 100 K are expected to superimpose with a small deviation in the atomic positions. The superposition of the 4 different complex units (2 from 2:1, 1 from 1:0 and 1 from 1:2) was performed using the crystal structures of the 3 crystals at 100 K. Figure 4.5 shows the superposition of the tautomer Co(*diox*)$_2$Py$_2$ complex unit (from crystal 2:1) and the other 3 Co(*diox*)$_2$Py$_2$ complex units that do not present VT in the range of investigated temperatures (crystals 1:0, 1:2, 2:1). It is important to emphasize that the only Co(*diox*)$_2$Py$_2$ molecule that presents VT occupies site A in crystal 2:1, which is the site that does not interact with the pyridine solvent molecule (in blue, Figure 4.4 for the crystal at 290 K). From the superposition of the non-tautomeric units on top of the tautomer one, a systematic relative torsion of the pyridine ligand planes is clear, while the atoms of dioxolene ligands lie approximately over the same plane (Figure 4.5). The superposition of all the non-tautomer molecules however, (Figure 4.6), shows a much better structural agreement. The values of the angles between the planes defined by the pyridine rings of each superposed molecule were calculated using Mercury and are shown in Table 4-3. Indeed, the torsion between the pyridines of non-tautomers is considerably smaller, confirming that even at 100 K, when all the complex units within the crystals are *ls*-Co^{III}(*diox*)$_2$Py$_2$, there are already structural differences between tautomer and non-tautomer, pointing to one structural signature of the VT.

Tautomer vs non-tautomer
From crystal 2:1 (blue) and 1:2 (gray)

From crystal 2:1 (blue) and 2:1 (red)

From crystal 2:1 (blue) and 1:0 (pink)
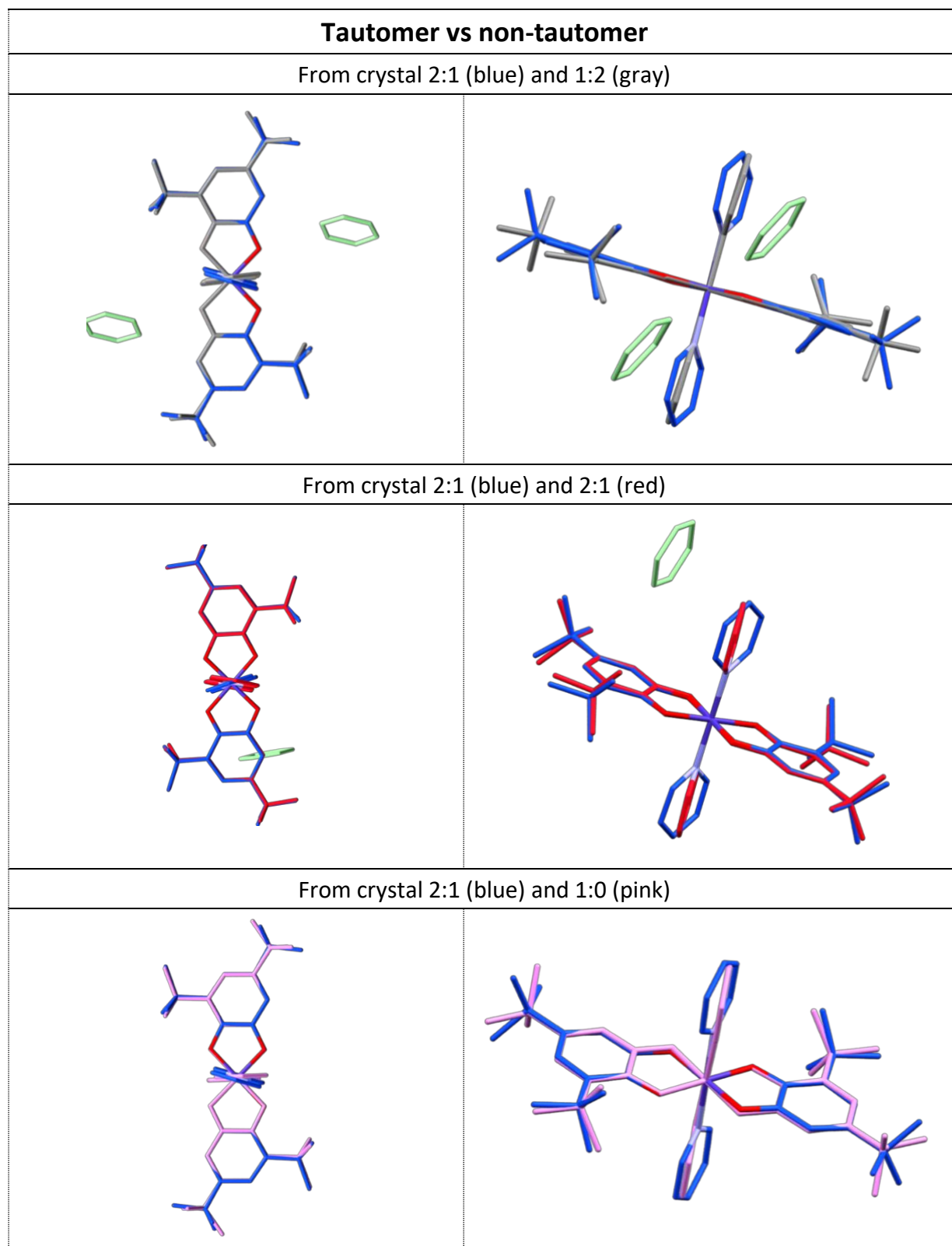
Figure 4.5 – Superposition of tautomer Co(diox)$_2$Py$_2$ unit from crystal 1:2 (blue) with non-tautomer units from crystal units from (a) 2:1 (gray), (b) 1:2 (red) and (c) 1:0 (pink). Left side pictures show the perspective perpendicularly to the dioxolenes plane. Right side pictures show the correspondent superposition sideways.

NON-Tautomer vs NON-tautomer
From crystal 1:2 (gray) and 2:1 (red)

From crystal 1:2 (gray) and 1:0 (pink)

From crystal 2:1 (red) and 1:0 (pink)
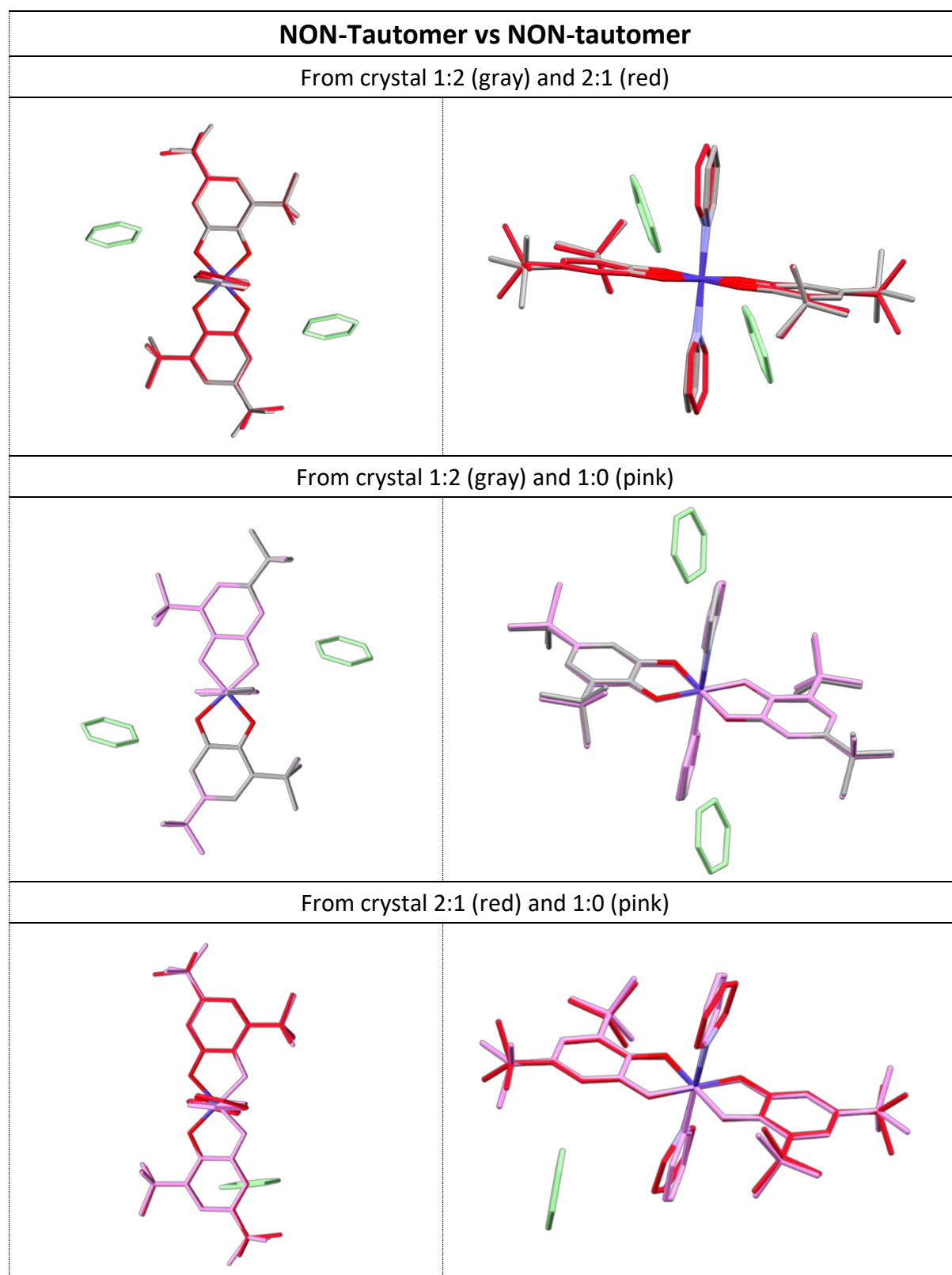
Figure 4.6 – Superposition of non- tautomer Co(diox)$_2$Py$_2$ units from (a) crystal 2:1 (red) and 1:2 (gray) (b) 1:0 (pink) and 1:2 (gray), and (c) 1:0 (pink) and 2:1 (red). Left side pictures show the perspective perpendicularly to the dioxolenes plane. Right side pictures show the correspondent superposition sideways.

Table 4-3 – Angles between the planes defined by pyridine ligands when Co(diox)$_2$Py$_2$ molecules from crystals 1:0, 1:2 and 2:1 are superposed. A and B are the tautomer and the non-tautomer molecules in the 2:1 crystal [Co(diox)$_2$Py$_2$·0.5Py] respectively. See figure Figure 4.4c.

Superposition type	Superposed units		Angle (°)
	Crystal(unit)	Crystal(unit)	
Tautomer vs non-tautomer	2:1(A)	1:2	23.02
	2:1(A)	2:1(B)	28.37
	2:1(A)	1:0	18.21
Non-Tautomer vs non-tautomer	1:2	2:1(B)	7.26
	1:2	1:0	5.10
	2:1(B)	1:0	12.13

Following this result, a more thorough and quantitative evaluation of the torsion angle between the plane defined by the pyridine derivative ligands and a vector lying in the plane of the dioxolenes was performed. A survey using the CSD tool, ConQuest[80] considered all *trans*-Co(*diox*)$_2$(PyL)$_2$ molecules (where PyL was a pyridine derived ancillary ligand) with Co octahedrally coordinated by oxygen atoms of two dioxolene ligands, and nitrogen atoms of monodentate pyridine derivative ligands in the CCDC[41] database. 56 structures were considered and for each of them, two vectors, from the Co atom to each one of the centroids of the dioxolene rings, were defined (Co-diox1 and Co-diox2). Also, the planes in which each pyridine derived ligand lied were defined (PyL1 and PyL2) and the Co-L (L = N ,O) distances were also considered. The vectors and planes are illustrated in Figure 4.7 and the list of structures identifiers considered in the search result is shown in the appendix section (Table 7-2)
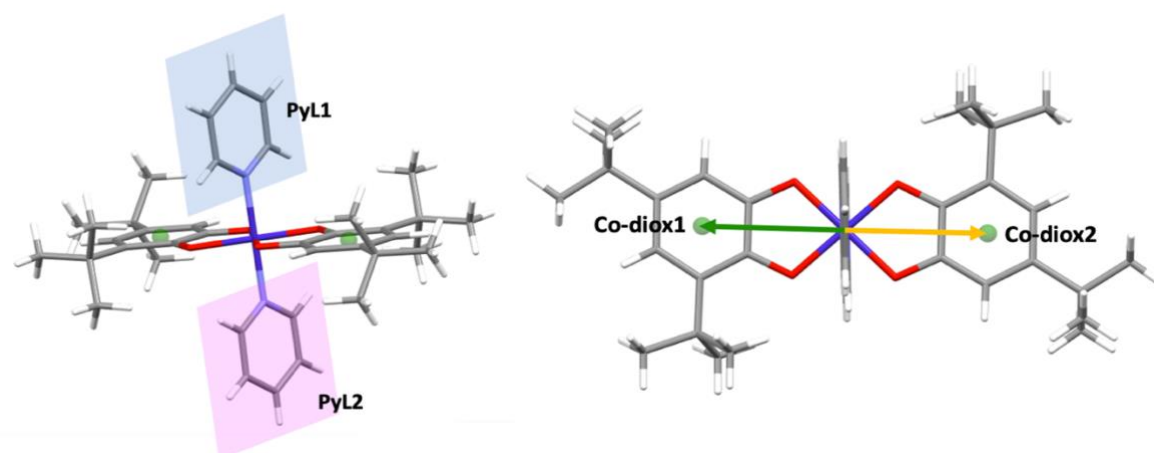
Figure 4.7 – Angles PyL1 and PyL2 and vectors Co-diox1 and Co-diox2 defined for Co(diox)$_2$(PyL)$_2$ molecules from the survey in the CCDC[41] database.

In further correlation analysis of surveyed values, the angles between the vectors PyL1 or PyL2 and the vectors Co-diox1 and Co-diox2 were evaluated as a function of the Co-L distances of each molecule surveyed (L = O and N). Average Co-O distances were computed taking all four

Co-O distances present in each complex surveyed, and average Co-N were calculated with both Co-N distances (see both plots at the appendix 7.2.4). The calculated angle (PyL/Co-diox) measures the torsion of the pyridine ligands with respect to a fixed direction in the dioxolene planes. As shown in Figure 4.8, PyL/Co-diox is correlated in a very well-defined fashion with the Co-N distance, with almost constant values of Co-N for PyL/Co-diox up to a critical value, and a significant increase of Co-N with PyL/Co-diox for angles larger than the critical value.
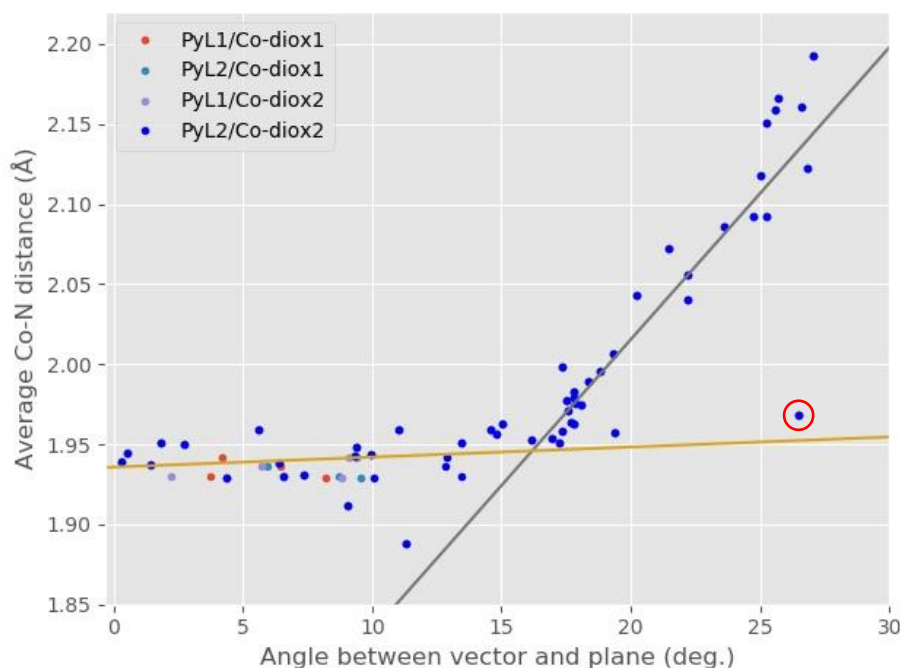
Figure 4.8 – Average Co-N distances as a function of the angle between the PyL planes and Co-diox vectors for all the structures surveyed (seeTable 7-2)

The quantitative analysis of the Co-N correlation with PyL/Co-diox consisted of a linear fit of both portions of the plot in Figure 4.8 and the evaluation of the critical angle value. First, the possibility of an exponential relation between Co-N and PyL/Co-diox was ruled out (see Figure 7.4). Then, the four datasets (PyL1/Co-diox1, PyL2/Co-diox1, PyL1/Co-diox2, PyL2/Co-diox2) were averaged and data points from the averaged dataset were sorted with respect to PyL/Co-diox. A first order polynomial fit of subgroups of the averaged dataset was performed in such a way that the n*th* fit excluded the (n-1) points with lower angle values. The evolution of the slope of the fitted line as a function of n is shown in Figure 4.9, where the slope increases until it reaches a plateau after n = 25 (dashed line). This point corresponds to the critical angle PyL/Co-diox = 16.98, and the linear fitting of the points before and after this value give the two lines depicted in Figure 4.9, described by equations (20)

and (21). The residuals of the fitted curves, *i.e.,* the sum of squared residuals of the least-squares fit are: 0.00063 for equation (20)

and 0.04233 for equation (21). The residuals for each fit point in Figure 4.9 are shown in the appendix 7.2.5.
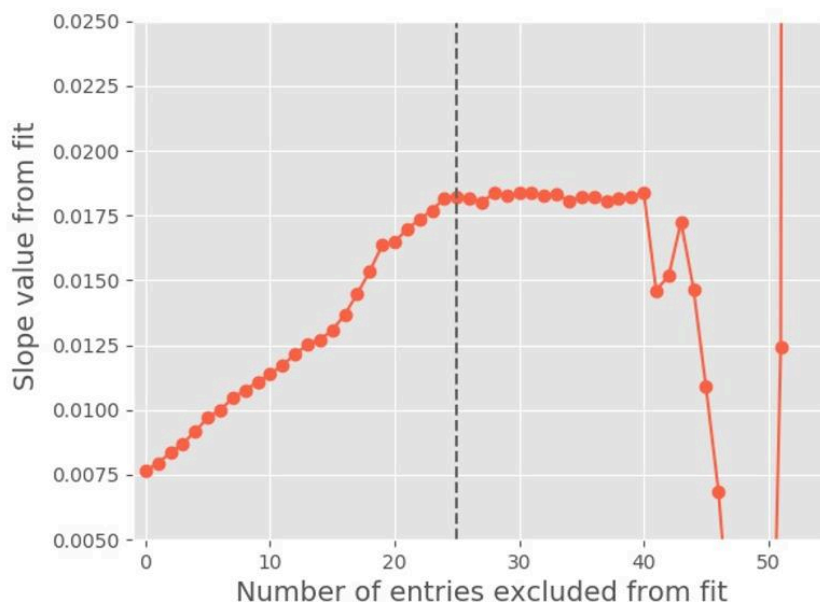
Figure 4.9 – Evolution of the slope of the linear fit performed for subsets of the average PyL/Co-diox dataset as a function of entries included.

$$D_{Co-N} = 0.00062\ \theta_{PyL/Co-diox} + 1.9357, \qquad if\ \theta < 16.98\ ° \qquad (20)$$

$$(21)$$

$$D_{Co-N} = 0.01824\ \theta_{PyL/Co-diox} + 1.6506, \qquad if\ \theta \geq 16.98\ °$$

The erratic values for the slope value of the fit as a function of points excluded is observed when only the last 14 points are considered (Figure 4.9), and this behavior can be explained by the presence of the outlier highlighted in Figure 4.8. For the sake of being consistent, this point was not removed from our analysis. However, the discrepant behavior of this structure (Co(diox)$_2$(OMe-Py)$_2$, id = YUWYUZ) can be understood from the large number of short contacts that the OMe-Py ligand makes with the molecules in its surroundings (see section 7.2.6), which seem to force a rigid geometrical configuration of this complex in the crystal.

The crystal packing of 1:2 and 2:1 along the *b*-axis, and of crystal 1:0 along the *a*-axis is shown in Figure 4.10 (for all a, b and c directions, see 7.2.2), which allows for the visualization and simplistic extrapolation of the movement of the nitrogen-based ligands with respect to the dioxolene planes. Our results endorse that Co(*diox*)$_2$Py$_2$ crystal packing adjudicates on the capabilities of the Co complexes to display VT or not in solid state. The need for mobility of the pyridine-derivative rings to allow VT interconversion is evident and points to a new approach on the investigation of the structural signature of the VT in solid state.

1:0

along a
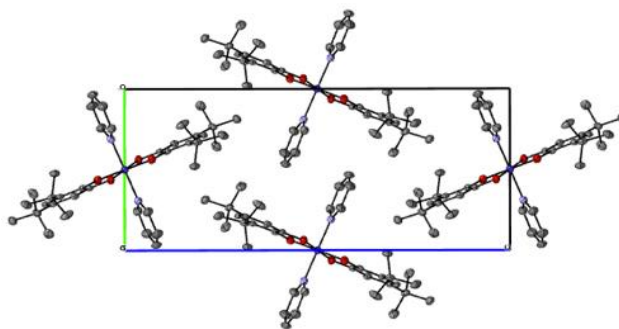
2:1

along b
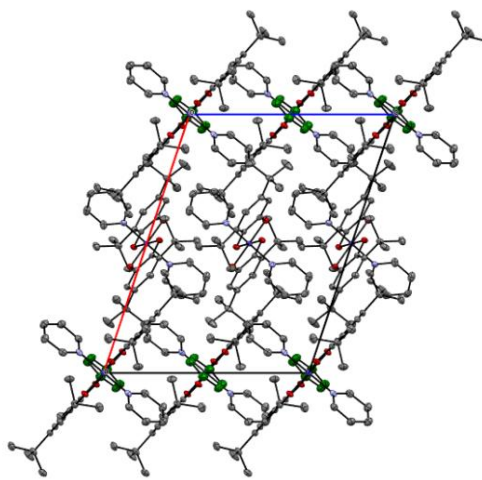
1:2

along b
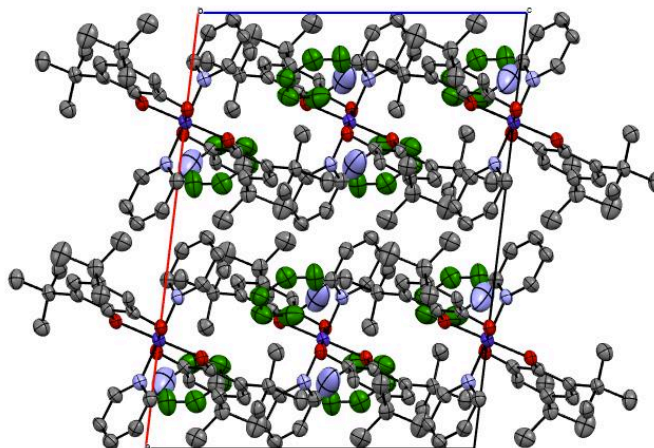
Figure 4.10 - Crystal packings of crystals 1:2 and 2:1 along the b-axis, and of crystal 1:0 along the a-axis. Pyridine solvent molecules are depicted in green for better visualization.

4.3.3 Co(diox)₂Py₂ in solution

4.3.3.1   UV-visible spectroscopy

The electronic absorption spectra of the Co(*diox*)$_2$Py$_2$ were measured for the complex dissolved in pyridine and hexanes at room temperature and are shown in Figure 4.11, where the inset zooms in on the longer wavelength region.

For the complex in hexanes, the band centered at 750 nm may be assigned as the characteristic MLCT band for *hs*-Co^{II} species[1,20]. On the other hand, for the complex in pyridine, an absorption band centered at 570 nm lies on the region that corresponds to the LMCT band for *ls*-Co^{III}, and the absorption shoulder near 420 nm, also characteristic from six-coordinate Co^{III} complexes, can be assigned to d-d transitions[46,34,24]. Strong absorption bands around 300 nm have been assigned to internal ligand transitions and very high UV absorption from the solvents is observed for wavelengths around and bellow 200 nm.
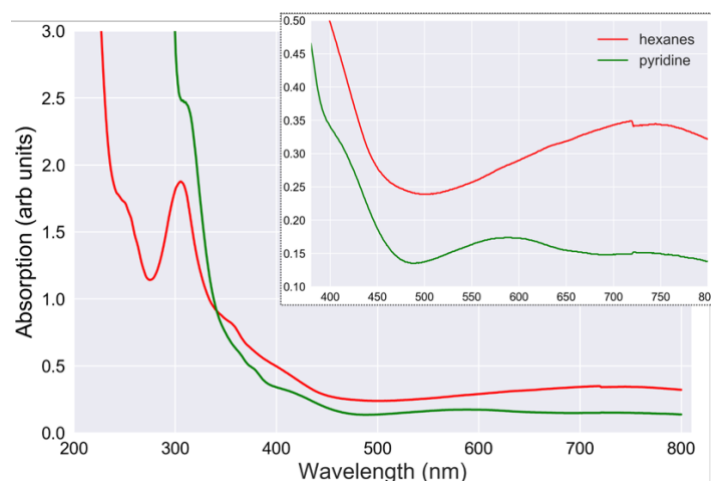
Figure 4.11 – UV-visible light absorption spectra of solutions of the Co(diox)₂Py₂ complex in pyridine (green) and hexanes (red) at room temperature.

The differences in the electronic absorption spectra of Co(*diox*)$_2$Py$_2$ in pyridine and in hexanes, and the association of the observed absorption bands to the correspondent electronic transitions shows that the complex assumes different oxidation states for each of the solvents: *ls*-Co^{III} in pyridine and *hs*-Co^{II} in hexanes. Additionally, solutions of Co(*diox*)$_2$Py$_2$ in pyridine and hexanes solvent assume different colors (Figure 4.12): blue when the complex is dissolved in pyridine and green when dissolved in hexanes, which already suggests the different oxidation states prior to any experiments.

Such strong impact of the surroundings in the electronic configuration of the tautomer at room temperature is a remarkable result that reiterates the possibility of tuning the VT of Co(*diox*)$_2$Py$_2$ in solution.

Figure 4.12 – Co(diox)$_2$Py$_2$ dissolved in hexanes (left) and in pyridine (right).

4.3.3.2 Electronic spin resonance (ESR)

The ESR spectra of Co(*diox*)$_2$Py$_2$ in pyridine and hexanes are shown in Figure 4.13. The spectrum of the complex in hexanes shows one peak around 1598 G, with an effective Zeeman factor of g = 4.20 and a peak around 3357 G, g = 2.00. The spectrum of the complex in pyridine exhibits a peak centered at 3357 G (g = 2.00) only. The g-factor of g = 2.00 indicates that the signal can be attributed to the ligand-based radical[48]. For the sample in pyridine, the magnitude of the signal attributed to the radical is higher than for the complex in hexanes and it is split into 8 peaks of similar intensity equally spaced by ΔB = 10 G indicating coupling between the radical with spin S = 1/2 and the ^{59}Co nucleus with spin I = 7/2 with hyperfine constant a$_0$ = 10 G[20,50,51]. This coupling indicates that the complex in pyridine contains a single radical and the absence of a cobalt related peak indicates that the cobalt ion has spin S = 0[50,51]. These results agree with the UV-visible spectroscopy results and point to the complex assuming the *ls*-Co^{III}(SQ)(Cat) state in pyridine solution at room temperature. Measured and calculated ESR spectra centered at g = 2.00 by Witt *et al.*, 2015[50] for the trans-6 complex at room temperature (Figure 2.5d) display these very same hyperfine splitting features.

For the complex in hexanes, the ESR signal from the free radical in the dioxolene ligands as they both assume the semiquinone configuration can still be measured. The absence of the hyperfine splitting features from their coupling to the Cobalt nucleus evidences the low overlap between the ligand-based and metal-based molecular orbitals due to larger bond lengths between the Co and its first neighbors, typical of *hs*-Co^{II} species. The main feature of the ESR spectrum of Co^{II}(SQ)$_2$Py$_2$ in hexanes is, however, the peak corresponding to g = 4.20, attributed to unpaired electrons located on the cobalt ion, since a high g-factor usually arises from electrons with significant spin-orbit coupling or zero-field splitting[51]. As explained in section 1.2, the *hs*-Co^{II}(SQ)$_2$Py$_2$ total spin S = 3/2 due to the unpaired d-electrons in the e$_g$ orbitals. Usually, Co^{II} is ESR silent at room temperature, given the fast relaxation of the coupling between its unpaired electrons and the magnetic field. Nevertheless, a very high signal for these unpaired electrons of the Co ion is observed for Co^{II}(SQ)$_2$Py$_2$ in hexanes, which leaves no

doubt that the complex assumes the *hs*-Co^{II}(SQ)$_2$Py$_2$ configuration at room temperature, corroborating with the UV-visible spectroscopy results.
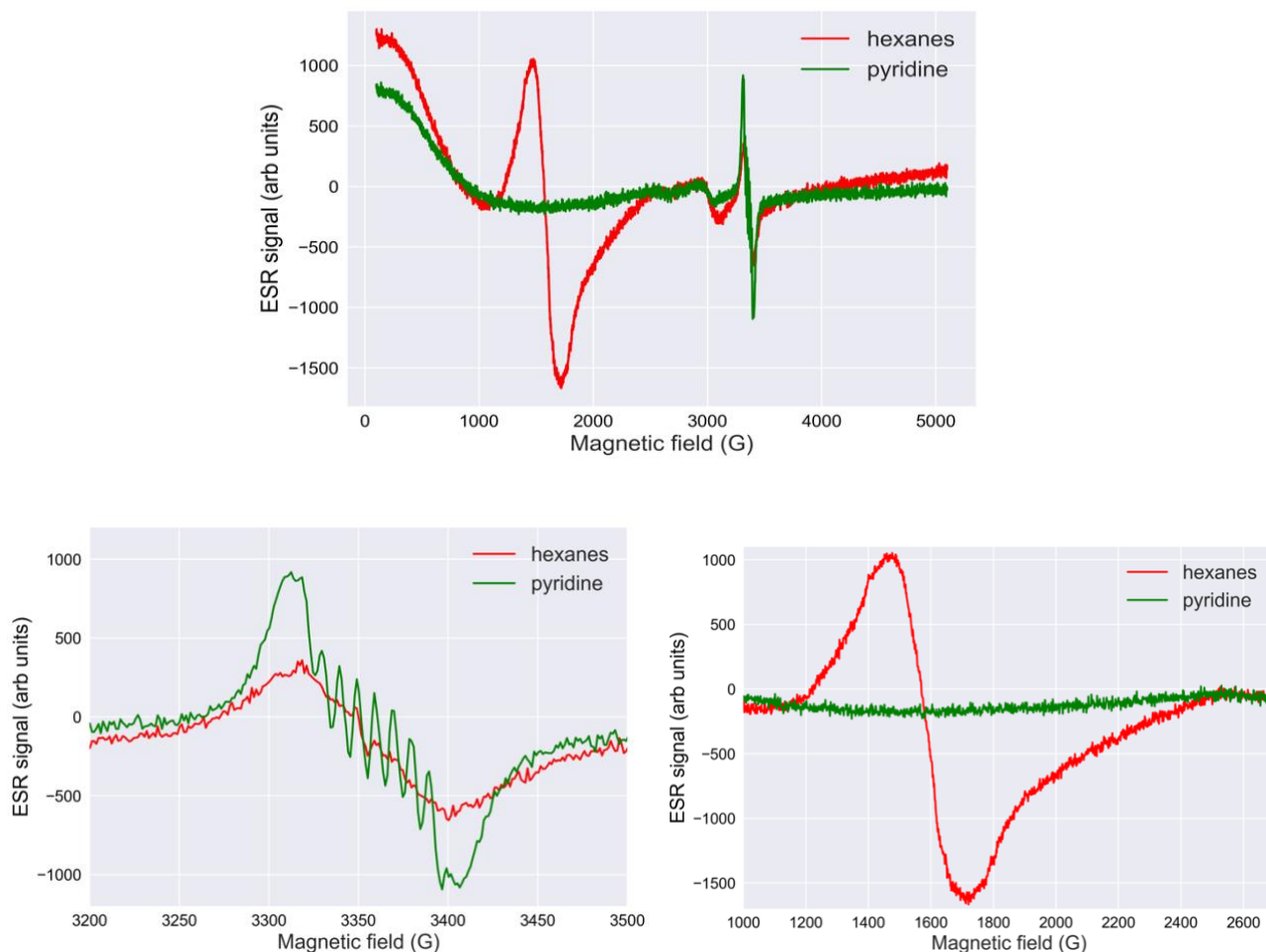
Figure 4.13 – ESR spectra recorded for Co(diox)$_2$Py$_2$ dissolved in hexanes and pyridine at room temperature. Top: Full spectra recorded for both solutions display main features that distinguish both solutions. Bottom left: zoom in on the spectral region around 3350 G (free radical). Bottom right: zoom in on the spectral region around 1600 G (hs-Co^{II}).

4.3.3.3   Transient absorption spectroscopy

All our results on Co(*diox*)$_2$Py$_2$, both in solid state and in solution, have demonstrated the versatility of such molecule as a valence tautomer and opened many possibilities for more experimental approaches. The ultrafast dynamics of valence tautomers is particularly intriguing given the complexity of such electronic transition processes, as described in section 1.6. Therefore, ultrafast transient absorption spectroscopy (TA) experiments were set and planned for the investigation of the VT in Co(*diox*)$_2$Py$_2$ in solution and room temperature. The evaluation of the response of the complex molecules at room temperature is particularly appealing given the simplification of experimental setups (no need for cryostats).

Sample stability tests, coherent artifact evaluation and initial transient absorption experiments were performed for the Co(*diox*)$_2$Py$_2$ complex dissolved in hexanes. The solution of the complex in pyridine is sensitive to O$_2$ exposure and displays signs of degradation (color change) some

hours after its preparation ($\sim 10\ h$). Therefore, initial TA tests were done with hexanes as solvent. The sample was kept in a quartz cuvette of 1 mm pathlength once the solvents used here damage the apparatus for sample flowing and sample contamination with plastic from tubes is immediate.

Sample stability as a function of laser power was the first test performed for pump pulse power equals to 19, 10 and 5 mW, measured right before the cuvette wall. Sample damage was monitored by UV-vis spectroscopy and Figure 4.14 shows the spectral changes recorded before and after 1h laser irradiation. Damage was observed in all tests, with considerable changes in the absorption bands centered at 400 nm and 750 nm. Color change was also observed after overnight pump-probe exposure tests, pointing towards the need of very careful sample monitoring. Given the smaller spectral changes after irradiation with 5 mW, this LASER power was chosen for further tests. A lower power is desirable; however, it also leads to lower signal to noise ratio and a compromise is needed.
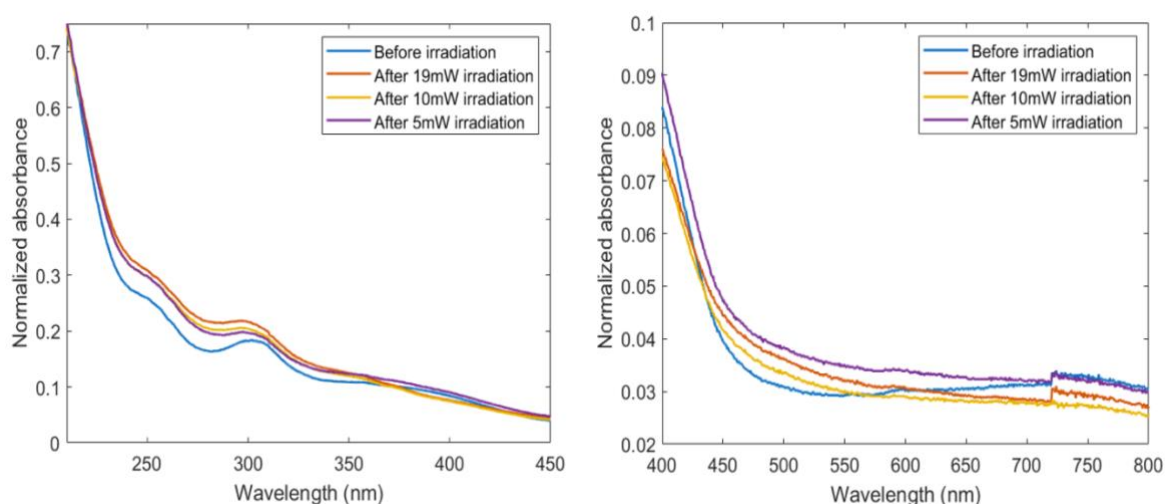
Figure 4.14 – UV-visible absorption spectra of Co(diox)$_2$(Py)$_2$ in hexanes before (blue curve) and after being exposed to pump-probe TA experiments for 19 mW (orange), 10 mW (yellow) and 5mW (purple) pump pulse power.

The TA measurements that followed the power dependent sample stability tests were not successful as a very severe contribution from the quartz-hexane interface caused the presence of a high valued ΔA feature in the 2D map (intensity x wavelength x time delay) (Figure 4.15), previously reported in the literature as a coherent artifact[81]. Such signal dominated over any possible signal from the sample and solving this issue requires a large number of new tests and setup adaptation, *e.g.,* adapting the flowing system for handling the sample in a jet. Our preliminary results on the TA of Co(*diox*)$_2$(Py)$_2$ allowed us to understand the sensitivity of the system and the critical influence of the solvent in the pump-probe signal.
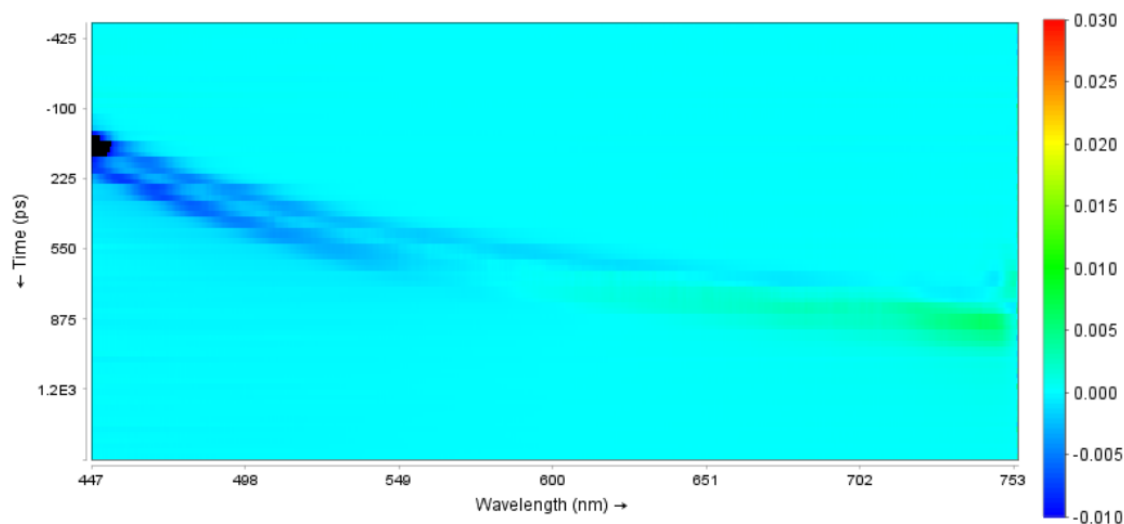
Figure 4.15 – Coherent artifact observed for a TA experiment with Co(diox)$_2$Py$_2$ in hexanes in a quartz cuvette with 1 mm pathlength.

4.4 Conclusions and perspectives

Our investigation of the Co(*diox*)$_2$Py$_2$ complex in different crystalline and solution environments has demonstrated the versatility of such cobalt complex and the pliancy of its valence tautomerism property. Our studies relied on many experimental techniques for the proper benchmarking of the influence of the surroundings in the electronic-states availability within the molecule, which has been shown to be greatly dependent on the crystal packing and solvent type.

The crystalline environment influence in the VT of Co(*diox*)$_2$Py$_2$ is clear from the different response to temperature of the complex crystallized in three forms, with complex to solvent ratio of 1:0, 1:2 and 2:1. The structural comparison of these 3 crystals lead to a novel way of evaluating the crystal packing influence in the VT due to the direct relation between the molar fraction of *hs*-Co^{II} species and the angle PyL/Co-diox, between the pyridine-derived and dioxolene ligands. We have shown that the mobility of the nitrogen-based ligand within the crystal lattice is a key feature to allow or forbid the VT in solid state, challenging the overall belief that the nitrogen-based ligand does not participate directly in the charge transfer during the VT interconversion. This also demonstrates that the molecular expansion is not the only geometrical signature of the VT.

Furthermore, the behavior of this complex in solution has reiterated its sensitivity to its surroundings, given the complete change of the oxidation state of the complex when dissolved in pyridine or hexanes. This points to a change in the energy of *ls*-Co^{III} and *hs*-Co^{II} states as a function of the polarity of the environment.

Our results altogether show that not only the electronic properties of the molecule itself, but clearly, its environment in solid state and solution will determine its ability to demonstrate valence tautomerism properties and should be taken into consideration whenever such molecules are being designed.

The results reported in this section along with the results of upcoming TA experiments at LSU, EPFL, (experiments scheduled for June 2021), upcoming XAS and XES experiments at the Swiss Light Source (proposal accepted – see 7.3.4, experiments to be scheduled for the second semester of 2021) and DFT results from studies of our collaborators in the *Laboratório de Estrutura Eletrônica*, UFMG, will allow a deeper and more accurate understanding of VT in Co(*diox*)$_2$(Py)$_2$. The complete assemble of results and analysis is ongoing. As previously described this work counts on great scientific collaborations which we have stablished with research groups from multiple institutes around the world: Universidade Federal de Minas Gerais (Brazil), University of Twente (Netherlands), North Carolina State University (NCSU), Paul Scherrer Institute (Switzerland) and École Polytechnique Fédérale de Lausanne (Switzerland).

5 Final conclusion

This doctoral work comprised the investigation of valence tautomerism (VT) in the cobalt dioxolene complexes Co(*diox*)$_2$(CN-Py)$_2$ and Co(*diox*)$_2$Py$_2$, both in solid state and in solution. It encompasses steps towards controlling the light-induced VT in solid state and towards the understanding of the role played by nitrogen-based ancillary ligands in the VT interconversion, as well as the role played by the surrounding environment. The detailed investigation of these complexes and their VT property comprised several complementary experimental techniques.

The results on benzene solvated crystals of Co(*diox*)$_2$(CN-Py)$_2$ reported for the first time an 80% yield in the light-induced VT at 30 K using visible light (450 nm) and the subsequent de-excitation of the photo-excited states with red 660 nm light. No disruption of solid state was observed, and the process was shown to be reversible. The control of magnetic and electronic properties with external stimuli was thoroughly fulfilled and stands up for the robustness of such material and points to its suitability to be engineered as a device.

For Co(*diox*)$_2$Py$_2$, on the other hand, the focus was the investigation of the key factors that limit or allow the VT in three crystals of the complex. The crystal packing impact on the VT in this molecule is quite intriguing, and our studies showed that such can be related to the need for mobility from the pyridine derivative ligands in *trans*-Co(*diox*)$_2$(PyL) complexes in solid state. In solution, however, the solvent was demonstrated to directly change the accessibility to higher energy *hs*-Co^{II} states in room temperature.

Overall, our work led to very interesting experimental results that stepped forward in the deeper understanding of the VT in cobalt complexes, with the highlights being the possibility of controlling the light-induced VT interconversion and the mobility of pyridine derivative ligands as key to the VT in solid state. The development of this research also counted on multiple collaborations, which allowed for the substantiality of our findings, that are now the basis for the continuity of this investigation.

For instance, our findings support the use of diffraction anomalous fine structure (DAFS) to investigate the VT in single crystals. DAFS is a technique that combines the selectivity of XRD and the atom specificity of spectroscopy, being therefore very promising in the investigation of the VT in symmetrically unrelated metallic sites within a single crystal. Thus, DAFS studies in 2:1 crystals of Co(*diox*)$_2$Py$_2$ are promising in the pursuit of the differentiation of the spectroscopic signature from both tautomer and non-tautomer sites that would manifest in the diffracted intensity *versus* X-ray energy of different Bragg peaks. Our preliminary results from energy resolved SCXRD experiments (see proposal in 7.3.1) with energies around the cobalt K-edge already show the anomalous behavior of the intensities of different Bragg peaks as a function of energy (Figure 5.1). These results demonstrate that the anomalous scattering signature can be assessed with SCXRD, and that it is site dependent. The complete

mathematical analysis of the spectroscopical signature of different crystal planes and the extraction of absorption spectra form the energy dependent SCXRD would allow the differentiation of the electronic structure information contained in each crystal plane, therefore providing a map for the VT in solid-state.
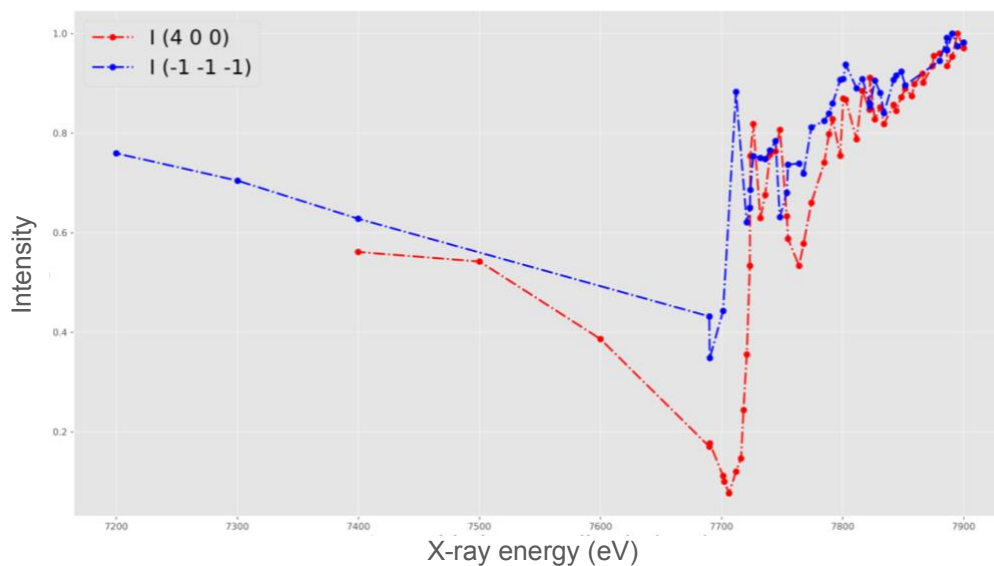
Figure 5.1 Diffracted intensity as a function of X-ray energy for the reflections 400 (red) and -1-1-1 (blue) for the 2:1 crystal of Co(Diox)$_2$(Py)$_2$ at 100 K.

6 References

(1)   Shultz, D. A. Valence Tautomerism in Dioxolene Complexes of Cobalt. *Magn. Mol. Mater. II Models Exp.* **2001**, 281–306.

(2)   Sato, O. Dynamic Molecular Crystals with Switchable Physical Properties. *Nat. Chem.* **2016**, *8* (7), 644–656. https://doi.org/10.1038/nchem.2547.

(3)   Karothu, D. P.; Weston, J.; Desta, I. T.; Naumov, P. Shape-Memory and Self-Healing Effects in Mechanosalient Molecular Crystals. *J. Am. Chem. Soc.* **2016**, *138* (40), 13298–13306. https://doi.org/10.1021/jacs.6b07406.

(4)   Tezgerevska, T.; Alley, K. G.; Boskovic, C. Valence Tautomerism in Metal Complexes: Stimulated and Reversible Intramolecular Electron Transfer between Metal Centers and Organic Ligands. *Coord. Chem. Rev.* **2014**, *268*, 23–40. https://doi.org/10.1016/j.ccr.2014.01.014.

(5)   Sato, O.; Tao, J.; Zhang, Y.-Z. Control of Magnetic Properties through External Stimuli. *Angew. Chem. Int. Ed.* **2007**, *46* (13), 2152–2187. https://doi.org/10.1002/anie.200602205.

(6)   Droghetti, A.; Sanvito, S. Electric Field Control of Valence Tautomeric Interconversion in Cobalt Dioxolene. *Phys. Rev. Lett.* **2011**, *107* (4), 047201. https://doi.org/10.1103/PhysRevLett.107.047201.

(7)   Pierpont, C. G. Studies on Charge Distribution and Valence Tautomerism in Transition Metal Complexes of Catecholate and Semiquinonate Ligands. *Coord. Chem. Rev.* **2001**, *216*, 99–125.

(8)   Gransbury, G. K.; Boulon, M.-E.; Petrie, S.; Gable, R. W.; Mulder, R. J.; Sorace, L.; Stranger, R.; Boskovic, C. DFT Prediction and Experimental Investigation of Valence Tautomerism in Cobalt-Dioxolene Complexes. *Inorg. Chem.* **2019**, *58* (7), 4230–4243. https://doi.org/10.1021/acs.inorgchem.8b03291.

(9)   Tao, J.; Maruyama, H.; Sato, O. Valence Tautomeric Transitions with Thermal Hysteresis around Room Temperature and Photoinduced Effects Observed in a Cobalt- Tetraoxolene Complex. *J. Am. Chem. Soc.* **2006**, *128* (6), 1790–1791.

(10)   Adams, D. M.; Dei, A.; Rheingold, A. L.; Hendrickson, D. N. Bistability in the [CoII (Semiquinonate) 2] to [CoIII (Catecholate)(Semiquinonate)] Valence-Tautomeric Conversion. *J. Am. Chem. Soc.* **1993**, *115* (18), 8221–8229.

(11)   Roux, C.; Adams, D. M.; Itié, J. P.; Polian, A.; Hendrickson, D. N.; Verdaguer, M. Pressure-Induced Valence Tautomerism in Cobalt o-Quinone Complexes: An x-Ray Absorption Study of the Low-Spin [Coiii (3, 5-Dtbsq)(3, 5-Dtbcat)(Phen)] to High-Spin [Coii (3, 5-Dtbsq) 2 (Phen)] Interconversion. *Inorg. Chem.* **1996**, *35* (10), 2846–2852.

(12)   Schmidt, R. D.; Shultz, D. A.; Martin, J. D. Magnetic Bistability in a Cobalt Bis(Dioxolene) Complex: Long-Lived Photoinduced Valence Tautomerism. *Inorg. Chem.* **2010**, *49* (7), 3162–3168. https://doi.org/10.1021/ic901998p.

(13)   Sato, O.; Cui, A.; Matsuda, R.; Tao, J.; Hayami, S. Photo-Induced Valence Tautomerism in Co Complexes. *Acc. Chem. Res.* **2007**, *40* (5), 361–369. https://doi.org/10.1021/ar600014m.

(14)   Schmidt, R. D.; Shultz, D. A.; Martin, J. D.; Boyle, P. D. Goldilocks Effect in Magnetic Bistability: Remote Substituent Modulation and Lattice Control of Photoinduced Valence Tautomerism and

Light-Induced Thermal Hysteresis. *J. Am. Chem. Soc.* **2010**, *132* (17), 6261–6273. https://doi.org/10.1021/ja101957c.

(15) Poneti, G.; Mannini, M.; Sorace, L.; Sainctavit, P.; Arrio, M.-A.; Otero, E.; Criginski Cezar, J.; Dei, A. Soft-X-Ray-Induced Redox Isomerism in a Cobalt Dioxolene Complex. *Angew. Chem. Int. Ed.* **2010**, *49* (11), 1954–1957. https://doi.org/10.1002/anie.200906895.

(16) Francisco, T. M.; Gee, W. J.; Shepherd, H. J.; Warren, M. R.; Shultz, D. A.; Raithby, P. R.; Pinheiro, C. B. Hard X-Ray-Induced Valence Tautomeric Interconversion in Cobalt-o-Dioxolene Complexes. *J. Phys. Chem. Lett.* **2017**, *8* (19), 4774–4778. https://doi.org/10.1021/acs.jpclett.7b01794.

(17) Ribeiro, M. A. Estudo de compostos de coordenação de cobalto e labilidade eletrônica, Universidade Federal de MInas Gerais, Belo Horizonte, 2013.

(18) Adams, D. M.; Dei, A.; Rheingold, A. L.; Hendrickson, D. N. Controlling Valence Tautomerism of Cobalt Complexes Containing the Benzosemiquinone Anion as Ligand. *Angew. Chem. Int. Ed. Engl.* **1993**, *32* (6), 880–882.

(19) Pierpont, C. G.; Jung, O.-S. Thermodynamic Parameters for Cobalt-Quinone Electron Transfer and Spin Transition Steps of the \ceCo^III(Bpy)($3,5$-DBSQ)($3,5$-DBCat) / Co^II(Bpy)($3,5$-DBSQ)2 Valence Tautomeric Equilibrium. *Inorg. Chem.* **1995**, *34* (16), 4281–4283. https://doi.org/10.1021/ic00120a041.

(20) Adams, D. M.; Noodleman, L.; Hendrickson, D. N. Density Functional Study of the Valence-Tautomeric Interconversion Low-Spin [Co ^{III} (SQ)(Cat)(Phen)] ⇌ High-Spin [Co ^{II} (SQ) $_2$ (Phen)]. *Inorg. Chem.* **1997**, *36* (18), 3966–3984. https://doi.org/10.1021/ic9611812.

(21) Hendrickson, D. N.; Pierpont, C. G. Valence Tautomeric Transition Metal Complexes. In *Spin Crossover in Transition Metal Compounds II*; Springer, 2004; pp 63–95.

(22) Adams, D. M.; Hendrickson, D. N. Pulsed Laser Photolysis and Thermodynamics Studies of Intramolecular Electron Transfer in Valence Tautomeric Cobalt O-Quinone Complexes. *J. Am. Chem. Soc.* **1996**, *118* (46), 11515–11528.

(23) Jung, O.-S.; Jo, D. H.; Lee, Y.-A.; Sohn, Y. S.; Pierpont, C. G. Ancillary Ligand Dependent Shifts in Charge Distribution for Cobalt–Quinone Complexes. *Angew. Chem. Int. Ed. Engl.* **1996**, *35* (15), 1694–1695.

(24) Beni, A.; Dei, A.; Laschi, S.; Rizzitano, M.; Sorace, L. Tuning the Charge Distribution and Photoswitchable Properties of Cobalt–Dioxolene Complexes by Using Molecular Techniques. *Chem. - Eur. J.* **2008**, *14* (6), 1804–1813. https://doi.org/10.1002/chem.200701163.

(25) Mulyana, Y.; Poneti, G.; Moubaraki, B.; Murray, K. S.; Abrahams, B. F.; Sorace, L.; Boskovic, C. Solvation Effects on the Valence Tautomeric Transition of a Cobalt Complex in the Solid State. *Dalton Trans.* **2010**, *39* (20), 4757–4767.

(26) Ribeiro, M. A.; Stasiw, D. E.; Pattison, P.; Raithby, P. R.; Shultz, D. A.; Pinheiro, C. B. Toward Controlling the Solid State Valence Tautomeric Interconversion Character by Solvation. *Cryst. Growth Des.* **2016**, *16* (4), 2385–2393. https://doi.org/10.1021/acs.cgd.6b00159.

(27) Dapporto, P.; Dei, A.; Poneti, G.; Sorace, L. Complete Direct and Reverse Optically Induced Valence Tautomeric Interconversion in a Cobalt-Dioxolene Complex. *Chemistry* **2008**, *14* (35), 10915–10918. https://doi.org/10.1002/chem.200801120.

(28) Alley, K. G.; Poneti, G.; Robinson, P. S. D.; Nafady, A.; Moubaraki, B.; Aitken, J. B.; Drew, S. C.; Ritchie, C.; Abrahams, B. F.; Hocking, R. K.; Murray, K. S.; Bond, A. M.; Harris, H. H.; Sorace, L.; Boskovic, C. Redox Activity and Two-Step Valence Tautomerism in a Family of Dinuclear Cobalt Complexes with a Spiroconjugated Bis(Dioxolene) Ligand. *J. Am. Chem. Soc.* **2013**, *135* (22), 8304–8323. https://doi.org/10.1021/ja4021155.

(29) Adams, D. M.; Li, B.; Simon, J. D.; Hendrickson, D. N. Photoinduced Valence Tautomerism in Cobalt Complexes Containing Semiquinone Anion as Ligand: Dynamics of the High-Spin[CoII(3,5-Dtbsq)2] to Low-Spin[CoIII(3,5-Dtbsq)(3,5-Dtbcat)] Interconversion. *Angew. Chem. Int. Ed. Engl.* **1995**, *34* (1314), 1481. https://doi.org/10.1002/anie.199514811.

(30) Sato, O.; Hayami, S.; Gu, Z.; Seki, K.; Nakajima, R.; Fujishima, A. Photo-Induced Long-Lived Intramolecular Electron Transfer in a Co Valence Tautomeric Complex. *Chem. Lett.* **2001**, *30* (9), 874–875. https://doi.org/10.1246/cl.2001.874.

(31) Poneti, G.; Mannini, M.; Sorace, L.; Sainctavit, P.; Arrio, M.-A.; Rogalev, A.; Wilhelm, F.; Dei, A. X-Ray Absorption Spectroscopy as a Probe of Photo- and Thermally Induced Valence Tautomeric Transition in a 1:1 Cobalt-Dioxolene Complex. *ChemPhysChem* **2009**, *10* (12), 2090–2095. https://doi.org/10.1002/cphc.200900098.

(32) Dai, J.; Kanegawa, S.; Li, Z.; Kang, S.; Sato, O. A Switchable Complex Ligand Exhibiting Photoinduced Valence Tautomerism. *Eur. J. Inorg. Chem.* **2013**, *2013* (24), 4150. https://doi.org/10.1002/ejic.201300531.

(33) Neuwahl, F. V. R.; Righini, R.; Dei, A. Femtosecond Spectroscopic Characterisation of the Two-Step Valence Tautomeric Interconversion Occurring in a Cobalt–Dioxolene Complex. *Chem. Phys. Lett.* **2002**, *352* (5), 408–414. https://doi.org/10.1016/S0009-2614(02)00013-1.

(34) Gentili, P. L.; Bussotti, L.; Righini, R.; Beni, A.; Bogani, L.; Dei, A. Time-Resolved Spectroscopic Characterization of Photo-Induced Valence Tautomerism for a Cobalt–Dioxolene Complex. *Chem. Phys.* **2005**, *314* (1), 9–17. https://doi.org/10.1016/j.chemphys.2005.01.020.

(35) Azzaroli, N.; Lapini, A.; Di Donato, M.; Dei, A.; Righini, R. Valence Tautomerism in Co-Dioxolene Complexes: Static and Time-Resolved Infrared Spectroscopy Study. *J Phys Chem B* **2013**. https://doi.org/10.1021/jp405334y.

(36) Als-Nielsen, J.; McMorrow, D. *Elements of Modern X-Ray Physics*; John Wiley & Sons, 2011.

(37) Report of the Executive Committee for 1991. *Acta Crystallogr. A* **1992**, *48* (6), 922–946. https://doi.org/10.1107/S0108767392008328.

(38) Warren, B. E. *X-Ray Diffraction*; Courier Corporation, 1969.

(39) Giacovazzo, C. *Fundamentals of Crystallography*, 2nd ed.; Giacovazzo, C., Ed.; IUCr texts on crystallography; Oxford University Press, 2002.

(40) Sheldrick, G. M. Crystal Structure Refinement with SHELXL. *Acta Crystallogr. Sect. C Struct. Chem.* **2015**, *71* (1), 3–8.

(41) Allen, F. H. The Cambridge Structural Database: A Quarter of a Million Crystal Structures and Rising. *Acta Crystallogr. B* **2002**, *58* (3), 380–388. https://doi.org/10.1107/S0108768102003890.

(42) Berman, H. M.; Westbrook, J.; Feng, Z.; Gilliland, G.; Bhat, T. N.; Weissig, H.; Shindyalov, I. N.; Bourne, P. E. The Protein Data Bank. *Nucleic Acids Res.* **2000**, *28* (1), 235–242. https://doi.org/10.1093/nar/28.1.235.

(43) Belsky, A.; Hellenbrandt, M.; Karen, V. L.; Luksch, P. New Developments in the Inorganic Crystal Structure Database (ICSD): Accessibility in Support of Materials Research and Design. *Acta Crystallogr. B* **2002**, *58* (3), 364–369. https://doi.org/10.1107/S0108768102006948.

(44) Harris, D. C.; Bertolucci, M. D. *Symmetry and Spectroscopy: An Introduction to Vibrational and Electronic Spectroscopy*; Courier Corporation, 1989.

(45) Perkampus, H.-H. *UV-VIS Spectroscopy and Its Applications*; Springer Science & Business Media, 2013.

(46)   Caneschi, A.; Dei, A.; Gatteschi, D.; Tangoulis, V. Antiferromagnetic Coupling in a Six-Coordinate High Spin Cobalt(II)–Semiquinonato Complex. *Inorg. Chem.* **2002**, *41* (13), 3508–3512. https://doi.org/10.1021/ic020243n.

(47)   Victória, H. F. V. Ressonância paramagnética eletrônica de radicais nitróxidos e nanobastões de ouro funcionalizados com marcadores de spin. Masters Dissertation, Universidade Federal de MInas Gerais, 2018.

(48)   Weil, J. A.; Bolton, J. R. *Electron Paramagnetic Resonance: Elementary Theory and Practical Applications*; John Wiley & Sons, 2007.

(49)   Abragam, A.; Bleaney, B. *Electron Paramagnetic Resonance of Transition Ions*; Oxford: New York, 1970.

(50)   Witt, A.; W. Heinemann, F.; M. Khusniyarov, M. Bidirectional Photoswitching of Magnetic Properties at Room Temperature: Ligand-Driven Light-Induced Valence Tautomerism. *Chem. Sci.* **2015**, *6* (8), 4599–4609. https://doi.org/10.1039/C5SC00130G.

(51)   Fleming, C.; Chung, D.; Ponce, S.; Brook, D. J. R.; DaRos, J.; Das, R.; Ozarowski, A.; Stoian, S. A. Valence Tautomerism in a Cobalt-Verdazyl Coordination Compound. *Chem. Commun.* **2020**, *56* (32), 4400–4403. https://doi.org/10.1039/D0CC01770A.

(52)   Greene, B. I.; Hochstrasser, R. M.; Weisman, R. B. Picosecond Transient Spectroscopy of Molecules in Solution. *J. Chem. Phys.* **1979**, *70* (3), 1247–1259.

(53)   Foggi, P.; Bussotti, L.; Neuwahl, F. V. Photophysical and Photochemical Applications of Femtosecond Time-Resolved Transient Absorption Spectroscopy. *Int. J. Photoenergy* **2001**, *3* (2), 103–109.

(54)   Berera, R.; van Grondelle, R.; Kennis, J. T. M. Ultrafast Transient Absorption Spectroscopy: Principles and Application to Photosynthetic Systems. *Photosynth. Res.* **2009**, *101* (2), 105–118. https://doi.org/10.1007/s11120-009-9454-y.

(55)   Touceda Patricia, T.; Vázquez Sandra, M.; Manuela, L.; Andrea, L.; Paolo, F.; Andrea, D.; Roberto, R. Transient Infrared Spectroscopy : A New Approach to Investigate Valence Tautomerism. *Phys. Chem. Chem. Phys.* **2012**, *14* (2), 1038–1047. https://doi.org/10.1039/C1CP22557J.

(56)   Snellenburg, J. J.; Laptenok, S. P.; Seger, R.; Mullen, K. M.; van Stokkum, I. H. Glotaran: A Java-Based Graphical User Interface for the R Package TIMP. **2012**.

(57)   Slavov, C.; Hartmann, H.; Wachtveitl, J. Implementation and Evaluation of Data Analysis Strategies for Time-Resolved Optical Spectroscopy. *Anal. Chem.* **2015**, *87* (4), 2328–2336.

(58)   Caneschi, A.; Cornia, A.; Dei, A. Valence Tautomerism in a Cobalt Complex of a Schiff Base Diquinone Ligand. *Inorg. Chem.* **1998**, *37* (13), 3419–3421.

(59)   Cador, O.; Chabre, F.; Dei, A.; Sangregorio, C.; van Slageren, J.; Vaz, M. G. F. Temperature-Induced Solid-State Valence Tautomeric Interconversion in Two Cobalt-Schiff Base Diquinone Complexes. *Inorg Chem* **2003**, *42* (20), 6432–6440. https://doi.org/10.1021/ic034210z.

(60)   Wu, S.-Q.; Liu, M.; Gao, K.; Kanegawa, S.; Horie, Y.; Aoyama, G.; Okajima, H.; Sakamoto, A.; Baker, M. L.; Huzan, M. S. Macroscopic Polarization Change via Electron Transfer in a Valence Tautomeric Cobalt Complex. *Nat. Commun.* **2020**, *11* (1), 1–8.

(61)   Kahn, O. Spin-Transition Polymers: From Molecular Materials Toward Memory Devices. *Science* **1998**, *279* (5347), 44–48. https://doi.org/10.1126/science.279.5347.44.

(62)   Hendrickson, D.; Guzei, I.; Rheingold, A.; others. Valence Tautomeric Cobalt O-Quinone Complexes in a Dual-Mode Switching Array. *Chem. Commun.* **1998**, No. 19, 2089–2090.

(63) Manrique-Juárez, M. D.; Rat, S.; Salmon, L.; Molnár, G.; Quintero, C. M.; Nicu, L.; Shepherd, H. J.; Bousseksou, A. Switchable Molecule-Based Materials for Micro- and Nanoscale Actuating Applications: Achievements and Prospects. *Coord. Chem. Rev.* **2016**, *308*, 395–408. https://doi.org/10.1016/j.ccr.2015.04.005.

(64) Panja, A.; Jana, N. Ch.; Bauzá, A.; Frontera, A.; Mathonière, C. Solvent-Triggered Cis/Trans Isomerism in Cobalt Dioxolene Chemistry: Distinguishing Effects of Packing on Valence Tautomerism. *Inorg. Chem.* **2016**, *55* (17), 8331–8340. https://doi.org/10.1021/acs.inorgchem.6b00402.

(65) Ribeiro, M. A.; Stasiw, D. E.; Pattison, P.; Raithby, P. R.; Shultz, D. A.; Pinheiro, C. B. Towards Controlling the Solid State Valence Tautomer In-Terconversion Character by Solvation. *Cryst. Growth Des.* **2016**, *16* (4), 2385–2393.

(66) Evangelio, E.; Rodriguez-Blanco, C.; Coppel, Y.; Hendrickson, D. N.; Sutter, J. P.; Campo, J.; Ruiz-Molina, D. Solvent Effects on Valence Tautomerism: A Comparison between the Interconversion in Solution and Solid State. *Solid State Sci.* **2009**, *11* (4), 793–800. https://doi.org/10.1016/j.solidstatesciences.2007.11.039.

(67) Brown, S. N. Metrical Oxidation States of 2-Amidophenoxide and Catecholate Ligands: Structural Signatures of Metal–Ligand π Bonding in Potentially Noninnocent Ligands. *Inorg. Chem.* **2012**, *51* (3), 1251–1260. https://doi.org/10.1021/ic202764j.

(68) Kabsch, W. Xds. *Acta Crystallogr. D Biol. Crystallogr.* **2010**, *66* (2), 125–132.

(69) Sheldrick, G. M. SHELXT–Integrated Space-Group and Crystal-Structure Determination. *Acta Crystallogr. Sect. Found. Adv.* **2015**, *71* (1), 3–8.

(70) Groom, C. R.; Bruno, I. J.; Lightfoot, M. P.; Ward, S. C. The Cambridge Structural Database. *Acta Crystallogr. Sect. B Struct. Sci. Cryst. Eng. Mater.* **2016**, *72* (2), 171–179. https://doi.org/10.1107/S2052520616003954.

(71) Liang, H. W.; Kroll, T.; Nordlund, D.; Weng, T.-C.; Sokaras, D.; Pierpont, C. G.; Gaffney, K. J. Charge and Spin-State Characterization of Cobalt Bis(o-Dioxolene) Valence Tautomers Using Co Kβ X-Ray Emission and L-Edge X-Ray Absorption Spectroscopies. *Inorg. Chem.* **2017**, *56* (2), 737–747. https://doi.org/10.1021/acs.inorgchem.6b01666.

(72) Banci, L.; Bencini, A.; Benelli, C.; Gatteschi, D.; Zanchini, C. Spectral-Structural Correlations in High-Spin Cobalt(II) Complexes. *Struct. Spec. Prop.* **1982**, *52*, 37–86. https://doi.org/10.1007/BFb0111296.

(73) Gliemann, G. A. B. P. Lever: Inorganic Electronic Spectroscopy, Vol. 33 Aus: Studies in Physical and Theoretical Chemistry, Elsevier, Amsterdam, Oxford, New York, Tokio 1984. 863 Seiten, Preis: $ 113, 50. *Berichte Bunsenges. Für Phys. Chem.* **1985**, *89* (1), 99–100. https://doi.org/10.1002/bbpc.19850890122.

(74) Dei, A.; Feis, A.; Poneti, G.; Sorace, L. Thermodynamics of Valence Tautomeric Interconversion in a Tetrachlorodioxolene:Cobalt 1:1 Adduct. *Inorganica Chim. Acta* **2008**, *361* (14–15), 3842–3846. https://doi.org/10.1016/j.ica.2008.02.044.

(75) Hendrickson, D. N. Electron Transfer in Mixed-Valence Complexes in the Solid State. In *Mixed Valency Systems: Applications in Chemistry, Physics and Biology*; Prassides, K., Ed.; NATO ASI Series; Springer Netherlands, 1991; pp 67–90. https://doi.org/10.1007/978-94-011-3606-8_5.

(76) Dei, A.; Sorace, L. Cobalt-Dioxolene Redox Isomers: Potential Spintronic Devices. *Appl. Magn. Reson.* **2010**, *38* (2), 139. https://doi.org/10.1007/s00723-010-0121-4.

(77) Witt, A.; Heinemann, F. W.; Sproules, S.; Khusniyarov, M. M. Modulation of Magnetic Properties at Room Temperature: Coordination-Induced Valence Tautomerism in a Cobalt Dioxolene

Complex. *Chem. – Eur. J.* **2014**, *20* (35), 11149–11162. https://doi.org/10.1002/chem.201402129.

(78)   Macrae, C. F.; Sovago, I.; Cottrell, S. J.; Galek, P. T. A.; McCabe, P.; Pidcock, E.; Platings, M.; Shields, G. P.; Stevens, J. S.; Towler, M.; Wood, P. A. Mercury 4.0: From Visualization to Analysis, Design and Prediction. *J. Appl. Crystallogr.* **2020**, *53* (1), 226–235. https://doi.org/10.1107/S1600576719014092.

(79)   Baldini, E.; Mann, A.; Borroni, S.; Arrell, C.; Van Mourik, F.; Carbone, F. A Versatile Setup for Ultrafast Broadband Optical Spectroscopy of Coherent Collective Modes in Strongly Correlated Quantum Systems. *Struct. Dyn.* **2016**, *3* (6), 064301.

(80)   Bruno, I. J.; Cole, J. C.; Edgington, P. R.; Kessler, M.; Macrae, C. F.; McCabe, P.; Pearson, J.; Taylor, R. New Software for Searching the Cambridge Structural Database and Visualizing Crystal Structures. *Acta Crystallogr. B* **2002**, *58* (3), 389–397. https://doi.org/10.1107/S0108768102003324.

(81)   Lorenc, M.; Ziolek, M.; Naskrecki, R.; Karolczak, J.; Kubicki, J.; Maciejewski, A. Artifacts in Femtosecond Transient Absorption Spectroscopy. *Appl. Phys. B* **2002**, *74* (1), 19–27.

7 Appendices

7.1 ESR line shapes

The line shapes of the Lorentzian and Gaussian ESR signals are shown in Figure 7.1 and Figure 7.2, along with their first- and second-derivatives line shapes. On the figures, $Y(x)$ is the absorption function, $Y'(x) \equiv \frac{dY(x)}{dx}$, $Y''(x) \equiv \frac{d^2Y(x)}{d^2x}$, Γ is the half-width at half-height of Y, Y_{max} is the peak amplitude of Y, $2Y'_{max}$ is the peak-to-peak amplitude of Y', Δx_{pp} is the peak-to-peak width of Y', Y''_{max} and Y''_{min} are the peak amplitude of the positive and negative lobes of Y'', respectively. For more details and mathematical descriptions, see Weil and Bolton, 2007[48].
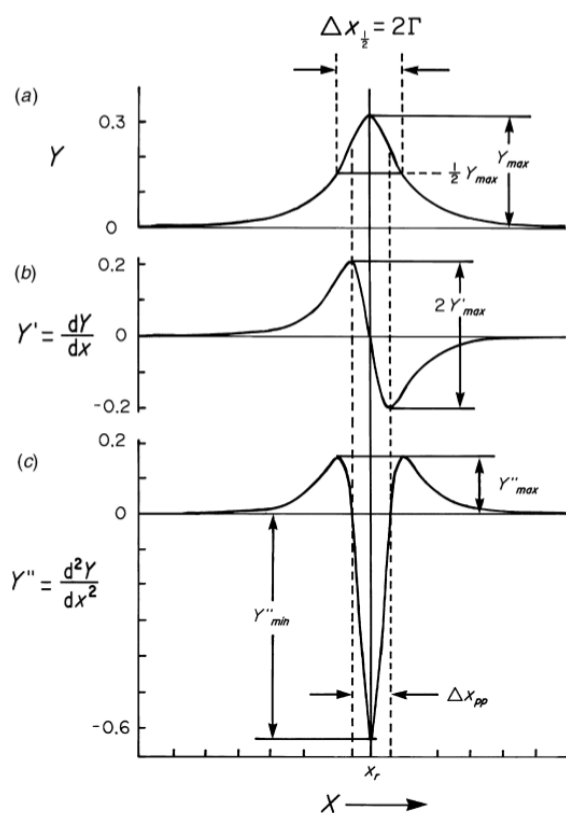
Figure 7.1 Lorentzian ESR lineshapes: (a) absorption spectrum; (b) first-derivative spectrum; (c) second-derivative spectrum. Figure from ([48])
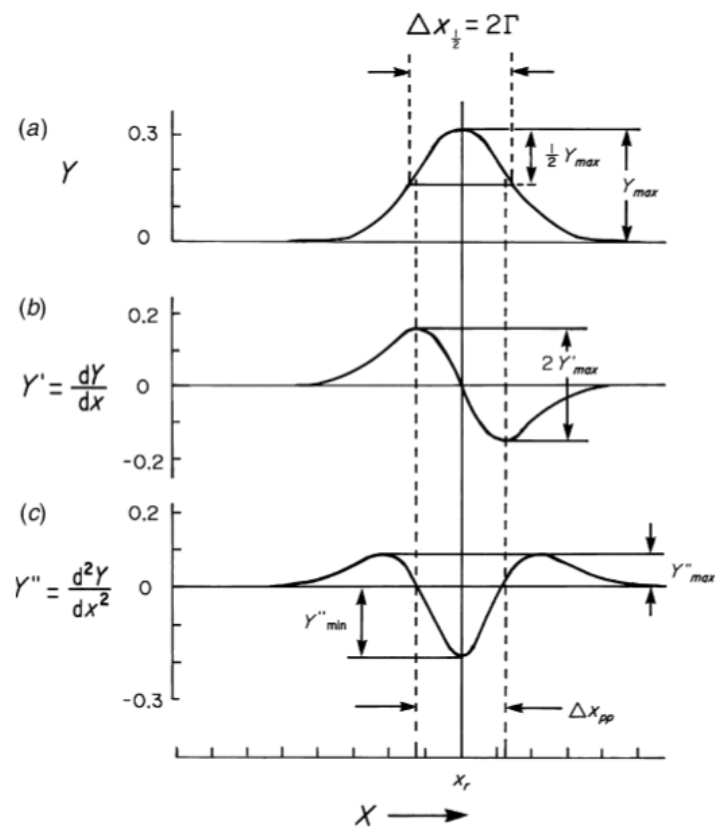
Figure 7.2 Gaussian ESR lineshapes: (a) absorption spectrum; (b) first-derivative spectrum; (c) second-derivative spectrum. Figure from ([48])

7.2 Supplementary information on Co(*diox*)₂Py₂

7.2.1 *Average Co-L distances*

The characteristic Co-L distances for the *hs*-Co^{II} and *ls*-Co^{III} forms of the Co(*diox*)$_2$Py$_2$ complex were obtained from averaging the corresponding values from structures deposited in the CCDC[41] databank. The list of structures used, and the corresponding bond lengths can be found below:

Table 7-1 – List of structures considered in the CONQUEST statistics survey for Co(diox)2(Py)2 complexes, the respective values of Co-O1, Co-O2 and Co-N distances, the average value of such distances and the associated oxidation state of the metal.

Name	Co-O1	Co-O2	Co-N	Co state
PUTFAM	1.898	1.897	1.956	
PUTFAM	1.883	1.881	1.959	
PUTFAM01	1.905	1.901	1.963	
PUTFAM01	1.884	1.88	1.951	
PUTFAM02	1.884	1.883	1.959	
PUTFAM03	1.88	1.886	1.944	
PUTFAM04	1.881	1.881	1.948	Co^{III}
PUTGAN	1.879	1.885	1.943	
PUTGER	1.919	1.9	1.937	
PUTGER	1.868	1.872	1.931	
PUTGER01	1.916	1.914	1.93	
PUTGER01	1.882	1.875	1.959	
YUWXUK	1.883	1.88	1.95	
AVERAGE	1.889	1.887	1.948	
PUTFAM02	1.976	1.96	2.043	
PUTFAM03	1.994	2.02	2.086	
PUTFAM04	2.042	2.011	2.118	Co^{II}
AVERAGE	2.004	1.997	2.082	

7.2.2 *Crystal packing for 1:0, 2:1 and 1:2.*

 The crystal packing within the unit cells of Co(*diox*)$_2$(Py)$_2$ crystals 1:0, 1:2 and 2:1 are shown on the tables below. Tables are named with crystal specification and pictures show the crystal packing as seen down the crystallographic axes a, b and c. Carbon atoms are depicted in gray,

oxygen in red, nitrogen in blue, cobalt in dark blue. Pyridine solvent carbon atoms are depicted in green. Hydrogen atoms are hidden for clarity.

Co(*diox*)$_2$Py$_2$

a

b

c

Co(*diox*)₂Py₂ + 0.5Py

a

b

c

Co(*diox*)₂Py₂ + 2Py
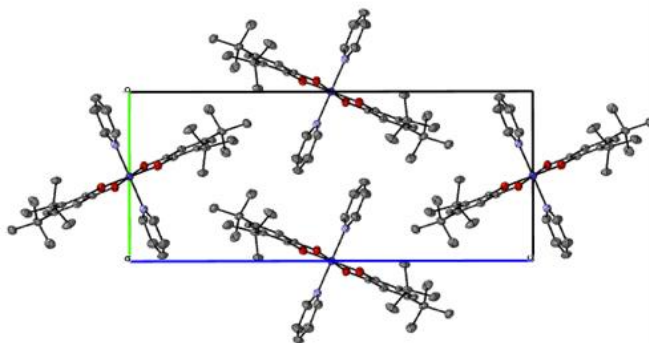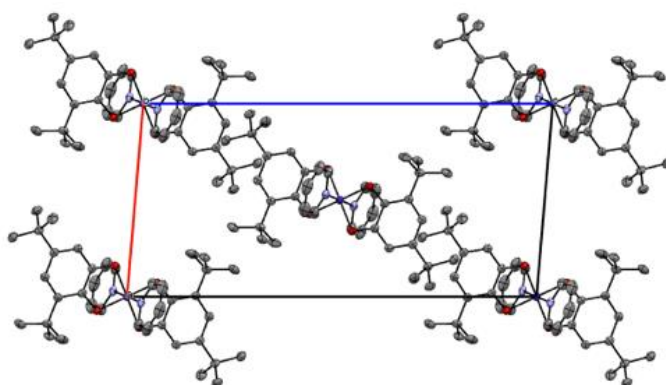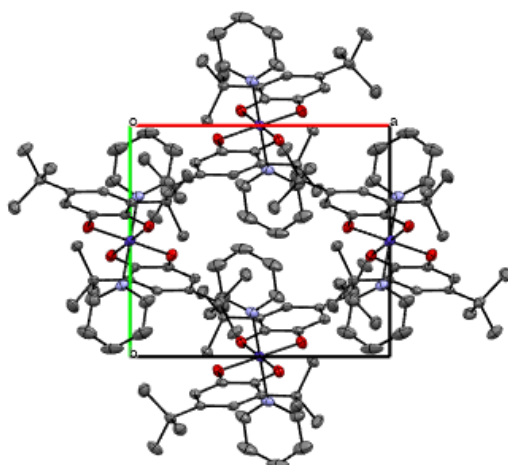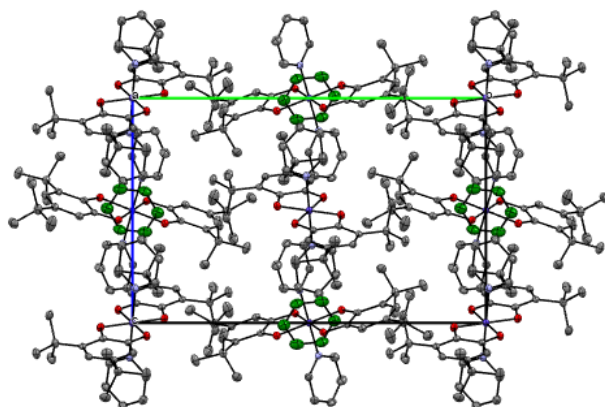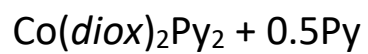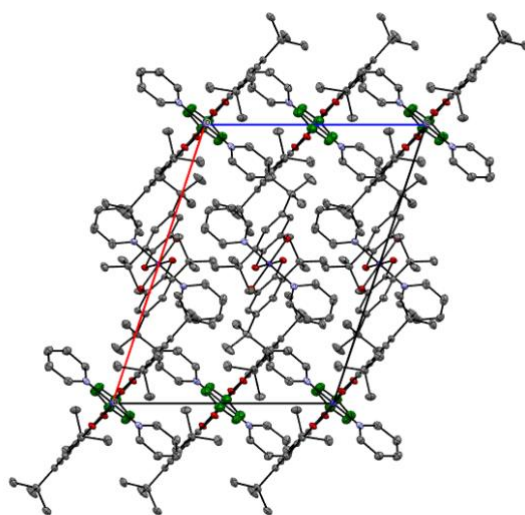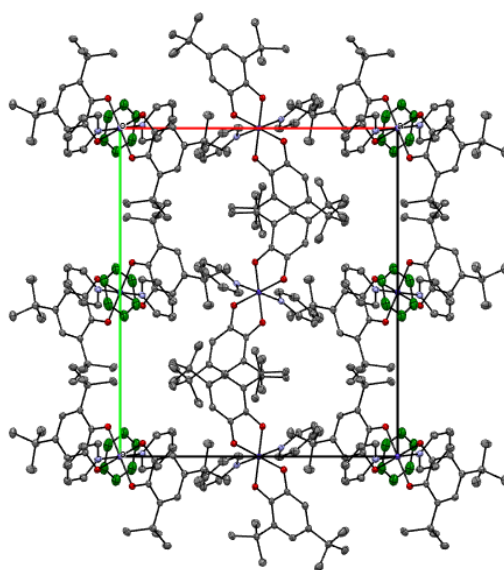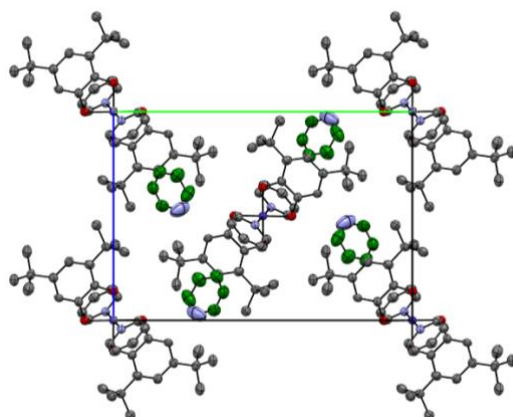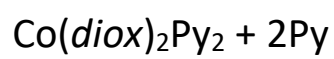
a
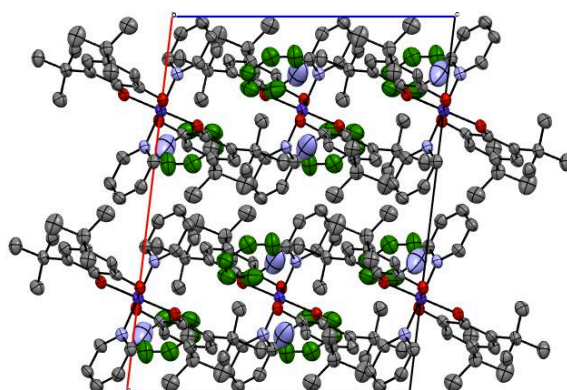
b
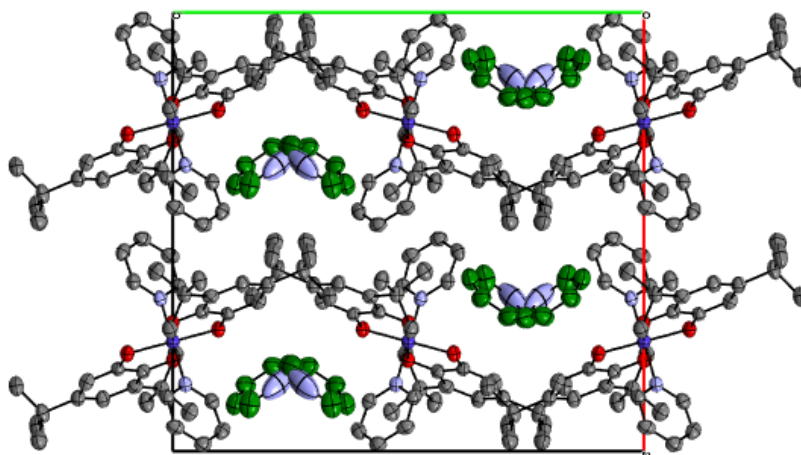
c

7.2.3 CSD survey details

Below is the list of structures surveyed from the CCDC[41] and included in the analysis of the angle between Py derivatives and dioxolene as a function of Co-N bond distances.

Table 7-2 - Structures considered in the statistics calculated. Surveyed from the CSD

BIKZUT	BILBOQ	KACCOI01	PUTFAM04
BIKZUT01	BILBOQ01	LOKPEI	PUTGAN
BIKZUT02	BILBOQ02	LUTKAN	PUTGER
BIKZUT03	EJUMON	LUTKER	PUTGER01
BIKZUT04	EJUMUT	MUJJIM	YEVMIW
BIKZUT05	EJUNAA	MUJJIM01	YUWXIY
BIKZUT06	EJUNEE	MUJJIM02	YUWXIY01
BIKZUT07	EJUNOO	MUJMEL	YUWXOE
BIKZUT08	EJUNUU	PUTFAM	YUWXUK
BIKZUT09	EJUPAC	PUTFAM01	YUWYAR
BIKZUT10	ILEDOU	PUTFAM02	YUWYEV
BIKZUT11	KACCOI	PUTFAM03	YUWYIZ

7.2.4 Co-N and Co-O vs. Co-diox/ PyL

The average Co-L distances were evaluated for L = N and O as a function of the angle between the PyL planes and the Co-diox vectors for the molecules surveyed from the CCDC[41] databank.
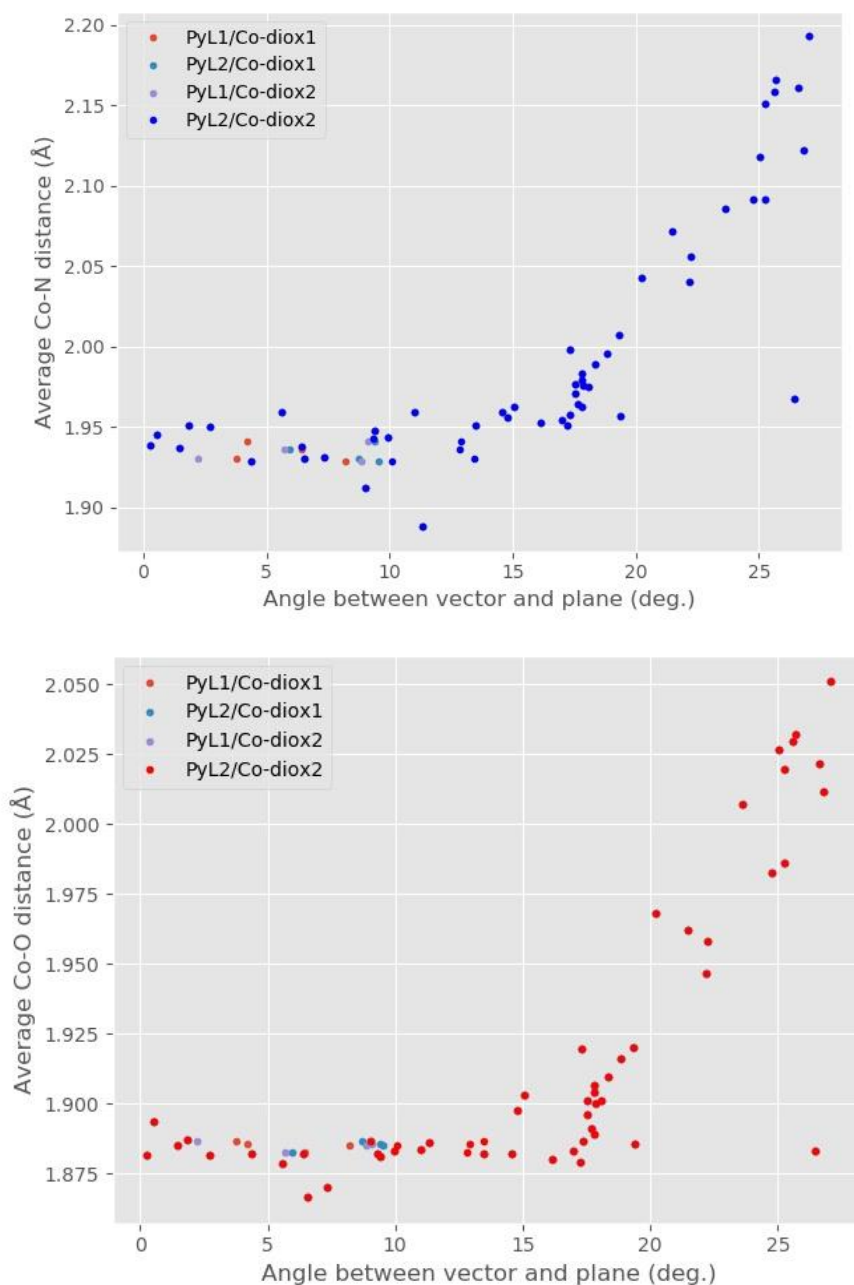
Figure 7.3 – Average Co-N and Co-O distances as a function of the angle between between PyL planes and Co-diox vectors for the molecules surveyed from the CCDC[41] databank (survey results: see Table 7-2).

To evaluate a possible exponential behavior, natural logarithm of the distances was plotted against the angle values between PyL1 plane and the Co-diox1. The non-linearity observed in the figure below discards such hypothesis.
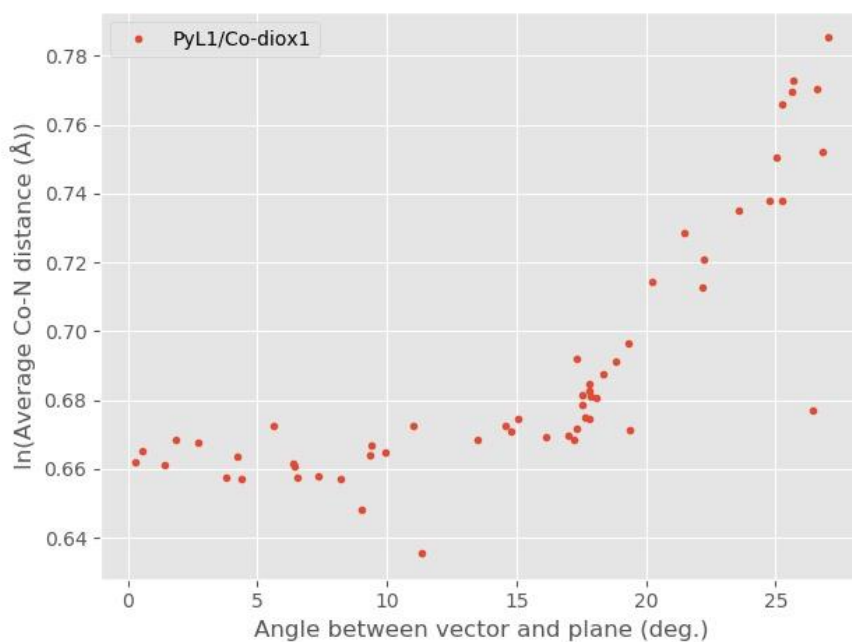
Figure 7.4 – Natural logarithm of Co-N distances as a function of the angle between between the PyL1 plane and the Co-diox1 vector for the molecules surveyed from the CCDC[41] databank (see Table 7-2).

7.2.5 Fit residuals

The residuals of the linear fits performed with Co-N vs. PyL/Co-diox data as a function of datapoints considered is shown below. The dashed line corresponds to the n = 25 point (see Figure 4.9 and discussion).
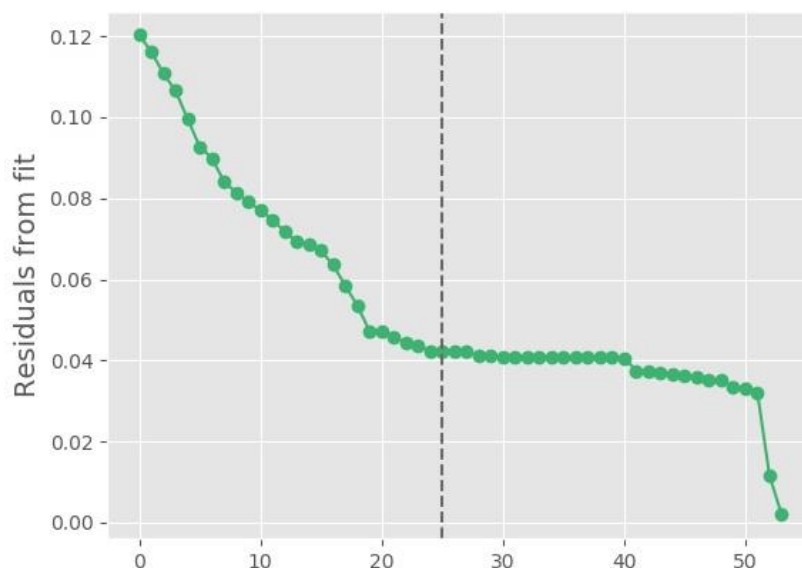
Figure 7.5 – Residuals of linear fit. The dashed line corresponds to n = 25.

7.2.6 Co(diox)₂(OMe – Py)₂ structure and pyridine environment
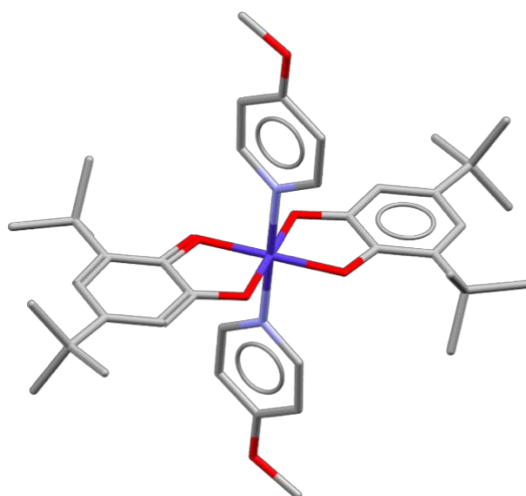
Figure 7.6 – Structure of the Co(diox)$_2$(OMe-Py)$_2$.
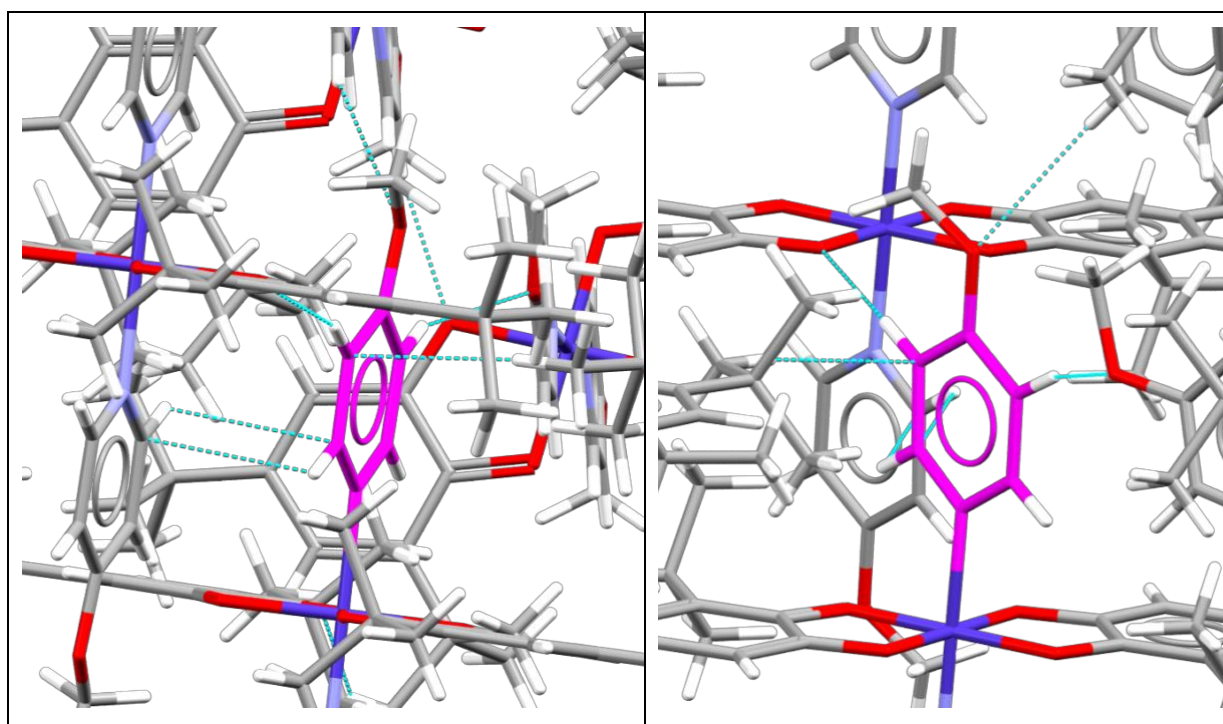
Figure 7.7 – Pyridine ligand environment and short contacts within the crystal lattice of the Co(diox)$_2$(OMe-Py)$_2$ crystal.

7.3 Submitted proposals for X-ray experiments beamtime

7.3.1 *Laboratório Nacional de Luz Síncrotron*

Proposals 20170455 (Structural Analysis of Valence Tautomers Candidates), 20160443 (Structural Studies of Molecular Bi-Stable Complexes) and 20180254 (Investigation of valence tautomerism using X-ray resonant diffraction) were accepted for Fast track and Standard measurements at the MX2 beamline. All three series of experiments were used to prove the concept.

_____

Investigation of Valence Tautomerism Using X-Ray Resonant Diffraction

Scientific background

The development of solid-state "smart" materials that exhibit bistability and can readily "switch" between two states when exposed to external stimuli is one of the key challenges of modern materials chemistry since such materials might have applications as sensors, signal processors information and storage devices. A Of the most promising among such materials are the valence tautomers (VT) which present electronic transitions within a molecular complex without substantial disruption of the solid-state structure. Complexes that undergo Valence Tautomerism interconversion (VTI) present a reversible entropy-driven rearrangement of intramolecular bonding electrons and a single-site spin crossover. VTI can be induced in complexes of some $3d^n$ ($4 \leq n \leq 7$) metallic ions with a variety of different redox active ligands by physical stimuli such as change of temperature, pressure, magnetic and. electric fields [2]. Long-lived metastable states have also been observed as a result of light irradiation, soft and hard X-rays [16] at very low temperatures in materials presenting VTI. The investigation of materials presenting VTI is generally on the metal ions and on the ligands associated as charge donors. Valence and spin states of the metal ions in VT and their respective changes have been indirectly determined by X-ray Diffraction and X-ray Absorption Near Edge Spectroscopy (*XANES*) techniques at different temperatures. Neither of them reveals how the electronic environment of a specific metal ion responds to a modification of external physical stimuli. Diffraction Anomalous Fine Structure (DAFS) combines the capabilities of X-ray Diffraction and X-ray Absorption Spectroscopy (XAS) into a single technique, thus it enables the determination of the valence state and the local structure of a selected element. It can also provide site-specific XAS and structural information for nonequivalent sites of an atomic species within a unit cell [4]. This unique feature makes DAFS the method of choice to investigate VTI in Cobalt-*o*-dioxolene complexes. The goal of this project is to characterize the local changes of the

electron density around nonequivalent crystallographic Cobalt ions in the structures of [Co(*o*-dioxolene)$_2$(R)$_2$] (where *o*-dioxolene = 3,5-di-t-butylsemiquinonate (SQ) and/or 3,5-di-t-butylcatecholate (Cat^{2-}) and R is Pyridine or Cyanopyridine) using DAFS techniques as a function of temperature.

Expected results.

VTI in **1** is characterized by an isotropic change in the Co–N and Co–O distances, an anisotropic change in the unit cell volume, the reorientation of the solvents molecules and pyridine ring planes and by the invariance in the intermolecular hydrogen-bonded lattice. Due to the steric hindrance of the *t*-butyl groups, only one oxygen atom of the *o*-dioxolene group coordinating the metal ion is involved in intermolecular interactions with cyanopyridine groups. Together all these structure accommodation effects, and in particular the strength and the number of direct contacts towards the *o*-dioxolene oxygen atoms seem to account for the VTI properties. In some materials, the VTI is cooperative – all metal ions change their oxidation state at a given temperature - and in some the effect is noncooperative and takes place in a large temperature interval. Thus, two relevant questions to be addressed are: (*i*) why do some metal ions change their oxidation state and others do not, at a given temperature? (*ii*) How the change of oxidation state of a metal within a molecule is transmitted to the others in the neighborhood? DAFS experiments consist in the measurement of the diffraction pattern as function of energy near the absorption edge of the desired metal ion. The DAFS signal will be used to draw the Cobalt oxidation state map from some crystallographic planes at each investigated temperature.

Previous characterization.

X-ray diffraction analysis of the compound **1** show that the Cobalt ions occupy crystallographic sites 2*a* and 2*d* from the space group $P2_1/1^2$. **1** shows a noncooperative VTI in which only the Cobalt ion in the 2*d* site interconvert from *hs*-Co^{2+} to *ls*-Co^{3+} form upon cooling (*ls*-low spin, *hs*=high spin) (Figure 1-a). We have been following the behavior of many reflections and the intensity of the reflection $(3, \bar{2}, 1)$ in particular, showed a disruptive behavior around the absorption edge energy of the Cobalt suggesting that it contain site-specific spectroscopic information (Figure 1-b).

Experimental method.

In order to determine which/how Cobalt atoms in the structure of the Cobalt complexes exchange their oxidation state during VTI, we plan to carefully follow the intensity of a group of reflections as a function of the X-ray energy and use the DAFS signal to draw an oxidation state map for some crystallographic planes at each measured temperature. We plan to perform a series of standard high resolution (~1.0 Å) complete single crystal X-ray diffraction experiments at the beam line MX2, using monochromatic radiation with energies ranging from 7000 eV to 7900 eV, in 50 K steps, from 290 K down to 100 K. Samples will be prepared at our laboratory and brought to LNLS in the form of single crystals in the solid state.
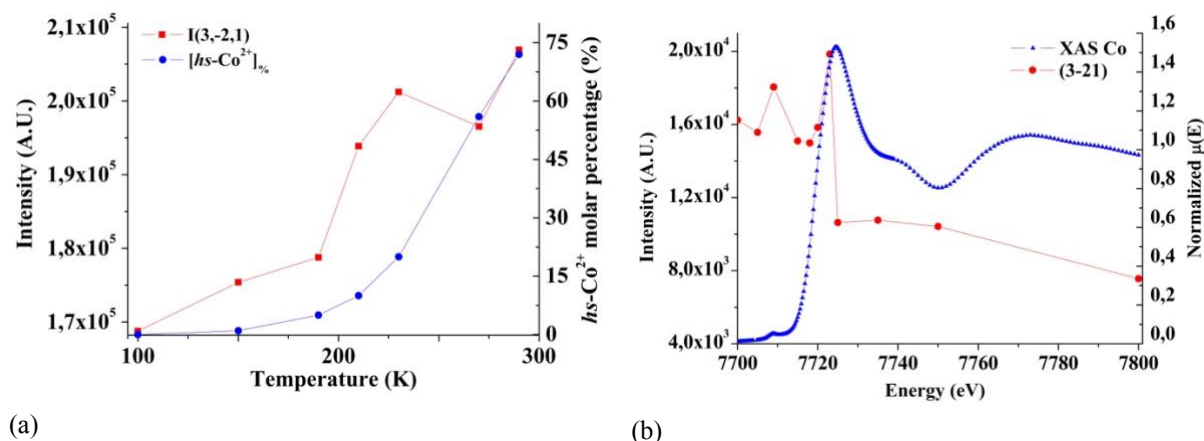
*Figure 1 – (a) Intensity of the reflection $(3,\bar{2},1)$ and hs-Co^{2+} molar percentage during VTI for complex **1**. (b) Intensity of reflection $((3,\bar{2},1))$ as function of the energy and XAS spectrum of Cobalt for complex **1**.*

Beam time requested justification.

DAFS information will be obtained from single crystal X-ray diffraction datasets varying temperature/energy. From our previous experiments, each complete single crystal X-ray diffraction dataset of **1**, at ~1.0 Å of resolution, takes around 10 minutes to be recorded in the MX2 beam line. We have previously obtained datasets varying energy in two different temperatures for the cobalt complex with Pyridine as a radical. Considering that we aim to perform the experiments at ~50 K intervals (between 290 K and 110 K) and at intervals as small as 4 eV near the absorption edge of the metal (slicing from 7500 eV e 7900 eV), we expect to perform near 360 data collections in around 72 hours. We emphasize that the crystal of the complexes are very resistant to the X-ray exposure and that one crystal of each complex should be enough for each temperature/energy run. Considering extra time to change energies, to stabilize sample temperatures and the LNLS refilling time, we ask for 4 days (8 sequential shifts) to conclude this project.

References.

O. Sato, Nat. Chem. 8, 644 (2016). [2] T. M. Francisco, W. J. Gee, H. J. Shepherd, M. R. Warren, D. A. Shultz, P. R. Raithby, and C. B. Pinheiro, J. Phys. Chem. Lett. 8, 4774 (2017). [3] T. Tezgerevska, K. G. Alley, and C. Boskovic, Coord. Chem. Rev. 268, 23 (2014). [4] R. D. Schmidt, D. A. Shultz, and J. D. Martin, Inorg. Chem. 49, 3162 (2010).

7.3.2 Diamond Light Source

The following proposals for single crystal X-ray diffraction experiments at the Diamond Light Source (UK) were submitted and accepted in 2018 (MT18816) and 2019 (CY22161). Experiments were performed using benzene solvated Co(*diox*)$_2$CN-Py$_2$ crystals for the evaluation of the photoinduced VT. Experimental details and results are described in Chapter 3.

_____

7.3.2.1 MT18816 - 2018

X-ray Induced Valence Tautomerism in Molecular Crystals at Low Temperatures

We wish to study the valence tautomerism in single crystals of [Co(o-diox)2(4-CN-py)2] induced by high intensity short wavelength synchrotron radiation, at temperatures between 30-100 K. In the series of experiments we wish to establish the level of tautomerism achieved by systematically changing the intensity of the X-rays (with filters), the temperature of the crystal (10 K steps between 30 and 100 K) and also irradiating the crystal with LED light of fixed wavelength to establish whether visible light contributed to the tautomerism. The results of this study will be important for all those working of structural studies of photoresponsive materials since it will provide new information on whether or not the X-ray probe is altering the nature of the material under investigation.

Scientific context

Introduction

The development of solid-state "smart" materials that exhibit bistability, and can readily "switch" between two states when exposed to external stimuli is one of the key challenges of modern materials chemistry since such materials might have applications as sensors, signal processors information storage devices and as pro-drug molecules.[1] Two of the most promising classes of such materials are spin-crossover[2] (SC) and valence tautomer (VT) complexes[3] as both involve electronic transitions within a single metal center or within a molecular complex, without substantial disruption of the solid-state structure. Complexes that undergo a valence tautomerism interconversion (VTI) present a reversible entropy-driven rearrangement of intramolecular bonding electrons and a single-site spin crossover. It creates two switchable redox isomers with different spectroscopic and magnetic properties.[4] VTI through a variety of external stimuli is well established. It was reported that VTI occurs under physical stimuli such as change of temperature, pressure, and magnetic and electric fields.[5] The investigations on materials presenting VTI are generally on the metal complexes with unique electronic, magnetic, electrochemical and structural properties. With detailed structural, electronic and thermodynamic information on VT in solid state, it is possible to characterize the effects of the variation of factors such as the symmetry of the environment, the nature of the ligands, solvate molecules and counter ions, as well as temperature, pressure, illumination and irradiation on

the rate of intramolecular electron transfer. In an experiment on I19 at Diamond (MT9635), we have recently serendipitously discovered that hard X-rays can induce VTI, and that there is both an intensity and radiation exposure time dependence on the interconversion rate.[7] *This shows that X-rays, as a probe, are altering the very nature of many structures under investigation at low temperatures, and consequently their properties. Such results extrapolate VTI studies and will be of interest to scientists investigating photoresponsive complexes.*

The goal of this proposal is to further investigate the VTI in the $[Co(o\text{-}diox)_2(4\text{-}CN\text{-}py)_2]\cdot$benzene complex 1 (o-diox = 3,5-di-t-butylsemiquinonate (SQ•-) and/or 3,5-di-t-butylcatecholate (Cat2-) radical; 4-CN-py = 4-Cyano-pyridine) using hard synchrotron X-ray radiation with different intensities and different light color illumination. We aim to investigate the interplay between hard X-ray and light illumination on the VTI properties.

Experiment proposed

In the experiments that we propose the use of synchrotron is crucial. From the preliminary experiments that we have carried out it is clear that synchrotron intensity radiation is essential to cause the VTI at the investigated temperatures. In our preliminary studies performed on beamline I19, the irradiation with hard X-rays and the light illumination effects on the VTI interconversion properties of 1 have been briefly explored in single crystal X-ray diffraction experiments. Following the structural changes that take place in the Co ion neighborhood it was possible to follow the temperature dependence of hs-Co^{2+} molar percentage of 1 in hard X-rays diffraction with (AHAXL) and without (AHAX) light illumination experiments. Illumination seems to both boost the metastable hs-Co^{2+} redox isomer interconversion (maximum conversion percentages approaching 90%) as well as change its temperature dependence (*Figure 1a*). The preliminary data also suggests some dynamics during the excitation to metastable hs-Co^{2+} states, as shown in *Figure 1b*.
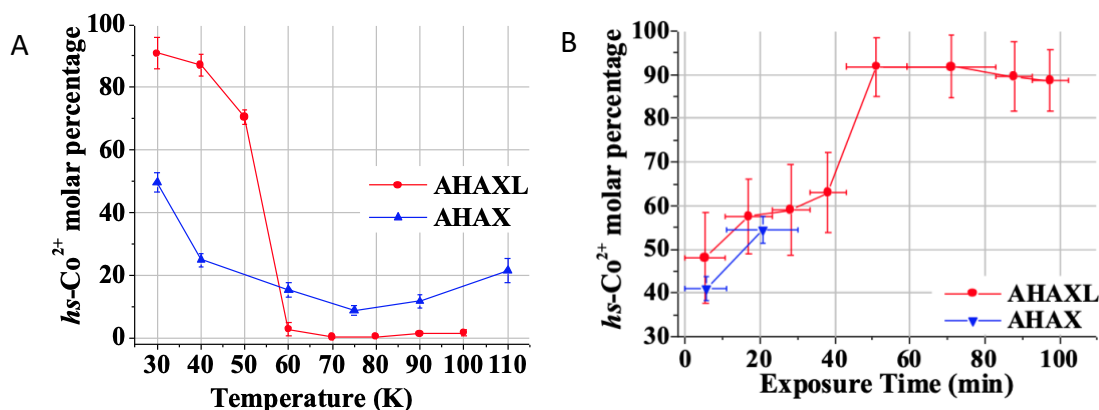
Figure 1 – (a) hs-Co²⁺ isomer mole percentage during VTI under sample exposure to a 78% attenuated in the dark (AHAX) and a 39% attenuated Hard X-ray beam with light illumination (AHAXL) (with LEDs). (b) Time evolution of hs-Co²⁺ isomer mole percentage.

Considering that hard X-rays and illumination irradiation induce the metastable hs-Co^{2+} redox isomer of 1 at low temperature and that similar materials present such interconversion only under light illumination at similar temperatures, our research question is "*is the excitation process that leads to the VTI the same for both processes?*" We speculate that nature of both

hard X-rays and light illumination interconversion processes on 1 are similar and triggered by the relaxation process(es) that follow electronic excitations caused by secondary electron generation after X-ray absorption but we do need better data to investigated that. We propose to perform experiments at the temperature range between 30 and 100K on I19 combining X-ray diffraction and light illumination. We also plan to simultaneously monitor the processes using the *in-situ* Raman spectrometer available on the beamline. We request 9 sequential shifts of beamtime in EH2 using radiation close to the Ag edge. Using crystals of similar sizes, we will benchmark the experiment by measuring the AHAX effect, with the full intensity X-ray beam (in the dark) at 10 deg intervals between 30-100 K, repeat the process with 70% X-ray, attenuation, and again with 90% X-ray attenuation (total of 24 data sets each taking approx. 1 h). We will then repeat the data collections, using the same conditions except that the crystal will be simultaneously irradiate (AHAXL) with white LED lights of known flux (24 data sets, 1 h each). Then, choosing the optimum X-ray intensity from the previous experiments we will carry out the 8 temperature collections irradiating the crystal with blue LEDs (420 nm) of known flux (8 h) and again with green LEDs (530 nm) (8 h).

Results expected

The experiments proposed will, for the first time, provide a systematic study of the VTI process in single crystals, using hard X-rays as the stimulus. We will also establish whether simultaneous irradiation with light and hard X-rays alters the % interconversion and provides new information as to whether the two interconversion occur by the same mechanism. This study has important implications for further studies on VT and spin-crossover materials, and will show whether the X-rays themselves alter the state of the material rather than merely acting as an "innocent" probe.

Publications

[1] (a) Souza, E. T., et. al. J Inorg Biochem. 2009, 103(1):1355-1365. (b) Sato, O., et. al. Angew. Chem. Int. Ed. 46, 2152–2187 (2007). (c) Sato, O. Nat. Chem. 8, 644–656 (2016). [2] (a) Muñoz, M. C. & Real, J. A. Coord. Chem. Rev. 255, 2068–2093 (2011). (b) Halcrow, M. A. Chem. Soc. Rev. 40, 4119 (2011). [3] (a) Pierpont, C. G. Coord. Chem. Rev. 216, 99–125 (2001). (b) Tezgerevska, T., Alley, K. G. & Boskovic, C. Coord. Chem. Rev. 268, 23–40 (2014). [4] Adams, D. M. & Hendrickson, D. N. J. Am. Chem. Soc. 118, 11515–11528 (1996). [5] Tezgerevska, T., et. al. Coord. Chem. Rev. 268, 23–40 (2014). [6] Sato, O., et. al. S. Acc. Chem. Res. 40, 361–369 (2007). (b) Schmidt, R. D., et. al.. Inorg. Chem. 49, 3162–3168 (2010). [7] Francisco, T. M., et. al. J. Phys. Chem. Lett, DOI: 10.1021/acs.jpclett.7b01794 (2017).

7.3.2.2   CY22161 - 2019

X-ray Induced Valence Tautomerism in Molecular Crystals at Low Temperatures

Introduction

The development of solid-state "smart" materials that exhibit bistability, and can readily "switch" between two states when exposed to external stimuli is one of the key challenges of modern materials chemistry since such materials might have applications as sensors, signal processors information storage devices and as pro-drug molecules.[1] Two of the most promising classes of such materials are spin-crossover[2] (SC) and valence tautomer (VT) complexes[2] as both involve electronic transitions within a single metal center or within a molecular complex, without substantial disruption of the solid-state structure. Complexes that undergo a valence tautomerism interconversion (VTI) present a reversible entropy-driven rearrangement of intramolecular bonding electrons and a single-site spin crossover. It creates two switchable redox isomers with different spectroscopic and magnetic properties.[3] VTI through a variety of external stimuli is well established with many examples in the literature. For instance, it was reported that VTI occurs under physical stimuli such as change of temperature, pressure, and magnetic and electric fields.[4] Long-lived metastable states were also observed because of light irradiation at very low temperatures in materials presenting VTI.[5]

The investigation on materials presenting VTI is generally on the metal ions and particularly in the electronic, magnetic, electrochemical and structural properties that combine to give a unique physical and chemical unit to the compounds. Ligands associated with the metal sites as charge donors contribute to these properties through coordination.[6] With detailed structural, electronic and thermodynamic information VT in solid state, it is possible to characterize the effects of the variation of factors such as the symmetry of the environment, the nature of the ligands, solvate molecules and counter ions, as well as temperature, pressure, illumination and irradiation on the rate of intramolecular electron transfer. In particular, we have recently found[7] that hard X-rays can induce VTI, and that there is both an intensity and radiation exposure time dependence on the interconversion rate. This in turn shows that X-rays, as a probe, might be altering the very nature of many structures under investigation at low temperatures, and consequently their properties. Such results extrapolate VTI studies and indeed may interest to the entire community investigating photoresponsive complexes. Recently, in AP23 (MT18816), we further probed the effect of X-ray intensity on the tautomerism, and carried our preliminary photoactivation studies. The goal of this proposal is to further investigate the VTI in the [Co(o-$diox$)$_2$(4-CN-py)$_2$]·benzene complex (1) (o-$diox$ = 3,5-di-t-butylsemiquinonate (SQ•$^-$) and/or 3,5-di-t-butylcatecholate (Cat^{2-}) radical; 4-CN-py = 4-Cyano-pyridine) using hard synchrotron X-ray radiation and illumination studies with specific wavelengths of light from across the visible spectrum.

Preliminary studies and Proposed experiments

Cobalt-dioxolene complexes have been largely studied due the presence of VTI. Well known cobalt VTI materials are the complexes with cathecolate (Cat) and seminquinone (SQ) ligands in which tautomeric valence equilibrium between hs-Co^{2+} and ls-Co^{3+} forms (hs=high spin, ls=low spin) can be induced thermally, mechanically or by illumination. The metastable hs-Co^{2+}

redox isomer photoexcitation of the complexes Co(o-diox)$_2$L$_2$ [L=(py$_2$, (4-OMe-py)$_2$, (4-Me-py)$_2$, (4-Me-py)$_2$, (4-Br-py)$_2$, (4-NO$_2$-py)$_2$)] was investigated using a SQUID magnetometer.[8] In that experiment samples were kept at 10 K and illuminated with white light source (150 W, λ= 400-850 nm). A photostationary limit for the metastable hs-Co^{2+} redox isomer conversion was never achieved as the value of $\chi_{para}.T$ never plateaus and continues to grow (albeit at a very slow rate) even after 12h of illumination (with maximum conversion percentages approaching 30%). This behavior was attributed to the inability of the incident light to fully penetrate the opaque samples and promote VTI and/or to a photoinduced decay process as result of absorption of certain light colors by hs-Co^{2+} form. In our previous studies performed onbeamline I19, the irradiation with hard X-rays and the light illumination effects on the VTI interconversion properties of 1 have been briefly explored in single crystal X-ray diffraction experiments. Following the structural changes that take place in the Co ion neighborhood.[9] it was possible to follow the time dependence of hs-Co^{2+} molar percentage of 1 in hard X-rays diffraction with (AHAXL) and without (AHAX) white light illumination experiments shown in *Figure 1a*. Such illumination seems to both boost the metastable hs-Co^{2+} redox isomer interconversion (light induced conversion percentages approaching 40%). From our last experiments with low X-ray flux, 1 reached the remarkable level of 80% of induction stimulated by blue light, as shown in *Figure 1b*.
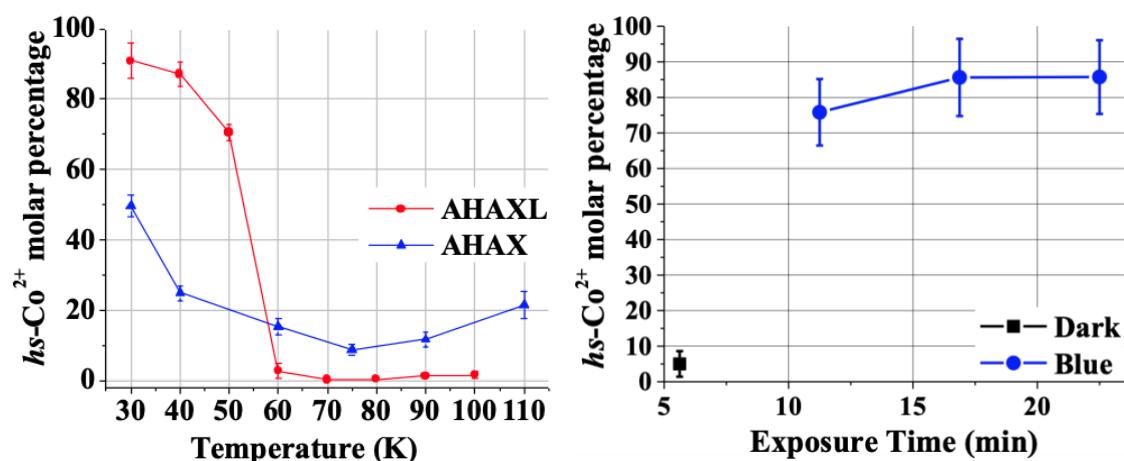
Figure 1 – (a) Time evolution of hs-Co^{2+} isomer mole percentage during VTI under sample exposure to a 78% attenuated in the dark (AHAX) and a 39% attenuated Hard X-ray beam with light illumination (AHAXL) (LED: 0996mA). (b) Time evolution of hs-Co^{2+} isomer mole percentage without light and illuminated with blue light (LED: $\lambda = 470$ nm)

Preliminary results obtained at the I19, in AP23, suggests that under low intensity of hard X-ray irradiation and blue light illumination the population of the hs-Co^{2+} metastable isomer of 1 increases in ~80%. However, as observed previously, under high intensity of Hard X-ray irradiation and white light illumination, the increases the population of the hs-Co^{2+} metastable isomer of 1 increases only by ~40%. Thus, there should be a light energy competing to direct and reverse hs-Co$^{2+} \Rightarrow ls$-Co^{3+}. Another important feature is that red light illumination seems not to affect the interconvertion.

We propose to check systematically over the visible spectra looking for wavelengths that cause or not the direct and reverse interconversion. Thus, we plan to perform the following experiments at the temperature range between 30 and 120K (using the Helix crystal cooling

apparatus) on I19 beamline combining X-ray diffraction and light illumination (using both LEDs and CW lasers):

- Single crystal diffraction in the dark;
- Single crystal diffraction with white light;
- Single crystal diffraction with violet light ($\lambda \sim$ 410.0 nm);
- Single crystal diffraction with blue light ($\lambda \sim$ 440.0 nm);
- Single crystal diffraction with green light ($\lambda \sim$ 530.0 nm);
- Single crystal diffraction with yellow light ($\lambda \sim$ 580.0 nm);
- Single crystal diffraction with red light ($\lambda \sim$ 632.0 nm);

From our previous experience, each complete single crystal X-ray diffraction data collection takes about 20 minutes, and considering samples changes, experiment set-up, laser alignment and further manipulation, we ask for 9 shifts (3 days) of beam time.

References

1. (a) Sato, O. Nat. Chem. 8, 644–656 (2016). (b) Manrique-Juárez, M. D. *et al.* Coord. Chem. Rev. 308, 395–408 (2016). 2. Tezgerevska, T., Alley, K. G. & Boskovic, C. Coord. Chem. Rev. 268, 23–40 (2014). 3. Adams, D. M. & Hendrickson, D. N. J. Am. Chem. Soc. 118, 11515–11528 (1996). 4. Tezgerevska, T., Alley, K. G. & Boskovic, C. Coord. Chem. Rev. 268, 23–40 (2014). 5. Schmidt, R. D., Shultz, D. A. & Martin, J. D. Inorg. Chem. 49, 3162–3168 (2010). 6. Pierpont, C. G. (2001). Coord. Chem. Rev., 219, 415-433. 7. Francisco, T. M, et. al., J Phys Chem Lett, 8, 4774-4778 (2017). 8. Schmidt, R. D., Shultz, D. A., Martin, J. D. & Boyle, P. D. J. Am. Chem. Soc. 132, 6261–6273 (2010). 9. Ribeiro, M. A., et. al. Cryst Growth & Design, 16, 2385-2393 (2016).

7.3.3 Stanford Synchrotron Radiation Light Source

The following proposal for X-ray experiments at the Stanford Synchrotron Radiation Lightsource was submitted in February, 2020. The proposal was rated 1.60/2.00 and expires on the 30th of November 2021. Unfortunately, due to the COVID-19 pandemic measures and restrictions, experiment time has been limited in facilities. Our group will submit one more beamtime request, associated to this proposal when the facility reopens for such calls, for the second semester of 2021.

Investigation of the electronic dynamics of the photo induced valence tautomerism in solid state Cobalt complexes using X-ray spectroscopy

The development and investigation of smart materials, which present bistability when exposed to external stimuli is a key challenge to material physics and chemistry. Among the various types of these materials, the valence tautomers are compounds which switch between different electronic and spin states and can be used as sensors, signal processors and memory storage since their solid structure do not present substantial rupture during the interconversion. With this proposal we aim to use X-ray absorption spectroscopy to carefully study the thermo and photo-induced electronic dynamics changes in cobalt 3,5-di-tert-butyl-semiquinone valence tautomer complexes in single crystal form.

Background and significance

Smart materials are designed to respond to mechanical, chemical, electric or magnetic stimuli from the environment having one or more of their properties significantly changed in a controlled manner. Among these materials, those that present electronic bistability and can readily switch between two electronic and/or spin states can be potentially used as sensors, signal processors and information storage devices [1], [2]. Two of the most promising classes of electronically bistable materials are those that present either spin-crossover (SC) or valence tautomerism (VT), as both properties involve electronic transitions within a single metal center or within a molecular complex without substantial disruption of the solid-state structure.

Valence tautomerism has been studied in molecules with a Cobalt metal center, nitrogen based ancillary ligands and semiquinone radicals [3]–[5]. These molecules have shown to be particularly interesting due to the ancillary ligand modulation of the valence tautomerism that presents itself in liquid and/or in solid state as single crystals in a reversible fashion [6], [7] being possibly dependent on the solid state arrangement of the complexes and on solvation [8]–[10]. The VT in such molecules can be induced by temperature as first and second order transitions with a wide range of characteristic T1/2 according to the ancillary ligand. In the low temperature regime, the VT is also shown to be induced with photo irradiation in multiple wavelengths. Interestingly, it can also be induced with soft and hard X-rays irradiation with high yield of metastable isomers [11], [12]. The nature and the dynamics of the photo-induced VT has not yet been thoroughly studied, though X-ray spectroscopy has shown to be a suitable technique to progress towards a deeper understanding of the involved electronic states in such phenomena [13]–[15]. Most importantly, the relaxation process of the photo excited states is

poorly understood, yet there is evidence of two relaxation mechanisms: a phonon assisted tunneling in temperatures T<20K and thermally assisted relaxation for higher T [9], [16], [17]. However, a photo induced de-excitation of the photo induced high energy metastable states has also been observed [13], which brings the question of how these complexes respond to temperature and photo-excitation in the electronic level. Our research group has been studying Cobalt 3,5-di-tert-butyl-semiquinone complexes (3,5-DTBQ) with pyridine (Py), Cyan-pyridine (CN-Py) and nitro pyridine (NO2-Py) as ancillary ligands. We have shown that the VT can be probed and monitored with X-ray diffraction experiments and that it can also be induced by irradiation of hard X-rays in the low temperature regime for the Co(3,5-DTBQ)2(CN-Py)2 [12] and blue light (Figure 1). Additionally, the complex Co(3,5-DTBQ)2Py2 also shows photo induced valence tautomerism when irradiated with green (532nm) [9], red (632nm), blue (446nm) LED light (unpublished results). With this proposal, we aim at using X-ray absorption spectroscopy to investigate the electronic states involved in the thermo induced VT and in the photo induced VT when different photo excitation wavelengths are used with single crystals as samples. Moreover, we aim to use the same technique to gain insight on the relaxation dynamics of the photo excited high energy states probing for the possible intermediate electronic states in the photo excitation and relaxation processes.
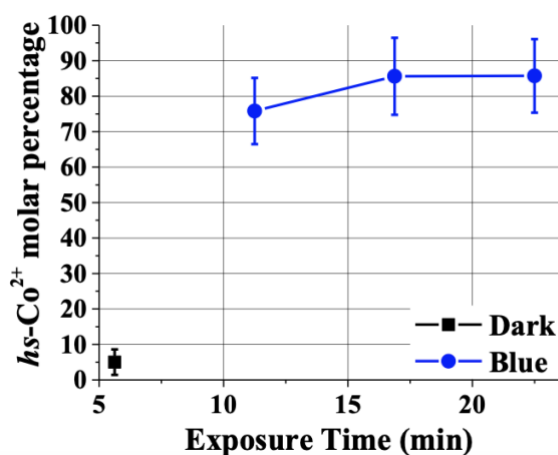
Figure 1: photo converted molar fraction of Cobalt 3,5-di-tert-butyl-semiquinone complex under blue light illumination.

Specific aims and planned experiments

The samples under investigation in this proposal are single crystals of the Co(3,5-DBSQ)2(CN-Py)2 complex (1) and the Co(3,5-DBSQ)2Py2 complex (2) as single crystals. Given our previous results in which we confirm the thermo induced VT and the photo induced VT in the low temperature regime using visible LED light and hard X-rays for complex 1 and visible LED light for complex 2, the following sequence of experiments should be performed to allow a proper evaluation of the electronic structure dynamics of the VT in single crystals:

- Acquire baseline XAS spectra for single crystals of complexes 1 and 2 at room temperature and at 10K for 1 to 2 hours, to show that the X-rays in the chosen energy range are not inducing any excited states on the samples, agreeing with previous results from X-ray diffraction experiments performed in these complexes.
- Acquire X-ray absorption spectra for single crystals of complexes 1 and 2 as a function of temperature, from room temperature down to 10K in at least 5 sequential cooling

and heating cycles aiming for a statistically reasonable set of data to study the temperature induced VT.

- Cool the samples down to 10K and irradiate them with LED or LASER light at selected wavelengths and acquire XAS spectra sequentially with the highest acquisition frequency allowed by the beamline;
- Immediately after the light irradiation is turned off, acquire XAS spectra sequentially with the highest acquisition frequency allowed by the beamline to evaluate the relaxation of the photo excited states.
- Repeat steps from 2 to 4 for other photo excitation temperatures (20K, 30K, 40K, 50K and 60 K) on step 2 so that different relaxation regimes can be assessed.

If the beamline absorption spectra acquisition rate is not compatible with the intermediate states dynamics in the transition, we can still probe the electronic states involved in the long-lived high energy metastable states (~3 hours for the relaxation of 50% of the photo induced high energy states population). Also, for the beamlines that can perform X ray scattering and absorption experiments simultaneous, the VT can be simultaneously monitored with single crystal X-ray diffraction.

Data Interpretation Methods

The analyses and interpretation of XAS spectra can be performed using the Demeter software [18], which counts on the Athena and Artemis routines for the evaluation of the near absorption edge and far from absorption edge regions of the XAS spectra. Also, we count on python scripts for data analyses and for the accountability of experimental issues (background subtraction, spectra deconvolution, etc). The valence tautomerism in Cobalt complexes has been reportedly evaluated from XAS spectra [13], [15] and the reported data analysis methodology serves as a baseline to our experiments.

Need for synchrotron radiation and SSRL

The X-ray absorption experiments proposed are fundamentally based on the X-ray energy scan with fine steps in energy that only synchrotron light sources can provide. The SSRL is one of the few facilities that can provide with a beamline in which X-ray spectroscopy and pump probe experiments can be performed with a beam spot as small as 10μm and that is also coupled with a high-resolution X-ray scattering studies setup (end stations 10-a and 10-b). At the SSRL it is also possible to perform X-ray absorption spectroscopy at a beamline specifically designed for experiments with single crystals (beamline 9-3). Both beamlines allow the energy scan in the range of our interest (7000-8000 eV) and also count on adequate single crystal sample environment that allows sample illumination and orientation. The sample orientation is an important factor that must be considered in our experiment as the crystal position with respect to the incident X-ray beam must be finely monitored to account for polarization effects. Moreover, the beamlines allow working in temperatures as low as 10K with the aid of a Helium jet that is commonly used in single crystal X-ray diffraction experiments.

References

[1]O. Sato, "Dynamic molecular crystals with switchable physical properties," Nat. Chem., vol. 8, no. 7, pp. 644–656, Jul. 2016. [2] D. P. Karothu, J. Weston, I. T. Desta, and P. Naumov, "Shape-Memory and Self-Healing Effects in Mechanosalient Molecular Crystals," J. Am. Chem. Soc., vol. 138, no. 40, pp. 13298–13306, Oct. 2016. [3] D. A. Shultz, "Valence tautomerism in

dioxolene complexes of cobalt," Magn. Mol. Mater. II Models Exp., pp. 281–306, 2001. [4] R. M. Buchanan, B. J. Fitzgerald, and C. G. Pierpont, "Semiquinone radical anion coordination to divalent cobalt and nickel. Structural features of the bis (3, 5-di-tert-butyl-1, 2-semiquinone) cobalt (II) tetramer," Inorg. Chem., vol. 18, no. 12, pp. 3439–3444, 1979. [5] J. Tao, H. Maruyama, and O. Sato, "Valence Tautomeric Transitions with Thermal Hysteresis around Room Temperature and Photoinduced Effects Observed in a Cobalt- Tetraoxolene Complex," J. Am. Chem. Soc., vol. 128, no. 6, pp. 1790–1791, 2006. [6]T. Tezgerevska, K. G. Alley, and C. Boskovic, "Valence tautomerism in metal complexes: Stimulated and reversible intramolecular electron transfer between metal centers and organic ligands," Coord. Chem. Rev., vol. 268, pp. 23–40, Jun. 2014. [7] O. Sato, A. Cui, R. Matsuda, J. Tao, and S. Hayami, "Photo-induced Valence Tautomerism in Co Complexes," Acc. Chem. Res., vol. 40, no. 5, pp. 361–369, May 2007. [8]"Goldilocks Effect in Magnetic Bistability: Remote Substituent Modulation and Lattice Control of Photoinduced Valence Tautomerism and Light-Induced Thermal Hysteresis - Journal of the American Chemical Society (ACS Publications)." [Online]. Available: https://cdn-pubs.acs.org/doi/10.1021/ja101957c. [Accessed: 27-Sep-2018]. [9] Y. Mulyana et al., "Solvation effects on the valence tautomeric transition of a cobalt complex in the solid state," Dalton Trans., vol. 39, no. 20, pp. 4757–4767, 2010. [10] M. A. Ribeiro, D. E. Stasiw, P. Pattison, P. R. Raithby, D. A. Shultz, and C. B. Pinheiro, "Toward Controlling the Solid State Valence Tautomeric Interconversion Character by Solvation," Cryst. Growth Des., vol. 16, no. 4, pp. 2385–2393, Apr. 2016. [11] G. Poneti et al., "Soft-X-ray-Induced Redox Isomerism in a Cobalt Dioxolene Complex," Angew. Chem. Int. Ed., vol. 49, no. 11, pp. 1954–1957, Mar. 2010. [12] T. M. Francisco et al., "Hard X-ray-Induced Valence Tautomeric Interconversion in Cobalt-o-Dioxolene Complexes," J. Phys. Chem. Lett., vol. 8, no. 19, pp. 4774–4778, Oct. 2017. [13] G. Poneti et al., "X-ray Absorption Spectroscopy as a Probe of Photo- and Thermally Induced Valence Tautomeric Transition in a 1:1 Cobalt–Dioxolene Complex," ChemPhysChem, vol. 10, no. 12, pp. 2090–2095, 2009. [14] J. A. van Bokhoven and C. Lamberti, X-Ray Absorption and X-Ray Emission Spectroscopy: Theory and Applications. John Wiley & Sons, 2016. [15] A. Bordage, V. Trannoy, O. Proux, H. Vitoux, R. Moulin, and A. Bleuzen, "In situ site-selective transition metal K-edge XAS: a powerful probe of the transformation of mixed-valence compounds," Phys. Chem. Chem. Phys., vol. 17, no. 26, pp. 17260–17265, 2015. [16] O. Sato, S. Hayami, Z. Gu, K. Seki, R. Nakajima, and A. Fujishima, "Photo-Induced Long-Lived Intramolecular Electron Transfer in a Co Valence Tautomeric Complex," Chem. Lett., vol. 30, no. 9, pp. 874–875, 2001. [17] R. D. Schmidt, D. A. Shultz, and J. D. Martin, "Magnetic Bistability in a Cobalt Bis(dioxolene) Complex: Long-Lived Photoinduced Valence Tautomerism," Inorg. Chem., vol. 49, no. 7, pp. 3162–3168, Apr. 2010. [18] B. Ravel and M. Newville, "ATHENA, ARTEMIS, HEPHAESTUS: data analysis for X-ray absorption spectroscopy using IFEFFIT," J. Synchrotron Radiat., vol. 12, no. 4, pp. 537–541, Jul. 2005.

7.3.4 Swiss Light Source

The following proposal has been submitted to the Swiss Light Source in March, 2021, aiming for XAS experiments of solutions of the Co(SQ)(Cat)(Py)$_2$ complex. The proposal has been accepted and experiments will be scheduled for the second semester of 2021.

Solvent dependent X-ray spectroscopy of Co($diox$)$_2$Py$_2$

Goal of the experiment

We aim to acquire cobalt K-edge X-ray absorption spectra and Kβ X-ray emission spectra of solutions of the Co($diox$)$_2$Py$_2$ complex to investigate the subtle effects modulating the electronic structure, and consequently the valence tautomerism (VT) effect as a function of different solvents. More specifically, we will get further insight into the electronic states of this complex in solution and on the VT as a function of solvent. We intend to evaluate the impact of the environment polarity in the electronic state of the cobalt complex by changing the solvent from pyridine to n-hexane and using mixtures of those in varying ratios. The data acquired in this proposed experiment will be correlated with quantum chemical calculations and will serve as reference for posterior pump-probe experiments, in which the dynamics of the VT as a function of solvent will also be investigated.

Background

Electronic bistability is an intriguing property which is the basis for molecular electronic devices. It is a property of materials from which electronic structures depend on external factors. The valence tautomerism (VT) is a form of electronic bistability involving metal atoms and electroactive ligands consisting of the simultaneous change of the metal spin state and a ligand to metal charge transfer 1,2. From all the materials reported to display VT, Cobalt o-dioxolene molecules have been extensively investigated when coordinated to nitrogen based ancillary ligands3–5. Such molecules switch from ls-CoIII to hs-CoII (ls: low spin, hs: high spin) as a function of temperature,3 visible light,5 soft and hard X-ray irradiation.6 Their VT can present itself in solution and in solid state as single crystals in a reversible fashion. VT in these compounds is known to be modulated by the ancillary lig-and, highly dependent on the solid state arrangement of the complexes and on crystal solvation.7–10

In our recent work, we focused our studies on the cobalt o-dioxolene complex with pyri-dine as ancillary ligand: Co($diox$)$_2$Py$_2$, where diox = SQ (3,5-di-tert-butyl-semiquinonate) or Cat (3,5-di-tert-butyl-cathecolate); and Py = pyridine. This complex has its VT com-pletely modulated by the crystal lattice and solvation. Co($diox$)$_2$Py$_2$ does not display VT in its non-solvated crystal form (1) 7, however it displays temperature and light induced va-lence tautomerism in one of the two molecules that compose its asymmetric unit of a pyr-idine solvated crystal with 2:1 complex/Py ratio (2) 11. The reason why the solvent present in the crystal lattice allows for the VT interconversion in only specific sites of the crystal has been solely attributed to the crystal environment11. However, our recent experimental results have strongly suggested that, even more than the crystal lattice itself, the polarity of the surroundings determines the oxidation

and spin state accessed by such complex. An accurate description of the VT effect including the influence of solvents has never been reported.

Electronic paramagnetic resonance (EPR) of Co(*diox*)$_2$Py$_2$ in solutions of pyridine and n- at room temperature show that the complex adopts the hs-CoII(SQ)(Cat)Py2 form when dissolved in the apolar n-hexanes, and the ls-CoIII(SQ)(Cat)Py2 form when dis-solved in polar pyridine (Figure 1). These results clearly point to the influence of the sol-vent on the accessibility of the ls-CoIII and hs-CoII energy levels.
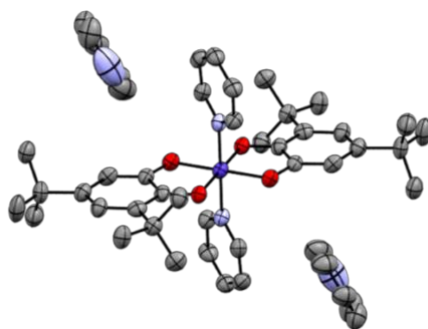
Figure 1 – structure of the solvated crystal (3). The asymmetric unit is displayed with one ls-Co^{III}(SQ)(Cat)Py$_2$ complex and two pyridines. C are displayed in gray, O in red, N in light blue and Co in dark blue.

Moreover, a new pyridine solvated Co(*diox*)$_2$Py$_2$ crystal, with a 2:1 pyridine/complex ratio (3) (Figure 2), was crystallized and characterized with single crystal X-ray diffraction ex-periments (SCXRD). Besides having the same disposition of metallic sites as crystal 2, the temperature dependent SCXRD showed that such crystal does not present the tem-perature-induced VT, supporting the idea that the pyridine rich environment traps the complex in the ls-CoIII state.

X-ray absorption (XAS) and X-ray emission (XES) spectroscopies are the ideal experi-ment to probe the electronic structure of the metal center in the Co(*diox*)$_2$Py$_2$ complex in solution as a function of the solvent. In the K pre-edge absorption features, the electronic occupation of electronic orbitals can be determined for different polar/apolar solvent rati-os and the geometry around the metal center in solution can be properly addressed in the EXAFS range. The Kβ XES lines provide the needed spin sensitivity (as they arise from different final state spin multiplets), thus providing extra electronic structure infor-mation which will help to elucidate the solvent influence in stabilizing a certain electronic configuration and the VT effect. Additional Co Kβ resonant XES (RXES) should provide unequivocal characterization of the local charge and spin-configuration of Co(*diox*)$_2$Py$_2$ compounds in different solvents, while allowing for disentangling covalency effects as recently pioneered by DeBeer, *et al.* 12.
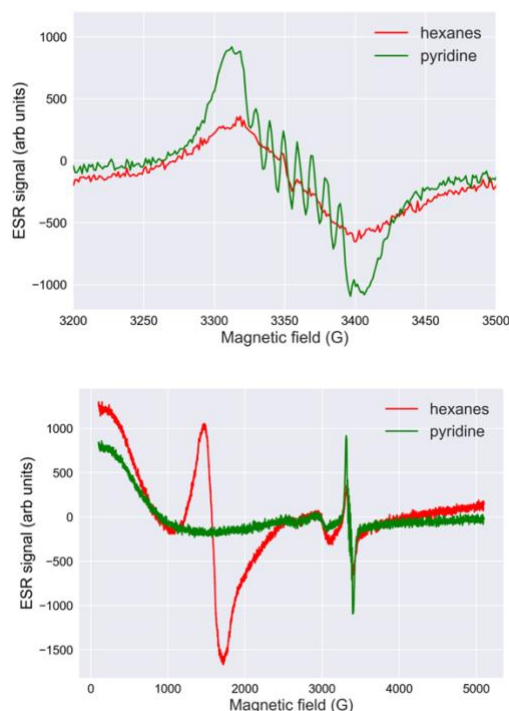
Figure 2 - EPR spectra for the Co(diox)$_2$Py$_2$ complex in pyridine and n-hexanes. (a) zoom in the EPR signal of the free radical of the molecule, centered at 3350 G (b) full range EPR spectra for both solutions.

C) Experimental method; specific requirements

The experiment consists in the acquisition of Co K-edge (total range of interest: 7690 to 7840 eV) XAS, while simultaneously measuring the Kβ XES of solutions of Co(*diox*)$_2$Py$_2$ in different hexanes:pyridine concentrations (0:5, 1:4, 2:3, 3:2, 4:1, 5:0). All measure-ments will be conducted at room temperature. The XAS will be detected in total fluores-cence yield (TFY) mode and the Kβ XES will be measured using the dispersive von Hamos spectrometer using Ge(111) analyzers at a Bragg angle of about 82o. The reso-nant XES measurements will be conducted simultaneously to the XAS, profiting from the dispersive character of the von Hamos spectrometer at SuperXAS. The non-resonant XES will be done by simply setting the incoming energy well above the Co K-edge and integrating the signal to obtain good statistics. If available, a Si(3111) monochromator should be used to provide better energy resolution around the pre-edge regions in the XAS and RXES spectra.

The sample will be held by a quartz capillary and circulated to avoid radiation damage (sample concentration and radiation stability tests are being carried out). The flow path will be closed to keep solvent from evaporating.

Results expected

The XAS spectra is expected to show characteristic hs-CoII and ls-CoIII features in the pre-edge region for the solutions of pure n-hexanes and pure pyridine, respectively, and these will be used as reference for the subsequent experiments. The improved resolution obtained by the use of a Si(311) monochromator should allow a detection of resulting subtle changes in the pre-edge features. An evolution from ls-CoIII to hs-CoII is expected to be observed as a function of

the hexanes:pyridine ratio (1:4, 2:3, 3:2, 4:1). In such, we expect to observe a convolution of the reference XAS spectra. The Co Kβ should show clear signatures of the spin characteristics, while at the same time, indicating the influ-ence of solvation, similarly as recently reported for a series of iron compounds 13. Part of our analysis will make use of temperature dependent XAS for another tautomer cobalt complex with a detailed study of the pre-edge features 14 as reference (Figure 3), com-bined with state-of-the-art quantum chemical calculations.
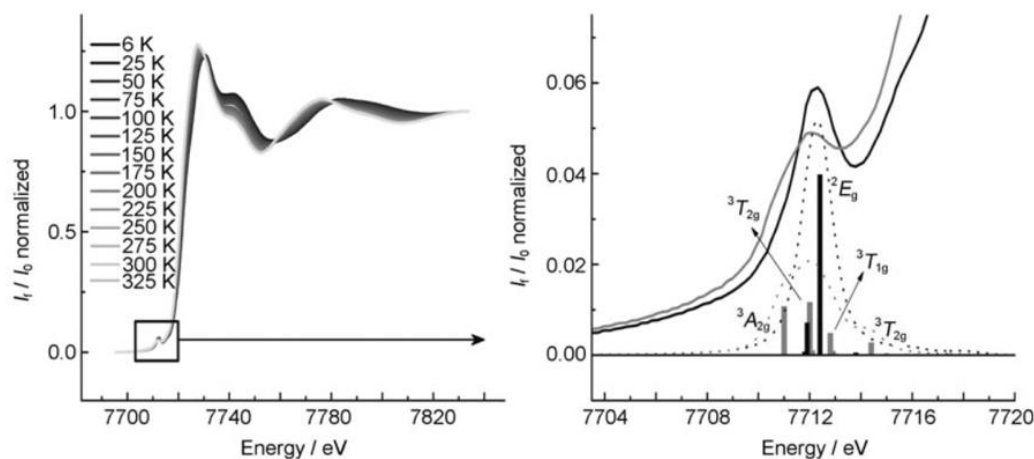
Figure 3 – Left: temperature dependent XAS results for a Cobalt dioxolene complex. On the right, the pre-edge features at 6 K (solid black line) and 325 K (solid grey line) are zoomed in and the contribution and the corresponding calculated pre-edge features (dotted black line for CoIII and dotted grey line for CoII) are shown.

Estimate and justification of the beamtime

We estimate our experiments can be performed in 4 days, totalizing 12 shifts of 8 hours each. Both the XAS and XES experiments proposed here can only be performed in a synchrotron light source, and the SuperXAS beamline is the best suited for our purposes given its energy range, flux and the presence of a dispersive von Hamos spectrometer.

References relevant to the experiment description

1. Shultz, D. A. Valence tautomerism in dioxolene complexes of cobalt. Magnetism: Molecules to Materials II: Models and Experiments 281–306 (2001). 2. Pierpont, C. G. Studies on charge distribution and valence tautomerism in transition metal complexes of catecholate and semiquinonate ligands. Coordination Chemistry Reviews 216, 99–125 (2001). 3. Tezgerevska, T., Alley, K. G. & Boskovic, C. Valence tautomerism in metal complexes: Stimulated and reversible intramolecular electron transfer between metal centers and organic ligands. Coordination Chemistry Reviews 268, 23–40 (2014).4. Dei, A. & Sorace, L. Cobalt-Dioxolene Redox Isomers: Potential Spintronic Devices. Applied Magnetic Resonance 38, 139 (2010). 5. Sato, O., Cui, A., Matsuda, R., Tao, J. & Hayami, S. Photo-induced Valence Tautomer-ism in Co Complexes. Accounts of Chemical Research 40, 361–369 (2007). 6. Francisco, T. M. et al. Hard X-ray-Induced Valence Tautomeric Interconversion in Co-balt-o-Dioxolene Complexes. J Phys
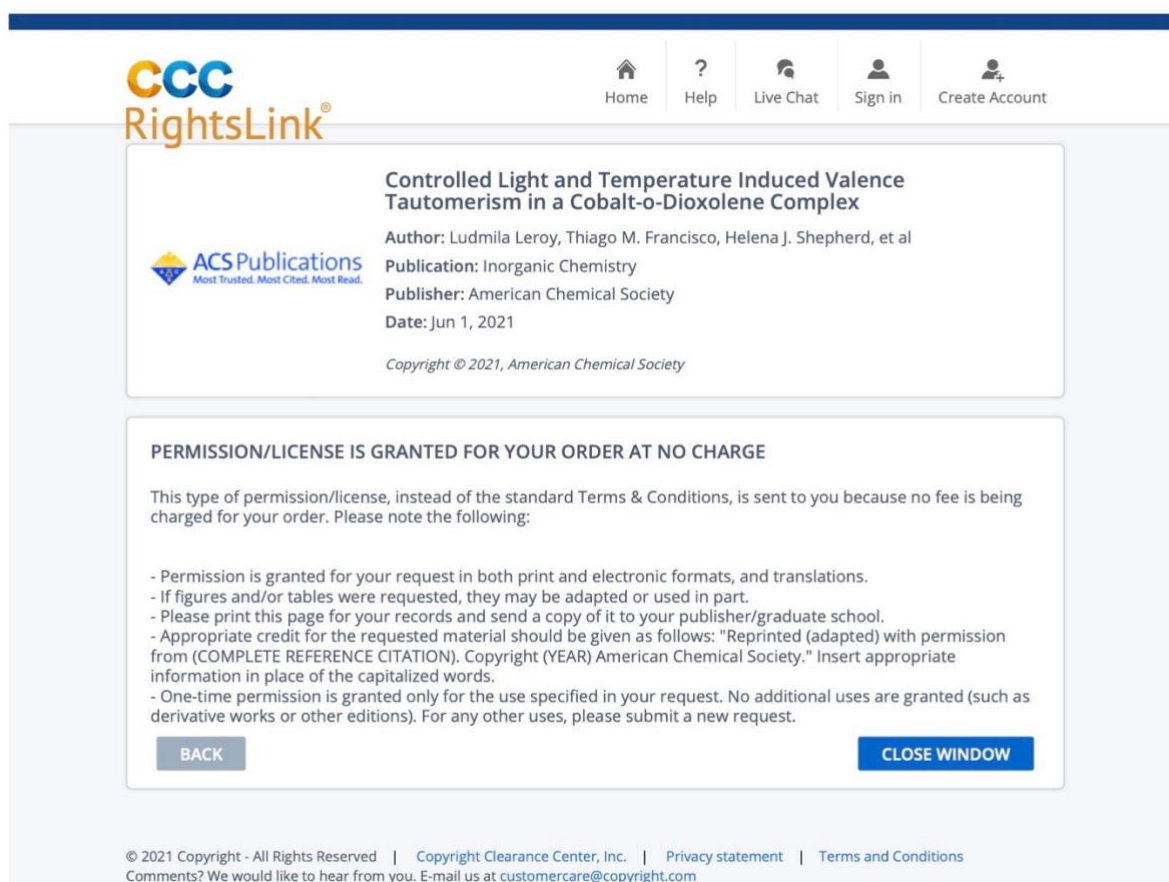
Chem Lett 8, 4774–4778 (2017). 7. Schmidt, R. D., Shultz, D. A., Martin, J. D. & Boyle, P. D. Goldilocks Effect in Magnetic Bistability: Remote Substituent Modulation and Lattice Control of Photoinduced Va-lence Tautomerism and Light-Induced Thermal Hysteresis. Journal of the American Chemical Society 132, 6261–6273 (2010). 8. Witt, A., Heinemann, F. W., Sproules, S. & Khusniyarov, M. M. Modulation of Magnetic Properties at Room Temperature: Coordination-Induced Valence Tautomerism in a Cobalt Dioxolene Complex. Chem. Eur. J. 20, 11149–11162 (2014). 9. Ribeiro, M. A. et al. Towards Controlling the Solid State Valence Tautomer In-terconversion Character by Solvation. Crystal Growth & Design 16, 2385–2393 (2016). 10. Evangelio, E. et al. Solvent effects on valence tautomerism: A comparison between the interconversion in solution and solid state. Solid State Sciences 11, 793–800 (2009). 11. Mulyana, Y. et al. Solvation effects on the valence tautomeric transition of a cobalt complex in the solid state. Dalton Transactions 39, 4757 (2010). 12. DeBeer, S., Castillo, R. G., Hahn, A. W., Kuiken, B. E. V. & Henthorn, J. T. Probing physical oxidation state via resonant X-ray emission spectroscopy: Applications to iron model complexes and nitrogenase. Angewandte Chemie International Edition n/a,. 13. Lafuerza, S., Carlantuono, A., Retegan, M. & Glatzel, P. Chemical Sensitivity of Kβ and Kα X-ray Emission from a Systematic Investigation of Iron Compounds. Inorg. Chem. 59, 12518–12535 (2020). 14. Poneti, G. et al. X-ray Absorption Spectroscopy as a Probe of Photo- and Thermally Induced Valence Tautomeric Transition in a 1:1 Cobalt-Dioxolene Complex. Chem-PhysChem 10, 2090–2095 (2009).

7.4 Publication

7.4.1 Copyright permission for 50% or more reproduction of the paper on thesis or dissertation granted to the author by the American Chemistry Society.

7.4.2 Published article

Article

Controlled Light and Temperature Induced Valence Tautomerism in a Cobalt-o-Dioxolene Complex

Ludmila Leroy, Thiago M. Francisco, Helena J. Shepherd, Mark R. Warren, Lucy K. Saunders, David A. Shultz, Paul R. Raithby, and Carlos B. Pinheiro*

Cite This: https://doi.org/10.1021/acs.inorgchem.1c00638

Read Online

ACCESS | Metrics & More | Article Recommendations | Supporting Information

ABSTRACT: The mononuclear cobalt complex of 3,5-di-*tert*-butylcatecholate and cyan-pyridine $(Co(diox)_2(4\text{-CN-py})_2)$ is a very versatile compound that displays valence tautomerism (VT) in the solid state, which is induced by temperature, light, and hard X-rays, and modulated by solvent in the crystal lattice. In our work, we used single crystal X-ray diffraction as a probe for the light-induced VT in solid state and demonstrate the controlled use of hard X-rays via attenuation to avoid X-ray-induced VT interconversion. We report photoinduced VT in benzene solvated crystals of $Co(diox)_2(4\text{-CN-py})_2$ illuminated with blue 450 nm light at 30 K with a very high yield (80%) of metastable *hs*-Co^{II} states, and we also show evidence of the de-excitation of these photoinduced metastable states using red 660 nm light. Such high-yield light-induced VT had never been experimentally observed in molecular crystals of cobalt tautomers, proving that the 450 nm light illumination is triggering a chain of events that leads to the *ls*-Co^{III} to *hs*-Co^{II} interconversion.
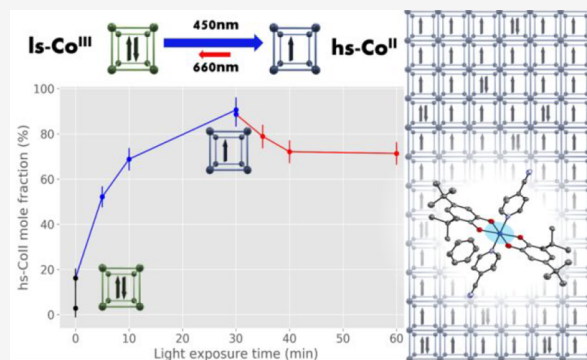
1. INTRODUCTION

Smart materials are those designed to respond to mechanical, chemical, electric, or magnetic stimuli from the surrounding environment having one or more of their properties significantly changed in a controlled manner. Among these materials, those that present electronic bistability in the form of spin-crossover[1] (SC) or valence tautomerism[2] (VT) can be used potentially as sensors, signal processors, and information storage devices, for they can readily switch between two spin and/or electronic states.[3−5] Of particular interest are the solid-state materials composed of molecules that present valence tautomerism at a single metal center or within a molecular complex without substantial disruption of the solid-state structure.[6,5,7]

Generally, the investigation of materials presenting VT is focused on the metal ions and the associated ligands that act as charge donors. In such materials, the VT process is accompanied by changes in structural, electronic, and thermodynamic properties and can therefore be characterized with a number of experimental approaches and theoretical calculations. Of particular significance is the understanding of the effects of the variation of external factors on the VT properties and dynamics. It has been established that the symmetry of the environment, the nature of the ligands associated with the metal center, the presence and nature of solvate molecules and counterions,[7−11] as well as temperature,[12] pressure,[13] illumination,[5] magnetic and electric

fields,[14] and irradiation[5,15,16] will affect the VT process. The yield and rate of intramolecular electron transfer, the lifetime of induced metastable states, and the stability of high-spin (*hs*) and low-spin (*ls*) states are some of the important properties that can be modulated and controlled by external stimuli.

Complexes that display VT are composed of a transition metal ion center, organic redox-active ligands that act as charge donors/acceptors, and organic ancillary ligands. Such complexes form solids in which intermolecular interactions extend over the lattice in one, two, or three dimensions. Of the materials that present VT in the solid-state, the family of complexes with a cobalt metal center, dioxolene molecules that act as redox-active ligands, and nitrogen-based ancillary ligands have been thoroughly studied in the past decades.[7] These compounds undergo the reversible valence and spin interconversion from *ls*-Co^{III}(SQ$^{\bullet-}$)(Cat^{2-})R to *hs*-Co^{II}(SQ$^{\bullet-}$)$_2$R (*ls*: low spin, *hs*: high-spin; SQ$^{\bullet-}$: semiquinone; Cat^{2-}: catecholate; R: 2 monodentate or 1 bidentate nitrogen based ligand). The interconversion is accompanied by a couple of reversible structural changes[9,16] that reflect the change of the

electronic population of the metal and ligand orbitals. In particular, the isotropic contraction/expansion of the Co−L (L = O, N atoms) coordination sphere has been shown to be systematic in such a way that the interatomic distances between the cobalt atom and its first neighboring atoms (the O atoms from the dioxolene and the N atoms from the ancillary ligand) can be used to compute the molar fraction of hs-Co^{II} and ls-Co^{III} within a crystal. Alternatively, the distances between the atoms of the redox-active ligand can also be used to compute the empirical "metrical oxidation state" (MOS), which gives a continuous measure of the apparent oxidation state of the ligand.[17] The values of all atomic distances within the complexes can be easily assessed through single-crystal X-ray diffraction experiments.

Within the family of cobalt complexes that present VT, the octahedral cobalt with two 4-cyan-pyridine (4-CN-py) molecules as ancillary ligands and two 3,5-di-*tert*-butyl-semiquinonate/catecholate as redox active ligands in trans configuration is a very versatile compound (named Co-($diox$)$_2$(4-CN-py)$_2$ from here on, where $diox$ is 3,5-di-*tert*-butyl-semiquinonate/catecholate). Its valence tautomerism has been shown to be controllable, being induced by temperature,[12] visible light irradiation,[18] and hard X-rays,[16] and modulated by the absence or presence of solvent in the crystal lattice.[8,9] This complex was demonstrated to behave similarly to light-induced excited-state spin trapping (LIESST) complexes for its highly stable photogenerated hs-Co^{II} form at temperatures lower than 50 K.[18] The stability of such excited states is believed to be due to lattice stabilization through hydrogen bonds.[9] However, the photoconversion induced by white light was shown to be inefficient (30% yield), even though the wide spectrum of the white light seemed to have allowed for a higher interconversion rate in comparison to monochromatic laser illumination.[18] The electronic absorption spectrum of the Co^{II}($diox$)$_2$(4-CN-py)$_2$ cast as dilute polystyrene films has also been reported,[12] and its metal to ligand charge transfer (MLCT) band is centered approximately at 740 nm (13 500 cm^{-1}) and ranges from 500 to 1000 nm (20 000 cm^{-1} to 10 000 cm^{-1}). Co($diox$)$_2$ complexes with different ancillary ligands have been shown to display MLCT bands near 800 nm (12 500 cm^{-1}) and ligand to metal charge transfer (LMCT) transitions between 525 and 665 nm (15 000 cm^{-1} to 19 000 cm^{-1}).[19−23] Subsequent research showed that the photointerconversion yield can be as high as 100% when the sample is irradiated with hard X-rays (25.5 keV).[16] The underlying process, named hard-X-ray-induced excited-spin-state trapping (HAXIESST), and the electronic dynamics involved are not yet understood.

In the present work, we continue to investigate the VT interconversion in benzene solvated Co($diox$)$_2$(4-CN-py)$_2$ crystals, and we demonstrate the photogeneration of metastable hs-Co^{II} centers from ls-Co^{III} centers at 30 K with 80% yield using 450 nm blue light (22 222 cm^{-1}). We also present evidence for the reverse de-excitation using 660 nm red light (15 151.5 cm^{-1}).

2. EXPERIMENTAL SECTION

2.1. Crystallization. The synthesis of Co($diox$)$_2$(4-CN-py)$_2$ followed the procedures reported previously.[18] Benzene solvated crystals were grown by slow evaporation of benzene under a N$_2$ atmosphere.[9] The procedures afforded dark blue needle crystals suitable for X-ray diffraction experiments.

2.2. Single-Crystal X-ray Diffraction Data Collection. The benzene solvated crystals were submitted to single-crystal X-ray diffraction (SCXRD) experiments at the I19-2 beamline of the Diamond Light Source (Oxfordshire, UK), using 25.5 keV X-rays and multiple attenuation values for the 200 μm × 200 μm beam. Samples were manually mounted on MiTeGen UV mounts in copper magnetic bases. Light-induced VT was probed in samples kept at 30 K; temperature-induced VT was probed from 30 to 300 K. All low-temperature SCXRD measurements had samples cooled using an open flow He cryostat (nHeliX, Oxford Cryosystems). Sample illumination was achieved using blue (450 nm) and red (660 nm) light from laser diodes (L450P1600MM and L660P120, ThorLabs, see Table S6 and Figure S8 of the Supporting Information). Homogenous illumination of the samples was possible using an in-house built illumination ring that was placed around the low-temperature device nozzle. The hutch lights were kept off for all the experiments, and during the SCXRD experiments, the diodes were turned off.

SCXRD data processing was performed using XDS[24] structure solution and structure refinement using SHELXT[25] and SHELXL,[26] respectively, with the aid of python scripts (available upon request) that automatically run XDS and SHELXL sequentially for all data sets. The retrieval and analysis of quality indicators of data processing and refinement were also made using python scripts.

SCXRD data and structure refinement statistics for all the crystals used in this work at 30 K are reported in Table S2 of the Supporting Information. I/sigma, cc1/2, and r1 parameter evolution for each experiment as a function of temperature and irradiation time are reported in Figures S1, S2, and S3 of the Supporting Information.

2.3. hs-Co^{II} Molar Fraction Calculation. The molar fraction of the cobalt centers with different oxidation states were computed following the equations proposed by Ribeiro et al.[9]

$$\gamma(hs\text{-}Co^{II})_L = (D_{exp}^{Co\text{-}L} - D_{Co^{III}}^{Co\text{-}L})/(D_{Co^{II}}^{Co\text{-}L} - D_{Co^{III}}^{Co\text{-}L}) \tag{1}$$

$$\gamma(hs\text{-}Co^{II}) = \frac{1}{3}\sum_L \gamma(hs\text{-}Co^{II})_L \tag{2}$$

where L denotes the atoms in the first coordination sphere of the cobalt center, $D^{Co\text{-}L}$ stands for the atomic distance between Co and L, and the subscripts denote the experimental value (exp) and the standard distances for both oxidation states of Co (Co^{II} and Co^{III}) averaged from distances surveyed in the Cambridge Structural Database (CSD)[27] and indicated in Table 1. The error for the calculated values of hs-Co^{II} was evaluated by the partial derivatives method.

Table 1. Reference Co−N and Co−O Distances Surveyed from CIF files 1559584−1559598 at the CCDC Databank

$D_{Co^{III}}^{Co\text{-}N} = 1.940(16)$ Å	$D_{Co^{II}}^{Co\text{-}N} = 2.151(7)$ Å
$D_{Co^{III}}^{Co\text{-}O1} = 1.889(6)$ Å	$D_{Co^{II}}^{Co\text{-}O1} = 2.060(5)$ Å
$D_{Co^{III}}^{Co\text{-}O2} = 1.872(12)$ Å	$D_{Co^{II}}^{Co\text{-}O2} = 2.045(2)$ Å

The MOS for the redox-active ligand was also computed using the method developed by Brown, 2012,[17] in order to corroborate with the hs-Co^{II} molar fraction calculation results (Section 3, Supporting Information).

3. RESULTS AND DISCUSSION

3.1. Structure Description. The [Co($diox$)$_2$(4-CN-py)$_2$]·benzene crystallizes in the monoclinic space group P2$_1$/c, with two Co($diox$)$_2$(4-CN-py)$_2$ molecules in the unit cell (Z = 2). The Co atom sits on a crystallographic center of symmetry, with one $diox$, one 4-CN-py ligand, and one benzene solvent molecule in the asymmetric unit. Because of the symmetry requirement, there is only one unique $diox$ ligand so that in the high-spin state of the complex the resultant SQ$^{•−}$ and/or Cat$^{2−}$

forms are superimposed. Therefore, X-ray diffraction technique affords only an average of the $SQ^{\bullet-}$ and/or Cat^{2-} forms in the $ls\text{-}[Co^{III}(SQ^{\bullet-})(Cat^{2-})]$ isomer. Figure 1 shows the molecular structure of the complex in a benzene solvated crystal at 30 K, solved by SCXRD.

Figure 1. Molecular structure of benzene solvated $Co(diox)_2(4\text{-CN-}py)_2$ crystal at 30 K. Atom colors: Co (dark blue), C (gray), N (light blue), and O (red). Hydrogens are hidden for clarity purposes.

3.2. X-ray Induced VT.

The valence tautomeric interconversion of $Co(diox)_2(4\text{-CN-py})_2$ can be induced by X-ray irradiation of the benzene solvated crystals at low temperatures, though the yield of $hs\text{-}Co^{II}$ photogeneration has been shown to be highly dependent on the incident X-ray flux.[16] This property has to be observed and controlled in order to ensure minimal interference of the X-ray irradiation when probing the VT induced by visible light illumination in SCXRD experiments. Initial SCXRD experiments were then used to probe the electronic state of the metallic center when the crystals were under hard X-ray (25.5 keV) irradiation. The estimation of the molar fraction $\gamma(hs\text{-}Co^{II})$ of $hs\text{-}Co^{II}$ states within the crystal was done based on the Co–L distances (L = O1, O2, and N) using eqs 1 and 2.

The evaluation of the molar fraction of X-ray induced $hs\text{-}Co^{II}$ in the crystal as a function of X-ray exposure time was achieved with multiple sequential SCXRD measurements performed on the same crystal at 30 K for 0.25 and 0.6 transmission (runs 1, 2, 3, 4, 5, and 6, 7, respectively; see Table S1 of the Supporting Information) of the X-ray beam. SCXRD data sets were acquired sequentially except for the fifth data set obtained after 30 min of irradiation by the nonattenuated X-ray beam (Figure 2). No rotation of the crystal was performed when full transmission of the beam was used, leading to a lower X-ray induced VT interconversion when compared to the rotating sample exposed to 0.25 and 0.6 beam transmission. The crystal information and crystallographic quality indicators of these experiments are shown in Table S1 of the Supporting Information.
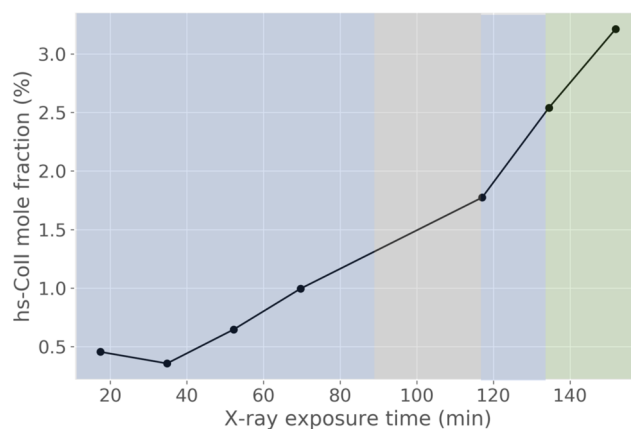
Figure 2. Molar fraction of $hs\text{-}Co^{II}$ species induced by X-ray irradiation during SCXRD experiments with the $[Co(diox)_2(4\text{-CN-}py)_2)]\cdot$benzene crystal at 30 K. The blue, gray, and green shaded regions correspond, respectively, to time intervals in which the crystal was exposed to 0.25, 1, and 0.6 transmission of the X-ray beam.

Figure 2 shows the calculated Co^{II} molar fraction as a function of X-ray irradiation time. The results revealed that for that specific beamline and for a crystal with dimensions of 100 μm × 50 μm × 50 μm, the $hs\text{-}Co^{II}$ molar fraction induced by X-ray irradiation was smaller than 3%, even for full beam transmission. In experiments 6 and 7, the molar fraction of metastable $hs\text{-}Co^{II}$ seems to grow faster than in the 5 previous experiments, and this is likely to be due to the exposure to high X-ray intensity during the SCXRD data collection. Nevertheless, only 3% of the metastable molar fraction was induced after the entire 140 min of hard X-ray irradiation. The average error for the calculated molar fraction was calculated to be 4%, which is already larger than the values observed. Using a conservative approach for subsequent experiments, the attenuation of the X-ray beam was chosen to ensure negligible X-ray VT conversion, in which $\gamma(hs\text{-}Co^{II})$ is smaller than 1% after 60 min of X-ray exposure. As expected, the calculated MOS of the dioxolene ligands corroborate with the change in the oxidation state of the Co calculated solely by Co–L (L = O1, O2, and N) interatomic distances (Figure S5).

3.3. Blue-Light-Induced VT.

Crystals of the nonsolvated $Co(diox)_2(4\text{-CN-py})_2$ have been shown to display light-induced valence tautomerism VT by Schmidt et al.[18] In that work, samples were kept at 10 K and illuminated with white light (from 450 to 850 nm, no spectrum shape is reported), and the presence of $hs\text{-}Co^{II}$ was monitored through magnetic susceptibility measurements. A photostationary limit for the metastable $hs\text{-}Co^{II}$ redox isomer conversion was never achieved, as the value of the magnetic susceptibility continued to grow (albeit at a very slow rate) even after 12 h of illumination, with maximum conversion percentages approaching 30%. Later, Francisco et al.[16] showed that more than 80% conversion to the metastable $hs\text{-}Co^{II}$ form at 30 K in solvated crystals is possible using nonattenuated hard X-rays, without any disruption of the crystal lattice or loss in crystal quality after recuperation of initial states. This last result proved that the crystal lattice does allow for the full VT interconversion. Moreover, it is known that the VT interconversion for certain Co complexes can be induced both ways, from $ls\text{-}Co^{III}$ to $hs\text{-}Co^{II}$ and vice versa, using different excitation and de-excitation wavelengths.[9] Therefore, it could be that for the $Co(diox)_2(4\text{-CN-py})_2$ crystal, in the work of Schmidt et al., both excitation
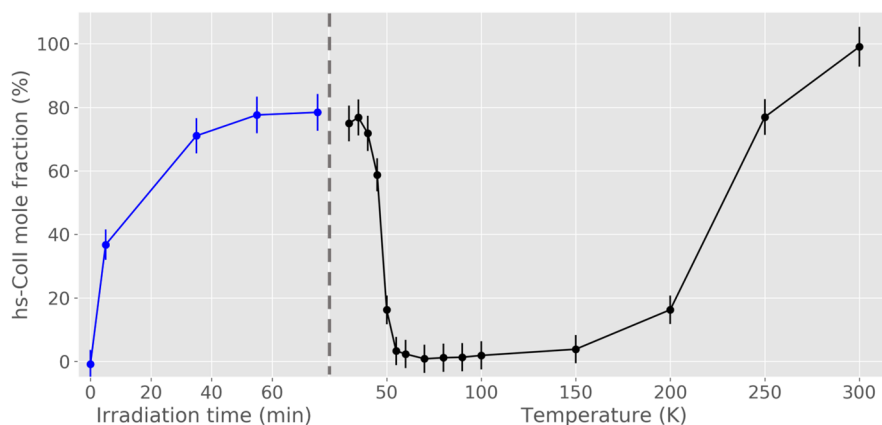
Figure 3. Molar fraction of hs-Co^{II} species in the [Co($diox$)$_2$(4-CN-py)$_2$)]·benzene crystal when exposed to blue 450 nm illumination (blue points) at 30 K and to an increase in temperature from 30 to 300 K (black points).

and de-excitation wavelengths were contained within the wide spectrum used, and concomitant excitation de-excitation processes limited the VT interconversion rate.[18]

In order to test such hypothesis, in this work, a benzene solvated crystal with dimensions of 300 μm × 100 μm × 100 μm was mounted, cooled down to 30 K, and illuminated with blue 450 nm laser diode light while being rotated with respect to the diode array using the goniometer. SCXRD data sets were acquired with 5% transmission of X-rays for 0, 5, 35, 55, and 75 min of LED illumination. The respective crystal structures were solved, and the metastable hs-Co^{II} molar fractions were calculated. Figure 3 shows that after 55 min of light illumination, an 80% metastable hs-Co^{II} conversion yield plateau is reached. This limit could be related to the penetration depth of the blue light through the crystal. The electronic absorption spectrum of the Co^{III}($diox$)$_2$(4-CN-py)$_2$ complex was supposed to have its LMCT centered approximately at 550 nm ($\sim$18 181 cm^{-1}).[20,22,23] The 450 nm (22 222 cm^{-1}) blue light used herein would lie in a low absorption cross-section region of the electronic absorption spectrum of the Co($diox$)$_2$(4-CN-py)$_2$ molecule. However, wavelengths lying in the edge of the LMCT band (<500 nm) have been reported to induce the VT in cobalt complexes via charge transfer, intersystem crossing, and vibrational relaxation,[23,28,29] but have also been assigned to d–d transitions for ls-Co^{III}.[22,30−33] In our experiments, 450 nm blue light irradiation at 30 K led to the highest ($\sim$80%) yield of photoinduced hs-Co^{II} interconversion observed in a Co($diox$)$_2$ complex in the solid state.

After the plateau was reached, the illumination was turned off, and a temperature-dependent sequence of SCXRD experiments shows the full recovery of ls-Co^{III} states (approximately 0% hs-Co^{II} molar fraction between 55 and 90 K) and the subsequent well-known second order (non-cooperative) VT interconversion in the characteristic temperature range of 150−230 K. At 300 K, 100% of the unit cells have units of the complex in the hs-Co^{II} state. After reaching room temperature, the crystal was again cooled to 30 K, and the SCXRD shows that the quality of the crystal is also recovered after all the interconversion cycles (Table S2, run 21). As expected, the calculated MOS of the dioxolene ligands corroborate with the change in the oxidation state of the Co calculated solely by Co−L (L = O1, O2, and N) interatomic distances (Figure S6).

The evolution of the data statistics and structural refinement quality indictors as a function of light illumination time and temperature indicates that the illumination does no more damage to the crystal than the increase in temperature (Figure S1), demonstrating the robustness of such material as a solid-state tautomer.

3.4. Red-Light-Induced VT. The high photoconversion yield of 450 nm blue light illumination observed in our experiment reinforces the belief that the broad white light spectrum used by Schmidt et al.[18] also contains the metastable state de-excitation wavelengths, limiting the observed interconversion yield. To test the hypothesis, a 660 nm laser diode was used to illuminate another benzene solvated crystal (80 μm × 40 μm × 40 μm) of Co($diox$)$_2$(4-CN-py)$_2$ at 30 K, which was submitted first to blue 450 nm light irradiation, to achieve the high-spin states, and to SCXRD experiments with 40% X-ray transmission. The higher transmission was necessary for sharper and more intense SCXRD images, because the crystal was substantially smaller than the ones previously used. Initially, sequential dark measurements were taken to establish the baseline for the X-ray induced interconversion. After that, the blue 450 nm laser diode was turned on and used to illuminate the rotating sample. SCXRD experiments were performed after set intervals of light irradiation (5, 10, and 30 min). Two data sets were sequentially collected after 30 min of blue light irradiation, and immediately after that, the red 660 nm laser diode was turned on to irradiate the rotating crystal. The SCXRD data sets were acquired after 5, 10, and 20 min of red-light irradiation.

The calculated hs-Co^{II} molar fraction for the solvated Co($diox$)$_2$(4-CN-py)$_2$ crystal structure under illumination in the described experimental sequence is shown in Figure 4. The X-rays induced around 16.22% ± 0.05% of metastable hs-Co^{II} even before the blue 450 nm irradiation, though the blue light lifted the interconversion yield to 90.60% ± 0.05% after 30 min of irradiation. The subsequent, partial de-excitation of the complexes is observed when the crystal is irradiated with the red 660 nm laser diode light. A decrease in the hs-Co^{II} molar fraction is observed until it reaches a plateau of 72.12% ± 0.05%. As expected, the calculated MOS of the dioxolene ligands corroborate with the change in the oxidation state of the Co calculated solely by Co−L (L = O1, O2, and N) interatomic distances (Figure S7).
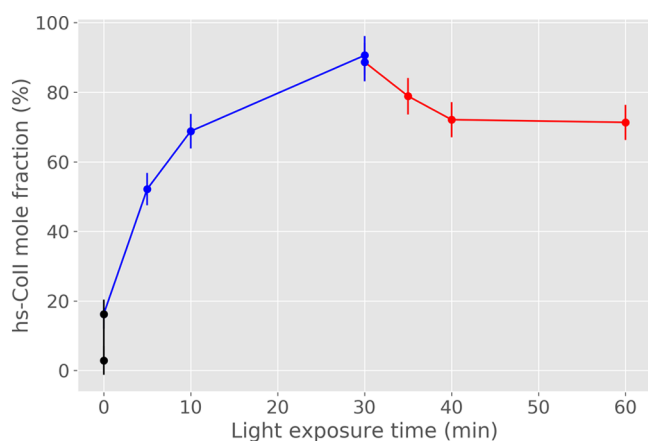
Figure 4. Molar fraction of *hs*-Co[II] species induced by X-rays (black dots), blue 450 nm light (blue dots), and red 660 nm light (red dots) as a function of irradiation time for the [Co(*diox*)$_2$(4-CN-py)$_2$)]·benzene crystal at 30 K.

The 660 nm (15 151 cm^{-1}) light lies on the MLCT transfer band region of the electronic spectra of Co[II](*diox*)$_2$ complexes and would be expected to induce the charge transfer.[12,19,21−23,31] However, its lower efficiency in inducing the VT could indicate that the penetration depth of such wavelength may be a limiting factor. It is important to note that many effects are being considered: the VT induced by the X-rays irradiation, the stability of the photoexcited states from the blue light and the back valence-tautomerism observed after illumination with 660 nm red light. The crystals are only being exposed to X-rays during the SCXRD experiments, which last for 4.35 min (0.4 s per image, 653 images per run; see Table S1 of the Supporting Information) and the metastable *hs*-Co[II] states are spin trapped at 30 K. The observed decay can only be due to the red 660 nm illumination, which is demonstrated to be more than sufficient to counterbalance the X-ray excitation.

The penetration depth issue for all the light radiation used in our experiments still remain unsolved, as we were not able to characterize it or characterize the dependence of the VT interconversion yields to the crystal size. If it is the case that the penetration of red 660 nm light is too small, the back VT will be severely limited.

4. CONCLUSIONS

In our work, we presented the light-induced VT with high yield of metastable states of the benzene solvated Co(*diox*)$_2$(4-CN-py)$_2$ crystal. The versatility of the tautomer studied here brings about a series of questions on the mechanisms of the tautomeric interconversion displayed by this material. Because of the very different nature of the visible white light and the hard X-rays used to induce the VT, along with their respective interconversion yields, it is plausible that they induce VT via different processes.

Despite the previously reported capability of hard X-rays to induce the VT interconversion, we demonstrated that the effect of the X-rays can be reduced and nearly eliminated by attenuating the X-ray beam to an appropriate flux. Therefore, the photoinduced VT interconversion was successfully probed using single-crystal X-ray diffraction at a synchrotron source with an attenuated X-ray beam making sure that the X-rays were not inducing the formation of metastable states.

Our findings show that the *ls*-Co[III] ⇔ *hs*-Co[II] transition in the benzene solvated Co(*diox*)$_2$(4-CN-py)$_2$ crystals, when induced by X-rays, light, or temperature, is reversible. Most importantly, we have shown that the *hs*-Co[II] metastable state can be photoinduced in [Co(*diox*)$_2$(4-CN-py)$_2$]·benzene single crystals when illuminated with 450 nm blue light at 30 K with a very high interconversion yield (80%) and relaxed back to the *ls*-Co[III] state when illuminated with 660 nm red light. However, the latter has a much smaller yield, which could be due to a small penetration depth in the crystalline sample. The high-yield light-induced metastable state generation reported for the 450 nm blue light irradiation had never been experimentally observed in molecular crystals of cobalt dioxolane tautomers.

The results presented here assured that the blue light illumination is triggering the entire chain of events that leads to *ls*-Co[III] to *hs*-Co[II] interconversion and that red 660 nm light induces the *hs*-Co[II] to *ls*-Co[III] relaxation process in a Co(*diox*)$_2$ solid-state crystals. They illustrate the overall picture of the VT phenomena in the solid state, evidencing the complexity of electronic events making up the valence tautomerism interconversion, and call for a deeper study of the electronic dynamics of the light-induced VT in different solid-state transition metal complexes.

Finally, we showed that solvated Co(*diox*)$_2$(4-CN-py)$_2$ crystals can undergo the VT interconversion reversibly without disruption of or damage to its crystallinity, which ensures the robustness of such materials and their potential to be used as sensors. Controlling and understanding the electronic properties of related bistable solid-state materials is a fundamental step toward the development of new devices.

■ ASSOCIATED CONTENT

ⓢ Supporting Information

The Supporting Information is available free of charge at https://pubs.acs.org/doi/10.1021/acs.inorgchem.1c00638.

Experiment details, crystal and SCXRD data statistics (PDF)

Accession Codes

CCDC 2058451−2058453 contain the supplementary crystallographic data for this paper. These data can be obtained free of charge via www.ccdc.cam.ac.uk/data_request/cif, or by emailing data_request@ccdc.cam.ac.uk, or by contacting The Cambridge Crystallographic Data Centre, 12 Union Road, Cambridge CB2 1EZ, UK; fax: +44 1223 336033.

■ AUTHOR INFORMATION

Corresponding Author

Carlos B. Pinheiro − *Physics Department, Universidade Federal de Minas Gerais, Belo Horizonte 31270-901, Brazil;* ⓞ orcid.org/0000-0002-8674-1779; Phone: +55-31-3409-6600; Email: cbpinheiro@ufmg.br

Authors

Ludmila Leroy − *Physics Department, Universidade Federal de Minas Gerais, Belo Horizonte 31270-901, Brazil;* ⓞ orcid.org/0000-0002-4272-0298

Thiago M. Francisco − *Physics Department, Universidade Federal de Minas Gerais, Belo Horizonte 31270-901, Brazil;* ⓞ orcid.org/0000-0001-8722-4127

Helena J. Shepherd − *School of Physical Sciences, University of Kent, Canterbury CT2 7NZ, United Kingdom;* orcid.org/0000-0003-0832-4475

Mark R. Warren − *Diamond Light Source, Ltd., Didcot OX11 0DE, United Kingdom*

Lucy K. Saunders − *Diamond Light Source, Ltd., Didcot OX11 0DE, United Kingdom*

David A. Shultz − *Department of Chemistry, North Carolina State University, Raleigh, North Carolina 27695, United States;* orcid.org/0000-0001-8121-6812

Paul R. Raithby − *Department of Chemistry, University of Bath, Bath BA2 7AY, United Kingdom;* orcid.org/0000-0002-2944-0662

Complete contact information is available at:
https://pubs.acs.org/10.1021/acs.inorgchem.1c00638

Notes

The authors declare no competing financial interest.

REFERENCES

(1) Kahn, O. Spin-Transition Polymers: From Molecular Materials Toward Memory Devices. *Science* **1998**, *279* (5347), 44−48.

(2) Ruiz, D.; Yoo, J.; Hendrickson, D. N.; Guzei, I. A.; Rheingold, A. L. Valence Tautomeric Cobalt O-Quinone Complexes in a Dual-Mode Switching Array. *Chem. Commun.* **1998**, No. 19, 2089−2090.

(3) Sato, O. Dynamic Molecular Crystals with Switchable Physical Properties. *Nat. Chem.* **2016**, *8* (7), 644−656.

(4) Manrique-Juárez, M. D.; Rat, S.; Salmon, L.; Molnár, G.; Quintero, C. M.; Nicu, L.; Shepherd, H. J.; Bousseksou, A. Switchable Molecule-Based Materials for Micro- and Nanoscale Actuating Applications: Achievements and Prospects. *Coord. Chem. Rev.* **2016**, *308*, 395−408.

(5) Sato, O.; Cui, A.; Matsuda, R.; Tao, J.; Hayami, S. Photo-Induced Valence Tautomerism in Co Complexes. *Acc. Chem. Res.* **2007**, *40* (5), 361−369.

(6) Shultz, D. A. Valence Tautomerism in Dioxolene Complexes of Cobalt. In *Magnetism: Molecules to Materials*; 2001; pp 281−306.

(7) Tezgerevska, T.; Alley, K. G.; Boskovic, C. Valence Tautomerism in Metal Complexes: Stimulated and Reversible Intramolecular Electron Transfer between Metal Centers and Organic Ligands. *Coord. Chem. Rev.* **2014**, *268*, 23−40.

(8) Panja, A.; Jana, N. Ch.; Bauzá, A.; Frontera, A.; Mathonière, C. Solvent-Triggered Cis/Trans Isomerism in Cobalt Dioxolene Chemistry: Distinguishing Effects of Packing on Valence Tautomerism. *Inorg. Chem.* **2016**, *55* (17), 8331−8340.

(9) Ribeiro, M. A.; Stasiw, D. E.; Pattison, P.; Raithby, P. R.; Shultz, D. A.; Pinheiro, C. B. Towards Controlling the Solid State Valence Tautomer In-Terconversion Character by Solvation. *Cryst. Growth Des.* **2016**, *16* (4), 2385−2393.

(10) Evangelio, E.; Rodriguez-Blanco, C.; Coppel, Y.; Hendrickson, D. N.; Sutter, J. P.; Campo, J.; Ruiz-Molina, D. Solvent Effects on Valence Tautomerism: A Comparison between the Interconversion in Solution and Solid State. *Solid State Sci.* **2009**, *11* (4), 793−800.

(11) Mulyana, Y.; Poneti, G.; Moubaraki, B.; Murray, K. S.; Abrahams, B. F.; Sorace, L.; Boskovic, C. Solvation Effects on the Valence Tautomeric Transition of a Cobalt Complex in the Solid State. *Dalton Transactions* **2010**, *39* (20), 4757.

(12) Schmidt, R. D.; Shultz, D. A.; Martin, J. D.; Boyle, P. D. Goldilocks Effect in Magnetic Bistability: Remote Substituent Modulation and Lattice Control of Photoinduced Valence Tautomerism and Light-Induced Thermal Hysteresis. *J. Am. Chem. Soc.* **2010**, *132* (17), 6261−6273.

(13) Roux, C.; Adams, D. M.; Itié, J. P.; Polian, A.; Hendrickson, D. N.; Verdaguer, M. Pressure-Induced Valence Tautomerism in Cobalt o-Quinone Complexes: An X-Ray Absorption Study of the Low-Spin $[Co^{III}(3,5\text{-}DTBSQ)(3,5\text{-}DTBCat)(Phen)]$ to High-Spin $[Co^{II}(3,5\text{-}DTBSQ)2(Phen)]$ Interconversion. *Inorg. Chem.* **1996**, *35* (10), 2846−2852.

(14) Droghetti, A.; Sanvito, S. Electric Field Control of Valence Tautomeric Interconversion in Cobalt Dioxolene. *Phys. Rev. Lett.* **2011**, *107* (4), No. 047201.

(15) Poneti, G.; Mannini, M.; Sorace, L.; Sainctavit, P.; Arrio, M.-A.; Otero, E.; Criginski Cezar, J.; Dei, A. Soft-X-Ray-Induced Redox Isomerism in a Cobalt Dioxolene Complex. *Angew. Chem., Int. Ed.* **2010**, *49* (11), 1954−1957.

(16) Francisco, T. M.; Gee, W. J.; Shepherd, H. J.; Warren, M. R.; Shultz, D. A.; Raithby, P. R.; Pinheiro, C. B. Hard X-Ray-Induced Valence Tautomeric Interconversion in Cobalt-o-Dioxolene Complexes. *J. Phys. Chem. Lett.* **2017**, *8* (19), 4774−4778.

(17) Brown, S. N. Metrical Oxidation States of 2-Amidophenoxide and Catecholate Ligands: Structural Signatures of Metal−Ligand π Bonding in Potentially Noninnocent Ligands. *Inorg. Chem.* **2012**, *51* (3), 1251−1260.

(18) Schmidt, R. D.; Shultz, D. A.; Martin, J. D. Magnetic Bistability in a Cobalt Bis(Dioxolene) Complex: Long-Lived Photoinduced Valence Tautomerism. *Inorg. Chem.* **2010**, *49* (7), 3162−3168.

(19) Adams, D. M.; Hendrickson, D. N. Pulsed Laser Photolysis and Thermodynamics Studies of Intramolecular Electron Transfer in Valence Tautomeric Cobalt O-Quinone Complexes. *J. Am. Chem. Soc.* **1996**, *118* (46), 11515−11528.

(20) Adams, D. M.; Noodleman, L.; Hendrickson, D. N. Density Functional Study of the Valence-Tautomeric Interconversion Low-Spin $[Co^{III}(SQ)(Cat)(Phen)] \rightleftharpoons$ High-Spin $[Co^{I} (SQ)_2 (Phen)]$. *Inorg. Chem.* **1997**, *36* (18), 3966−3984.

(21) Caneschi, A.; Dei, A.; Gatteschi, D.; Tangoulis, V. Antiferromagnetic Coupling in a Six-Coordinate High Spin Cobalt-(II)−Semiquinonato Complex. *Inorg. Chem.* **2002**, *41* (13), 3508−3512.

(22) Beni, A.; Dei, A.; Laschi, S.; Rizzitano, M.; Sorace, L. Tuning the Charge Distribution and Photoswitchable Properties of Cobalt−Dioxolene Complexes by Using Molecular Techniques. *Chem. - Eur. J.* **2008**, *14* (6), 1804−1813.

(23) Azzaroli, N.; Lapini, A.; Di Donato, M.; Dei, A.; Righini, R. Valence Tautomerism in Co-Dioxolene Complexes: Static and Time-Resolved Infrared Spectroscopy Study. *J. Phys. Chem. B* **2013**, *117*, 15492.

(24) Kabsch, W. Xds. *Acta Crystallogr., Sect. D: Biol. Crystallogr.* **2010**, *66* (2), 125−132.

(25) Sheldrick, G. M. SHELXT−Integrated Space-Group and Crystal-Structure Determination. *Acta Crystallogr., Sect. A: Found. Adv.* **2015**, *71* (1), 3−8.

(26) Sheldrick, G. M. Crystal Structure Refinement with SHELXL. *Acta Crystallogr., Sect. C: Struct. Chem.* **2015**, *71* (1), 3−8.

(27) Groom, C. R.; Bruno, I. J.; Lightfoot, M. P.; Ward, S. C. The Cambridge Structural Database. *Acta Crystallogr., Sect. B: Struct. Sci., Cryst. Eng. Mater.* **2016**, *72* (2), 171−179.

(28) Gentili, P. L.; Bussotti, L.; Righini, R.; Beni, A.; Bogani, L.; Dei, A. Time-Resolved Spectroscopic Characterization of Photo-Induced Valence Tautomerism for a Cobalt−Dioxolene Complex. *Chem. Phys.* **2005**, *314* (1), 9−17.

(29) Liang, H. W.; Kroll, T.; Nordlund, D.; Weng, T.-C.; Sokaras, D.; Pierpont, C. G.; Gaffney, K. J. Charge and Spin-State Characterization of Cobalt Bis(o-Dioxolene) Valence Tautomers Using Co Kβ X-Ray Emission and L-Edge X-Ray Absorption Spectroscopies. *Inorg. Chem.* **2017**, *56* (2), 737−747.

(30) Banci, L.; Bencini, A.; Benelli, C.; Gatteschi, D.; Zanchini, C. Spectral-Structural Correlations in High-Spin Cobalt(II) Complexes. *Struct. Bonding (Berlin)* **1982**, *52*, 37−86.

(31) Gliemann, G. A. B. P. Lever: Inorganic Electronic Spectroscopy, Vol. 33 aus: Studies in Physical and Theoretical Chemistry, Elsevier, Amsterdam, Oxford, New York, Tokio 1984. 863 Seiten, Preis: $ 113, 50. *Berichte der Bunsengesellschaft für physikalische Chemie* **1985**, *89*, 99−100.

(32) Dei, A.; Feis, A.; Poneti, G.; Sorace, L. Thermodynamics of Valence Tautomeric Interconversion in a Tetrachlorodioxolene:Cobalt 1:1 Adduct. *Inorg. Chim. Acta* **2008**, *361* (14−15), 3842−3846.

(33) Gransbury, G. K.; Boulon, M.-E.; Petrie, S.; Gable, R. W.; Mulder, R. J.; Sorace, L.; Stranger, R.; Boskovic, C. DFT Prediction and Experimental Investigation of Valence Tautomerism in Cobalt-Dioxolene Complexes. *Inorg. Chem.* **2019**, *58* (7), 4230−4243.

7.5 PhD timeline

7.5.1 Main doctoral work activities per semester

2017/2	Literature study and doctoral project elaboration
	Synthesis of the $[Co(O_6C_6H_2(t\text{-but})_2)_2]_4$ precursor for the syntheses of all Co complexes studied here
2018/1	Academic credits: Electromagnetic theory II
	Teaching experience: Experimental physics – Mechanics and themodynamics
2018/2	Academic credits: Quantum mechanics II
	Teaching experience: Experimental physics – Electromagnetism and optics
	Extended X-ray Absorption Fine Structure Summer School, 2018. Stanford Synchrotron Radiation Lightsource (SSRL)
	Synthesis of $Co(diox)_2(Py)_2$ and $Co(diox)_2(CN\text{-Py})_2$ at Shultz lab, NCSU – North Carolina, USA
	XRD experiments at LNLS
2019/1	PrInt project elaboration
	PrInt fellowship awarded
2019/2	Middle term evaluation exam
	Exchange studies period started
2020/1	Experiments at SLS
	TA experiments
	COVID-19 pandemic lockdown
2020/2	Paper writing
	SLS experiments
2021/1	Paper publishing
	Thesis elaboration

7.5.2 X-ray beamtime participation

LNLS – Brazil   2018 - **MX2** – Investigation of Valence Tautomerism Using X-Ray Resonant Diffraction (team member

EXFEL –   2019 – **FXE** – Single-shot visualization of the multi-center ultrafast response in photoexcited spinel Co_3O_4 by femtosecond non-resonant XES and diffraction (team member)

Germany

SLS –   2020 – **PXII – X10 SA** - In-house experiments, DAFS studies of cobalt complexes (first author)

Switzerland

2020 – **SuperXAS** – In house experiments, Temperature dependent XAS of $CsPbBr_3$ (team member)

SwissFEL –   2020 – 2021 – **ALVRA** - Commissioning experiments (team member)

Switzerland

2021 – **BERNINA** - Commissioning experiments (team member)

SACLA – Japan   2021 – **BL3** – Ultrafast solvation dynamics probed by femtosecond X-ray absorption (fs-XAS), X-ray emission (fs-XES) and X-ray diffuse scattering (fs-XDS) experiments. (team member)

7.5.3 Institutional administrative work

Graduate students' representative, Physics department council – 2018 to 2019

7.5.4 Peer review experience

Journal, Communications Biology, ISSN: 2399-3642 (2020-08-30) / Nature Publishing Group.

7.5.5 Collaborative work – master students

- Ultrafast transient absorption in $CoSQ_2Py_2$ – Ellen Kiens, master's internship
- Density functional theory in $CoSQ_2Py_2$ – Lucas Pimenta, master's dissertation

7.6 Python scripts for SCXRD data reduction and refinement pipeline

The following pages contain the python scripts written for data processing and refinement of multiple XRD datasets from crystals with the same unit cell, named AvalanX.

The script *avalanx.inp* contains the definition of global parameters used in the AvalanX pipeline and must be filled with crystal information, data directories and work directory each time the pipeline is recruited. An example is shown below:

```
### the following parameters are global AvalanX parameters
##locations

DATASETS_NAME = 'temp_scan'
AVALANX_SCRIPTS_DIR = '/Users/ludmilaleroy/XRD/avalanx/avalanx-python'
WORK_DIR_PATH = '/Users/ludmilaleroy/XRD/SLS10062020'
DATASETS_DIR = '/Users/ludmilaleroy/XRD/RAWXRD_DATA/'

### the following parameters are input values for XDS
ORGX= 241
ORGY= 414
UNIT_CELL = '7.3 22.12 14.99 90 97 90'
SPACE_GROUP_NUMBER = 14
STRONG_PIXEL = 6
MINIMUM_NUMBER_OF_PIXELS_IN_A_SPOT = 6
GENINHO= 'geninpavlxRUN.INP'
INCLUDE_RESOLUTION_RANGE='50 1'

### the following parameters are input values for avalanx_scale
### MERGE=TRUE
### STRICT_ABSORPTION_CORRECTION=TRUE

### the following parameters are input values for avalanx_refine
INS_MODEL_ADDRESS =
'/Users/ludmilaleroy/XRD/avalanx/outtest0805/cosqpy_100k_model.ins'
UNITS_PER_CELL = '2'

### the folowing parameters are input values for avalanx_dafs
NAME_HKL_FILE ='XDS_ASCII_scaled_2.HKL'     #'INTEGRATE.HKL'
NAME_INP = 'XDS.INP'
REFLECTION_1 = ['2','0','0']
REFLECTION_2 = ['1','0','0']
REFLECTION_3 = ['4','0','0']
REFLECTION_4 = ['1','1','1']
REFLECTION_5 = ['-2','0','0']
REFLECTION_6 = ['-1','0','0']
REFLECTION_7 = ['-4','0','0']
REFLECTION_8 = ['-1','-1','-1']
```

```
REFLECTION_9 = ['0','2','0']
REFLECTION_10 = ['0','0','2']
REFLECTION_11 = ['0','4','0']
REFLECTION_12 = ['3','0','0']

### the following parameters are output graph settings
ENERGY_UNIT = 'ANGS'           ## NM          EV              CM-1
PLOT_X = 'ENERGY'
PLOT_Y = 'INTENSITY'           ## ABS_COEFF
```

Once *avalanx.inp* is correctly filled, *avalanx_dataprocessing.py* recruit XDS[68] iteratively, generating one XDS.INP file for each dataset. It will count on the XDS.INP generator, which has been slightly modified to perform in the pipeline and here is named *geninpavlxRUN.inp*. The data processing generates one folder with XDS files for each dataset processed. These files are used by *avalanx_refine.py*, which recruits SHELXL for the refinement of a standard *shelx.ins* file (shelx instruction file that contains the crystal structure under investigation). For anisotropic refinement, *avalanx_refine_anis.py* is required.

Note: XDS and SHELX must be installed and added to $PATH.

The following pages contain the following scripts, which were written for diffraction anomalous fine structure studies in single crystals:

- *avalanx_dataprocessing.py;*
- *geninpavlxRUN.inp;*
- *avalanx_refine.py;*
- *avalanx_refine_anis.py;*
- *avalax_dafs.py;*
- *avalanx_scale.py.*

```python
import os
from shutil import copyfile
from sys import argv

# Functions
def edit_inp(file_name):
    # file_name = os.path.join(AVALANX_SCRIPTS_DIR, 'XDS.INP')

    f_fonte = open(file_name, 'r')
    f_dest = open('temp.INP', 'w')

    for line in f_fonte:
        if line.startswith('UNIT_CELL_CONSTANTS'):
            f_dest.write('UNIT_CELL_CONSTANTS= %s  ! put correct
            values if known\n' % UNIT_CELL)
        elif line.startswith('SPACE_GROUP_NUMBER'):
            f_dest.write('SPACE_GROUP_NUMBER= %d      ! 0 if
            unknown\n' % SPACE_GROUP_NUMBER)
        elif line.startswith('ORGX='):
            f_dest.write('ORGX= %s ORGY= %s          \n' % (ORGX,
            ORGY))
        elif line.startswith('STRONG_PIXEL'):
            f_dest.write('STRONG_PIXEL= %d          ! COLSPOT: only
            use strong reflections (default is 3)\n' % STRONG_PIXEL)
        elif line.startswith('MINIMUM_NUMBER_OF_PIXELS_IN_A_SPOT'):
            f_dest.write('MINIMUM_NUMBER_OF_PIXELS_IN_A_SPOT=
            %d                     !default of 6 is sometimes to high\n' %
            MINIMUM_NUMBER_OF_PIXELS_IN_A_SPOT)
        else:
            f_dest.write(line)
    f_dest.close()
    f_fonte.close()

    os.rename('temp.INP', file_name)
    return file_name

# def edit_inp_generator():
#     file_name =
#     os.path.join(AVALANX_SCRIPTS_DIR, 'geninpavlxRUN.INP')
#     f_fonte = open(file_name, 'r')
#     f_dest = open('temp.INP', 'w')
#
#     for line in f_fonte:
#         if line.startswith('UNIT_CELL_CONSTANTS'):
#             f_dest.write('UNIT_CELL_CONSTANTS= %s  ! put correct
#             values if known\n' % UNIT_CELL)
#         elif line.startswith('SPACE_GROUP_NUMBER'):
#             f_dest.write('SPACE_GROUP_NUMBER= %d      ! 0
#     if unknown\n' % SPACE_GROUP_NUMBER)
#         elif line.startswith('STRONG_PIXEL'):
#             f_dest.write('STRONG_PIXEL= %d             ! COLSPOT:
#     only use strong reflections (default is 3)\n' % STRONG_PIXEL)
#         elif line.startswith('MINIMUM_NUMBER_OF_PIXELS_IN_A_SPOT'):
#             f_dest.write('MINIMUM_NUMBER_OF_PIXELS_IN_A_SPOT=
#     %d                  !default of 6 is sometimes to high\n' %
#     MINIMUM_NUMBER_OF_PIXELS_IN_A_SPOT)
#         else:
#             f_dest.write(line)
#     f_dest.close()
#     f_fonte.close()
#
#     os.rename('temp.INP', file_name)
#     return file_name

#
def search_detector_distance(endereco, snippet='DETECTOR_DISTANCE'):
    fh = open(endereco, 'r')
    DD = None
    for line in fh:
        if line.startswith(snippet):
            parts = line.split('=')
            parts = parts[1].split('!')
            DD = float(parts[0])
    # print(parts[1])

    return DD

def search_energy(endereco, snippet='X-RAY_WAVELENGTH'):
    fh = open(endereco, 'r')
    Energy = None
    for line in fh:
        if line.startswith(snippet):
            parts = line.split('=')
            Energy = float(parts[1])
#             print(parts[1])

    return Energy
#
```

```python
def get_prefix(file_list):
    prefix = None
    file_list.sort()
    for name in file_list:
        if name.endswith('.cbf') or name.endswith('.h5'):
            idx_ = name.rfind('_')
            prefix = name[0:idx_]
            break

    return prefix

# Define inp file address
inp_address = argv[1] # input file - user defined
    # for after: write instructions of
    how it must be written

# Execute general definitions
fh = open(inp_address, 'r')
for line in fh:
    exec(line)

if not os.path.exists(WORK_DIR_PATH):
    os.mkdir(WORK_DIR_PATH)

if not os.path.exists(WORK_DIR_PATH + os.sep + 'dataprocessing'):
    os.mkdir(WORK_DIR_PATH + os.sep + 'dataprocessing')

if not os.path.exists(WORK_DIR_PATH + os.sep + 'dataprocessing' + os.sep + DATASETS_NAME):
    os.mkdir(WORK_DIR_PATH + os.sep + 'dataprocessing' + os.sep + DATASETS_NAME)

# DATASETS_NAME = 'p200_teste'

# AVALANX_SCRIPTS_DIR ----->  where scripts are
# WORK_DIR_PATH ----->  where avalanx writes
# DATASETS_DIR ----->  where all the data is stored

# ### the following parameters are global AvalanX parameters

# ##locations

#
# AVALANX_SCRIPTS_DIR = '/home/leonardo/MEGA/Python-curso/Lud/avalanx_lud'
# WORK_DIR_PATH = '/home/leonardo/Documentos/Dados_lud/xrdDATAref/xrdDATAref/py200jun2'
# DATASETS_DIR = '/home/leonardo/Documentos/Dados_lud/xrddata/'
#
# ##
#
#
#
# ### the following parameters are input values for XDS
#
# ORGX= 241
# ORGY= 414
# UNIT_CELL = '12 4.5 6 90 90 90'
# SPACE_GROUP_NUMBER = 14
# STRONG_PIXEL = 6
# MINIMUM_NUMBER_OF_PIXELS_IN_A_SPOT = 3
#
# ### the following parameters are input values for avalanx_dafs
#
# NAME_HKL_FILE = 'afterconv.hkl'
# NAME_INP = 'XDS.INP'
# REFLECTION_1 = ['1','0','0']
# REFLECTION_2 = ['4','0','0']
# ## REFLECTION_3 = h k l
# ## REFLECTION_4 = h k l
# ## REFLECTION_5 = h k l
#
# ### the following parameters are output graph settings
#
# ENERGY_UNIT = 'ANGS'          ## NM      EV      CM-1
# PLOT_X = 'ENERGY'
# PLOT_Y = 'INTENSITY'          ## ABS_COEFF

LIST_DDxE = [] #list of detector distance X energy

# Edit XDSINP generator file and change it to executable
# XDSINP_generetor_address = edit_inp_generator()
# print('chmod +x %s' % XDSINP_generetor_address)
# os.system('chmod +x %s' % XDSINP_generetor_address)

# Read list od dirs of dataset
list_data_dirs = os.listdir(DATASETS_DIR)

XDSINP_GEN_COMMAND = AVALANX_SCRIPTS_DIR + os.sep + GENINHO + ' ' + DATASETS_DIR + os.sep + '%s' + os.sep + '%s_?????.cbf"'''
PREFIX_OUTPUT = 'avxdp_'
print(XDSINP_GEN_COMMAND)

list_failures = [[], []]

for dir in list_data_dirs:
    print(dir)
    # create dir in WORK_DIR_PATH
    dir_output = os.path.join(WORK_DIR_PATH, 'dataprocessing', DATASETS_NAME, PREFIX_OUTPUT + dir)
```

```python
if not os.path.exists(dir_output):
    os.mkdir(dir_output)

file_list = os.listdir(DATASETS_DIR + os.sep + dir)
# print(file_list)
prefix = get_prefix(file_list)
# print(prefix)
os.chdir(dir_output)
# execute the xds inp generator
os.system(XDSINP_GEN_COMMAND % (dir, prefix))

if not os.path.exists('XDS.INP'):
    continue

XDSINP = edit_inp('XDS.INP')

DD = search_detector_distance('XDS.INP')
Energy = search_energy('XDS.INP')
LIST_DDxE.append((DD, Energy))
os.system('xds XDS.INP')
###############################################
files_generated = os.listdir()

if 'XDS_ASCII.HKL' not in files_generated:
    list_failures[0].append(DATASETS_DIR + os.sep + dir)
    continue

# copyfile(AVALANX_SCRIPTS_DIR + os.sep + 'XSCALE.INP',
# dir_output + os.sep + 'XSCALE.INP')
# os.system('xscale ') #+ AVALANX_SCRIPTS_DIR + os.sep + 'XSCALE.INP')
#
# files_generated = os.listdir()
#
# if 'scaled.ahkl' not in files_generated:
#     list_failures[1].append(DATASETS_DIR + os.sep + dir)
#     continue
#
# copyfile(AVALANX_SCRIPTS_DIR + os.sep + 'XDSCONV.INP',
# dir_output + os.sep + 'XDSCONV.INP')
# os.system('xdsconv')

if len(list_failures[0]) > 0:
    log_xds_address = os.path.join(WORK_DIR_PATH, "dataprocessing",
        DATASETS_NAME, 'xds_failures.log')
    fh_xds_failures = open(log_xds_address, 'w')
    for dir in list_failures[0]:
        fh_xds_failures.write(dir + '\n')
    fh_xds_failures.close()

if len(list_failures[1]) > 0:
    log_xscale_address = os.path.join(WORK_DIR_PATH,
        'dataprocessing', DATASETS_NAME, 'xscale_failures.log')
    fh_xscale_failures = open(log_xscale_address, 'w')
    for dir in list_failures[1]:
        fh_xscale_failures.write(dir + '\n')
    fh_xscale_failures.close()

if len(LIST_DDxE)>0:
    DDxE_address = os.path.join(WORK_DIR_PATH, 'dataprocessing',
        DATASETS_NAME, 'DDxE.txt')
    fh_DDxE = open(DDxE_address, 'w')
    for dd,ee in LIST_DDxE:
        fh_DDxE.write('%f %f\n' % (dd, ee))
    fh_DDxE.close()

# print(list_failures)
# Go back to script
os.chdir(AVALANX_SCRIPTS_DIR)
```

```
1   #!/bin/
2   bash
3   #
    # purpose: generate
    XDS.INP
4   # tested with some datasets from ALS, SSRL, SLS, ESRF, BESSY,
    SPring-8 and PF; only MAR, ADSC/SMV, PILATUS, Eiger, RAXIS (in-
    house), Bruker (PHOTON II) detectors;
5   # for other detectors, values marked with XXX must be manually
    filled in.
6   #
7   # revision 0.03 . Kay Diederichs 2/
    2010
8   # revision 0.04 . Kay Diederichs 4/2010 - include alternative ORGX,
    ORGY calculations for ADSC
9   # revision 0.05 . Kay Diederichs 5/2010 - grep for "Corrected" in
    addition to "marccd"; needed for BESSY
10  # revision 0.06 . KD 6/2010 - add UNTRUSTED_RECTANGLE and
    UNTRUSTED_ELLIPSE; use `whereis catmar` and so on
11  # revision 0.07 . KD 6/2010 - decide about ORGX/Y info in MAR
    header being pixels or mm; other fixes
12  # revision 0.08 . KD 6/2010 - fixes for Pilatus
    6M
13  # revision 0.09 . KD 6/2010 - get rid of requirement for
    mccd_xdsparams.pl and/or catmar; rather use "od"
14  # revision 0.10 . Tim Gruene 7/2010 - set link 'images' to image
    directory if path exceeds 72 characters
15  # revision 0.11 . KD 7/2010 - for MarCCD: look for distance info at
    different byte position
16  # revision 0.12 . KD 7/2010 - fix for negative
    PHISTART
17  # revision 0.13 . KD 8/2010 - store correct NX NY QX QY in
    XDS.INP
18  # revision 0.14 . KD 1/2011 - SENSOR_THICKNESS for Pilatus;
    MINIMUM_NUMBER_OF_PIXELS_IN_A_SPOT=3
19  # revision 0.15 . KD 2/2011 - add comment for -ive sign of APS 19-
    ID and Australian Synchrotron rotation axis
20  # revision 0.16 . KD 3/2011 - SENSOR_THICKNESS=0.01 for ADSC and
    MarCCD. Add comment about SILICON=
21  # revision 0.17 . KD 3/2011 - make it work for .bz2 frames; improve
    screen output
22  # revision 0.18 . KD 4/2011 - faster by doing "strings" only once;
    revert "images/$1##/*/}" "correction"
23  # revision 0.19 . KD 6/2011 - bugfix for
    0.18
24  # revision 0.20 . KD 7/2011 - redirect stderr of /bin/ls to /dev/

25  # null
    # revision 0.21 . KD 11/2011 - SEPMIN, CLUSTER_RADIUS hints; read
    NX NY from header (for Pilatus 2M)
26  # revision 0.22 . KD 12/2011 - Pilatus 2M UNTRUSTED_RECTANGLE
    lines, SENSOR_THICKNESS from header
27  # revision 0.23 . KD 1/2012 - add UNTRUSTED_QUADRILATERAL, remove
    MINIMUM_ZETA (0.05 is default now)
28  # revision 0.24 . KD 3/2012 - remove revision 0.10 since XDS now
    takes much longer paths
29  # revision 0.25 . KD 3/2012 - remove revision 0.22 for PSI Pilatus
    2M; see http://www.globalphasing.com/autoproc/wiki/
    index.cgi?TroubleShootingKnownIssues
30  # revision 0.26 . KD 7/2012 - Mac-compatibility: replace od flags --
    skip-bytes= and --read-bytes= with -j and -N (thanks to Oliver
    Clarke for working this out!)
31  # revision 0.27 . KD 11/2012 - EXCLUDE_RESOLUTION_RANGE lines and
    generic Pilatus Flat_field test
32  # revision 0.28 . Keitaro 11/2012 - for MarCCD: read oscillation
    range from the position 1024+736 (fix for omega rotation)
33  # revision 0.29 . KD 1/2013 - include UNTRUSTED_RECTANGLES for
    Pilatus 6M; never hurts but needed if the beamline software does
    not mark them with -2 or such
34  # revision 0.30 . Keitaro 3/2013 - for ADSC: write all possible
    beam center conventions in XDS.INP as comments
35  # revision 0.31 . Keitaro 3/2013 - add comment for reversed phi for
    SPring-8
36  # revision 0.32 . Keitaro 3/2013 - add RAXIS support, only tested
    with RAXIS IV++ and VII.
37  # revision 0.33 . Keitaro 5/2013 - automatically set ROTATION_AXIS=-
    1 0 0 for SPring-8 BL32XU/41XU/44XU beamlines based on detector
    serial numbers.
38  # revision 0.34 . Keitaro 5/2013 - recognize ADSC detectors in
    Photon Factory and choose correct beam center convention based on
    detector serial numbers.
39  # revision 0.35 . KD 6/2013 - reduce 7000 to 6000 for shadow
    detection; insert comment about *_RESOLUTION_RANGE lines
40  # revision 0.36 . KD 6/2013 - insert NUMBER_OF_PROFILE_GRID* lines
    for Pilatus (suggested by C.Vonrhein)
41  # revision 0.37 . Keitaro 10/2013 - fix for MX225HS detector on
    SPring-8 BL32XU (Ignore case when matching marccd in header); see
    also rev-0.39
42  # revision 0.38 . KD 2/2014 - change defaults for REFINE(IDXREF)
    and REFINE(INTEGRATE) such that more stable results are obtained
    for difficult datasets
43  # revision 0.39 . Keitaro 4/2014 - automatically set ROTATION_AXIS=-
    1 0 0 for MX225HS at SPring-8 BL32XU.
44  # revision 0.40 . Jan Gebauer /KD 4/2014 - simple implementation of
    MAR345 detector
45  # revision 0.41 . recognize header starting with R-AXIS instead of
    RAXIS
```

- 46 # revision 0.42 . Keitaro 5/2014 automatically set ROTATION_AXIS=-1 0 0 for Q315 at SPring-8 BL38B1.
- 47 # revision 0.43 . Keitaro 5/2014 add experimental support of dTREK format (raxis_smv)
- 48 # revision 0.44 . Keitaro 5/2014 automatically set ROTATION_AXIS=-1 0 0 for PILATUS3 at SPring-8 BL41XU.
- 49 # revision 0.45 . KD cope with blanks in filenames
- 50 # revision 0.46 . Keitaro 6/2014 automatically set ROTATION_AXIS=-1 0 0 for Mar225 at SPring-8 BL26B2.
- 51 # revision 0.47 . Keitaro 7/2014 more generic dTREK format support (Saturn and RAXIS)
- 52 # revision 0.48 . Kip Guja 11/2014 add detector serial number for ALS 5.0.2 to beam center convention 1
- 53 # revision 0.49 . Nobuhisa 2/2015 add detector serial number for AichiSR BL2S1 to beam center convention 1
- 54 # revision 0.50 . KD 03/2015 workaround for Mar-1 change of parameter name "DISTANCE" to "POSITION" in REFINE(*) keywords
- 55 # revision 0.51 . Keitaro 03/2015 add .gz and .xz support and remove limitation – frame numbers can start with any.
- 56 # revision 0.52 . Keitaro 05/2015 fix ADSC beam center convention for SPring-8 and DET_SN acquisition for PILATUS (didn't work on Mac)
- 57 # revision 0.53 . KD add ADSC beam center convention for APS Argonne but only as commented line in XDS.INP (not detector serial no)
- 58 # revision 0.54 . KD add ADSC S/N 911 for APS Argonne, and fix spurious output arising from THETADISTANCE (?!)
- 59 # revision 0.55 . KD add ADSC S/N 446 for APS, and check w/ 12 datasets from data.sbgrid.org. No rule found: S/N 916 @ APS 24_ID_E !
- 60 # revision 0.56 . Keitaro 12/2015 show error message when user's input didn't match any files
- 61 # revision 0.57 . KD 12/2015 start to take care of vertical ROTATION_AXIS at Diamond I24 – for now only introduce comment
- 62 # revision 0.58 . Keitaro 01/2016 fix for dTREK image: take 'rotation axis' information from header
- 63 # revision 0.59 . KD 04/2016 check for ADSC detector _after_ dtrek detector, to correct wrong choice for https://zenodo.org/ record/45756
- 64 # revision 0.60 . KD 04/04/2016 ADSC detector SN=458 at APS 19-ID has reverse phi (https://zenodo.org/record/45756)
- 65 # revision 0.61 . Keitaro 10/04/2016 Add Eiger hdf5 support (may be incomplete; UNTRUSTED_RECTANGLE=s not set) NEED h5dump.
- 66 # revision 0.62 . Keitaro 11/04/2016 Can give foo_master.h5 instead of foo_?????.h5.
- 67 # revision 0.63 . Keitaro 13/04/2016 Set UNTRUSTED_RECTANGLE=s for EIGER 9M and 16M (KD).
- 68 # revision 0.64 . KD 16/06/2016 reverse phi @APS 19ID (reported by Wolfram Tempel)
- 69 # revision 0.65 . Keitaro 07/09/2016 Fix for "too many arguments" problem in ls

- 70 # revision 0.66 . KD 15/09/2016 add Bruker PHOTON II with .cbf frames
- 71 # revision 0.67 . KD 02/10/2016 add BM30A (ADSC SERIAL 924) reverse_phi
- 72 # revision 0.68 . KD 24/10/2016 add -H option (follow symlinks) to "find" command (thanks to Jan Gebauer!)
- 73 # revision 0.69 . KD 04/11/2016 add CMOS-1 MBC Detector at ALS 4.2.2
- 74 # revision 0.70beta . KD 08/12/2016 ROTATION_AXIS=0 -1 0 at Diamond I24; depending on CBF header
- 75 # revision 0.70 . KD 12/01/2017 remove error message if h5dump does not find /entry/sample/transformations/omega/vector
- 76 # revision 0.71 . KD 27/02/2017 implement rule for S/N 916 @ APS 24_ID_E
- 77 # revision 0.72 . KD 8/03/2017 fix nframes lookup in Eiger master file
- 78 # revision 0.73 . KD 18/05/2017 for Andrey Nascimento: add Pilatus 2M S/N 24-0109 with ROTATION_AXIS==-1 0 0
- 79 # revision 0.74 . Keitaro 02/08/2017 Add PILATUS3 6M, S/N 60-0127 at CHESS F1 with ROTATION_AXIS==-1 0 0
- 80 # revision 0.75 . KD 30/08/2017 reversed ORGX and ORGY for marCCD @ BM14 (Indian beamline @ ESRF)
- 81 # revision 0.76 . KD 4/09/2017 include POSITION into REFINE(IDXREF) because latest XDS is more robust. Add comments to keywords.
- 82 # revision 0.77 . KD 19/12/2017 obtain QX QY from CBF header.
- 83 # revision 0.78 . KD 21/12/2017 if possible and sensible, provide LIB= line with hardcoded /usr/local/lib64/dectris-neggia.so .
- 84 # revision 0.79 . KD 16/01/2018 read OVERLOAD from Pilatus miniCBF header instead of fixing at 1048576
- 85 # revision 0.80 . KD 13/02/2018 remove DISTANCE keyword from REFINE() list; remove POSITION from REFINE(IDXREF)
- 86 # revision 0.81 . KD 21/02/2018 when encountering CBF files from Eiger (ESRF), treat as Pilatus detector
- 87 # revision 0.82 . KD 01/03/2018 STARTING_ANGLE for MarCCD/Pilatus/ PHOTON, enabling to use dials.rs_mapper with spot2pdb.
- 88 # revision 0.83 . KD 25/06/2018 for ADSC detector #458 at APS BM19, revert the definition of ROTATION_AXIS=-1 0 0. See "Beamline notes" in this wiki.
- 89 # revision 0.84 . KD 10/10/2018 implement Pilatus detector with d*TREK header
- 90 # revision 0.85 . Jie Nan 09/01/2019 STARTING_ANGLE for Eiger at SSRF BL18U-1 with ROTATION_AXIS==1 0
- 91 # revision 0.86 . Keitaro 03/05/2019 Add PILATUS3 6M, S/N 60-0123 at SSRF BL18U-1 with ROTATION_AXIS==1 0
- 92 # revision 0.87 . KD 12/10/2019 Add PILATUS XXX, S/N XX-XXX at SSRF BL19U1 and MarCCD detector #43 at BL17B1 with ROTATION_AXIS==1 0 0
- 93 # revision 0.88 . KD 16/10/2019 fixes for SSRF, add "-maxdepth 1" to "find -H ..."
- 94 # revision 0.89 . KD 21/10/2019 add ADSC S/N 905 at ALS 8.2.1, S/N 928 at Australian Synchrotron MX2 beamline; final SSRF fixes
- 95 # revision 0.90 . KD 25/10/2019 add OLDMAR detector type. Tested w/ SRGrid data set 6. Anomalous signal may have wrong hand!

```
 95  # revision ... might incur.
 96  # revision 0.91 . KD 16/01/2020 Allow negative starting angle for
 97  # Eiger (found -33 at SLS !).
 98  # revision 0.92 . KD 27/02/2020 read *_master.h5 from Diamond Light
     Source
 99  # revision 0.93 . KD 13/03/2020 print out 2theta for MarCCD
     (DETECTOR_*_AXIS can be derived from this)
100  # revision 0.94 . KD 16/03/2020 bugfix for Bruker-cbf to make bc
     accept e.g. 3.1e-005 by using awk printf "%.5f" instead of awk
     print
101  REVISION="0.94 (16-Mar-2020)"
102  #
103  # usage: e.g. generate_XDS.INP "/file/system/frms/
     mydata_1_???.img"
104  # make sure to have the two quotation marks
     !
105  # the ? are wildcards for the frame
     numbers.
106  #
107  # known
     problems:
108  # - for ADSC detectors, there are at least three ways to obtain
     ORGX and ORGY values from the header (see below);
109  # - the same might be a problem for MAR headers, too (not sure
     about this)
110  # - on Mac OS X, the Xcode command line tools (from https://
     developer.apple.com/download/more/) are
     needed.
111  #
112  # - add the -x option to the first line, to see where an error
     occurs
113  # - comment out the removal of tmp1 and tmp2 in the last
     line
114  #
115  # notes for debugging of the
     script:
116  # ===== Start of script
     =====
117  echo generate_XDS.INP version $REVISION . Obtain the latest version
     from
118  echo http://strucbio.biologie.uni-konstanz.de/xdswiki/index.php/
     generate_XDS.INP
119  if [ "$1" == "help" ] || [ "$1" == "-help" ] || [ "$1" == "-h" ];
     then
120  echo usage: generate_XDS.INP \"/file/system/frms/
     mydata_1_???.img\"   \(_with_ the quotation
     marks!\)
121  echo if the frames are compressed with bzip2, leave out the .bz2
     extension!
122  exit
123  fi
124  #
125  #
     defaults:
126  #
127  # conversion radian / degrees:
128  DEGTOR=57.2957795
129
130  DETECTOR="XXX MINIMUM_VALID_PIXEL_VALUE=XXX
     OVERLOAD=XXX"
131  REVERSE_PHI="no"
132  ORGX=XXX
133  ORGY=XXX
134  DETECTOR_DISTANCE=XXX
135  OSCILLATION_RANGE=XXX
136  X_RAY_WAVELENGTH=XXX
137  QX=XXX
138  QY=XXX
139  NX=XXX
140  NY=XXX
141  SENSOR_THICKNESS=0
142  TRUSTED_REGION="0.0 1.2 ! partially use corners of detector (0
     1.4143: use all
     pixels)"
143  # define the MAXIMUM_NUMBER_OF_PIXELS_IN_A_SPOT
```

```
143 # default MINIMUM_NUMBER_OF_PIXELS_IN_A_SPOT
144 MNOPIAS=3
145 # default DIRECTION_OF_DETECTOR_X-AXIS
146 DIRECTION_OF_DETECTOR_X_AXIS="1 0 0"
147 # default FRACTION_OF_POLARIZATION
148 pol_frac=0.98
149 STARTING_ANGLE=0
150 dtrek_det=""
151 SEPMIN=7.0
152 CLUSTER_RADIUS=3.5
153
154 dname=`echo "$1" | xargs dirname`
155 test "${dname}" == "" && dname="."
156 bname=`echo "$1" | xargs basename`
157 # see how we are called:

158 NAME_TEMPLATE_OF_DATA_FRAMES="${dname}/${bname}"
159 # list frames matching the wildcards in NAME_TEMPLATE_OF_DATA_FRAMES
160 # don't accept the "direct beam" shot at SLS/Pilatus PX-I and PX-II
161 # cope with blanks in directory / file name
162 IFS=$'\n'
163 find -H $dname -maxdepth 1 -name "$bname" -or -name "${bname}.gz" -or -name "${bname}.xz" | egrep -v
    "_00000.cbf|_000.img" | sort > tmp1
164 if [ ! -s tmp1 ]
165 then
166 echo "Error! No files matched: $1"
167 rm -f tmp1
168 exit 1
169 fi
170 unset IFS
171 # we can continue - the frames are found
172
173 if echo $NAME_TEMPLATE_OF_DATA_FRAMES | grep '_master.h5$' > /dev/null; then
174 NAME_TEMPLATE_OF_DATA_FRAMES=`echo "$NAME_TEMPLATE_OF_DATA_FRAMES"
    | sed -e 's/_master.h5$/_??????.h5/'`
175 else
176 # Find the first '?' position and the number of '?' to determine
    DATA_RANGE=.
177 pos1=`echo "$NAME_TEMPLATE_OF_DATA_FRAMES" | awk '{print index($0,
    "?")}'`
178 pos2=`echo "$NAME_TEMPLATE_OF_DATA_FRAMES" | sed -e 's/[^\?]//g' |
    awk '{print length+$pos1 - 1}'`
179 data_first=`cut -b $pos1-$pos2 tmp1 | head -n1 | bc`
180 data_last=`cut -b $pos1-$pos2 tmp1 | tail -n1 | bc`
181 DATA_RANGE="$data_first $data_last"
182
183 # set SPOT_RANGE to first half of DATA_RANGE

184 data_num=`wc -l tmp1 | awk '{print $1}'`
185 data_half=`echo "scale=0; $data_num/2" | bc -
    l`

186 data_half=`echo "if ($data_half==1) 1;if ($data_half>1)
    $data_half" | bc -l`
187 spot_last=`echo "scale=0; $data_first+$data_half-1" | bc -l`
188 SPOT_RANGE="$data_first $spot_last"
189 fi
190
191 FIRSTFRAME=`head -1 tmp1`
192 echo $FIRSTFRAME | grep "\.h5$" && is_h5=1 || is_h5=0
193
194 if [ "$is_h5" == 1 ]; then
195 # nframes=`h5dump -A -g "/entry/data" $FIRSTFRAME | grep
    "DATASPACE SIMPLE" | sed -e "s/,.*//" | awk '{a+=$5}END{print a}'`

196 nframes=`h5dump -d "/entry/instrument/detector/detectorSpecific/
    nimages" $FIRSTFRAME | awk '/\(0\): [0-9]/{print $2}'`
197 DATA_RANGE="1 $nframes"
198 SPOT_RANGE="1 `echo "scale=0; if (${nframes}<2) 1; if
    (${nframes}>1) ${nframes}/2"|bc -l`"
199 fi
200
201 echo DATA_RANGE=$DATA_RANGE
202
203 # find out detector type
204 DET=XXX
205 IFS=$'\n'
206 echo $FIRSTFRAME | grep -q '\.bz2$' && bzcat $FIRSTFRAME > tmp1 &&
    FIRSTFRAME=tmp1
207 # for mac/linux compatibility, zcat foo.gz doesn't work on mac.
208 echo $FIRSTFRAME | grep -q '\.gz$' && zcat < $FIRSTFRAME > tmp1 &&
    FIRSTFRAME=tmp1
209 echo $FIRSTFRAME | grep -q '\.xz$' && xzcat $FIRSTFRAME > tmp1 &&
    FIRSTFRAME=tmp1

210 unset IFS
211 if [ "$is_h5" == 0 ]; then
212 strings $FIRSTFRAME > tmp2
213 # TODO: whenever FIRSTFRAME is used below, it should be copied to
214 # tmp2 (using IFS as above), and tmp2 should be used instead

215 # this was done for "mccd", but still has to be done for the
216 # "raxis" detector types
    # the reason is that FIRSTFRAME may contain a blank, which makes
    # some commands fail
217 egrep -q 'marccd|Corrected' tmp2 &&
    DET=mccd
218 grep -q PILATUS tmp2                 && DET=pilatus
219 grep -iq Eiger tmp2                  &&
    DET=pilatus
220 head -n1 tmp2 | grep -q "RAXIS" && DET=raxis
```

```
221 head -n1 tmp2 | grep -q "^R-AXIS" && DET=raxis
222 grep -q "^SOURCE_WAVELENGTH= *1" tmp2 && DET=dtrek
223 grep -q "BEAM_CENTER_X tmp2" &&
      DET=adsc
224 grep -q mar345 tmp2          && DET=MAR345
225 grep -q BRUKER tmp2 && grep -q CBF tmp2 && DET=Bruker-cbf
226 grep -q CMOS1 tmp2 && DET=adsc-CMOS1
227 grep -q MARCONTROL tmp2 && DET=OLDMAR
228 else
229 h5dump -d "/entry/instrument/detector/description" $FIRSTFRAME |
230 grep -i Eiger > /dev/null && DET=eiger
231 fi
232 # identify other detector types in the same way
233
234 # parse ASCII header of first frame
235
236 if [ "$DET" == "XXX" ]; then
237 echo "this is not a MAR, ADSC/SMV or PILATUS detector - fill in
      XXX values manually!"
238 DETECTOR="XXX MINIMUM_VALID_PIXEL_VALUE=XXX
      OVERLOAD=XXX"
239
240 # find parameters of first frame
241 elif [ "$DET" == "mccd" ]; then
242 echo Data from a MarCCD detector
243 # http://www.sb.fsu.edu/~xray/Manuals/marCCD165header.html has
      header information
244
245 DETECTOR="CCDCHESS MINIMUM_VALID_PIXEL_VALUE= 1 OVERLOAD= 65500"
246 SENSOR_THICKNESS=0.01
247 # use first frame of dataset to obtain parameters
248
249 # Check detector serial number and recognize beamline for
      reversed-phi setting.
250 # Known detectors for reversed-phi in SPring-8: 24: BL26B2
      Mar225, 31: BL32XU MX225HE, 38: BL44XU MX225HE, 42: BL44XU
      MX300HE, 40: BL41XU MX225HE, 106: BL32XU MX225HS
251 # same for SSRF: BL17B1 rayonix MX300. As on 2019-10-13, this
      also needs doubling of ORGX and ORGY. But the beamline staff
      (Wenming) wants to fix the header.
252 REVERSEPHI_SNs="
253 24
254 31
255 38
256 40
257 42
258 43
259 106
260 "
261 # get detector serial number and check if it is included in the
      list
262 DET_SN=`grep "Detector Serial Number =" tmp2 | sed "s/Detector
      Serial Number = //"`
263 if echo "${DET_SN}${REVERSEPHI_SNs}" | sort | uniq -d | grep [0-
      9] > /dev/null; then
264 REVERSE_PHI="yes"
265 fi
266
267 # offsets are documented; values can be found in
      mccd_xdsparams.pl script
268 IFS=$'\n'
269 cp $FIRSTFRAME tmp2
270 unset IFS
271 let
      SKIP=1024+80
272 NX=$(od -t dI -j $SKIP -N 4 tmp2 | head -1 | awk '{print $2}')
273 let
      SKIP=$SKIP+4
274 NY=$(od -t dI -j $SKIP -N 4 tmp2 | head -1 | awk '{print $2}')
275
276 let SKIP=1720
277 DETECTOR_DISTANCE=$(od -t dI -j $SKIP -N 4 tmp2 | head -1 | awk
      '{print $2}')
278 DETECTOR_DISTANCE=`echo "scale=3; $DETECTOR_DISTANCE/1000" | bc -
      l`
279
280 # Mar 12, 2020 KD
281 let SKIP=1724
282 TWOTHETA=$(od -t dI -j $SKIP -N 4 tmp2 | head -1 | awk '{print
      $2}')
283 TWOTHETA=`echo "scale=3; $TWOTHETA/1000" | bc -l`
284 echo 2THETA= $TWOTHETA
285
286 let SKIP=1024+256+128+256+44
287 STARTING_ANGLE=$(od -t dI -j $SKIP -N 4 tmp2 | head -1 | awk
      '{print $2}')
288 STARTING_ANGLE=`echo "scale=2; $STARTING_ANGLE/1000" | bc -l`
289 echo STARTING_ANGLE= $STARTING_ANGLE
290
291 let
      SKIP=1024+256+128+256+4
292 ORGX=$(od -t dI -j $SKIP -N 4 tmp2 | head -1 | awk '{print
      $2}')
293 ORGX=`echo "scale=2; $ORGX/1000" | bc -l`
```

```bash
294  let
     SKIP=$SKIP+4
295  ORGY=$(od -t dI -j $SKIP -N 4 tmp2 | head -1 | awk '{print
     $2}')
296  ORGY=`echo "scale=2; $ORGY/1000"` | bc -l`
297  # fixed Aug 30, 2017 after IUCr2017 @ Hyderabad
298  if [ "$DET_SN" == "4" ]; then
299      TEMP=$ORGY
300      ORGY=$ORGX
301      ORGX=$TEMP
302      echo reversed ORGX and ORGY for marCCD @ ESRF BM14
303  fi
305  let SKIP=1024+736
306  OSCILLATION_RANGE=$(od -t dI -j $SKIP -N 4 tmp2 | head -1 | awk
     '{print $2}')
307  OSCILLATION_RANGE=`echo "scale=3; $OSCILLATION_RANGE/1000"` | bc -
     l`
309  let
     SKIP=1024+256+128+256+128+4
310  QX=$(od -t dI -j $SKIP -N 4 tmp2 | head -1 | awk '{print
     $2}')
311  QX=`echo "scale=10; $QX/1000000"` | bc -l
312  let
     SKIP=$SKIP+4
313  QY=$(od -t dI -j $SKIP -N 4 tmp2 | head -1 | awk '{print
     $2}')
314  QY=`echo "scale=10; $QY/1000000"` | bc -l
316  let SKIP=1024+256+128+256+128+12
317  X_RAY_WAVELENGTH=$(od -t dI -j $SKIP -N 4 tmp2 | head -1 | awk
     '{print $2}')
318  X_RAY_WAVELENGTH=`echo "scale=5; $X_RAY_WAVELENGTH/100000"` | bc -
     l`
320  # at most BLs, ORGX and ORGY are in pixels, but sometimes in mm ....
     guess:
321  NXBYFOUR=`echo "scale=0; $NX/4"` | bc -l
322  ORGXINT=`echo "scale=0; $ORGX/1"` | bc -l
323  if [ $ORGXINT -lt $NXBYFOUR ];
324  then
     ORGX=`echo "scale=1; $ORGX/$QX"` | bc -
     l`
325  ORGY=`echo "scale=1; $ORGY/$QY"` | bc -
     l`
326  echo MARCCD detector: header ORGX, ORGY seem to be in mm ...
     converting to pixels
327  else
328  echo MARCCD detector: header ORGX, ORGY seem to be in pixel
     units
329  fi
330  elif [ "$DET" == "adsc" ]; then
331  DETECTOR="ADSC MINIMUM_VALID_PIXEL_VALUE= 1 OVERLOAD= 65000"
333  echo Data from ADSC detector. Obtaining ORGX, ORGY depends on
     beamline setup:
335  SENSOR_THICKNESS=0.01
336  sed s/\;// tmp2 >
337  tmp1
     mv tmp1
     tmp2
339  # find X_RAY_WAVELENGTH!
340  X_RAY_WAVELENGTH=`grep WAVELENGTH tmp2 | head -1 | sed s/
     WAVELENGTH=//`
342  # find NX, QX, ORGX and ORGY:
343  NX=`grep SIZE1 tmp2 | tail -1 | sed s/SIZE1=//`
344  NY=`grep SIZE2 tmp2 | tail -1 | sed s/SIZE2=//`
345  QX=`grep PIXEL_SIZE tmp2 | sed s/PIXEL_SIZE=//`
346  QY=$QX
347  BEAM_CENTER_X=`grep BEAM_CENTER_X tmp2 | sed s/BEAM_CENTER_X=/
     /`
348  BEAM_CENTER_Y=`grep BEAM_CENTER_Y tmp2 | sed s/BEAM_CENTER_Y=/
     /`
350  COMMENT_ORGXY=""
351  ! Following are possible beam center interpretations for ADSC
     detectors"
352  # at ESRF, PF, ALS 5.0.2, AS MX2 and ... (pls fill in!) the
     following should be used:
353  ORGX1=`echo "scale=1; $BEAM_CENTER_Y/$QX"` | bc -l`
354  ORGY1=`echo "scale=1; $BEAM_CENTER_X/$QX"` | bc -l`
355  echo - at ESRF, PF, ALS 8.2.1, APS Argonne BLs use:
```

```bash
356	•
357	! ORGX= $ORGX1 ORGY= $ORGY1 ! For ESRF, PF, APS, AS MX2 ..."
358	# this 2nd alternative convention should be used at the following
	beamlines (pls complete the list): ALS 5.0.3, ...
359	ORGX2=`echo "scale=1; $NX-$BEAM_CENTER_X/$QX" | bc -l`
360	ORGY2=`echo "scale=1; $BEAM_CENTER_Y/$QX" | bc -l`
361	echo - at e.g. ALS 5.0.3 use: ORGX=$ORGX2
	ORGY=$ORGY2
	•
362	COMMENT_ORGXY="${COMMENT_ORGXY}
363	! ORGX= $ORGX2 ORGY= $ORGY2 ! For ALS 5.0.3,..."
364	# this 3rd alternative convention should be used at the following
	beamlines (pls complete the list): ALS 8.2.2, ...
365	# this alternative is written into the generated XDS.INP ! You have
	to correct this manually in XDS.INP, or adjust this script.
366	ORGX3=`echo "scale=1; $NX-$BEAM_CENTER_X/$QX" | bc -l`
367	ORGY3=`echo "scale=1; $BEAM_CENTER_Y/$QX" | bc -l`
368	echo - at e.g. ALS 8.2.2 use: ORGX=$ORGX3 ORGY=$ORGY3 - this
	is written to XDS.INP if beamline is not detected
369	•
	COMMENT_ORGXY="${COMMENT_ORGXY}
370	! ORGX= $ORGX3 ORGY= $ORGY3 ! For ALS 8.2.2,..."
371	# this 4th alternative convention should be used at the following
	beamlines (pls complete the list): SPring-8, ...
372	ORGX4=`echo "scale=1; $BEAM_CENTER_X/$QX" | bc -l`
373	ORGY4=`echo "scale=1; $BEAM_CENTER_Y/$QX" | bc -l`
374	echo - at e.g. Spring-8 use: ORGX=$ORGX4 ORGY=$ORGY4
375	COMMENT_ORGXY="${COMMENT_ORGXY}
376	! ORGX= $ORGX4 ORGY= $ORGY4 ! For SPring-8,..."
377	•
378	# Decision of beam center convention based on detector serial
	numbers.
379	DET_SN=`grep DETECTOR_SN tmp2 | sed -e "s/DETECTOR_SN=//"`
380	echo Detector serial number is $DET_SN
381	# For convention 1; Known PF detectors = 449: NW12A Q210,
	472: NE3A Q270, 474: BL17A Q270, 912: BL5A Q315, 923: ALS
	BL5.0.2 Q315, 933: AichiSR BL2S1 Q315, 916: APS 24 IDE, 928:
	AS MX2
382	ORG1_SNs="
383	449
384	472
385	474
386	912
387	923
388	933
389	911
390	446
391	916
392	905
393	928
394	"
395	ORG4_SNs="
396	915
397	"
398	if echo "${DET_SN}${ORG1_SNs}" | sort | uniq -d | grep [0-9]
	> /dev/null; then
399	ORGX=$ORGX1
400	ORGY=$ORGY1
401	echo the following was chosen based on detector serial
	number:
402	elif echo "${DET_SN}${ORG4_SNs}" | sort | uniq -d | grep [0-
	9] > /dev/null; then
403	ORGX=$ORGX4
404	ORGY=$ORGY4
405	echo the following was chosen based on detector serial
	number:
406	else
407	ORGX=$ORGX3
408	ORGY=$ORGY3
409	echo the following default was chosen because the detector
	serial number was not special-cased:
410	fi
411	•
412	# Check detector serial number and recognize beamline for
	reversed-phi setting.
413	# Known detectors for reversed-phi in SPring-8: 915: BL38B1
	Q315; APS 19-ID: 458; BM30A: 924
414	# 928 is at Australian Beamline MX2
415	# revision 0.83 of this script removes 458 from the list!
416	REVERSEPHI_SNs="
417	915
418	924
419	928
420	"
421	if echo "${DET_SN}${REVERSEPHI_SNs}" | sort | uniq -d | grep
	[0-9] > /dev/null; then
422	REVERSE_PHI="yes"
423	fi
424	•
425	# find DETECTOR_DISTANCE and
	OSCILLATION_RANGE:
426	DETECTOR_DISTANCE=`grep ^DISTANCE tmp2 | sed s/DISTANCE=//`
427	OSCILLATION_RANGE=`grep OSC_RANGE tmp2 | sed s/OSC_RANGE=//`
428	•
429	elif [ "$DET" == "adsc-CMOS1" ]; then
430	DETECTOR="ADSC MINIMUM VALID PIXEL VALUE= 1 OVERLOAD= 65000"
```

```
431    echo Data from CMOS1 MBC detector.
432    SENSOR_THICKNESS=0.01
   •
433    sed s/\;// tmp2 >
   •   tmp1
434    mv tmp1
   •   tmp2
   •
435    X_RAY_WAVELENGTH=`grep WAVELENGTH tmp2 | head -1 | sed s/
       WAVELENGTH=//`
436    NX=`grep SIZE1 tmp2 | tail -1 | sed s/SIZE1=//`
437    QX=`grep PIXEL_SIZE tmp2 | sed s/PIXEL_SIZE=//`
438    NY=`grep SIZE2 tmp2 | tail -1 | sed s/SIZE2=//`
   •   `
439    QY=$QX
   •
440    ORGX=`grep BEAM_CENTER_X tmp2 | sed s/BEAM_CENTER_X=//`
441    ORGY=`grep BEAM_CENTER_Y tmp2 | sed s/BEAM_CENTER_Y=//`
442    REVERSE_PHI="yes"
443    DETECTOR_DISTANCE=`grep ^DISTANCE tmp2 | sed s/DISTANCE=/-/
   •   `
444    OSCILLATION_RANGE=`grep OMEGA_DELTA tmp2 | sed s/OMEGA_DELTA=//`
445    DIRECTION_OF_DETECTOR_X_AXIS="-1 0
       0"
   •
446
447    elif [ "$DET" == "pilatus" ]; then
448    echo Data from a Pilatus
   •   detector
449    sed s/#// tmp2 >
   •   tmp1
450    mv tmp1
   •   tmp2
451    OVERLOAD=1048574
452    SEPMIN=4
453    CLUSTER_RADIUS=2
454    grep -q Count_cutoff tmp2 && OVERLOAD=`awk '/Count_cutoff/{print
       $2}' tmp2`
455    DETECTOR="PILATUS MINIMUM_VALID_PIXEL_VALUE=0 OVERLOAD=
       $OVERLOAD !PILATUS"
456    QY=0.172
   •   QX=0.172
457    # the default above guards against missing Pixel_size line in CBF
       header
458    grep -q Pixel_size tmp2 && QX=`awk '/Pixel_size/{print 1000*$2}'
       tmp2`
459    grep -q Pixel_size tmp2 && QY=`awk '/Pixel_size/{print 1000*$5}'
       tmp2`
460
461    # find SENSOR_THICKNESS:

462    SENSOR_THICKNESS=`grep thickness tmp2 | sed -e s/'Silicon
       sensor, thickness'// | awk '{print $1*1000}'`
463    # find
       X_RAY_WAVELENGTH:
   •
464    X_RAY_WAVELENGTH=`grep Wavelength tmp2 | sed -e s/Wavelength/
       / -e s/A// | awk '{print $1}'`
465
466    # find NX and NY; 2463/2527 is 6M, 1475/1679 is 2M
467    NX=`grep X-Binary-Size-Fastest-Dimension tmp2 | awk '{print
       $2}'`
468    NY=`grep X-Binary-Size-Second-Dimension tmp2 | awk '{print
       $2}'`
469
470    # find ORGX and ORGY:
471    ORGX=`grep Beam_xy tmp2 | sed -e s/\(// -e s/\)// -e s/\,// |
       awk '{print $2}'`
472    ORGY=`grep Beam_xy tmp2 | sed -e s/\(// -e s/\)// -e s/\,// |
       awk '{print $3}'`
473
474    # find DETECTOR_DISTANCE, OSCILLATION_RANGE, and
       STARTING_ANGLE:
475    DETECTOR_DISTANCE=`awk '/Detector_distance/{print $2}' tmp2`
476    DETECTOR_DISTANCE=`echo "$DETECTOR_DISTANCE*1000" | bc -l`
477
478    OSCILLATION_RANGE=`awk '/Angle_increment/{print $2}' tmp2`
479    STARTING_ANGLE:
480    STARTING_ANGLE=`awk '/Start_angle/{print $2}' tmp2`
481    echo STARTING_ANGLE= $STARTING_ANGLE
482
483    # get detector serial number and check if it is included in
       the list
484    # Known detectors for reversed-phi in SPring-8: BL41XU
485    # Known detectors for reversed-phi in APS: 19ID PILATUS3 6M
       60-0132
486    # Known detectors for reversed-phi at MX2 beamline (Brazilian
       Synchrotron National Laboratory - LNLS)
487    # Known detectors for reversed-phi at CHESS F1 PILATUS3 6M, S/
       N 60-0127
488    # Known detectors for reversed-phi at SSRF BL18U1 (S/N 60-
       0123) and BL19U1 (S/N XX-XXX) (!; 2019-10-19; staff will fix
       this)
489    DET_SN=`grep "Detector:" tmp2 | sed "s/^.*Detector: *//"`
490    REVERSEPHI_SNs="
491    PILATUS3 6M, S/N 60-0125
492    PILATUS3 6M, S/N 60-0132
493    PILATUS 2M, S/N 24-0109
494    PILATUS3 6M, S/N 60-0127
495    PILATUS3 6M, S/N 60-0132
```

```
493   "PILATUS 6M, S/N 60-0123
496   "
497   if echo "${DET_SN}${REVERSEPHI_SNs}" | sort | uniq -d | grep
          [0-9] > /dev/null; then
  •       REVERSE_PHI="yes"
498   fi
499   if [ "$DET_SN" == "PILATUS XXX, S/N XX-XXX" ] ; then
500       REVERSE_PHI="yes"
501       echo inverted rotation axis at SSRF BL19U1
502   fi
503
504   # Diamond I24:
505   if [ "$DET_SN" == "PILATUS3 6M, S/N 60-0119" ] ; then
506       if grep -q "Oscillation_axis X_CW +SLOW" tmp2 ; then
507           rotation_axis="0 -1 0"
508       fi
509   fi
510   # insert similar code for Petra P14 here
511
512
513   elif [ "$DET" == "eiger" ]; then
514   # find out if HDF5 from Diamond (DLS=1) or Dectris (DLS=0)
515   DLS=0
516   OVERLOAD=`h5dump -d "/entry/instrument/detector/detectorSpecific/
  •       countrate_correction_count_cutoff" $FIRSTFRAME 2>/dev/null` ||
517   if [ "$DLS" == 1 ]; then
518       echo Eiger HDF5 from Diamond
519       OVERLOAD=`h5dump -d "/entry/instrument/detector/
  •           saturation_value" $FIRSTFRAME | awk '/\(0\):/{print $2}'`
520       OSCILLATION_RANGE=`h5dump -d "/entry/data/omega" $FIRSTFRAME |
  •           awk '/\(0\): [0-9]/{print $3-$2}'`
521       STARTING_ANGLE=`h5dump     -d "/entry/data/omega" $FIRSTFRAME |
  •           awk '/\(0\): [0-9]/{print $2}' | sed -e "s/,//"`
522       echo OSCILLATION_RANGE=$OSCILLATION_RANGE
  •           STARTING_ANGLE=$STARTING_ANGLE
523   # rotation_axis=`h5dump -a "/entry/sample/transformations/omega/
  •       vector" $FIRSTFRAME 2>/dev/null | grep "(0):" | sed -e "s/.*:.//;
  •       s/,//g"`
524   # the above gives -1 0 0 for DLS data instead of the correct 1 0
  •       0, so commented out for now
525   else
526       echo Eiger HDF5 from Dectris
527       OVERLOAD=`h5dump -d "/entry/instrument/detector/
  •           detectorSpecific/countrate_correction_count_cutoff" $FIRSTFRAME
  •           | awk '/\(0\):/{print $2}'`
528       OSCILLATION_RANGE=`h5dump -d "/entry/sample/goniometer/
  •           omega_range_average" $FIRSTFRAME | awk '/\(0\): [0-9]/{print
  •           $2}'`
529   # STARTING_ANGLE:   the \- was introduced in version 0.91 to allow
  •       negative values :

530   STARTING_ANGLE=`h5dump -d "/entry/sample/goniometer/
  •       omega_start" $FIRSTFRAME | awk '/\(0\): [\-0-9]/{print $2}'`
531   # If rotation vector set (NeXus)
532   rotation_axis=`h5dump -a "/entry/sample/transformations/omega/
  •       vector" $FIRSTFRAME 2>/dev/null | grep "(0):" | sed -e "s/.*:.//
  •       ; s/,//g"`
533   fi
534   # Eiger 16M SSRF BL17U1
  •       SN=`h5dump -d "/entry/instrument/detector/detector_number"
  •       $FIRSTFRAME | awk '/\(0\): [0-9]/{print $2}'`
535   if [ "$SN" == "E-32-0111" ]; then
  •       rotation_axis="-1 0 0"
536   fi
537   echo SSRF BL17U1 with inverted rotation axis
538   fi
539
540   DETECTOR="EIGER MINIMUM_VALID_PIXEL_VALUE=0 OVERLOAD= $OVERLOAD"
541   QX=`h5dump -d "/entry/instrument/detector/x_pixel_size"
  •       $FIRSTFRAME | awk '/\(0\): [0-9]/{print $2*1000}'`
542   QY=`h5dump -d "/entry/instrument/detector/y_pixel_size"
  •       $FIRSTFRAME | awk '/\(0\): [0-9]/{print $2*1000}'`
543
544   echo OVERLOAD=$OVERLOAD
545   SENSOR_THICKNESS=`h5dump -d "/entry/instrument/detector/
  •       sensor_thickness" $FIRSTFRAME | awk '/\(0\): [0-9]/{print
  •       $2*1000}'`
546   X_RAY_WAVELENGTH=`h5dump -d "/entry/instrument/beam/
  •       incident_wavelength" $FIRSTFRAME | awk '/\(0\): [0-9]/{print $2}'`
547
548   NX=`h5dump -d "/entry/instrument/detector/detectorSpecific/
  •       x_pixels_in_detector" $FIRSTFRAME | awk '/\(0\): [0-9]/{print
  •       $2}'`
549   NY=`h5dump -d "/entry/instrument/detector/detectorSpecific/
  •       y_pixels_in_detector" $FIRSTFRAME | awk '/\(0\): [0-9]/{print
  •       $2}'`
550
551   # find ORGX and ORGY:
552   ORGX=`h5dump -d "/entry/instrument/detector/beam_center_x"
  •       $FIRSTFRAME | awk '/\(0\): [0-9]/{print $2}'`
553   ORGY=`h5dump -d "/entry/instrument/detector/beam_center_y"
  •       $FIRSTFRAME | awk '/\(0\): [0-9]/{print $2}'`
554
555   # find DETECTOR_DISTANCE :
556   DETECTOR_DISTANCE=`h5dump -d "/entry/instrument/detector/
  •       detector_distance" $FIRSTFRAME | awk '/\(0\): [0-9]/{print
  •       $2*1000}'`
557
558   SEPMIN=4
559   CLUSTER_RADIUS=2
560
561   elif [ "$DET" == "raxis" ]; then
562   echo Data from a RAXIS detector
```

```bash
563  DETECTOR="RAXIS MINIMUM_VALID_PIXEL_VALUE=0   OVERLOAD=20000000"
564
565  #let SKIP=768
566  #NX=$(od -t x -j $SKIP -N 4 $FIRSTFRAME |awk 'NR==1{print toupper($2)}'|perl -nle '@array= $_ =~/.{2}/g; print "ibase=16;obase=A;".join("",reverse @array)'|bc)
567  NX=$(python -c 'import struct; f=open("'$FIRSTFRAME'","rb");f.seek(768);print "%.4d"%struct.unpack(">i",f.read(4))')
568  NY=$(python -c 'import struct; f=open("'$FIRSTFRAME'","rb");f.seek(772);print "%.4d"%struct.unpack(">i",f.read(4))')
569
570  DETECTOR_DISTANCE=$(python -c 'import struct; f=open("'$FIRSTFRAME'","rb");f.seek(344);print "-%.4f"%struct.unpack(">f",f.read(4))')
571
572  ORGX=$(python -c 'import struct; f=open("'$FIRSTFRAME'","rb");f.seek(540);print "%.4f"%struct.unpack(">f",f.read(4))')
573  ORGY=$(python -c 'import struct; f=open("'$FIRSTFRAME'","rb");f.seek(544);print "%.4f"%struct.unpack(">f",f.read(4))')
574
575  OSCILLATION_RANGE=$(python -c 'import struct; f=open("'$FIRSTFRAME'","rb");f.seek(524);phis,phie=struct.unpack(">ff",f.read(8));print "%.4f"%(phie-phis)')
576
577  QX=$(python -c 'import struct; f=open("'$FIRSTFRAME'","rb");f.seek(776);print "%.6f"%struct.unpack(">f",f.read(4))')
578  QY=$(python -c 'import struct; f=open("'$FIRSTFRAME'","rb");f.seek(780);print "%.6f"%struct.unpack(">f",f.read(4))')
579
580  X_RAY_WAVELENGTH=$(python -c 'import struct; f=open("'$FIRSTFRAME'","rb");f.seek(292);print "%.6f"%struct.unpack(">f",f.read(4))')
581
582  elif [ "$DET" == "dtrek" ]; then
583  echo "Data from a RAXIS or Saturn or Pilatus detector with dTREK format"
584
585  sed s/\;// tmp2 > tmp1
586  mv tmp1 tmp2
587
588  dname=`grep "DETECTOR_NAMES=" tmp2 | sed -e "s/.*=//"`
589  flip=1
590  if [ "$dname" == "CCD_" ]; then
591  DETECTOR="SATURN MINIMUM_VALID_PIXEL_VALUE=1"
592  dtrek_det="saturn"
593  # Find rotation axis. Warning: currently not support flipping
594  # (det(tmpmat)<0)
595  # I'm not sure this method is really valid - but at least
596  mosflm seems to read this to determine rotation axis.
597  tmpmat=(`grep ${dname}SPATIAL_DISTORTION_VECTORS= tmp2 | tail -1 | sed -e "s/,.*=//"`)
598  rotx=`echo "scale=6; -1.0*${tmpmat[0]}" | bc -l`
599  roty=`echo "scale=6; -1.0*${tmpmat[1]}" | bc -l`
600  rotation_axis="$rotx $roty 0"
601  if [ `echo "(${tmpmat[1]}*${tmpmat[2]})-(${tmpmat[0]}*${tmpmat[3]})/1"|bc` -lt 0 ]; then
602  echo ""
603  echo "WARNING! not-supported SPATIAL_DISTORTION_VECTORS header detected."
604  echo "Please report this to XDSwiki author."
605  fi
606  elif [ "$dname" == "PILT_" ]; then
607  DETECTOR="PILATUS MINIMUM_VALID_PIXEL_VALUE=0"
608  dtrek_det="pilatus"
609  flip=-1
610  SENSOR_THICKNESS=0.45    # TODO: read from header
611  CLUSTER_RADIUS=1.5
612  SEPMIN=3
613  rotation_axis="0 1 0"    # TODO: read from header
614  # 2theta
615  TWOTHETA=`awk '/PILT_GONIO_VALUES=/{print $2}' tmp2`
616  echo TWOTHETA=$TWOTHETA
617  R1=`echo "scale=7;   c($TWOTHETA/$DEGTOR)" | bc -l`
618  R3=`echo "scale=7; -s($TWOTHETA/$DEGTOR)" | bc -l`
619  DIRECTION_OF_DETECTOR_X_AXIS="$R1 0 $R3"
620  elif [ "$dname" == "RX_" ]; then
621  DETECTOR="RAXIS MINIMUM_VALID_PIXEL_VALUE=0"
622  dtrek_det="raxis"
623  else
624  DETECTOR="XXX MINIMUM_VALID_PIXEL_VALUE=XXX"
625  dtrek_det="unknown"
626  fi
627  # find OVERLOAD
628  SATURATED_VALUE=`grep SATURATED_VALUE tmp2 | head -1 | sed s/
629  SATURATED_VALUE=//`
630  DETECTOR="${DETECTOR}  OVERLOAD=${SATURATED_VALUE}"
631  # find X_RAY_WAVELENGTH:
632  X_RAY_WAVELENGTH=(`grep SOURCE_WAVELENGTH tmp2 | head -1 | sed s/
633  SOURCE_WAVELENGTH=//`)
634  X_RAY_WAVELENGTH=${X_RAY_WAVELENGTH[1]}
```

```bash
635  # find NX,NY,QX,QY
636  # NX,NY should be read from *_DETECTOR_DIMENSIONS?
637  NX=`grep SIZE1 tmp2 | tail -1 | sed s/SIZE1=//`
638  NY=`grep SIZE2 tmp2 | tail -1 | sed s/SIZE2=//`
639  DET_SIZE=(`grep ${dname}DETECTOR_SIZE tmp2 | tail -1 | sed s/
     .*_DETECTOR_SIZE=//`)
640  QX=`echo "scale=6; ${DET_SIZE[0]} / $NX" | bc -l`
641  QY=`echo "scale=6; ${DET_SIZE[1]} / $NY" | bc -l`
642
643  # find ORGX, ORGY
644  SPATIAL_DISTORTION_INFO=(`grep ${dname}SPATIAL_DISTORTION_INFO
     tmp2 | tail -1 | sed s/.*_SPATIAL_DISTORTION_INFO=//`)
645  ORGX=${SPATIAL_DISTORTION_INFO[0]}
646  ORGY=${SPATIAL_DISTORTION_INFO[1]}
647
648  # find DETECTOR DISTANCE
649  GONIO_NAMES=(`grep ${dname}GONIO_NAMES= tmp2 | tail -1 | sed s/
     .*_GONIO_NAMES=//`)
650  GONIO_VALUES=(`grep ${dname}GONIO_VALUES= tmp2 | tail -1 | sed s/
     .*_GONIO_VALUES=//`)
651  # GONIO_UNITS=(`grep ${dname}GONIO_UNITS= tmp2 | tail -1 | sed s/
     .*_GONIO_UNITS=//`)
652  for i in `seq 1 ${#GONIO_NAMES[*]}`
653  do
654      idx=$(($i-1))
655      if [ "${GONIO_NAMES[$idx]}" == "Distance" ]; then
656          DETECTOR_DISTANCE="${GONIO_VALUES[$idx]}"
657          # TODO: Check unit!! - ${GONIO_UNITS[$idx]}
658      fi
659      if [ $flip -gt 0 ]; then
660          DETECTOR_DISTANCE="-${GONIO_VALUES[$idx]}"
661          # TODO: Check unit!! - ${GONIO_UNITS[$idx]}
662          echo "using distance <0"
663      fi
664  done
665
666  # find OSCILLATION_RANGE
667  ROTATION=(`grep "^ROTATION=" tmp2 | tail -1 | sed s/ROTATION=//`)
668  OSCILLATION_RANGE=${ROTATION[2]}
669
670
671  elif [ "$DET" == "MAR345" ]; then
672      echo "Data from a Mar345 image plate detector"
673      DETECTOR="MAR345 MINIMUM_VALID_PIXEL_VALUE=0 OVERLOAD=130000"
674      NX=`awk '/FORMAT/{print $2}' tmp2`
675      NY=$NX
676      QX=`awk '/PIXEL/{print $3/1000.}' tmp2`
677      QY=`awk '/PIXEL/{print $5/1000.}' tmp2`
678      if grep -q 'CENTER' tmp2; then
679          echo Beam center found.

680          ORGX=`grep 'CENTER' tmp2 | awk '{print $3}'`
681          ORGY=`grep 'CENTER' tmp2 | awk '{print $5}'`
682      else
683          echo No beam center was found. Setting beam center to the middle
           of the detector.
684          ORGX=`echo $NX / 2 | bc`
685          ORGY=`echo $NY / 2 | bc`
686      fi
687      DETECTOR_DISTANCE=`grep 'DISTANCE' tmp2 | awk '{print
         $2}'`
688      X_RAY_WAVELENGTH=`grep 'WAVELENGTH' tmp2 | awk '{print $2}'`
689      OSCILLATION_RANGE=`grep 'PHI' tmp2 | awk '{print $5-$3}'`
690      TRUSTED_REGION="0 0.99"
691
692  elif [ "$DET" == "OLDMAR" ]; then
693      echo "Data from old type MAR image plate detector"
694      DETECTOR="MAR MINIMUM_VALID_PIXEL_VALUE=0 OVERLOAD=130000"
695      X_RAY_WAVELENGTH=`grep 'WAVELENGTH' tmp2 | awk '{print $2}'`
696      NX=`awk 'NR==2 {print $2}' tmp2`
697      NY=$NX
698      QX=`awk 'NR==2 {print $15}' tmp2`
699      QY=$QX
700      ORGX=`awk 'NR==2 {print $19}' tmp2`
701      ORGY=`awk 'NR==2 {print $20}' tmp2`
702      DETECTOR_DISTANCE=`awk 'NR==2 {print $22}' tmp2`
703      X_RAY_WAVELENGTH=`awk 'NR==2 {print $21}' tmp2`
704      OSCILLATION_RANGE=`awk 'NR==2 {print $24-$23}' tmp2`
705      TRUSTED_REGION="0 0.99"
706      rotation_axis="0 1 0"
707      echo unsure if sign of anomalous signal is correct - please verify
708      or try both hands!

709  elif [ "$DET" == "Bruker-cbf" ]; then
710
711      echo "Data from a Bruker-cbf detector"
712
713      # MINIMUM_NUMBER_OF_PIXELS_IN_A_SPOT:
714      MNOPIAS=6
715      # use complete detector including corners:
716      TRUSTED_REGION="0 1.42"
717      # polarization
718      pol_frac=`awk '/polarizn_source_ratio/{print $2}' tmp2`
719      pol_frac=`echo "${pol_frac}+0.5" | bc -l`
720      OVERLOAD=`awk '/_array_intensities.overload/{print $2}' tmp2`
721      DETECTOR="BRUKER MINIMUM_VALID_PIXEL_VALUE=0 OVERLOAD=${OVERLOAD}"
722      NX=`awk '/X-Binary-Size-Fastest-Dimension/{print $2}' tmp2`
723      NY=`awk '/X-Binary-Size-Second-Dimension/{print $2}' tmp2`
724      QX=`awk '/ELEMENT_X ELEMENT_X/{print $4}' tmp2`
725      QY=`awk '/ELEMENT_Y ELEMENT_Y/{print $4}' tmp2`
726
```

```
727 # ORGX/Y-offsets relative to center of detector:
728 ORGX=`grep " 0 0 ? ?" tmp2 | awk '/ H /{print $2}'`
729 ORGY=`grep " 0 0 ? ?" tmp2 | awk '/ V /{print $2}'`
730 # total ORGX/Y
731 ORGX=`echo "scale=2; ${NX}/2+($ORGX/$QX)" | bc -l`
732 ORGY=`echo "scale=2; ${NY}/2-($ORGY/$QY)" | bc -l`
733 •
734 DETECTOR_DISTANCE=`grep "0 0 ? ?" tmp2 | awk '/DX /{print $2}'`
735 •
736 X_RAY_WAVELENGTH=`awk '/diffrn_radiation_wavelength.wavelength/ {print $2}' tmp2`
737 # fix 16.3.20: instead of print, use printf "%.5f", because bc does
    not accept e.g. 3.1e-005
738 OMEGA=`awk '/OMEGA \? \? \?/{printf "%.5f",$5}' tmp2`
739 DELTAOMEGA=`awk '/OMEGA \? \? \?/{printf "%.5f",$6}' tmp2`
740 PHI=`awk '/PHI \? \? \?/{printf "%.5f",$5}' tmp2`
741 DELTAPHI=`awk '/PHI \? \? \?/{printf "%.5f",$6}' tmp2`
742 KAPPA=`awk '/CHI \? \? \?/{printf "%.5f",$5}' tmp2`
743 # echo OMEGA DELTAOMEGA PHI DELTAPHI KAPPA= $OMEGA $DELTAOMEGA $PHI
    $DELTAPHI $KAPPA
744 •
745 # test whether the absolute value of deltaomega is > absolute value
    of deltaomega
746 if (( $(echo "${DELTAPHI}^2 > ${DELTAOMEGA}^2"|bc -l) )); then
747     echo PHI scan
748     R3=`echo "scale=7; s($KAPPA/$DEGTOR)*s($OMEGA/$DEGTOR)" | bc -l`
749     R1=`echo "scale=7; s($KAPPA/$DEGTOR)*c($OMEGA/$DEGTOR)" | bc -l`
750     R2=`echo "scale=7; c($KAPPA/$DEGTOR)" | bc -l`
751     rotation_axis="$R1 $R2 $R3"
752     OSCILLATION_RANGE=${DELTAPHI}
753     STARTING_ANGLE=${PHI}
754     # here we could check if DELTAPHI is <0, and if so, negate it and
    rotation_axis
755 else
756     echo OMEGA scan
757     rotation_axis="0 -1 0"
758     OSCILLATION_RANGE=${DELTAOMEGA}
759     STARTING_ANGLE=${OMEGA}
760     # here we could check if DELTAOMEGA is <0, and if so, negate it and
    rotation_axis
761 fi
762 echo STARTING_ANGLE= $STARTING_ANGLE          ! only read by
    IDXREF
763 •
764 # 2theta
765 TWOTHETA=`awk '/TWOTHETA \? \? \?/{print $5}' tmp2`
766 echo TWOTHETA=$TWOTHETA
767 R1=`echo "scale=7; c($TWOTHETA/$DEGTOR)" | bc -l`
768 R3=`echo "scale=7; s($TWOTHETA/$DEGTOR)" | bc -l`
769 DIRECTION_OF_DETECTOR_X_AXIS="$R1 0 $R3"

770 # end of Bruker-cbf section
771 else
772     echo should never come here
773     exit 1
774 fi
775 •
776 echo ORGX= $ORGX ORGY= $ORGY – check these values with adxv !
777 echo DETECTOR_DISTANCE= $DETECTOR_DISTANCE ! only read by XYCORR,
    IDXREF
778 echo OSCILLATION_RANGE= $OSCILLATION_RANGE  ! only read by IDXREF
779 echo X-RAY_WAVELENGTH= $X_RAY_WAVELENGTH   ! only read by
    IDXREF
780 •
781 # now we know everything that is required to generate XDS.INP
782 •
783 cat > XDS.INP << eof
784 ! written by generate_XDS.INP version $REVISION
785 JOB= XYCORR INIT COLSPOT IDXREF DEFPIX INTEGRATE CORRECT
786 ORGX= $ORGX ORGY= $ORGY  ! values from frame header; only read by
    XYCORR, IDXREF
787 $COMMENT_ORGXY
788 DETECTOR_DISTANCE= $DETECTOR_DISTANCE !read by XYCORR, IDXREF.
    Negative if detector normal points to crystal.
789 OSCILLATION_RANGE= $OSCILLATION_RANGE
790 STARTING_ANGLE= $STARTING_ANGLE
791 X-RAY_WAVELENGTH= $X_RAY_WAVELENGTH
792 NAME_TEMPLATE_OF_DATA_FRAMES=$NAME_TEMPLATE_OF_DATA_FRAMES
793 ! REFERENCE_DATA_SET=xxx/XDS_ASCII.HKL ! e.g. to ensure consistent
    indexing
794 DATA_RANGE=$DATA_RANGE
795 SPOT_RANGE=$SPOT_RANGE
796 ! BACKGROUND_RANGE=1 10 ! rather use defaults (first 5 degree of
    rotation)
797 •
798 SPACE_GROUP_NUMBER= 14             ! 0 if unknown
799 UNIT_CELL_CONSTANTS= 16.71 18.77 12.54 90 108.11 90  ! put correct
    values if known
800 INCLUDE_RESOLUTION_RANGE=50 0  ! after CORRECT, insert high resol
    limit; re-run CORRECT
801 ! IDXREF now obeys INCLUDE_RESOLUTION_RANGE and
    EXCLUDE_RESOLUTION_RANGE to exclude ice-rings
802 •
803 FRIEDEL'S_LAW=FALSE        ! This acts only on the CORRECT step
804 ! If the anom signal turns out to be, or is known to be, very low
    or absent,
805 ! use FRIEDEL'S_LAW=TRUE instead (or comment out the line); re-run
    CORRECT
806 •
```

```
807  ! remove the "!" in the following line: (is removed for avalanX, dafs experiments)
808  STRICT_ABSORPTION_CORRECTION=TRUE
809  ! if the anomalous signal is strong: in that case, in CORRECT.LP the three
810  ! "CHI^2-VALUE OF FIT OF CORRECTION FACTORS" values are significantly> 1, e.g. 1.5
811
812  ! exclude (mask) untrusted areas of detector, e.g. beamstop shadow :
813  ! UNTRUSTED_RECTANGLE= 1800 1950 2100 2150 ! x-min x-max y-min y-max ! repeat
814  ! UNTRUSTED_ELLIPSE= 2034 2070 1850 2240 ! x-min x-max y-min y-max ! if needed
815  ! UNTRUSTED_QUADRILATERAL= x1 y1 x2 y2 x3 y3 x4 y4 ! see documentation
816
817  ! parameters with changes wrt default values:
818  TRUSTED_REGION=$TRUSTED_REGION
819  VALUE_RANGE_FOR_TRUSTED_DETECTOR_PIXELS=3000. 30000. ! often 7000 or 8000 is ok, 3000 to 30000 for small molecules
820  STRONG_PIXEL= 7          ! COLSPOT: only use strong reflections (default is 3)
821  MINIMUM_NUMBER_OF_PIXELS_IN_A_SPOT= 6        !default of 6 is sometimes to high
822
823  !!! The following were added by Ludmila Leroy for avalanX dealing with small molecules:
824
825  TEST_RESOLUTION_RANGE= 10. 1.
826  MINIMUM_FRACTION_OF_INDEXED_SPOTS=0.2
827
828
829  !The following is the untrusted rectangle from the beam sropper shadow that should be added manually
830  !by avalanX users, or otherwise, commentted. The values change for each particular experiment.
831
832  UNTRUSTED_RECTANGLE= 0 789 841 899 ! for the cosgay dafs experiment LNLS
833
834  ! close spots/long cell axis: reduce SEPMIN and CLUSTER_RADIUS from their defaults of 7 and 3.5
835  SEPMIN=$SEPMIN  CLUSTER_RADIUS=$CLUSTER_RADIUS ! 4 and 2 for Pixel Array Detectors
836  ! since XDS 01-MAR-2015, POSITION supersedes DISTANCE.
837  ! nowadays headers are usually correct so refine POSITION in INTEGRATE but not IDXREF if low to medium resolution
838  ! however, if the spots from COLSPOT extend to 2A then POSITION could, and if 1.5A POSITION should be refined
839  REFINE(IDXREF)=CELL BEAM ORIENTATION AXIS ! add POSITION if high
840  resolution, or DETECTOR_DISTANCE inaccurate
841  REFINE(INTEGRATE)= POSITION BEAM ORIENTATION ! AXIS CELL . If 1.5A or higher it is ok to refine CELL
842  ! REFINE(CORRECT)=CELL BEAM ORIENTATION AXIS POSITION ! Default is: refine everything
843
844  ! parameters specifically for this detector and beamline:
845  DETECTOR= $DETECTOR
846  SENSOR_THICKNESS= $SENSOR_THICKNESS
847  ! attention CCD detectors: for very high resolution (better than 1A) make sure to specify SILICON
848  ! as about 32* what CORRECT.LP suggests (absorption of phosphor is much higher than that of silicon).
849  ! Better: read the article http://strucbio.biologie.uni-konstanz.de/xdswiki/index.php/SILICON .
850  NX= $NX NY= $NY  QX= $QX  QY= $QY ! to make CORRECT happy if frames are unavailable
851
852  eof
853
854  if [ "$DET" == "eiger" ] && [ "$is_h5" == 1 ]; then
855    if [ "$DLS" == 0 ] ; then
856      if [ -e /usr/local/lib64/dectris-neggia.so ]; then
857        echo LIB=/usr/local/lib64/dectris-neggia.so >> XDS.INP
858      else
859        echo !LIB=/usr/local/lib64/dectris-neggia.so >> XDS.INP
860        echo /usr/local/lib64/dectris-neggia.so was not found - specify location manually!
861      fi
862
863    else
864      if [ -e /usr/local/lib64/durin-plugin.so ]; then
865        echo LIB=/usr/local/lib64/durin-plugin.so >> XDS.INP
866        echo LIB= line was written to XDS.INP
867      else
868        echo !LIB=/usr/local/lib64/durin-plugin.so >> XDS.INP
869        echo /usr/local/lib64/durin-plugin.so was not found - specify location manually!
870      fi
871    fi
872  fi
873  if [ "$DET" == "raxis" -o "$dtrek_det" == "raxis" ]; then
874    cat >> XDS.INP << eof
875  DIRECTION_OF_DETECTOR_X-AXIS=1 0 0
876  DIRECTION_OF_DETECTOR_Y-AXIS=0 -1 0
877  INCIDENT_BEAM_DIRECTION=0 0 1      ! only read by IDXREF
878  ROTATION_AXIS=0 1 0                ! only read by IDXREF
879  !FRACTION_OF_POLARIZATION=0.98     ! uncomment if synchrotron; only used by CORRECT
```

```bash
880 POLARIZATION_PLANE_NORMAL=1 0 0   ! only used by CORRECT
881 eof
882 else
883 if [ "$rotation_axis" != "" ]; then
884 echo "ROTATION_AXIS= $rotation_axis   ! only read by IDXREF" >>
    XDS.INP
885 elif [ "$REVERSE_PHI" == "no" ]; then
886 echo 'ROTATION_AXIS=1 0 0   ! Australian Synchrotron, SERCAT ID-22
    (?), APS 19-ID (?), ESRF BM30A, SPring-8, SSRF need -1 0 0.
    Diamond ID24 needs 0 -1 0' >> XDS.INP
887 else
888 echo 'ROTATION_AXIS=-1 0 0   ! if this is wrong, please contact
    author.' >> XDS.INP
889 fi
890 if [ "$dtrek_det" == "saturn" ]; then
891 cat >> XDS.INP << eof
892 DIRECTION_OF_DETECTOR_X-AXIS=-1 0 0
893 DIRECTION_OF_DETECTOR_Y-AXIS= 0 1 0
894 eof
895 else
896 cat >> XDS.INP << eof
897 DIRECTION_OF_DETECTOR_X-AXIS=$DIRECTION_OF_DETECTOR_X_AXIS
898 DIRECTION_OF_DETECTOR_Y-AXIS=0 1 0
899 eof
900 fi
901 cat >> XDS.INP << eof
902 INCIDENT_BEAM_DIRECTION=0 0 1   ! only read by IDXREF
903 FRACTION_OF_POLARIZATION=${pol_frac}   ! better value is provided
    by beamline staff!
904 POLARIZATION_PLANE_NORMAL=0 1 0   ! only used by CORRECT
905 eof
906 fi
907 cat >> XDS.INP << eof
908 !used by DEFPIX and CORRECT to exclude ice-reflections / ice rings
909 !fine-grained list is in Thorn et al http://journals.iucr.org/d/
    issues/2017/09/00/hi5647/index.html
910 !EXCLUDE_RESOLUTION_RANGE= 3.93 3.87 !ice-ring at 3.897 Angstrom
911 !EXCLUDE_RESOLUTION_RANGE= 3.70 3.64 !ice-ring at 3.669 Angstrom
912 !EXCLUDE_RESOLUTION_RANGE= 3.47 3.41 !ice-ring at 3.441 Angstrom
913 !EXCLUDE_RESOLUTION_RANGE= 2.70 2.64 !ice-ring at 2.671 Angstrom
914 !EXCLUDE_RESOLUTION_RANGE= 2.28 2.22 !ice-ring at 2.249 Angstrom
915 !EXCLUDE_RESOLUTION_RANGE= 2.102 2.042 !ice-ring at 2.072 Angstrom
   — strong
916 !EXCLUDE_RESOLUTION_RANGE= 1.978 1.918 !ice-ring at 1.948 Angstrom
   — weak
917 !EXCLUDE_RESOLUTION_RANGE= 1.948 1.888 !ice-ring at 1.918 Angstrom
   — strong
918 !EXCLUDE_RESOLUTION_RANGE= 1.913 1.853 !ice-ring at 1.883 Angstrom
   — weak
919 !EXCLUDE_RESOLUTION_RANGE= 1.751 1.691 !ice-ring at 1.721 Angstrom
   — weak
920 ! additional ice-ring resolution ranges: 1.524 1.519, 1.473 1.470,
    1.444 1.440, 1.372 1.368, 1.367 1.363,
    1.299 1.296, 1.275 1.274, 1.261 1.259, 1.224 1.222, 1.171 1.168,
    1.124 1.122 (compiled by GlobalPhasing)
921 eof
922 if [ "$DET" == "adsc-CMOS1" ]; then
923 echo "DELPHI=15 ! refine less often than the default of 5" >>
    XDS.INP
924 elif [ "$DET" == "Bruker-cbf" ]; then
925 echo UNTRUSTED_RECTANGLE= 0 1468   2451 2631   >> XDS.INP
926 elif [ "$DET" == "pilatus" -o "$DET" == "eiger" ]; then
927 cat >> XDS.INP << eof
928 NUMBER_OF_PROFILE_GRID_POINTS_ALONG_ALPHA/BETA=13 ! Default is 9 -
    Increasing may improve data
929 NUMBER_OF_PROFILE_GRID_POINTS_ALONG_GAMMA=13   ! accuracy,
    particularly if finely-sliced on phi,
930 !                                                and does not
931 !                                                seem to have any downsides.
932 !
933 eof
934 if [ $NX == "1475" ]; then
935 cat >> XDS.INP << eof
936 if ! grep -q flat_field tmp2 ; then
937 cat >> XDS.INP << eof
938 ! flat_field correction; they cut away one additional pixel
    adjacent
939 ! to each UNTRUSTED_RECTANGLE
940 ! the following specifications are for a detector _without_ proper
941 !EXCLUSION OF VERTICAL DEAD AREAS OF THE PILATUS 2M DETECTOR
942 UNTRUSTED_RECTANGLE= 980   990   0 1680
    UNTRUSTED_RECTANGLE= 486   496   0 1680
943 !EXCLUSION OF HORIZONTAL DEAD AREAS OF THE PILATUS 2M DETECTOR
944 UNTRUSTED_RECTANGLE= 0 1476   194 214
945 UNTRUSTED_RECTANGLE= 0 1476   406 426
946 UNTRUSTED_RECTANGLE= 0 1476   618 638
947 UNTRUSTED_RECTANGLE= 0 1476   830 850
948 UNTRUSTED_RECTANGLE= 0 1476   1042 1062
949 UNTRUSTED_RECTANGLE= 0 1476   1254 1274
950 UNTRUSTED_RECTANGLE= 0 1476   1466 1486
951 eof
952 else
953 cat >> XDS.INP << eof
954 !EXCLUSION OF VERTICAL DEAD AREAS OF THE PILATUS 2M DETECTOR
955 UNTRUSTED_RECTANGLE= 487 495   0 1680
956 UNTRUSTED_RECTANGLE= 981 989   0 1680
957 !EXCLUSION OF HORIZONTAL DEAD AREAS OF THE PILATUS 2M DETECTOR
958 UNTRUSTED_RECTANGLE= 0 1476   195 213
959 UNTRUSTED_RECTANGLE= 0 1476   407 425
```

```
 960     UNTRUSTED_RECTANGLE=    0 1476  619  637
 961     UNTRUSTED_RECTANGLE=    0 1476  831  849
 962     UNTRUSTED_RECTANGLE=    0 1476 1043 1061
 963     UNTRUSTED_RECTANGLE=    0 1476 1255 1273
 964     UNTRUSTED_RECTANGLE=    0 1476 1467 1485
 965 eof
 966 fi
 967 elif [ $NX == "2463" ]; then
 968 # Pilatus 6M
 969 # FIXME: here we could test if a Flat_field correction was applied
   •
 970 # like we do for 2M
   •
 971     cat >> XDS.INP << eof
 971     UNTRUSTED_RECTANGLE=  487  495    0 2528
 972     UNTRUSTED_RECTANGLE=  981  989    0 2528
 973     UNTRUSTED_RECTANGLE=1475 1483    0 2528
 974     UNTRUSTED_RECTANGLE=1969 1977    0 2528
 975     UNTRUSTED_RECTANGLE=    0 2464  195  213
 976     UNTRUSTED_RECTANGLE=    0 2464  407  425
 977     UNTRUSTED_RECTANGLE=    0 2464  619  637
 978     UNTRUSTED_RECTANGLE=    0 2464  831  849
 979     UNTRUSTED_RECTANGLE=    0 2464 1043 1061
 980     UNTRUSTED_RECTANGLE=    0 2464 1255 1273
 981     UNTRUSTED_RECTANGLE=    0 2464 1467 1485
 982     UNTRUSTED_RECTANGLE=    0 2464 1679 1697
 983     UNTRUSTED_RECTANGLE=    0 2464 1891 1909
 984     UNTRUSTED_RECTANGLE=    0 2464 2103 2121
 985     UNTRUSTED_RECTANGLE=    0 2464 2315 2333
 986 eof
 987 elif [ $NX == "3110" -a $NY == "3269" ]; then
 988 # Eiger 9M
 989     cat >> XDS.INP << eof
 990 !EXCLUSION OF VERTICAL DEAD AREAS OF THE EIGER 9M DETECTOR
 991     UNTRUSTED_RECTANGLE= 1029 1042    0 3269
 992     UNTRUSTED_RECTANGLE= 2069 2082    0 3269
 993 !EXCLUSION OF HORIZONTAL DEAD AREAS OF THE EIGER 9M DETECTOR
 994     UNTRUSTED_RECTANGLE=    0 3110  513  553
 995     UNTRUSTED_RECTANGLE=    0 3110 1064 1104
 996     UNTRUSTED_RECTANGLE=    0 3110 1615 1655
 997     UNTRUSTED_RECTANGLE=    0 3110 2166 2206
 998     UNTRUSTED_RECTANGLE=    0 3110 2717 2757
 999 eof
1000 elif [ $NX == "4150" -a $NY == "4371" ]; then
1001 # Eiger 16M
1002     cat >> XDS.INP << eof
1003 !EXCLUSION OF HORIZONTAL DEAD AREAS OF THE EIGER 16M DETECTOR + ONE
   •
     PIXEL ON EACH SIDE
1004     UNTRUSTED_RECTANGLE=    0 4150  513  553
1005     UNTRUSTED_RECTANGLE=    0 4150 1064 1104
1006     UNTRUSTED_RECTANGLE=    0 4150 1615 1655
1007     UNTRUSTED_RECTANGLE=    0 4150 2166 2206
1008     UNTRUSTED_RECTANGLE=    0 4150 2717 2757
1009     UNTRUSTED_RECTANGLE=    0 4150 3268 3308
1010     UNTRUSTED_RECTANGLE=    0 4150 3819 3859
1011 !EXCLUSION OF VERTICAL DEAD AREAS OF THE EIGER 16M DETECTOR + ONE
     PIXEL ON EACH SIDE
1012     UNTRUSTED_RECTANGLE= 1029 1042    0 4371
1013     UNTRUSTED_RECTANGLE= 2069 2082    0 4371
1014     UNTRUSTED_RECTANGLE= 3109 3122    0 4371
1015 eof
1016 fi
1017 fi
1018 echo XDS.INP is ready for use. The file has only the most important
   • keywords.
1019 echo Full documentation, including complete detector templates, is
   • at
1020 echo http://www.mpimf-heidelberg.mpg.de/~kabsch/xds . More
   • documentation in XDSwiki
1021 echo After running xds, inspect, using XDS-Viewer, at least the
   • beamstop mask in
1022 echo BKGPIX.cbf, and the agreement of predicted and observed spots
   • in FRAME.cbf!
1023 rm -f tmp1 tmp2
1024
```

```python
import os
import shutil
from sys import argv

### avalanx.inp

### the following parameters are global AvalanX parameters


# ##locations

# DATASETS_NAME = 'py100'

# AVALANX_SCRIPTS_DIR = '/Users/ludmilaleroy/XRD/avalanx/avalanx-
# python'
# WORK_DIR_PATH = '/Users/ludmilaleroy/XRD/avalanx/outtest_'
# DATASETS_DIR = '/Users/ludmilaleroy/XRD/RAWXRD_DATA/diamond'

# ##



# ### the following parameters are input values for XDS
# ORGX= 241
# ORGY= 414
# UNIT_CELL = '7.3 22.12 14.99 90 97 90'
# SPACE_GROUP_NUMBER = 14
# STRONG_PIXEL = 6
# MINIMUM_NUMBER_OF_PIXELS_IN_A_SPOT = 6
# GENINHO= 'geninpavlxRUN.INP'
# FRIEDELS_LAW = 'TRUE'

# ### the following parameters are input values for avalanx_dafs

# NAME_HKL_FILE ='XDS_ASCII_scaled_2.HKL' #'INTEGRATE.HKL'
# NAME_INP = 'XDS.INP'
# REFLECTION_1 = ['2','0','0']
# REFLECTION_2 = ['1','0','0']
# REFLECTION_3 = ['4','0','0']
# REFLECTION_4 = ['1','1','1']
# REFLECTION_5 = ['-2','0','0']
# REFLECTION_6 = ['-1','0','0']
# REFLECTION_7 = ['-4','0','0']
# REFLECTION_8 = ['-1','-1','-1']
# REFLECTION_9 = ['0','2','0']
# REFLECTION_10 = ['0','0','2']
# REFLECTION_11 = ['0','4','0']
# REFLECTION_12 = ['3','0','0']


# ### the following parameters are output graph settings


# ENERGY_UNIT = 'ANGS'        ## NM      EV      CM-1
# PLOT_X = 'ENERGY'
# PLOT_Y = 'INTENSITY'        ## ABS_COEFF


# ### MERGE=TRUE
# ### STRICT_ABSORPTION_CORRECTION=TRUE


### .ins header and modifiables


# TITL cosqpy2_100k_a.res in P-1
# REM Old TITL cosqpy sls 10062020 pmx10 300k
# REM SHELXT solution in P-1: R1 0.213, Rweak 0.000, Alpha 0.051
# REM <I/s> 0.000 for 0 systematic absences, Orientation as input
# REM Formula found by SHELXT: Co2 08 C100 N4
# CELL 0.82655 17.7 18.77 13.226 90 96.684 90
# ZERR 1 0.001 0.1 0.1 0 0.1 0
# LATT 1
# SFAC Co O C N H
# DISP C 0.0052 0.0023 16.0976
# DISP Co 0.3434 1.2687 6068.3518
# DISP H -0 0 0.63
# DISP N 0.0094 0.0046 28.7478
# DISP O 0.0162 0.0086 48.7782
# UNIT 1 4 82 6 105

# L.S. 4
# PLAN 41
# CONF
# BOND
# list 4
# fmap 2
# MORE -1
# BOND $H
# ACTA
# WGHT 0.1
# FVAR 0.35255
# REM <olex2.extras>
# REM <HklSrc "%./cosqpy2_100k.hkl">
# REM </olex2.extras>

# Define inp file address
inp_address = argv[1]  # input file - user defined
                       # for after: write instructions of
                       # how it must be written
```

```python
 99  # Execute general definitions
100  fh = open(inp_address, 'r')
101  for line in fh:
102      exec(line)
103
104  ### avalanx_scale global variables
105
106  avalanx_step ='refine'
107
108  ## creating a refine folder
109
110  refine_folder_path = WORK_DIR_PATH + os.sep + avalanx_step
111  if not os.path.exists(refine_folder_path):
112      os.mkdir(refine_folder_path)
113
114  os.mkdir(refine_folder_path + os.sep + DATASETS_NAME)
115
116  ### makes a list of all the directories in the dataprocessing folder
117
118  avxdp_folders = []
119
120  list_avxdp = os.listdir(WORK_DIR_PATH + os.sep + 'dataprocessing' +
121  os.sep + DATASETS_NAME )
122  print(list_avxdp)
123  for direc in list_avxdp:
124      condition = os.path.isdir(WORK_DIR_PATH + os.sep +
125  'dataprocessing' + os.sep + DATASETS_NAME + os.sep + direc)
126      print(condition)
127      if condition:
128          avxdp_folders.append(direc)
129
130  print(avxdp_folders)
131
132  ## defining the function that modifies XDSCONV.INP
133
134  ### XDSCONV.INP standard
135
136  # INPUT_FILE=scaled.ahkl
137  # !INCLUDE_RESOLUTION_RANGE=50 1   ! optional
138  # OUTPUT_FILE=afterconv.hkl   SHELX    ! Warning: do _not_ name this
139  file "temp.mtz"!
140  # FRIEDEL'S_LAW=FALSE         ! default is FRIEDEL'S_LAW=TRUE
141
142  def xconv_inp_modifier(file_name):
143      f_fonte = open(file_name, 'r')
144      f_dest = open('temp.INP', 'w')
145
146      for line in f_fonte:
147          if line.startswith('INPUT_FILE'):
148              f_dest.write('INPUT_FILE= %s \n'    % NAME_HKL_FILE)
149
150          elif line.startswith('!INCLUDE_RESOLUTION_RANGE'):
151              f_dest.write('INCLUDE_RESOLUTION_RANGE= %s \n' %
152  INCLUDE_RESOLUTION_RANGE)
153
154          elif line.startswith('OUTPUT_FILE'):
155              f_dest.write('OUTPUT_FILE= xdsconv_output.hkl   SHELX \n')
156          elif line.startswith('FRIEDEL'):
157              f_dest.write('  FRIEDEL' + "\"" + 'S_LAW= %s' %
158  FRIEDELS_LAW)
159
160          else:
161              f_dest.write(line)
162      f_dest.close()
163      f_fonte.close()
164
165      os.rename('temp.INP', file_name)
166      return file_name
167
168  # função que busca o wavelength utilizado no dataset pra escrever no
169  CELL do .ins
170  # dentro do for onde chamaremos essa função, endereco = WORK_DIR/
     dataprocessing/datasets_name/folder/XDS.INP
171
172  def search_wavelength(endereco, snippet='X-RAY_WAVELENGTH'):
173
174      fh = open(endereco, 'r')
175      energy = None
176      for line in fh:
177          if line.startswith(snippet):
178              parts = line.split('=')
179              energy = float(parts[1])
180              print(parts[1])
181
182      return energy
183
184  ### ESSA FUNÇÃO É RECRUTADA NO INS_MODIFIER ONLY
185
186  # função que busca a célula refinada dada pelo CORRECT para
187  colocarmos no CELL do .ins
188  # dentro do for onde chamaremos essa função, endereco = WORK_DIR/
     dataprocessing/datasets_name/folder/CORRECT.LP
189
```

```python
190     def search_correct_cell(endereco, snippet=' UNIT CELL PARAMETERS'):
191
192         fh = open(endereco, 'r')
193         correct_cell = None
194         for line in fh:
195             if line.startswith(snippet):
196     #            print(str(line))
197                 parts = line.split()
198                 correct_cell_parts = parts[3:]
199                 correct_cell = parts[3]+' '+parts[4]+' '+parts[5]+'
200     '+parts[6]+' '+parts[7]+' '+parts[8]
    #            print(correct_cell)
201
202         return correct_cell
203
204     ### ### ESSA FUNÇÃO É RECRUTADA NO INS_MODIFIER ONLY
205
206     # função que busca os erros na célula refinada dada pelo CORRECT
207     # para colocarmos no ZERR do .ins
    # dentro do for onde chamaremos essa função, endereco = WORK_DIR/
    dataprocessing/datasets_name/folder/CORRECT.LP
208
209     def search_correct_cell_err(endereco, snippet=' E.S.D. OF CELL
    PARAMETERS'):
210
211         fh = open(endereco, 'r')
212         correct_cell_err = None
213         for line in fh:
214             if line.startswith(snippet):
215     #            print(str(line))
216                 parts = line.split()
217                 correct_cell_err_parts = parts[4:]
218                 correct_cell_err =str(float(parts[4]))+'
    '+str(float(parts[5]))+' '+str(float(parts[6]))+'
    '+str(float(parts[7]))+' '+str(float(parts[8]))+'
    '+str(float(parts[9]))
                    print(correct_cell_err)
219
220
221         return correct_cell_err
222
223
224     ### defining the function that modifies the model.ins
225     #### from CORRECT.LP
226     ### E.S.D. OF CELL PARAMETERS   1.1E-02 5.7E-03 5.1E-03 0.0E+00 1.1E-
    02 0.0E+00
227     ### UNIT CELL PARAMETERS       18.181    18.912    13.341  90.000
    96.186  90.000
228
229
230     # TITL cosapvpv2 100k a.res in P-1

231     # CELL 0.82655 17.7 18.77 13.226 90 96.684 90
232     # ZERR 1 0.001 0.1 0.1 0 0.1 0
233     # LATT 1
234     # SFAC Co O C N H
235     # DISP C 0.0052 0.0023 16.0976
236     # DISP Co 0.3434 1.2687 6068.3518
237     # DISP H -0 0 0.63
238     # DISP N 0.0094 0.0046 28.7478
239     # DISP O 0.0162 0.0086 48.7782
240     # UNIT 1 4 82 6 105
241
242     # L.S. 4
243     # PLAN 41
244     # CONF
245     # BOND
246     # list 4
247     # fmap 2
248     # MORE -1
249     # BOND $H
250     # ACTA
251     # WGHT 0.1
252     # FVAR 0.35255
253
254
255
256
257     REM_INS = 'REM this .ins file has been modified by avalanX refine
    \nREM dataset folder = %s/%s  \n'
258
259
260     def ins_modifier(ins_address, folder):
261
262         ## ins_address is the ins that has just been copied to the folder
263
264         f_fonte = open(ins_address, 'r')
265         f_dest = open('temp.INP', 'w')
266
267         for line in f_fonte:
268             if line.startswith('TITL'):
269                 f_dest.write(line + '\n' + REM_INS % (DATASETS_NAME,
    folder))
270
271             elif line.startswith('CELL'):
272                 folder_path =
    WORK_DIR_PATH+os.sep+'dataprocessing'+os.sep+DATASETS_NAM
    E+os.sep+folder
273                 wavelength = search_wavelength(folder_path+'/XDS.INP')
274                 correct_cell = search_correct_cell(folder_path+'/
    CORRECT.LP')
275                 f_dest.write('CELL ' + str(wavelength) + ' ' +
```

```python
                correct_cell + '\n')

        elif line.startswith('ZERR'):
            folder_path =
WORK_DIR_PATH+os.sep+'dataprocessing'+os.sep+DATASETS_NAM
E+os.sep+folder
            correct_cell_err = search_correct_cell_err(folder_path+'/
CORRECT.LP')
            f_dest.write('ZERR ' + UNITS_PER_CELL + ' ' +
correct_cell_err + '\n')

        elif line.startswith('SHEL'):
            f_dest.write('SHEL %s \n' % INCLUDE_RESOLUTION_RANGE)

        else:
            f_dest.write(line)

    f_dest.close()
    f_fonte.close()

    os.rename('temp.INP', ins_address)
    return ins_address


### create a folder to work on the refinement process from the
model.ins

for folder in avxdp_folders:
    ref_dir = WORK_DIR_PATH + os.sep + avalanx_step + os.sep +
DATASETS_NAME + os.sep + 'avxref_'+folder
    os.mkdir(ref_dir)

    ### copies .HKL and model .ins and xdsconv.INP

    hkl_file_path = WORK_DIR_PATH + os.sep + folder + os.sep + 'dataprocessing' +
os.sep + DATASETS_NAME + os.sep + folder + os.sep + NAME_HKL_FILE
    correct_file_path = WORK_DIR_PATH + os.sep + 'dataprocessing' +
os.sep + DATASETS_NAME + os.sep + folder + os.sep + 'CORRECT.LP'

    if os.path.exists(hkl_file_path):
        shutil.copy(hkl_file_path, ref_dir)
        shutil.copy(correct_file_path, ref_dir)

    else:
        print('The folder %s does not have the required files : %s
and/or CORRECT.LP' % (folder, NAME_HKL_FILE))
        continue

    shutil.copy(INS_MODEL_ADDRESS, ref_dir + os.sep +
'given_model.ins')
    shutil.copy(AVALANX_SCRIPTS_DIR + os.sep + 'XDSCONV.INP',
ref_dir)

    ### modifies XCONV.INP and runs xdsconv
    xconv_inp_modifier('XDSCONV.INP')

    os.chdir(ref_dir)
    ### (I am at refine/folder/ from now on until this iteration
finishes)

    os.system('xdsconv')

    ### rename all files with the folder name
    shutil.copy(ref_dir + os.sep + 'xdsconv_output.hkl', ref_dir +
os.sep + str(folder) + '.hkl')
    shutil.copy(ref_dir + os.sep + 'given_model.ins', ref_dir +
os.sep + str(folder) + '.ins')

    ### call a function to modify ins with the proper parameters
    ### and write a remark on .ins about the dataset and avalax work
    new_ins = ins_modifier(ref_dir + os.sep + str(folder) + '.ins',
folder)

    ### call SHELXL
    os.system('shelxl ' + str(folder))
```

```python
import os
import shutil
from sys import argv


def res_modifier(res_file):

    ### the res file should have the name: folder.res

    f_fonte = open(res_file, 'r')
    f_dest = open('temp.res', 'w')

    for line in f_fonte:

        if line.startswith('REM    WGHT'):
            parts = line.split()
            f_dest.write(parts[1] + ' ' + parts[2] + ' ' + parts[3] +
            '\nANIS')


        else:
            f_dest.write(line)

    f_dest.close()
    f_fonte.close()

    os.rename('temp.res', res_file)
    return res_file




inp_address = argv[1] # input file - user defined
                      # for after: write instructions of
                      # how it must be written


# Execute general definitions
fh = open(inp_address, 'r')
for line in fh:
    exec(line)

### avalanx_scale global variables

avalanx_step ='refine_anis'


## creating a refine folder

refine_folder_path = WORK_DIR_PATH + os.sep + avalanx_step
if not os.path.exists(refine_folder_path):
    os.mkdir(refine_folder_path)


## copies the DATASETS_NAME folder with all avalanx_refine output to
# the new refine_anis
shutil.copytree(WORK_DIR_PATH + os.sep + 'refine' + os.sep +
DATASETS_NAME, refine_folder_path + os.sep + DATASETS_NAME)

list_refined_datasets = os.listdir(refine_folder_path + os.sep +
DATASETS_NAME)

for dir in list_refined_datasets:
    dirsplit = dir.split('avxref_')
    folder = dirsplit[1]
    os.chdir(refine_folder_path + os.sep + DATASETS_NAME + os.sep +
dir)

    os.rename(folder + '.ins', folder + '.ins.old')
    shutil.copy(folder + '.res', folder + '.res.old')
    res_modifier(folder + '.res')
    os.rename(folder + '.res', folder + '.ins')
    os.system('shelxl ' + folder)
```

```python
import os
from shutil import copyfile
import numpy as np
import matplotlib.pyplot as plt
from scipy.cluster.vq import kmeans, vq
# import


def wav2ev(x):
    return 12398.4193/x


def search_reflection(reflection, endereco):
    """
    """

    """
    dados = []

    fh = open(endereco, 'r')
    for line in fh:
        line0 = line.split()
        if line0[0:3] == reflection:
            data = [float(item) for item in line0[3:]]
            dados.append(data)
    fh.close()

    return dados


def search_energy(endereco, snippet="'X-RAY_WAVELENGTH'"):
    fh = open(endereco, 'r')
    Energy = None
    for line in fh:
        if line.startswith(snippet):
            parts = line.split('=')
            Energy = float(parts[1])
            # print(parts[1])
    return Energy


def split_multiple_reflection(data, multiplicity):
    psi = data[:, IDX_PSI]
    codebook, distortion = kmeans(psi, multiplicity)
    ######################################################
    ######################################################
    ### Tratar uma possível má clusterização
    ######################################################333
    code, dist = vq(psi, codebook)
    split_data = []
    for k in range(multiplicity):
        split_data.append(data[code==k])

    return split_data


def dafs_reflection_raw(reflection):
    ######################################################
    ######################################################
    # avalanx_step = "avalanx_dafs"

    if not os.path.exists(avalanx_step_path):
        os.makedirs(avalanx_step_path)

    # os.chdir(os.path.join(pwd_initial, work_dir))
    # os.makedirs(avalanx_step)

    # address_hkl = os.path.join(address_main, directory, name_hkl)
    # address_inp = os.path.join(address_main, directory, name_inp)
    address_main = WORK_DIR_PATH + os.sep + 'dataprocessing' +
    os.sep + DATASETS_NAME
    list_directories = os.listdir(address_main)

    list_dirs_failed = []
    list_dirs_failed_inp = []

    list_energies = []
    list_intensities = []

    Dados = []

    multiplicity = 1

    for directory in list_directories:
        if os.path.isdir(os.path.join(address_main, directory)):
            address_hkl = os.path.join(address_main, directory,
            NAME_HKL_FILE)
            address_inp = os.path.join(address_main, directory,
            NAME_INP)

            if os.path.exists(address_hkl):
                data = search_reflection(reflection, address_hkl)
            else:
                list_dirs_failed.append(directory)
                continue

            if os.path.exists(address_inp):
                energy = search_energy(address_inp)
                # print(energy)
                ### Search distance
            else:
                list_dirs_failed.append(directory)
                continue

            if energy==None:
                list_dirs_failed_inp.append(directory)
```

```python
        continue

    if len(data)==0:
        continue

    mult0 = len(data)

    if mult0 > multiplicity:
        multiplicity = mult0


    for dados_ref in data:
        Dados.append(dados_ref)
        list_energies.append(energy)
        print(intensity, reflection, directory)
        # list_intensities.append(intensity[0]) # It always gets
          just the first intensity
    print('Multiplicity of reflection %s %s %s is %d' %
tuple(reflection + [multiplicity]))

    list_energies = np.array(list_energies)
    Dados = np.array(Dados)
    ### Add energies list as last column
    Dados = np.hstack((Dados, list_energies.reshape(-1,1)))

    split_data_list = [Dados]

    if multiplicity > 1:
        #tenta separar os dados
        split_data_list = split_multiple_reflection(Dados,
multiplicity)


    for idx_dados, Dados in enumerate(split_data_list):
        index = Dados[:,-1].argsort()
        Dados = Dados[index, :]

        name_file = reflection[0] + reflection[1] + reflection[2] +
'_%2d' % idx_dados +'.txt'
        address_file = os.path.join(avalanx_step_path, name_file)

        np.savetxt(address_file, Dados)


        # #### generate plots
        # fig = plt.figure()
        # ax = fig.gca()
        # ax2 = ax.twiny()
        #
        # fs = 16
        # symb = ',_'
        # ext = 'png'
        #
        # plot_output = reflection[0] + reflection[1] +
reflection[2] + '.' + ext
        # address_plot = os.path.join(avalanx_step_path, plot_output)
        #
        # ax.plot(list_energies, Dados[:, 0], symb) ###############
        # ax.set_xlabel(r'Wavelength ($\AA$)', fontsize=fs) ########
        # ax.set_ylabel('Intensity a.u.', fontsize=fs)
        #
        # energy_ev = 12398.4193/list_energies
        #
        # # ax2 = ax.secondary_xaxis('top', functions=(wav2ev,
wav2ev))
        # ax2.plot(energy_ev, Dados[:, 0], symb)
        # ax2.invert_xaxis()
        #
        # ax2.set_xlabel('Energy (eV)', fontsize = fs, labelpad=15)
        # ax.grid()
        #
        # # ax.ticklabel_format(axis='y', style='sci',
scilimits=(0,0))
        #
        # ax.set_title('Reflection: '+reflection[0]+' ' +
reflection[1] + ' ' + reflection[2], fontsize=18, pad=20)
        # fig.tight_layout()
        # fig.savefig(address_plot) ###########
        #


# Define inp file address
inp_address = "avalanx.inp"  # input file - user defined

fh_variables = open(inp_address, 'r')
REFLECTIONS = []
reflections_counter = 0
for line in fh_variables:
    # print(line)
    exec(line)
    if line.startswith('REFLECTION_'):
        reflections_counter += 1
        exec('REFLECTIONS.append(REFLECTION_%d)' %
reflections_counter)

avalanx_step_path0 = WORK_DIR_PATH + os.sep + 'dafs'

if not os.path.exists(avalanx_step_path0):
    os.mkdir(avalanx_step_path0)
```

```python
189    if not os.path.exists(avalanx_step_path0+ os.sep + DATASETS_NAME):
190        os.mkdir(avalanx_step_path0 + os.sep + DATASETS_NAME)
191
192    avalanx_step_path = avalanx_step_path0 + os.sep + DATASETS_NAME
193
194    if NAME_HKL_FILE == 'XDS_ASCII.HKL':
195        IDX_PSI = -2
196    elif NAME_HKL_FILE == 'INTEGRATE.HKL':
197        IDX_PSI = -3
198    elif NAME_HKL_FILE == 'XDS_ASCII_scaled_2.HKL':
199        IDX_PSI = -3
200
201
202    for reflection in REFLECTIONS:
203        dafs_reflection_raw(reflection)
204
```

```python
import os
from shutil import copyfile
from sys import argv

# Functions
def edit_inp_generator():
    file_name = os.path.join(AVALANX_SCRIPTS_DIR, 'geninpav1xRUN.INP')

    f_fonte = open(file_name, 'r')
    f_dest = open('temp.INP', 'w')

    for line in f_fonte:
        if line.startswith('UNIT_CELL_CONSTANTS'):
            f_dest.write('UNIT_CELL_CONSTANTS= %s    ! put correct
values if known\n' % UNIT_CELL)
        elif line.startswith('SPACE_GROUP_NUMBER'):
            f_dest.write('SPACE_GROUP_NUMBER= %d        ! 0 if
unknown\n' % SPACE_GROUP_NUMBER)
        elif line.startswith('STRONG_PIXEL'):
            f_dest.write('STRONG_PIXEL= %d          ! COLSPOT: only
use strong reflections (default is 3)\n' % STRONG_PIXEL)
        elif line.startswith('MINIMUM_NUMBER_OF_PIXELS_IN_A_SPOT'):
            f_dest.write('MINIMUM_NUMBER_OF_PIXELS_IN_A_SPOT=
%d                           !default of 6 is sometimes to high\n' %
MINIMUM_NUMBER_OF_PIXELS_IN_A_SPOT)
        else:
            f_dest.write(line)

    f_dest.close()
    f_fonte.close()

    os.rename('temp.INP', file_name)
    return file_name

def search_detector_distance(endereco, snippet='DETECTOR_DISTANCE'):
    fh = open(endereco, 'r')
    DD = None
    for line in fh:
        if line.startswith(snippet):
            parts = line.split('=')
            parts = parts[1].split('!')
            DD = float(parts[0])
            # print(parts[1])

    return DD


def search_energy(endereco, snippet='X-RAY_WAVELENGTH'):
    fh = open(endereco, 'r')
    Energy = None
    for line in fh:
        if line.startswith(snippet):
            parts = line.split('=')
            Energy = float(parts[1])
            # print(parts[1])

    return Energy

def get_prefix(file_list):
    prefix = None
    file_list.sort()
    for name in file_list:
        if name.endswith('.cbf') or name.endswith('.h5'):
            idx_ = name.rfind('_')
            prefix = name[0:idx_]
            break

    return prefix

# Define inp file address
inp_address = argv[1] # input file - user defined
                                # for after: write instructions of
                                # how it must be written

# Execute general definitions
fh = open(inp_address, 'r')
for line in fh:
    exec(line)

if not os.path.exists(WORK_DIR_PATH):
    os.mkdir(WORK_DIR_PATH)

if not os.path.exists(WORK_DIR_PATH + os.sep + 'dataprocessing'):
    os.mkdir(WORK_DIR_PATH + os.sep + 'dataprocessing')

if not os.path.exists(WORK_DIR_PATH + os.sep + 'dataprocessing' +
os.sep + DATASETS_NAME):
    os.mkdir(WORK_DIR_PATH + os.sep + 'dataprocessing' + os.sep +
DATASETS_NAME)

# DATASETS_NAME = 'p200_teste'

# AVALANX_SCRIPTS_DIR ----> where scripts are
# WORK_DIR_PATH -----> where avalanx writes
# DATASETS_DIR -----> where all the data is stored

# ### the following parameters are global AvalanX parameters
```

```python
 93  #
 94  #
 95  # ##locations
 96  #
 97  # AVALANX_SCRIPTS_DIR = '/home/leonardo/MEGA/Python-curso/Lud/
        avalanx_lud'
 98  # WORK_DIR_PATH = '/home/leonardo/Documentos/Dados_lud/xrdDATAref/
        xrdDATAref/py200jun2'
 99  # DATASETS_DIR = '/home/leonardo/Documentos/Dados_lud/xrdDATAref/'
100  # ##
101  # ##
102  #
103  #
104  #
105  # ### the following parameters are input values for XDS
106  #
107  # UNIT_CELL = '12 4.5 6 90 90 90'
108  # SPACE_GROUP_NUMBER = 14
109  # STRONG_PIXEL = 6
110  # MINIMUM_NUMBER_OF_PIXELS_IN_A_SPOT = 3
111  #
112  # ### the following parameters are input values for avalanx_dafs
113  #
114  # NAME_HKL_FILE = 'afterconv.hkl'
115  # NAME_INP = 'XDS.INP'
116  # REFLECTION_1 = ['1','0','0']
117  # REFLECTION_2 = ['4','0','0']
118  # REFLECTION_3 = h k l
119  # REFLECTION_4 = h k l
120  # ## REFLECTION_5 = h k l
121  # ##
122  # ### the following parameters are output graph settings
123  #
124  # ENERGY_UNIT = 'ANGS'      ## NM      EV      CM-1
125  # PLOT_X = 'ENERGY'
126  # PLOT_Y = 'INTENSITY'      ## ABS_COEFF
127  #
128  LIST_DDxE = []  #list of detector distance X energy
129
130  # Edit XDSINP generator file and change it to executable
131  XDSINP_generetor_address = edit_inp_generator()
132  print('chmod +x %s' % XDSINP_generetor_address)
133  os.system('chmod +x %s' % XDSINP_generetor_address)
134
135  # Read list od dirs of dataset
136  list_data_dirs = os.listdir(DATASETS_DIR)
137
138  XDSINP_GEN_COMMAND = XDSINP_generetor_address + ' "' + DATASETS_DIR
        + os.sep + '%s' + os.sep + '%s_?????.cbf"'
139  PREFIX_OUTPUT = 'avxdp '
140  print(XDSINP_GEN_COMMAND)
141
142  list_failures = [[], []]
143
144  for dir in list_data_dirs:
145      print(dir)
146      # create dir in WORK_DIR_PATH
147      dir_output = os.path.join(WORK_DIR_PATH, 'dataprocessing',
            DATASETS_NAME, PREFIX_OUTPUT + dir)
148
149      if not os.path.exists(dir_output):
150          os.mkdir(dir_output)
151
152      file_list = os.listdir(DATASETS_DIR + os.sep + dir)
153      # print(file_list)
154      prefix = get_prefix(file_list)
155      # print(prefix)
156      os.chdir(dir_output)
157      # execute the xds inp generator
158      os.system(XDSINP_GEN_COMMAND % (dir, prefix))
159      if not os.path.exists('XDS.INP'):
160          continue
161      DD = search_detector_distance('XDS.INP')
162      Energy = search_energy('XDS.INP')
163      LIST_DDxE.append((DD, Energy))
164      os.system('xds XDS.INP')
165      ##############################################
166      ##############################################
167      files_generated = os.listdir()
168      if 'XDS_ASCII.HKL' not in files_generated:
169          list_failures[0].append(DATASETS_DIR + os.sep + dir)
170          continue
171
172      copyfile(AVALANX_SCRIPTS_DIR + os.sep + 'XSCALE.INP', dir_output
            + os.sep + 'XSCALE.INP')
173      os.system('xscale ')  #+ AVALANX_SCRIPTS_DIR + os.sep +
            'XSCALE.INP')
174
175      files_generated = os.listdir()
176
177      if 'scaled.ahkl' not in files_generated:
178          list_failures[1].append(DATASETS_DIR + os.sep + dir)
179          continue
180
181      copyfile(AVALANX_SCRIPTS_DIR + os.sep + 'XDSCONV.INP',
            dir_output + os.sep + 'XDSCONV.INP')
182      os.system('xdsconv')
183
184
185  if len(list_failures[0]) > 0.
```

```python
        log_xds_address = os.path.join(WORK_DIR_PATH, 'dataprocessing',
        DATASETS_NAME, 'xds_failures.log')
        fh_xds_failures = open(log_xds_address, 'w')
        for dir in list_failures[0]:
            fh_xds_failures.write(dir + '\n')
        fh_xds_failures.close()

    if len(list_failures[1]) > 0:
        log_xscale_address = os.path.join(WORK_DIR_PATH,
        'dataprocessing', DATASETS_NAME, 'xscale_failures.log')
        fh_xscale_failures = open(log_xscale_address, 'w')
        for dir in list_failures[1]:
            fh_xscale_failures.write(dir + '\n')
        fh_xscale_failures.close()

    if len(LIST_DDxE)>0:
        DDxE_address = os.path.join(WORK_DIR_PATH, 'dataprocessing',
        DATASETS_NAME, 'DDxE.txt')
        fh_DDxE = open(DDxE_address, 'w')
        for dd,ee in LIST_DDxE:
            fh_DDxE.write('%f %f\n' % (dd, ee))
        fh_DDxE.close()

    # print(list_failures)
    # Go back to script
    os.chdir(AVALANX_SCRIPTS_DIR)
```